Bioengineered Silk Based Small Diameter Vascular Grafts

A Thesis

Submitted in Partial Fulfillment of the Requirements for the Degree of

DOCTOR OF PHILOSOPHY

by

PRERAK GUPTA

Department of Biosciences and Bioengineering
Indian Institute of Technology Guwahati
Guwahati-781039, Assam, India

July 2021

Dedicated to my Family and Friends

INDIAN INSTITUTE OF TECHNOLOGY GUWAHATI

DEPARTMENT OF BIOSCIENCES AND BIOENGINEERING

STATEMENT

I do hereby declare that the research findings of this thesis is the result of research work carried out by me in the Department of Biosciences and Bioengineering, Indian Institute of Technology Guwahati, Guwahati, India, under the supervision of Prof. Biman B. Mandal.

As per the general norms of reporting research findings, due acknowledgments have been made, wherever the research findings of other researchers have been cited in this thesis.

Date: 07/01/2022

Prerak Gupta

INDIAN INSTITUTE OF TECHNOLOGY GUWAHATI

DEPARTMENT OF BIOSCIENCES AND BIOENGINEERING

CERTIFICATE

It is certified that the work described in this thesis entitled "**Bioengineered Silk Based Small Diameter Vascular Grafts**" by **Mr. Prerak Gupta** for the award of degree of Doctor of Philosophy is an authentic record of the results obtained from the research work carried out under my supervision in the Department of Biosciences and Bioengineering, Indian Institute of Technology Guwahati, India, and this work has not been submitted elsewhere for the award of any other degree.

CERTIFIED

Biman B. Mandal, Ph.D.

(Thesis Supervisor)

Prerak Gupta

(Candidate)

Roll No: 156106029

Date: 07/01/2022

ACKNOWLEDGEMENT

I take this opportunity to thank and acknowledge everyone who has generously extended their support throughout my Ph.D. journey. First and foremost, I extend my sincere gratitude and heartfelt thanks to my supervisor and mentor, Professor Biman B. Mandal, for providing me an excellent opportunity to become a part of his young and dynamic research group. His continuous support and guidance have prodigiously been a constant source of motivation in my research pursuits that have helped me become an independent researcher. I am grateful to him for his insightful suggestions and scientific discussions over the years, which have helped shape this thesis. Being in his lab has been a truly enriching experience for me, both personally and academically.

I would also like to thank my Doctoral committee members Dr. Shankar Prasad Kanaujia, Dr. Manish Kumar from the Department of Biosciences and Bioengineering, IITG, and Dr. Akshai Kumar A.S from the Department of Chemistry, IITG, for their invaluable suggestions and scientific inputs to improve my thesis work.

I would also like to thank the present and former Heads of the Department of Biosciences and Bioengineering, IITG; Professor Latha Rangan, Professor Kannan Pakshirajan, and Professor V. Venkata Dasu for extending their support through various academic and research activities. I acknowledge the Department of Biosciences and Bioengineering, IITG, administrative and technical staff for providing and maintaining the research infrastructure. I would also like to acknowledge the Central Instruments Facility (CIF), IITG, for providing high-end instruments.

Special thanks to my Fulbright mentor, Professor David A. Vorp, University of Pittsburgh, USA, for hosting me in his laboratory during the fellowship tenure and extending his support and guidance through my research activities. I would also like to thank Dr. Justin S. Weinbaum for his guidance and scientific discussions. Their support and scientific inputs have significantly benefitted this thesis work. Thanks for providing an enriching learning experience during my short stay. I would also like to thank Dr. Konstantinos Verdelis, Dr. Jonathan P. Vande Geest, Dr. Kazi Islam, Dr. Morgan V Fedorchak, Dr. Charles S Sfeir, and Professor Steven R. Little from the University of Pittsburgh, USA, for extending their support for experimental work.

I would also like to thank all the collaborators, Professor Samit K. Nandi, Professor Debaki Ghosh (West Bengal University of Animal and Fishery Sciences, Kolkata, India), Dr. Gaurab Ranjan Chaudhuri, Dr. Rup Narayan Bhattacharya (R. G. Kar Medical College and Hospital, Kolkata, India) for helping with animal experiments. I also thank Dr. Manoj Agarwala (GNRC Institute of Medical Sciences, Guwahati, India) for extending his help. I acknowledge Professor Niranjan Karak, Department of Chemical Sciences, Tezpur University, Dr. Neeladri Das, Department of Chemistry, Indian Institute of Technology Patna, and Dr. Nabanita Saha, Centre of Polymer Systems, Tomas Bata University, Czech Republic, for the scientific collaborations.

My special thanks to Dr. Nandana Bhardwaj, Sr. scientist, STANVAC, for extending generous help and support, especially during the initial days of my Ph.D. Her valuable scientific inputs have rationally helped me on several occasions during my research work. She has been a continuous source of motivation.

It is indeed my pleasure to thank all of my lab mates for providing a very positive, cooperative, and scientific lab environment that has helped me overcome both professional and personal setbacks effectively. I want to thank Dr. Manishekhar, Dr. Praveen, Dr. Dimple, Bibhas, Yogendra, Shreya, Joseph, Janani for extending their help during the initial days of my Ph.D. time. The very beginning of my Ph.D. journey would not have been so smooth without your help, thanks a lot! My sincere thanks to current and former lab members Dr. Ankit, Ashutosh, Bibrita, Chitra, Souradeep, Sayanti, Ananya, Priyanka, Omkar, Salma, Sohenii, Suvro, Namit, Garima, Prateek, Sai, Bharat, Sadanand, Waseem, Kunal, Smriti, Anupam, Dr. Rocktotpal, Dr. Biswajeet, Dr. Deepika, Dr. Aparajita, Dr. Rajiv, Dr. Chandramauli, Dr. Bhaskar, Sangeeta, Monisha, Krishnamurthy, Prerna, Triya, Sakshi, Princy, Tarishi, Mimi, Vaishali, and Swapnil for a great company, scientific feedback, and formal discussions, and providing countless memories that I would cherish forever.

I would also like to thank all members of the Vorp lab, Dr. Timothy Chung, Dr. Katherine Lorentz, Dr. Aneesh Ramaswamy, Dr. Eoghan Cunnane, Dr. Darren Haskett, and Yogev, for extending their valuable help and support in every possible manner. It was indeed a remarkable learning experience for me. Their time and efforts are greatly appreciated.

I acknowledge the generous funding support from various agencies. The Ministry of Education (MoE), formerly the Ministry of Human Resource Development (MHRD), is acknowledged for providing research fellowship. Institute of International Education (IIE), New

York, and United States-India Educational Foundation (USIEF) are acknowledged for providing Fulbright-Nehru Doctoral Research Fellowship to pursue research in a USA laboratory. Science and Engineering Research Board (SERB), Department of Science and Technology (DST) is acknowledged for providing international travel assistance to attend a scientific conference.

Finally, I would like to remember my parents, brother, and other family members for their unconditional love and support throughout my Ph.D. journey. Their patience, countless personal sacrifices, and extraordinary faith have motivated me to persistently make extra efforts towards my academic pursuits. I am glad to remember my one-year-old nephew Reyansh for giving me moments of joy and happiness.

Thanks to the Lord, the Almighty, for showering his grace at each and every step!

Prerak Gupta

CONTENTS

ABBREVIATIONS

%	Percent
2D	Two-dimensional
3D	Three-dimensional
AA/*A. assama*	*Antheraea assama*
ADMSCs	Adipose-derived mesenchymal stem cells
AFM	Atomic force microscope
ANGPT1	Angiopoietin 1
APTT	Activated partial thromboplastin time
ASG	Anterior silk gland
AT III	Antithrombin III
bFGF	Basic fibroblast growth factor
BM/*B. mori*	*Bombyx mori*
BM-MNCs	Bone marrow mononuclear cells
BSA	Bovine serum albumin
°C	Degree celsius
CABG	Coronary artery bypass grafting
$CaCl_2$	Calcium chloride
cc	Cubic centimeter
CCL2	Chemokine (C-C motif) ligand 2
CCR7	C-C chemokine receptor type 7
CD133	Cluster of differentiation 133
CD163	Cluster of differentiation 163
CD31	Cluster of differentiation 31
CD54	Cluster of differentiation 54
CD68	Cluster of differentiation 68
cm	Centimeter
COX-2	Cyclooxygenase 2
CT	Computed tomography

CVDs	Cardiovascular diseases
DAPI	4′,6-diamidino-2-phenylindole
DI water	Deionized water
DMOG	Dimethyloxalylglycine
dWJ	Decellularized Wharton's jelly
ECFCs	Endothelial colony forming cells
ECGS	Endothelial cell growth supplement
ECM	Extracellular matrix
ECs	Endothelial cells
EDC	1-Ethyl-3-(3-dimethylaminopropyl) carbodiimide
EDTA	Ethylenediaminetetraacetic acid
EGF	Epidermal growth factor
ELISA	Enzyme-linked immunosorbent assay
eNOS	Endothelial nitric oxide synthase
EPCs	Endothelial progenitor cells
ePTFE	Expanded polytetrafluoroethylene
ESRD	End-stage renal disease
EVs	Extracellular vesicles
FBGCs	Foreign body giant cells
FBR	Foreign body response
FBS	Fetal bovine serum
FDA	Food and Drug Administration
FESEM	Field emission scanning electron microscope
FITC	Fluorescein isothiocyanate
g	Gram
GM-CSF	Granulocyte-macrophage colony-stimulating factor
GSH	Glutathione
GSNO	S-nitrosoglutathione
h	Hour
H&E	Hematoxylin and Eosin
HAVs	Human acellular vessels

HCl	Hydrochloric acid
HDF	Human dermal fibroblast
HFP	Hexafluoro-2-propanol
hSV	Human saphenous vein
HUASMC	Human umbilical artery smooth muscle cell
HUVEC	Human umbilical vein endothelial cell
IFC	Immunofluorescence
IFN-γ	Interferon gamma
IGF-1	Insulin-like growth factor 1
IgG	Immunoglobulin G
IHC	Immunohistochemistry
IL-10	Interleukin-10
IL-13	Interleukin-13
IL-1β	Interleukin 1 beta
IL-2	Interleukin-2
IL-4	Interleukin-4
IL-6	Interleukin-6
IL-8	Interleukin-8
iPSCs	Induced pluripotent stem cells
IVC	Inferior vena cava
JV	Jugular vein
kDa	Kilodalton
kg	Kilogram
LDH	Lactate dehydrogenase
LiBr	Lithium bromide
LIMA	Left internal mammary artery
LPS	Lipopolysaccharide
M	Molar
MCP-1	Monocyte chemoattractant protein-1
MHC II	Major histocompatibility complex II
min	Minute

mL	Milliliter
mm	Millimeter
mM	Millimolar
mmHg	Millimeter mercury
MMP	Matrix metalloproteinase
MPa	Megapascal
MPs	Microparticles
MSCs	Mesenchymal stem cells
MSG	Middle silk gland
MVEC	Microvascular endothelial cells
MWCO	Molecular weight cut-off
N	Newton
N/m	Newton/meter
Na_2CO_3	Sodium carbonate
NaCl	Sodium chloride
NaOH	Sodium hydroxide
NBF	Neutral buffered formalin
NHS	N-Hydroxysuccinimide
NK cells	Natural killer cells
nm	Nanometer
NO	Nitric oxide
PAD	Peripheral artery disease
PAI-1	Plasminogen activator inhibitor-1
PBS	Phosphate buffered saline
PCL	Polycaprolactone
PCR	Polymerase chain reaction
PCRO	Picrosirius red
PDGF	Platelet-derived growth factor
PDMS	Polydimethylsiloxane
PE	Polyester
PEG	Poly (ethylene glycol)

PEO	Poly (ethylene oxide)
PEUU	Poly (ester-urethane) urea
PF4	Platelet factor 4
pg	Picogram
PGA	Poly (glycolic Acid)
PGDE	Poly (ethylene glycol diglycidyl ether)
PGI2	Prostacyclin
PGS	Poly (glycerol sebacate)
pIMA	Porcine internal mammary artery
PLA	Poly (lactic Acid)
PLCL	Poly (L-lactide-co-caprolactone)
PLGA	Poly (lactic-co-glycolic acid)
PLLA	Poly (L-lactic acid)
PMA	Phorbol 12-myristate 13-acetate
PR/*P. ricini*	*Philosamia ricini*
PRP	Platelet rich plasma
PSG	Posterior silk gland
psi	Pound per square inch
PT	Prothrombin time
PTFE	Polytetrafluoroethylene
PU	Polyurethane
PVA	Polyvinyl alcohol
RGD	Arginine-Glycine-Aspartic acid
RMS	Root mean square
rpm	Rotations per minute
RT	Room temperature
SD	Standard deviation
SDS	Sodium dodecyl sulfate
sec	Second
SF	Silk fibroin
SIS	Small intestinal submucosa

SMCs	Smooth muscle cells
SMGS	Smooth muscle cell growth supplement
SM-MHC	Smooth muscle myosin heavy chain
SVF	Stromal vascular fraction
SVG	Saphenous vein grafts
TAT	Thrombin-antithrombin
TCP	Tissue culture plate
TEBVs	Tissue-engineered blood vessels
TEVGs	Tissue-engineered vascular grafts
TF	Tissue factor
TGF-β	Transforming growth factor beta
TNF-α	Tumor necrosis factor alpha
tPA	Tissue plasminogen activator
TT	Thrombin time
U	Units
UV	Ultraviolet
VE-cadherin	Vascular endothelial cadherin
VEGF	Vascular endothelial growth factor
VVG	Verhoeff-van gieson
vWF	Von Willebrand factor
w/v	Weight/volume
w/w	Weight/weight
WHO	World health organization
wt.	Weight
α	Alpha
αSMA	Alpha smooth muscle actin
β	Beta
µg	Microgram
µL	Microliter
µm	Micrometer
ϕ	Diameter

LIST OF TABLES

LIST OF FIGURES

CHAPTER 1

Introduction and review of literature

This chapter provides a progressive overview of vascular tissue engineering, which has made prodigious progress in recent years by converging multidisciplinary approaches. While traditional therapeutic methods rely on bypassing the severely damaged vessels with synthetic counterparts and no growth potential, contemporary perspectives focus on biodegradable conduits bestowing inherent remodeling capability. In this regard, various synthetic and natural bioresorbable materials are appraised, followed by the current implications of silk in the field.

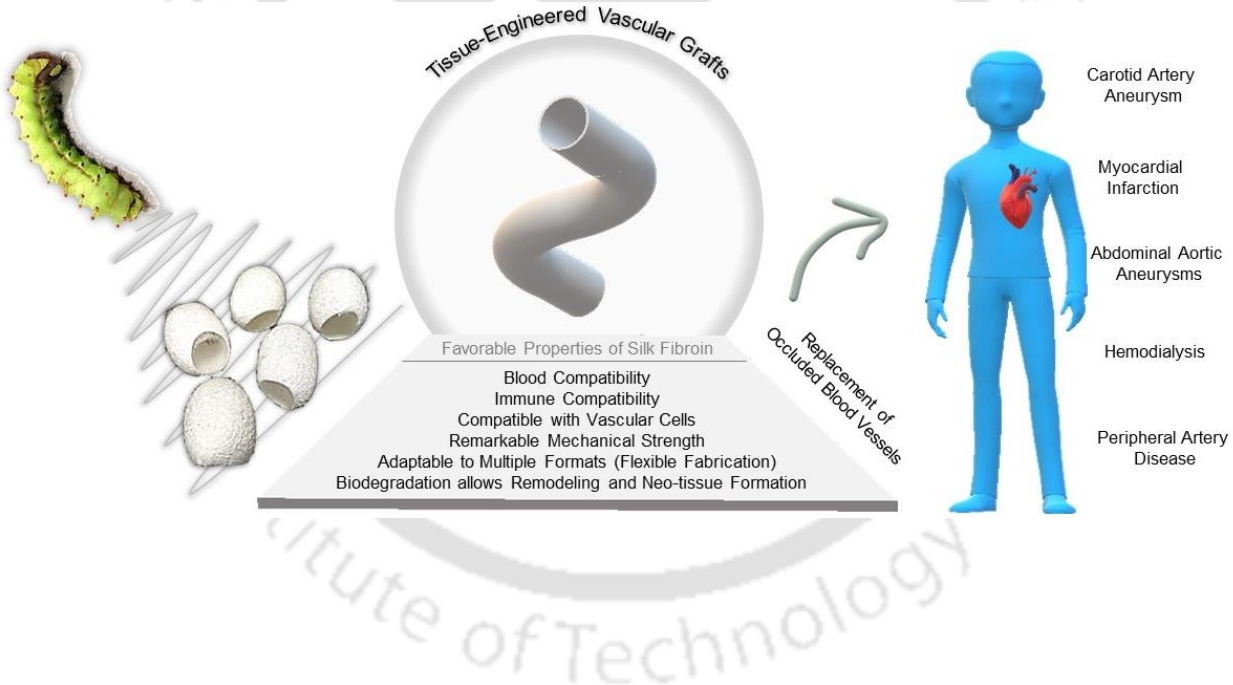

Publications:

Prerak Gupta *and Biman B, Mandal. Tissue-Engineered Vascular Grafts: Emerging Trends and Technologies.* ***Advanced Functional Materials****, 2021, 2100027. (DOI: 10.1002/adfm.202100027)*

Prerak Gupta *and Biman B. Mandal. Silk Biomaterials for Vascular Tissue Engineering Applications. (Revision submitted to '****Acta Biomaterialia****')*

Introduction and review of literature

1.1 Introduction

Alarming mortality rates due to cardiovascular diseases (CVDs) arising from blockage or narrowing of vital blood vessels are of serious concern. The global disease burden and subsequent deaths are projected to escalate exponentially, with an estimated 23.4 million deaths in 2030 [1, 2]. The majority of CVDs stem from narrowing or blockage of vital blood vessels, which results in interrupted blood supply to the target organ and eventual ischemia. Some of the most commonly occurring CVDs are peripheral artery disease, cerebrovascular disease, deep vein thrombosis, and coronary artery disease. Bypassing the blood supply through an autologous graft via surgical intervention is currently the clinicians' preferred treatment choice [3]. Following are some of the reasons why autologous grafts are presently the gold standard for bypass surgeries: 1) they are physiologically the natural analogs of the diseased blood vessel which do not evoke immune response after implantation, hence no chance of graft rejection; 2) their lumen is naturally lined with endothelial cells which prevent thrombosis and SMC proliferation; 3) graft compliance and mechanical properties closely match the recipient site which attenuates the chance of intimal hyperplasia; 4) being originated from the patient him(her)self, no regulatory clearance is required; 5) they are readily available and finally; 6) they can grow in size with patient's age. Commonly used autografts are saphenous vein, radial artery, and mammary artery [3].

The primary setback of using autologous grafts is donor site morbidity. In several cases, their unavailability due to prior harvesting or diseased condition exacerbates the situation precluding the possibility of auto-grafting. In this scenario, another viable option for clinicians is prosthetics [4]. Synthetic grafts (e.g., Gore-Tex and Dacron) currently dominate the global vascular grafts market, with an estimated value of 2.01 billion USD in 2018. A substantial portion is contributed by endovascular stent-grafts, hemodialysis access grafts, and peripheral vascular grafts (source: www.grandviewresearch.com). Notably, the application of synthetic grafts is limited to larger blood vessel (>6 mm diameter) replacement, and they face daunting obstacles when implemented for high pressure, small diameter blood vessels (<6 mm diameter) due to thrombosis and stenosis [5]. Besides, they are prone to chronic foreign body reaction, calcification, and risk of infection. The reason behind the poor performance of synthetic grafts is compliance mismatch and their non-biological composition [6]. Researchers are venturing into the surface

modification of these grafts to prevent thrombosis [7]. Amidst all the success, if we look at the vascular graft market with a clinical perspective, limited innovative products are coming up with the ever-persistent inability of synthetic grafts for smaller vessel replacement.

In pursuit of finding a clinically feasible alternative for small-diameter vessel replacement, tissue-engineered vascular grafts (TEVGs) are currently a popular choice [3, 8]. The aim of TEVGs is to provide the structural framework for host cells to re-grow the functional tissue. The overall idea is to design a scaffold (a tubular scaffold in this context) using a biodegradable polymer, seeding patient-specific cells, maturation in a naturally simulated dynamic microenvironment, and implantation into the patient. With time, the graft polymer is degraded and replaced by a newly formed ECM in a precisely balanced manner preserving the structural integrity, leaving behind a native-like regenerated tissue [5]. These lab-made grafts have the potential to mimic the autografts properties with high fidelity. Research in the field is now profoundly focused on conferring autologous grafts' properties into TEVGs for their clinical translation. Vascular tissue engineering has grown remarkably in the past few decades since the seminal groundwork laid by Weinberg and Bell in 1986 [9]. Scientists have investigated a plethora of different approaches to creating a clinically feasible small-diameter blood vessel that has remarkably improved our understanding. While various synthetic and natural biomaterials have been explored to create bioresorbable vascular grafts, silk renders several advantages in terms of biocompatible degradation products, abundant availability and affordability.

Silk is an ancient textile material that has long been used as sutures in surgery owing to its biocompatibility and remarkable tensile strength. This natural protein biopolymer is produced by various insects (silkworms, scorpions, spiders, and flies) [10]. SF biomaterials provide numerous favorable inherent properties, that has enabled their remarkable performance in the past few decades as a potential biomaterial for various tissue engineering applications [11-13]. Among other variants, regenerated silk fibroin obtained from *Bombyx mori* silkworm cocoons is widely explored for regenerative medicine. Some of the silk-made bioengineered products have been approved by FDA for clinical implementation, including SERI surgical scaffold® and Silk Voice® [13]. Few exemplary characteristic properties of SF biomaterial that make it a suitable choice for tissue engineering applications include: 1) biocompatibility, 2) tunable biodegradation, 3) minimally immunogenic, 4) ability to adapt various formats (3D scaffolds, thin films, nanofibers, microspheres, nanoparticles, hydrogels, etc.), 5) extraordinary mechanical strength, 6) easy

accessibility, 7) cost-effective, 8) easy green processing [11, 14]. In addition to the other potential areas of regenerative medicine, silk biomaterials are actively being investigated to explore their potential for vascular tissue engineering applications [15]. Despite the remarkable promising aspects of SF biomaterials in various domains of tissue engineering, their implementation in creating tissue-engineered vascular grafts has witnessed a comparative scarcity. Moreover, a significant proportion of prior literature suggests the predominant application of silk fibroin obtained from domesticated *Bombyx mori* silk variety, possibly due to wide availability. Other non-mulberry silk varieties have sparsely been explored in this domain, possibly due to their geographical restrictions. Nevertheless, lately, researchers are actively investigating silk-based TEVGs prepared by diverse fabrication methodologies in pre-clinical settings, and have shown very encouraging outcomes.

In this thesis, we have progressively explored various approaches to fabricate clinically viable silk-based small-diameter vascular grafts. Towards this end, both mulberry (*Bombyx mori*) and non-mulberry (*Antheraea assama* and *Philosmia ricini*) silk varieties are explored in the domain of vascular tissue engineering. In addition, crucial factors were identified that would improve the clinical feasibility of vascular grafts. These factors rely on either biomaterial property (biocompatibility, immune compatibility, blood compatibility, biodegradation, mechanical properties, cost-effectiveness) or fabrication approach (fabrication time/ready availability). From a biomaterial perspective, silk fibroin remains a rational choice, whereas various fabrication approaches are pragmatically investigated. This thesis work first investigates the cell-biomaterial interaction to substantiate the suitability of silk for vascular regeneration. The first fabrication approach capitalizes on the principle of bionics, wherein a cellular multilayered TEVG is explored while recapitulating the native-like cellular arrangement. In the second approach, a novel bi-layered vascular graft is developed, and the fabrication time is further reduced from months to days by implementing human SVF cells (without culture) instead of vascular cells. The third and fourth approaches set out to provide a ready available vascular graft while completely bypassing the cell seeding step. In these cases, the bioactivity is preserved by means of functionalizing the acellular grafts with decellularized human Wharton's jelly matrix and CCL2, which locally provide cell-secreted bioactive paracrine factors conferring constructive graft remodeling. Research work carried out in this thesis offers the excellent pre-clinical success of developed vascular grafts in animal models (rats/rabbits).

1.2 Review of literature

1.2.1 Structural components of blood vessels

Blood vessels are comprised of three concentric layers: 1) tunica adventitia, 2) tunica media, and 3) tunica intima (**Figure 1.1**). Each layer has distinct cell types and ECM proteins arranged in a specific manner. The innermost tunica intima consists of a longitudinally aligned monolayer of endothelial cells along the lumen resting on a thin basement membrane. It provides a natural anticoagulant surface, maintains vascular tone, and regulates the nutrient transport from blood to the parenchymal tissue. The middle layer consists of multiple layers of circumferentially aligned SMCs densely packed in elastin and collagen matrix, confining distensibility. Microvascular pericytes are also present in tunica media. Multiple cell types (including fibroblasts, macrophages, B cells, T cells, myofibroblasts, dendritic cells, hematopoietic, mesenchymal, and endothelial progenitor cells) reside in outermost adventitial layer. In larger blood vessels, a capillary network (vasa vasorum) is present in the adventitia, which provides nutrition to the vessel wall [16].

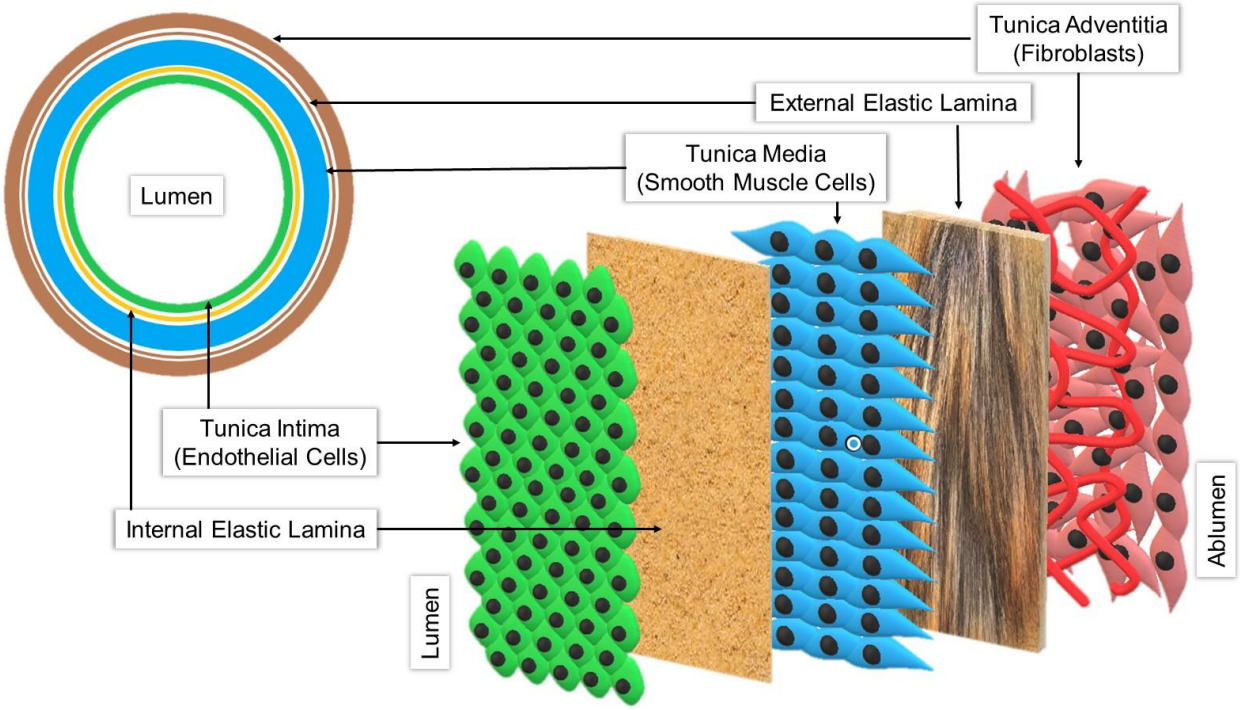

Figure 1.1. *Scheme representing the multilayered components of a blood vessel.*

1.2.2 An overview of vascular tissue engineering

Coronary artery blockage leads to the inadequate blood supply to the heart muscle, causing ischemia and eventually myocardial infarction. Atherosclerosis, which was conventionally

believed to be solely originating from the deposition of cholesterol plaques along the wall and is now known to be associated with inflammation, is the most common cause of artery blockage [17, 18]. In 1960, Robert Goetz and colleagues performed the first coronary artery bypass grafting (CABG) using Rosenak (tantalum) rings [19], and later in 1962, David Sabiston successfully anastomosed right coronary artery with saphenous vein graft without rings in a completely hand sewn manner [20]. It was the starting point of bypass surgery using autologous grafts, which remains the gold standard after almost six decades. The saphenous vein, internal mammary artery, and radial artery are the most frequently used autologous grafts; however, the literature suggests that the chances of vein graft failure are more likely than arterial grafts for CABG [21]. The anatomical differences between veins and arteries make vein grafts more susceptible to aneurysms and thrombosis when used for an arterial replacement. The longevity of arterial grafts is markedly superior. The outperformance of arterial grafts could be attributed to either higher prostacyclin production [22] or a mature vasa vasorum network in the arterial adventitia, which ensures better blood supply in the vessel wall [23]. Among various autografts, the left internal mammary artery (LIMA) remains the most preferable and successful choice of clinicians for CABG because of its patency rates (better than SVG) post revascularization. The superior patency of LIMA is attributed to lesser fenestrations in the endothelial layer, higher production of NO, and other antithrombotic molecules (tissue plasminogen activator and heparin). The limited permeability of endothelial cell layer makes it impervious for lipoproteins, hence minimal chances of atherosclerosis [24].

Soon after CABG became the standard therapeutic approach for coronary artery disease, doctors realized the limited availability of autografts and started exploring synthetic grafts (most commonly used are: Dacron and PTFE). Synthetic grafts were developed before the routine use of autologous grafts. Almost a decade after the development of Dacron by J.T. Dickinson and J.R. Whinfield, DeBakey was the first to use them for aortic reconstructive surgery in the early 1950s. Since then, Dacron grafts have been the regularly used synthetics for large diameter vessel revascularization, including lower extremity bypass surgery and aortic replacement [25]. Dr. Roy Plunkett developed another key player in the field, PTFE, at DuPont in the late 1940s; however, its expanded derivative (ePTFE) was launched in the market because of its better compliance and porosity than the former one. ePTFE grafts witnessed first implementation in the vascular surgery field in the mid-1970s as a lower extremity bypass conduit. At present, ePTFE grafts are frequently used for arterio-venous and lower extremity bypass grafting [25]. While synthetics were successful

for replacing larger vessels (>6mm diameter), they performed poorly when used for smaller vessels. Hence continued the search for a suitable grafting vessel. In the 1960s, Charles Sparks first started using silicone tubular structures for arterial replacements [26] and later moved on to a tissue-engineering approach to developing autologous biological tubes. These patient-specific grafts were prepared by subcutaneous implantation of a silicone mandril in the patient's leg, which produced fibrotic tissue tubes as a result of foreign body response and referred to as 'Sparks mandril'. The clinical trials of Sparks mandril were continued up to the late 1970s, but their dismal patency rate and aneurysmal behavior forced researchers to abandon them [27].

In the 1980s, in a seminal study, Weinberg and Bell came up with the idea of producing the first *in vitro* TEVG consisting of vascular cells [9]. They created a native-like multilayered vessel composed of collagen gel embedded with bovine aortic vascular cells (fibroblasts, smooth muscle cells, and endothelial cells). The incorporation of Dacron sleeves facilitated tubular integrity and improved mechanical strength. Organogenesis, Inc. tried taking up this technology but failed to bring out any viable product [5]. Nonetheless, this was the starting point for tissue-engineered vascular grafts, and the idea still exists today after 34 years. Following the groundwork laid by Weinberg and Bell, many investigators started looking into various aspects aiming to create a functional blood vessel analog. Zilla, Deutsch, and colleagues showed strong evidence of synthetic grafts' clinical success (ePTFE) seeded with autologous endothelial cells [28]. In a long-term study over 15 years, they implanted 341 ePTFE grafts in a cohort of human subjects at femoropopliteal and femorodistal locations. The grafts' lumen was first coated with fibrin glue, followed by lining with autologous endothelial cells obtained from segments of saphenous, basilica, external jugular, and cephalic veins. After years, the primary patency rates of endothelialized ePTFE grafts were comparable with vein grafts validating their feasibility in clinical settings [28]. Despite encouraging outcomes, this technology's prevalent adoption is limited, likely due to the need to harvest an optimal amount of autologous endothelial cells and their expansion. Moreover, ensuring the long-term adherence of endothelial cells to synthetic surfaces is another challenging task.

In 1998, Nicolas L'Heureux and colleagues came up with the idea of creating a completely biological tissue-engineered blood vessels without using any supporting material [29]. The concept relied on the self-assembly of cell sheets, which were prepared by maintaining a confluent monolayer culture of SMCs and fibroblasts for extended periods in the presence of sodium

ascorbate. The obtained cell sheets were rolled sequentially onto inert mandrel and matured in a pulsatile bioreactor for at least 8 weeks. The long-term maturation allowed cohesion of consecutive cell-sheet layers providing a self-assembled tubular graft. Endothelial cells were seeded in the lumen at the later stage. The burst strength of these mechanically robust grafts was nearly 2000 mmHg, attributed to an organized collagen matrix [29]. Interposition grafting in the canine model demonstrated optimal suturability. Completely biological TEBVs supposedly have multiple theoretical advantages, including inherent self-renewing potential, on-demand remodeling, precludes foreign body reaction, and minimal chances of graft infection. Cytograft Tissue Engineering, Inc. took up this technology for phase I clinical trials in a hemodialysis access setting. Unfortunately, the outcomes were not very encouraging, as the implanted grafts showed signs of dilatation over time [30-32].

The groundwork of the currently most advanced engineered blood vessel was laid by Niklason *et al.* in the late 1990s [33]. For the first time, the investigators used a rapidly degrading polymer, PGA, as supporting material for growing vascular cells. The degraded byproducts of PGA are metabolized by cells without inducing a chronic immune response. Bovine SMCs and ECs were cultured onto tubular PGA scaffold under physiologically relevant pulsatile perfusion system for extended periods, creating native-like blood vessel constructs. Implantation in the porcine right saphenous artery revealed good patency after four weeks. Derivatives of this technology were further developed to render immune compatibility and ready availability. In 2003, the same group showed cells' removal from engineered vessels without compromising the mechanical properties [34]. The underlying idea was to obtain a tubular construct consisting of natural ECM derived from allogenic or xenogenic SMCs, followed by decellularization. The resulting vessels can be stored for longer periods. When required, the grafts can be retrieved, seeded with autologous ECs, and implanted in the patient. The technology was transferred to Humacyte, Inc, which initiated the clinical trials in hemodialysis access setting [35]. Notably, the HAVs were tested without autologous ECs seeding but were shown to have a mature endothelial layer in 16 weeks' explants. HAVs are currently in phase III clinical trials, wherein their applicability as hemodialysis conduit is being tested compared with ePTFE grafts and fistulas [3]. Tissue-engineered vascular grafts composed of biodegradable polymers became a trend after Shinoka first implanted a synthetic biodegradable scaffold in 2001 [36]. The patient was born with a single ventricle and pulmonary atresia. The PCL-PLA copolymer-based tubular scaffold (10 mm

diameter) was seeded with autologous vascular cells isolated from a peripheral vein and used for pulmonary reconstruction with no postoperative complication. The intention was that the implanted graft would grow with patient age and would not require repetitive surgical interventions. Following this breakthrough, Shinoka and Breuer have been exploring the polymeric biodegradable scaffolds in combination with autologous BM-MNCs. It brings down the graft fabrication time from days to hours rendering clinical feasibility. These scaffolds were used in a clinical trial in Japan targeting extracardiac Fontan procedure in children born with single ventricle physiology. The TEVGs were implanted in a low pressure, high flow system, and long-term (10 years) outcomes showed positive results [37-39]. In continuation, an FDA approved U.S. phase I clinical trial investigated the use of these TEVGs in congenital heart surgery [40]. Researchers observed frequent graft narrowing post six months' transplantation requiring angioplasty, which led to a premature clinical trial closure. When analyzed with advanced computational modeling, the observed data revealed the eventual reversal of stenosis over time. Hence, the model was further validated, wherein seeded TEVGs were implanted in 24 lambs as Fontan conduits connecting the pulmonary artery with IVC [40]. The hypothesis stands true even in animal models suggesting the possibility of avoiding angioplasty for patients showing early asymptomatic stenosis; however, regular medical monitoring is required. In addition to the material centric and self-assembly approaches, allogenic and xenogenic grafts are also under active investigation by several research groups [41, 42]. The primary setback of these vessels is acute/chronic rejection, which leads to allograft vasculopathy [43].

Significant efforts have been invested over the past few decades, yet the search for a translatable 'off the shelf' small-diameter vascular substitute continues. On a positive note, various prototypes are in various stages of clinical trials, and hopefully, few are on the verge of success. With the improved understanding gained through past experience, it is crucial to identify and avoid the critical failure mechanisms in the future. One imperative notion is that engineered vessel need not to recapitulate all compositional, physiological, and cellular aspects of native tissue, rather focusing on a few critical aspects should serve the purpose. Foundational and follow up studies in the field indicate a few indispensable criteria for a successful tissue-engineered vascular graft. Especially, while designing a low flow high-pressure arterial substitute, it is necessary to provide blood compatible/anti-thrombogenic lumen. The blood-contacting surface should also prevent platelet adhesion and activation to maintain long-term patency. Immune compatibility is another

crucial aspect. Autologous implants are the only candidates having the privilege of uncontested acceptance; whereas, any foreign (non-self) object activates a cascade of innate/adaptive immune system, leading to rejection. With the latest scientific advancements, the role of the host immune system in constructive graft remodeling is now established [44-46]; however, regulating the immune response in a balanced manner remains a pre-requisite. An exuberant reaction may lead to eventual hyperplasia and stenosis [40]. Another notable aspect is to ascertain the mechanical stability of the implanted graft during remodeling, wherein simultaneous occurrence of matrix degradation and neo-tissue formation takes place in a dynamic microenvironment. An imbalance of these two would succumb graft integrity and may result in aneurysm formation in the long run. Biomechanics of the bioengineered graft needs to be optimized, keeping in mind the initial (including suture retention, dynamic compliance, tensile properties, and burst strength) and post-implantation factors (degradation and remodeling). Besides these mechanical and biological pre-requisites, successful clinical translation demands their ready availability and automated reproducibility. Economic factors like low cost and affordability should not be avoided during the course of graft manufacturing.

1.2.3 Current limitations and emerging strategies in vascular tissue engineering

1.2.3.1 Surface modification with bioactive molecules rendering antithrombogenic effects

Naturally, a continuous endothelium, consisting of endothelial cell monolayer, prevents blood clotting and maintains vascular tone by regulating/synthesizing a series of bioactive molecules including tPA, PAI-1, heparans, plasminogen, thrombin, AT III and plasmin, etc. [47, 48]. Damage in the endothelium exposes underlying ECM proteins, allowing platelet adhesion and initiating the blood coagulation cascade. Activated platelets release several adhesion proteins and pro-thrombotic molecules resulting in a fibrin clot formation. Platelet activation also regulates the expression of cell adhesion molecules (CD31, CD54, E-selectin, and P-selectin) on the ECs' surface, which mediate platelet and leukocyte binding with ECs [49]. Functionalizing TEVGs with natural anticoagulant molecules is the most fundamental approach to prevent acute thrombosis in vascular grafts (**Figure 1.2A**). In this regard, heparin, a natural polysaccharide has been used widely in clinic as an independent anticoagulant molecule. Heparin prevents the platelet adhesion on the lumen wall by interacting with AT III enhancing its affinity towards thrombin [50]. Endothelial cells, present at the interface between flowing blood and vessel wall, experience

constant shear stress stimulating the release of NO via upregulation of eNOS. It leads to PGI_2 mediated vasodilation and inhibits platelet aggregation [49]. NO immobilization has shown tremendous scope towards preventing acute thrombosis in bioengineered vascular grafts [51, 52]. In a recent endeavor, keratin-based vascular graft surfaces were shown to produce NO. The GSH activity breaks the intrinsic disulfides of keratin into thiols catalyzing GSNO, which results in NO production [53, 54]. Enzyme prodrug therapy is another approach, wherein galactosidase immobilized vascular grafts effectively produce NO by decomposing the NO prodrug at the localized site following *in situ* catalysis [55]. Engraftment of TEVG with conjugated linoleic acid confers antithrombotic properties [56]. In order to produce highly effective antithrombotic surfaces, co-immobilization of heparin and NO is envisioned to closely mimic the biochemical effects exerted by the endothelium at the interface of blood and vessel wall [57]. To create a biochemical analog of natural endothelium, coating glycocalyx-like hydrogel comprising of hyaluronic acid on to decellularized TEVGs has shown protective effects against thrombus formation. This novel methodology shields the underlying collagen layer, thereby preventing platelet adhesion and activation [58]. Although most of these technologies have shown remarkable outcomes by preventing blood clot formation in laboratory conditions and pre-clinical trials, their validation in clinical settings is necessary to warrant their translation.

1.2.3.2 Surface modification for rapid endothelialization

Functionalization of vascular grafts with anti-thrombotic molecules ensures the prevention of acute thrombosis; however, their long-term success predominantly relies on endothelialization. Conventionally, seeding autologous vascular endothelial cells before implantation has shown comparable results with vein grafts in clinical settings [28]. One notable advantage of autologous ECs is that the patient need not to undergo immunosuppressive therapy after graft implantation [59]. Despite clinical applicability, restricted adoption of this technology was observed primarily due to limitations associated with autologous ECs harvesting [48, 60]. In addition, *in vitro* expansion of cells and longer maturation time pose further complications owing to their limited regeneration and proliferative capacity. Another setback with *in vitro* endothelialized grafts is the possibility of cell detachment upon implantation under the influence of blood flow [48]. Considering limitations associated with *in vitro* endothelialization of vascular grafts, research impetus is now shifted towards *in situ* endothelialization strategies of TEVGs. After implantation,

the graft is endothelialized by one of the following three mechanisms: 1) Transanastomotic growth, wherein host intimal endothelial cells migrate at the anastomotic site towards the graft center in response to the natural injury-induced mechanism, 2) Transmural growth, wherein endothelial cells reach the lumen via newly formed capillaries through the graft wall, and 3) Fallout process, wherein circulating progenitor cells populate the implanted TEVG (**Figure 1.2B**) [59]. The homeostasis of the vessel wall is disturbed following TEVG implantation arising from altered blood flow patterns and variations in vessel wall stresses. It subsequently triggers the secretion of adhesive proteins from ECs, recruiting leukocytes followed by activation of inflammatory cascade and healing response [61]. In most animal studies implementing smaller TEVGs (1-2 cm), transanastomotic endothelialization is uncontested; however, there is no consensus for longer grafts [6, 62]. Moreover, in humans, natural transanastomotic ingrowth is limited to 1-2 cm [59]. In this scenario, the remaining two mechanisms seem to be predominantly responsible for graft endothelialization in humans. Transmural capillary formation principally relies on foreign body response and granular tissue formation on the ablumen surface [63]. This newly formed tissue allows angiogenesis, resulting in capillary formation. However, it is unclear why these newly formed capillaries grow towards the graft lumen assisting endothelialization. Studies have shown that graft porosity is crucial in order to allow capillary ingrowth [64]. A paucity of information about the underlying mechanism of transmural capillary ingrowth and ambiguous results indicate the need for a further concerted investigation, but the possibility of transmural endothelialization of TEVGs cannot be avoided. Recent innovative approaches are focused on engineering the interface of blood and TEVGs to capture the circulating EPCs and other endothelial forming cells aiming faster endothelialization [52].

1.2.3.3 Preventing intimal hyperplasia

Intimal hyperplasia is a pathological condition characterized by thickening of the vessel wall resulting from overgrowth and migration of medial SMCs into the intimal layer due to endothelium damage [65]. In a healthy blood vessel, endothelium maintains homeostasis by releasing PGI_2 and NO to prevent platelet activation and eventual blood clotting. In addition, it regulates underlying SMCs by restricting their proliferation and assisting a quiescent, differentiated state, exhibiting a contractile phenotype [66]. Any inadvertent damage in the endothelium exposes the medial layer and consequently activates platelets. It initiates the modulation of SMCs' phenotype from

quiescent contractile to a highly proliferative state, causing intimal thickening. Differentiation of adventitial fibroblasts to myofibroblasts also participates in the former event [67]. Surgical implantation of vascular graft damages the endothelium and exposes the medial layer, putting them at high risk of developing intimal hyperplasia. Inducing rapid endothelialization is not enough to prevent the thickening of the graft wall. An effective solution demands concerted efforts to contemporaneously developing innovative approaches, which eventually could prevent graft stenosis. In addition to surgical intervention, which damages the native blood vessel; biological and mechanical properties of TEVGs are the key regulator of hyperplasia development [65]. Inflammation is actively involved with intimal hyperplasia; hence, the level of inflammatory response initiated after TEVG implantation would determine the severity of subsequent stenosis. Inhibition of MCP-1, platelets, and NK cells is effective in abrogating stenosis [45]. Besides other mechanical properties, TEVGs' compliance mismatch with the native vessel is proposed to be responsible for graft stenosis [68]. Aberrant blood flow, wall shear stress, and wall stress further exacerbate the condition [65].

Strategies applied to prevent intimal hyperplasia in bioengineered vascular grafts primarily focus on incorporating drug molecules attenuating SMCs' proliferation and platelet adhesion (**Figure 1.2C**). Potential target drugs to serve the aforementioned purpose include sirolimus or rapamycin [69, 70], cilostazol, aspirin [71] and paclitaxel [72]. In addition, bioresorbable grafts functionalized with imatinib, a PDGF and c-kit receptor kinase inhibitor, attenuated the neotissue formation in mice [73]. Burst release of the drug driven by blood flow minimizes cell-drug interaction, challenging the overall idea. In a novel approach, resveratrol functionalized single-walled carbon nanotubes were coated to form an irregular mesh onto TEVG lumen. The coating was resistant to blood shear stress. Drug internalization by macrophages promoted a pro-healing phenotype and aided in maintaining the graft patency [74].

Anti-proliferative and anti-inflammatory therapeutic approaches have shown their effectiveness in preventing intimal hyperplasia in native and synthetic blood vessel grafts. However, it is surprising that despite being the most fundamental aspect of the development of intimal hyperplasia, compliance mismatch between the native vessel and TEVG is generally overlooked by most, and hypo compliant (stiffer) grafts are implemented. One arguable aspect is that whether it is absolutely necessary to match the graft compliance with the target blood vessel, considering the viewpoint that the majority of research in the field is focused on producing

bioresorbable vascular grafts, which tend to quickly lose their initial compliance as a result of degradation and subsequent remodeling. In an ongoing clinical trial study, with the help of computational modeling and based on outcomes of bioresorbable TEVGs implantation in an ovine model, the spontaneous reversal of stenosis was demonstrated [40].

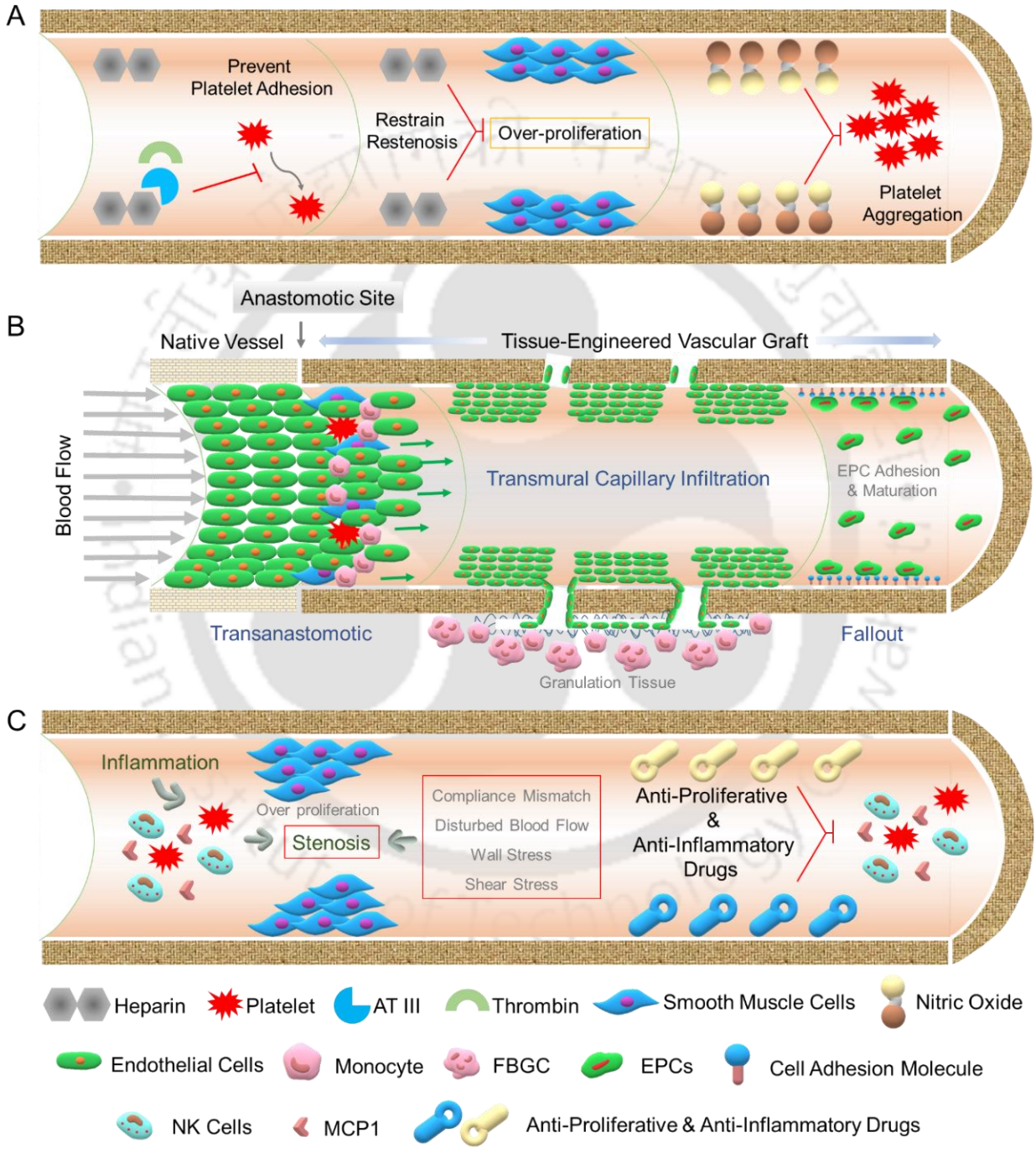

Figure 1.2. *Strategies to improve TEVG performance by surface modification. (A) Scheme representing approaches to prevent thrombosis. (B) An overview of TEVG endothelialization*

mechanisms (transanastomotic growth, transmural capillary infiltration, and fallout process) post-implantation. (C) Strategies to prevent intimal hyperplasia and stenosis by inhibiting the over-proliferation of smooth muscle cells and suppressing the exuberant inflammatory response.

1.2.3.4 Creating biomimetic vascular grafts

Recapitulating the native-like structural properties has long been a goal of tissue engineering following principles of bionics. Blood vessels have a complex structure comprising three distinct layers, homing various vascular cells in a unique arrangement. The structural complexity maintains tissue homeostasis by regulating biological and physical properties. The luminal layer (intima) of the blood vessel is comprised of ECs' monolayer aligned in the direction of blood flow, radially aligned SMCs form the medial layer, and randomly oriented fibroblasts are present in the adventitia [8]. In addition to cell types, collagen, and elastin fibers in the arterial wall are aligned at a particular angle, governing the mechanical properties [75]. Engineering at the cell-substrate interface opens up remarkable avenues to manipulate cell function [76]. An overview of the biomimetic approaches adopted to regulate vascular cell function is provided in **Figure 1.3**. ECs cultured on unidirectionally aligned surface patterns maintained intercellular junctions under the disturbed flow, in contrast to randomly oriented cells. The nanoscale oriented intimal geometry can regulate the graft hemocompatibility and spur *in situ* endothelialization [77, 78]. Similarly, unidirectional alignment of SMCs cultured on micro-patterned substrate help switching from proliferative to contractile phenotype [79], which would eventually help preventing the possibility of intimal hyperplasia. These observations indicate the potential of creating biomimetic grafts endowing native-like ECM and cellular arrangement.

Different research groups have adopted diverse fabrication technologies to produce native-like TEVG. Inspired by the radial alignment of SMCs, tubular scaffolds with circumferentially aligned PLLA nanofibers were prepared by electrospinning using parallel auxiliary electrodes. The resulting aligned substrates induced SMCs' unidirectional alignment by contact guidance, showing implications for TEVG applications [80]. Recapitulating the mechanical and structural anisotropy of native blood vessels, aligned sheets of fibroblast-derived ECM were rolled over a mandrel providing a potential TEVG alternative, while no animal data was provided [81]. In a concerted effort, immobilization of heparin on topographically aligned luminal surface resulted in superior neovessel remodeling, long-term patency, and rapid *in situ* endothelialization in rabbit carotid artery after three months [82]. In an intriguing bioinspired approach, researchers have engineered

the intimal interface by manufacturing self-cleaning actuating surface topography emphasizing the prevention of platelet adhesion and eventual thrombosis [83]. Driven by systolic and diastolic blood pressure, it was postulated that the transition between smooth and wrinkled surfaces and resulting bending energy prevents platelets' interfacial adhesion. In a follow-up study, the same research group revealed that the antithrombotic property of the wrinkled luminal topography depends on its dynamic behavior, and constrained luminal corrugations are susceptible to platelet adhesion [84]. These observations could epitomize the self-cleaning ability of natural blood vessel intima. The overall biomimetic approach covers two broad perspectives. While circumferential alignment of medial SMCs aims to improve mechanical properties and prevent hyperplasia by restricting the cellular overgrowth, the nanolamellar luminal topography targets orchestrating the anti-thrombotic surface by preventing platelet adhesion.

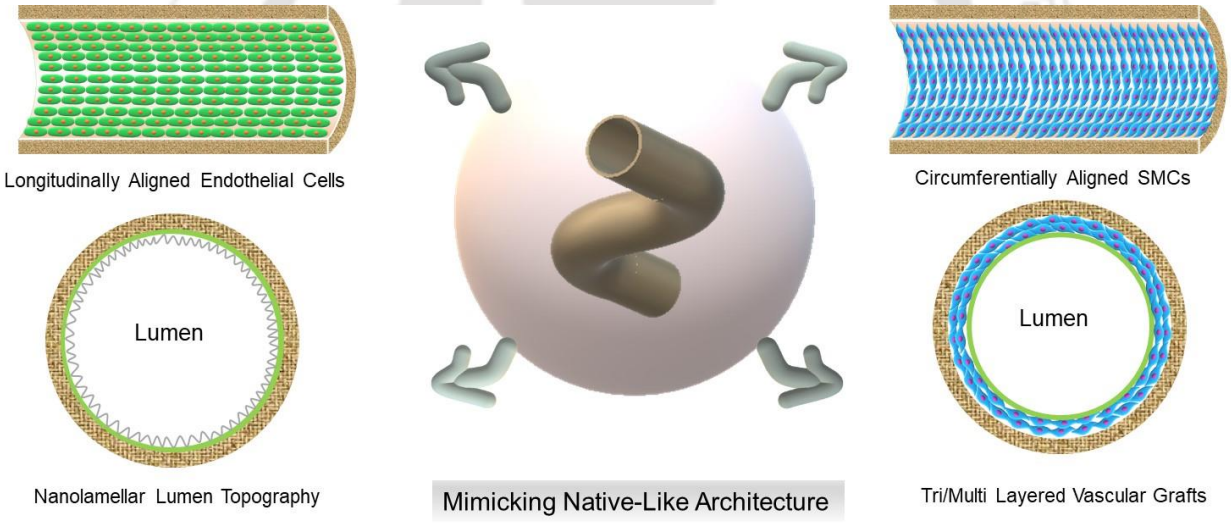

Figure 1.3. *Biomimetic approaches of TEVG fabrication. Schematic overview of various strategies adopted to recapitulate the native-like cellular arrangement in tissue-engineered vascular grafts.*

1.2.3.5 Acellular vascular grafts: bypassing cell incorporation

Since the beginning, when Weinberg and Bell (1986) proposed the idea of creating tissue-engineered vascular grafts using autologous primary vascular cells, research impetus in the field is focused on implementing a diverse array of cells fostering an off-the-shelf TEVG, as summarized in **Table 1.1**. Cell-laden grafts have performed better than cell-free grafts; but the former approach poses several impediments. For instance, culture and expansion of patient-specific vascular cells is a time-consuming and costly process, challenging its clinical feasibility.

Moreover, the diminished expansion ability of adult vascular cells restrains a broader adoption of this technique. Vascular progenitor cells are a suitable alternative, but their scarce availability hampers the idea. Subsequently, the focus shifted to various stem cells to obtain larger vascular cell populations via lineage-specific differentiation [85]. Direct seeding of patient-specific stem cells in TEVGs before implantation soon became tremendously popular in the field, considering their abundant availability and bypassing the need for culture expansion [86, 87]. Autologous BM-MNCs seeded TEVGs were the first to enter into clinic [36] and have long been a part of active clinical investigation [40]. Bone marrow and adipose tissue-derived MSCs also remain a substantial choice for researchers towards creating an off-the-shelf system [88, 89]. Nevertheless, it is believed that acellular grafts would presumably follow a shorter path towards clinical translation as compared to the seeded ones. Contemporaneously with cellular TEVGs, acellular grafts are also being investigated routinely. Three different approaches are broadly adopted: 1) Cell-free biodegradable polymeric grafts, 2) Decellularization of native blood vessels and 3) Decellularization of grafts prepared by *in vitro* cellular self-assembly (**Figure 1.4**).

Table 1.1. *Cell types used for vascular tissue engineering applications.*

Cell type	Prominent sources	Comments	Ref.
Primary Vascular Cells			
Endothelial cells	• Human umbilical vein endothelial cells (HUVEC) • Microvascular endothelial cells (MVEC) • Biopsies from patient blood vessels	• Naturally aligned along the direction of blood flow • Provide a natural anti-thrombotic surface • Endothelialized grafts with autologous cells prevent thrombosis • Patient-specific cells bypass the need for immunosuppressive therapy • Limited availability and long *in vitro* expansion time restrict their direct implementation for TEVGs	[28, 30, 59]
Smooth muscle cells	• Human umbilical artery smooth muscle cells (HUASMC)	• Naturally aligned circumferentially, provide contractile function and maintain elasticity	[3, 90, 91]

	• Biopsies from patient blood vessels	• Responsible for rendering mechanical stability to a blood vessel via ECM secretion • Synthetic/proliferative phenotype leads to overgrowth and intimal hyperplasia • Engineered HAVs, which are in phase III clinical trials for hemodialysis access, are prepared from allogenic SMCs/PGA scaffolds	
Fibroblasts	• Dermal fibroblasts • Biopsies from patient blood vessels	• Naturally present in the outermost adventitial layer of blood vessels • Provide mechanical resilience by ECM production • Predominantly used for preparing cell-sheet based and fibrin embedded engineered vessels	[29, 30, 92, 93]
Vascular Progenitor Cells			
Perivascular pericytes	Any tissue with capillary bed (muscle, fat, saphenous vein segments, etc.)	• Cells found in microvasculature interspersed between endothelial cells • Have mesenchymal stem cells (MSC) like features • Secrete pro-angiogenic factors • Allogenic cells show immune compatibility	[94-96]
Endothelial progenitor cells (EPCs) and endothelial colony forming cells (ECFCs)	• Bone marrow • Adipose tissue • Human peripheral blood • Placenta • Perivascular cell fractions	• Encompass a broad category of cells capable of differentiating into endothelial cells	[95, 97]
Stem Cells			

Mesenchymal stem cells (bone marrow mononuclear cells, stromal vascular fraction and adipose-derived mesenchymal stem cells)	• Bone marrow • Umbilical cord blood • Adipose tissue	• Guide TEVG remodeling via paracrine signaling • Immunomodulatory • Immunocompatible • Due to the availability of abundant sources and easy processing, their implementation in TEVG markedly reduces graft fabrication time • MSC derived extracellular vesicles have shown remarkable therapeutic potential • Their secretome has angiogenic potential	[40, 44, 98]
Induced pluripotent stem cells (iPSCs)	• Somatic cells (Fibroblasts) • Peripheral blood	• Can be obtained in high quantity and differentiated into vascular cell lineage (ECs and SMCs) • Minimally or non-immunogenic • Allogenic implementation is feasible	[99, 100]

1.2.3.5.1 Cell-free biodegradable polymeric grafts

Notwithstanding the benefits of cell seeding, acellular polymeric grafts are one of the prodigious choices that pragmatically epitomize the most compelling candidate for clinical translation [5, 101-103]. The advantageous aspects of implementing this approach are: 1) minimal batch to batch variation, 2) the whole process is automated, conferring better chances of reproducibility, 3) bypass the need of culturing cells and long-term maturation, 4) removing cellular component would confer immune compatibility, 5) avoid chances of disease transmission, 6) can be functionalized with a plethora of bioactive molecules to improve graft performance, 7) can be made readily available for patients in need. However, this technology lags in terms of lack of bioactivity, one of the key pre-requisites of TEVG success, generally conferred by cell seeding for cellular grafts. Seeded MSCs not only provide anti-thrombogenicity [104] but also help in graft remodeling [44]. Emerging technologies are now trying to imitate the effect of cell-seeding in acellular polymeric grafts by orchestrating their functionalization with bioactive moieties. This innovative approach could be the most suitable strategy for acellular TEVGs' clinical translation, pending identification of a suitable combination.

1.2.3.5.2 Decellularization of native blood vessels

Allogenic and xenogenic blood vessels are suitable alternative for vascular reconstruction provided they are devoid of any cellular immunogenic materials orchestrating immune compatibility. Both allogenic and xenogenic vessels from various sources are under active investigation to explore their ability as a suitable grafting option. The main advantage of using native vessels is that it mitigates the limitations associated with the availability of autologous grafts. Moreover, they intrinsically contain the well-organized ECM proteins assisting in desired graft mechanics. Notwithstanding these advantages, their immunogenicity remains the prime setback for wider clinical adoption [101].

Decellularized xenografts from porcine, bovine, ovine, and other rodent sources have been tested in either pre-clinical or clinical settings. Xenografts from bovine are clinically available for hemodialysis access (e.g., ProCol®, Artegraft®, SynerGraft®, Solcograft®), however, their performance is not satisfactory as they are prone to thrombosis and aneurysm formation [105]. Another commercialized xenograft is CorMatrix, derived from porcine SIS was also found to be inefficient for a low-flow high-pressure system as it showed significant stenosis [106]. From a clinical perspective, the clinical performance of xenografts has not been very successful. Research impetus is now shifted towards exploring various allografts with innovative modifications to improve their bioactivity and long-term performance while mitigating their immunogenicity.

1.2.3.5.3 Decellularization of grafts prepared by *in vitro* culture

Driven by the challenges associated with decellularization of native vessels and encouraging evidence suggesting the dependence of graft mechanics on structural organization of conserved ECM proteins, underlaid the idea of decellularizing *in vitro* bioengineered vessels. This strategy bypasses the need for autologous biopsy from the patient and leverages the capability of vascular cells' self-assembly under *in vitro* conditions. Following methodologies described in foundational studies [33, 107], bioengineered vascular conduits were prepared by culturing bovine/porcine SMCs onto PGA mesh followed by long-term maturation in bioreactors. Furthermore, bioengineered HAVs entered into clinical trial studies, wherein they were implanted for hemodialysis access in a human patient cohort having an end-stage renal disease. Interestingly, HAVs barely exhibited any post-cannulation bleeding, and 1-year follow-up showed excellent secondary patency without dilatation [35]. In a subsequent study, the implanted HAVs were

investigated for host cell infiltration and remodeling over 200 weeks, revealing their transformation into living blood vessel [108]. Considering the prodigious performance of HAVs in pre-clinical and clinical studies for hemodialysis access, recently, they were implanted for arterial reconstruction (femoral-to-popliteal and above-knee bypass) in humans with great success [109, 110]. As of now, HAVs remain the most successful engineered biological vessel in human clinical trials.

In addition to HAVs comprising of allogenic SMCs and PGA mesh (wherein both of them are subsequently removed, leaving behind collagenous tubular framework), researchers are exploring the inherent self-assembling property of fibroblasts to prepare a completely biological graft. In a partial decellularization approach, TEBVs consisting of inner endothelium cultured on decellularized cell membrane and a living adventitia were developed by long term maturation of fibroblast cell sheets derived from human skin biopsies [111]. Notably, cultured fibroblasts are devoid of MHC II antigens, hence are minimally immunogenic. Allogenic, fibroblast-derived TEBVs were further rendered non-immunogenicity by dehydration in lieu of decellularization and clinically investigated in humans for hemodialysis access by implanting them as shunts. This case study revealed the clinical applicability of scaffold-free cell-derived TEBVs [112]. In recent work, the same research group has shown the production of yarns derived from cell-assembled sheets as true ‘bio’ material for versatile tissue-engineering applications [93].

In another effective approach, donor fibroblast cells were embedded in a tubular fibrin gel and subjected to pulsatile flow maturation for 5 weeks, followed by decellularization. Intriguingly, the resulting tubes had the growth potential post-implantation as evinced by their implantation replacing pulmonary arteries in a growing lamb model [113]. The application of cell-free biological graft was further extended to hemodialysis access in baboons [92]. Graft prepared from human neonatal fibroblasts (15 cm long, 6 mm diameter) were implanted in the axillary-brachial upper arm or axillary-cephalic position and explanted after six months. Explant analysis suggested graft recellularization with host cells with 60% primary patency with no signs of calcification and stenosis [92]. Outcomes of these studies spur the notion that acellular biological grafts can grow with the host age and undergo *in vivo* recellularization rendering natural-like vessel characteristics.

Clinical outcomes of this technology, wherein acellular grafts are prepared by long-term *in vitro* maturation, have made it the most advanced approach in the current scenario. As described earlier, the leading groups in the field have shown the remarkable potential of cell-free grafts for

hemodialysis access and arterial replacement. With the advent of technology, these grafts are already in different phases of clinical trials.

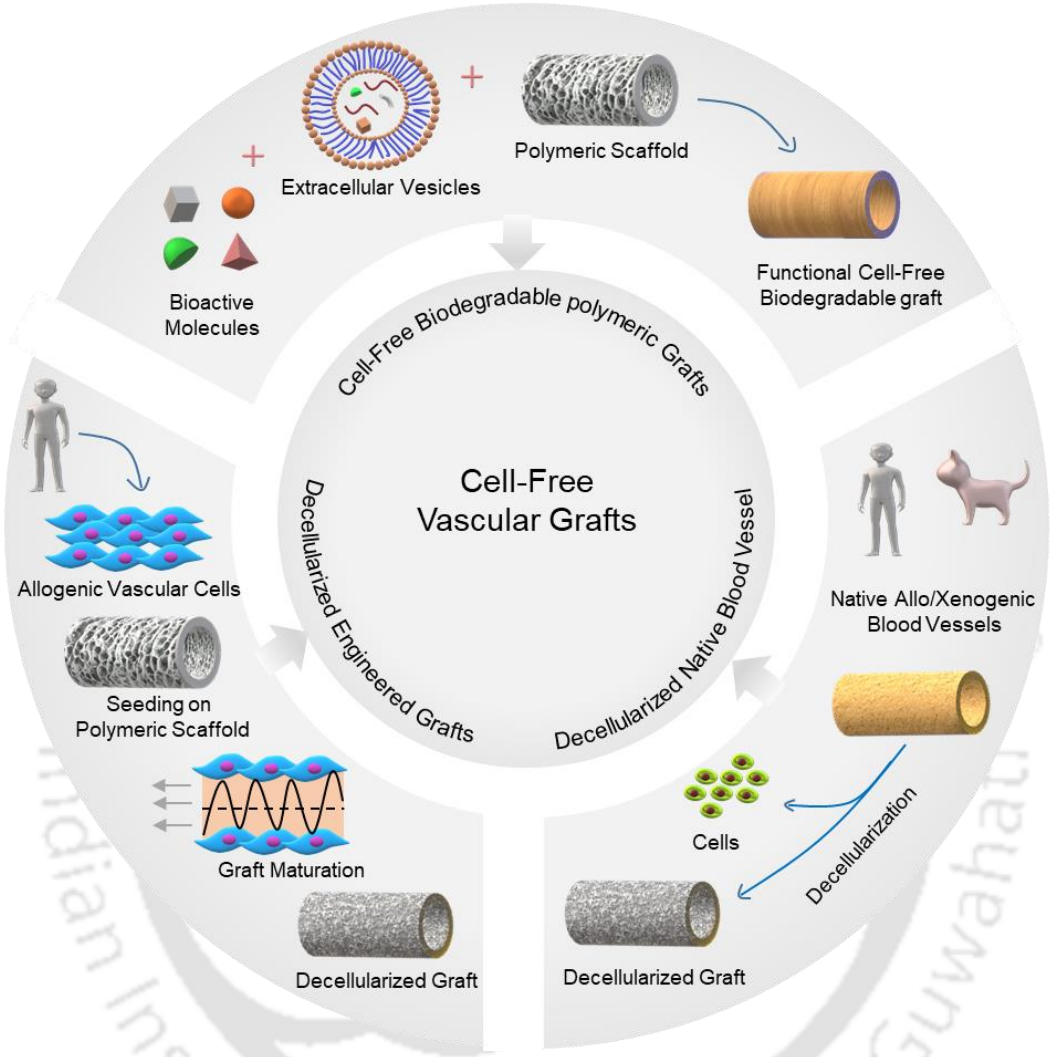

Figure 1.4. *Acellular TEVGs. Scheme representing various methodologies adopted to obtain cell-free/acellular vascular grafts.*

1.2.4 An update on clinical trials

With the advent of technological advancements, recent decades marked enormous progress in the development of translatable tissue-engineered vascular grafts. Few technologies are already in the advanced stages of human clinical trials; however, none of the TEVG has hit the market yet. Leading groups worldwide have ventured to find biodegradable alternatives for both venous and arterial flow systems to advance patient care. Pertinent to note that most successful TEVGs in clinical trials are based on distinct approaches and for different clinical targets. To cite a few,

Shinoka and Breuer adopted autologous BM-MNCs seeded polymeric grafts for venous grafts, whereas Niklason and colleagues resorted to obtaining a cell-free graft (HAVs) comprising primarily of cell-derived ECM for hemodialysis access. Tranquillo's group developed biological conduits by embedding fibroblasts into fibrin gel. A completely biological cell-sheet based technology was adopted by L'Heureux and colleagues. Xeltis, a European clinical-stage medical device company, utilized an acellular supramolecular polymer-based bioresorbable TEVG for performing Fontan procedure in clinical trials in Russia. Encouraging results from these trials provide compelling evidence asserting that TEVGs will soon become a clinical reality. A list of ongoing/completed clinical trials investigating TEVGs in humans is summarized in **Table 1.2**.

Table 1.2. *List of ongoing/completed clinical trials examining advanced stage biodegradable tissue-engineered vascular grafts. (Source: https://clinicaltrials.gov/)*

Identifier	Title	Clinical trial period/status	Phase	Sponsor
NCT01034007	A pilot study investigating the clinical use of tissue engineered vascular grafts in congenital heart surgery	Dec 2009-Jan 2018 (Completed)	Phase I	Christopher Breuer
NCT04467671	Two-year study of the safety and efficacy of the second-generation tissue engineered vascular grafts (TEVG-2)	July 2020-Aug 2027 (Ongoing)	Phase II	Nationwide Children's Hospital
NCT00850252	Use of a lifeline graft in the A-V shunt model	Sep 2004-Dec 2012 (Completed)	Phase I/II	Cytograft Tissue Engineering
NCT01872208	Evaluation of the safety and efficacy of a vascular prosthesis as an above-knee bypass graft in patients with PAD	Oct 2013-June 2024 (Ongoing)	NA	Humacyte, Inc.
NCT01840956	Safety and efficacy of a vascular prosthesis for hemodialysis access in patients with end-stage renal disease	May 2013-May 2016 (Completed)	Phase I	Humacyte, Inc.

NCT01744418	Evaluation of the safety and efficacy of a vascular prosthesis for hemodialysis access in patients with ESRD	Dec 2012-April 2026 (Ongoing)	NA	Humacyte, Inc.
NCT03005418	Humacyte human acellular vessel (HAV) in patients with vascular trauma	Sep 2018-Sep 2024 (Ongoing)	Phase II	Humacyte, Inc.
NCT02887859	Humacyte's HAV for femoro-popliteal bypass in patients with PAD	Dec 2016-Dec 2024 (Ongoing)	Phase II	Humacyte, Inc.
NCT04135417	Safety and efficacy assessment of HAV (manufactured using large-scale system) in patients needing vascular access for dialysis	Nov 2019-Feb 2024 (Ongoing)	Phase II	Humacyte, Inc.
NCT02644941	Comparison of the human acellular vessel (HAV) with ePTFE grafts as conduits for hemodialysis	May 2016-Sep 2022 (Ongoing)	Phase III	Humacyte, Inc.
NCT03183245	Comparison of the human acellular vessel (HAV) with fistulas as conduits for hemodialysis	Sep 2017-Sep 2024 (Ongoing)	Phase III	Humacyte, Inc.
NCT03631056	Individual patient expanded access for human acellular vessel (HAV)	Ongoing	NA	Humacyte, Inc.
NCT04545112	Xeltis coronary artery bypass graft (XABG) first in human (FIH) (XABG-FIH)	Sep 2020-March 2026 (Ongoing)	NA	Xeltis
NCT03405636	Xeltis pulmonary valved conduit safety and performance study	Sep 2020-Oct 2026 (Ongoing)	NA	Xeltis
NCT03022708	Xeltis bioabsorbable pulmonary valved conduit early feasibility study (Xplore2)	May 2017-Dec 2023	NA	Xeltis

1.2.5 Silk biomaterials for vascular tissue engineering applications

1.2.5.1 Silk: varieties and molecular structure

There exists a plethora of natural sources (insects and arachnids) producing silk biopolymer. It is the structural component that is used as a protective shield assisting in their life-cycle completion. Few prevalent examples of silk-producing living beings include Lepidopterans (silkworms), Arachnids (spiders), Tetranychidae (mites), and Hymenopterans (wasps, bees) [13]. From a tissue engineering perspective, SF produced by silkworms and spiders has persistently been explored and taken a giant leap from being a textile material to sutures to modern regenerative medicine [11, 114]. Pertinent to mention that SF derived from different sources have unique characteristic structural composition, which ultimately defines their biological and physicochemical properties. Based on the feeding habits, silkworms are broadly categorized into two types: mulberry and non-mulberry [115, 116]. As the classification name dictates, silkworms feeding on mulberry plant leaves encompass mulberry types, whereas rest of the silkworms belong to non-mulberry types. Being a domesticated variety, mulberry *Bombyx mori* silkworms are available worldwide; hence have widely been explored for various tissue-engineering applications. Non-mulberry wild silk varieties are geographically restricted to specific zones: *Antheraea pernyi* (China), *Antheraea yamamai* (Japan), *Antheraea mylitta* (Central India), *Antheraea assamensis* (mostly north-east India), and *Philosamia ricini* (diverse distribution across Asia), etc. [117]. It is worth mentioning here that SF produced from different silkworms possess characteristic physico-chemical and biological properties dictated by difference in their structural composition.

The life-cycle of a silkworm comprises four different stages. The eggs laid by the female silkworm moth proceed to the larvae stage post-hatching, which includes five instars. Silk fibroin can be obtained either from silk glands or cocoons. To obtain SF from glands, researchers have used silkworms at the fifth instar stage to extract the aqueous protein [118]. The silk glands have three distinct segments, namely ASG, MSG, and PSG. SF is produced in the PSG portion, whereas glue-like sericin is produced in MSG. A high concentration (~25 wt.%) mixture of these two proteins is pushed to ASG to initiate the cocoon formation [119]. Notably, SF isolated directly from the silk gland comprises primarily of random coil conformation and is water-soluble. After completing the fifth instar, the matured larvae start forming cocoons (comprised of structural SF protein and silk sericin) followed by subsequent transformation into pupae and moth [13]. Cocoons are another source to obtain silk fibroin [14]. SF isolated from mulberry *Bombyx mori* cocoons has

predominantly been investigated for tissue engineering purposes. The natural process of cocoon formation (or spinning) involves extrusion of a combination of core structural SF protein (70-80%) and glue-like silk sericin protein (20-30%) through silkworm spinneret in the form of fibers [120, 121]. The structural transformation of SF silk-I (primarily α-helix and random coil conformation) to silk-II (anti-parallel β-sheets) occurs during the spinning process, which facilitates semi-crystalline SF structure in cocoons having remarkable mechanical properties [116, 119]. Due to the change in conformation towards β-sheets, the SF protein present in cocoons is water stable. Scientists have used various chemical-based methods to remove silk sericin and regenerate the cocoon SF into water-soluble protein [14].

Mulberry and non-mulberry SF proteins vary in their structural composition. While mulberry SF (*Bombyx mori*) consists of a heterodimer combining three polypeptides (a heavy/H chain of ~390 kDa linked to a light/L chain of ~25 kDa via covalent disulfide bond, and a P25 glycoprotein of ~27 kDa associated with six H-L chains by hydrophobic interactions), non-mulberry SF contains only homodimers of H chains of variable molecular weights (ranging 197-230 kDa) for different varieties [122, 123]. Structural dissimilarities in SF proteins are a result of the unique genetic makeup of silkworms. Intriguingly, L chain and P25 related genes were lost during evolution for non-mulberry silkworms [123]. H chain of mulberry and non-mulberry SF comprises of repetitive crystalline regions linked through non-repetitive amorphous regions; however, both types contain distinct sets of amino acids. The crystalline region of mulberry SF includes copies of two hexapeptides: GAGAGY and GAGAGS (hydrophobic amino acids); whereas, amorphous regions predominantly contain hydrophilic amino acids (threonine, serine, glutamine, and asparagine) [124, 125]. On the contrary, the crystalline region of non-mulberry SF has poly-alanine repeats, rendering superior mechanical properties to wild silk proteins. Arginine-rich R motifs and glycine-rich G motifs are present in the non-repetitive regions of H chains of non-mulberry SF [13, 124, 126]. More importantly, the inherent presence of RGD tripeptides (a cell-binding motif) in the H chain of non-mulberry SF makes it a particularly interesting biomaterial from regenerative medicine perspective. The H chain of non-mulberry SF possesses variable numbers of RGD tripeptides. For example, *Antheraea pernyi* (10), *Antheraea assamensis* (01), *Antheraea mylitta* (05), *Antheraea yamamai* (12), *and Philosamia ricini* (01) [126-130]. The most common aqueous SF isolation method from mulberry cocoons involves degumming (a process of removing silk sericin glue protein) to obtain SF fibers. Which are further dissolved in

chemical solvents (most common being lithium bromide-LiBr) followed by dialysis against Milli-Q water [14]. Notably, the same protocol is not adopted for non-mulberry SF fibers due to their insolubility in LiBr. As a result, researchers have shifted to use silk glands isolated from fifth instar larvae, instead of cocoons to obtain aqueous non-mulberry SF solution (**Figure 1.5**) [118]. Among others, natural SF obtained from mulberry *Bombyx mori* cocoons has primarily been investigated for fabricating TEVGs, whereas other non-mulberry silk varieties are in the infancy stage for vascular tissue engineering applications.

Figure 1.5. *Scheme representing sources of silk protein (cocoons and glands) and its amenability for fabricate into various formats.*

1.2.5.2 Favorable properties of silk towards vascular regeneration

In a quest to improve the clinical feasibility of tissue-engineered vascular grafts, multidisciplinary scientific efforts have converged to identify the favorable properties of vascular scaffolds. While biological properties are of utmost importance, physicochemical attributes of the vascular scaffolds pragmatically determine their clinical outcomes. Moreover, the remodeling and neo-tissue formation in an implanted TEVG can be manually controlled by manipulating the graft's properties [131, 132]. Few of the contemporary expectations from an ideal TEVG include: 1) mechanical resilience and stability throughout the graft remodeling, 2) *in situ* biodegradation facilitating constructive graft remodeling, 3) ability to attract and recruit host cells along with providing a congenial microenvironment for their growth, 4) hemocompatibility, 5) minimal immunogenicity. With the advent of technology, researchers are now developing advanced

computational models that can predict the TEVG performance based on design parameters [133, 134]. Pertinent to note that remodeling of an implanted TEVG predominantly relies on their design parameters (e.g., pore size, porosity, wall thickness, nanofiber diameter, etc.) [135, 136]. Hence, it is important to manually regulate these factors during graft fabrication. A polymer with the ability to adopt multiple forms with tunable properties would become a rationally optimistic candidate for preparing vascular scaffolds. Silk biomaterials have long been used in medicine as sutures and now established their promising aspects in various tissue engineering fields, including for vascular grafts. The inherent occurrence of many of the aforementioned properties manifests the implications of silk biomaterial for vascular regeneration rendering desirable outcomes.

1.2.5.2.1 Mechanical properties

The prime reason for a long history of using silk as sutures is credited to its remarkable mechanical properties. Variable amino acid compositions of different silk varieties render diverse mechanical strength of native silk fibers [13]. Other influential factors that determine the mechanical properties include the spinning process, flow distribution, humidity, temperature, degree of sericin binding, fiber morphology, and reeling rate [137]. Naturally, silkworm silk-spinning facilitates the structural transformation from amorphous to semi-crystalline, induced by attaining a pH/ionic gradient while extruding the highly concentrated silk through spinneret under high shear force [119]. A recent study reports that *Bombyx mori* silk fibers obtained from larvae in different instars have distinct mechanical properties [138]. Particularly, at the beginning and end of each instar stage, silkworms spin some amount of silk. The study revealed the directly proportional co-relation of mechanical properties with the presence of amount of β-sheet content. In another work, a structure-mechanics relationship was further validated for various mulberry and non-mulberry silk varieties [139]. The study encompassing the investigation of mulberry (*Bombyx mori*) and non-mulberry (*Philosamia ricini, Antheraea assamensis, Antheraea pernyi, and Antheraea mylitta*) revealed the superior extensibility and toughness of non-mulberry silk fibers than the mulberry one. The former observation was attributed to crystallinity, β-sheet content and overall structure of non-mulberry silk owing to the presence of poly-alanine repeats in their native polypeptide structure [139]. Notably, the mechanical properties of native silk fibers only matter if they are directly being implemented for tissue engineering application without considerable post-

processing. From a vascular tissue engineering perspective, braiding native silk fibers to obtain tubular constructs is one way to fabricate tubular constructs [140, 141].

Regenerated SF, on the other hand, has prevalently been used, wherein the mechanical properties rely on scaffold format and degree of crystallization and β-sheet formation. Important to note that the mechanical properties of silk-based matrices (e.g., porous scaffolds, nanofibrous electrospun mats, hydrogels and thin films, etc.) can be tailored by various means. For instance, mechanical attributes of composite silk matrices (silk blended with different synthetic polymers) remain comparable despite the presence of non-mulberry SF in electrospun mats [142]. Moreover, the crystallinity of regenerated BM silk films can be tuned by varying annealing temperatures. While silk I structure with minimal crystallinity is retained at lower temperatures (4℃), water vapor annealing at 100℃ induced silk II transition having ~60% crystallinity and high β-sheet content, resulting in a significant increase in elasticity modulus, yield stress, and tensile strength [143]. Other influential factors by which silk structural conformations can be manipulated include relative humidity [144] and choice of organic solvent (methanol, ethanol, and others) [145].

1.2.5.2.2 Biodegradation

The contemporary idea of tissue engineering is to restore the function of diseased tissue or organ in the best possible biomimetic manner exploiting the body's regenerative capability. The concept capitalizes on the biodegradation of an engineered scaffold, which allows the growth of biological tissue over time [5]. Ideally, the implanted scaffold should degrade without producing any toxic byproducts and, at the same time, should support the growth and infiltration of host cells. One of the foremost challenging aspects of tissue engineering is to delineate the peculiar balance between the rate of scaffold degradation and neo-tissue formation (**Figure 1.6**). Among others, tissue-engineered vascular conduits experience sustained luminal hemodynamic pressure, which is much higher in the arterial system than venous circulation. It is imperative to ensure that the implanted TEVG should be able to withstand the hemodynamic pressure while fostering the neo-tissue formation [3]. For designing a TEVG pertaining aforementioned qualities, the biomaterial should be biodegradable and concomitantly provide an option to manipulate the rate of biodegradation under *in situ* dynamic microenvironment as per need. Silk biopolymer is one of the ideal candidates in this regard. There exist several potential ways by which the crystallinity of SF can be manipulated. It infers that SF may provide remarkable opportunities, wherein the criterion of

tunable biodegradation can be fulfilled by means of altering the β-sheet content of fabricated scaffolds. Moreover, silk is a protein polymer consisting of polypeptides. The degradation byproducts of SF are either small-length peptides or individual amino acids, which can be metabolized by host cells without triggering any adverse effects [146].

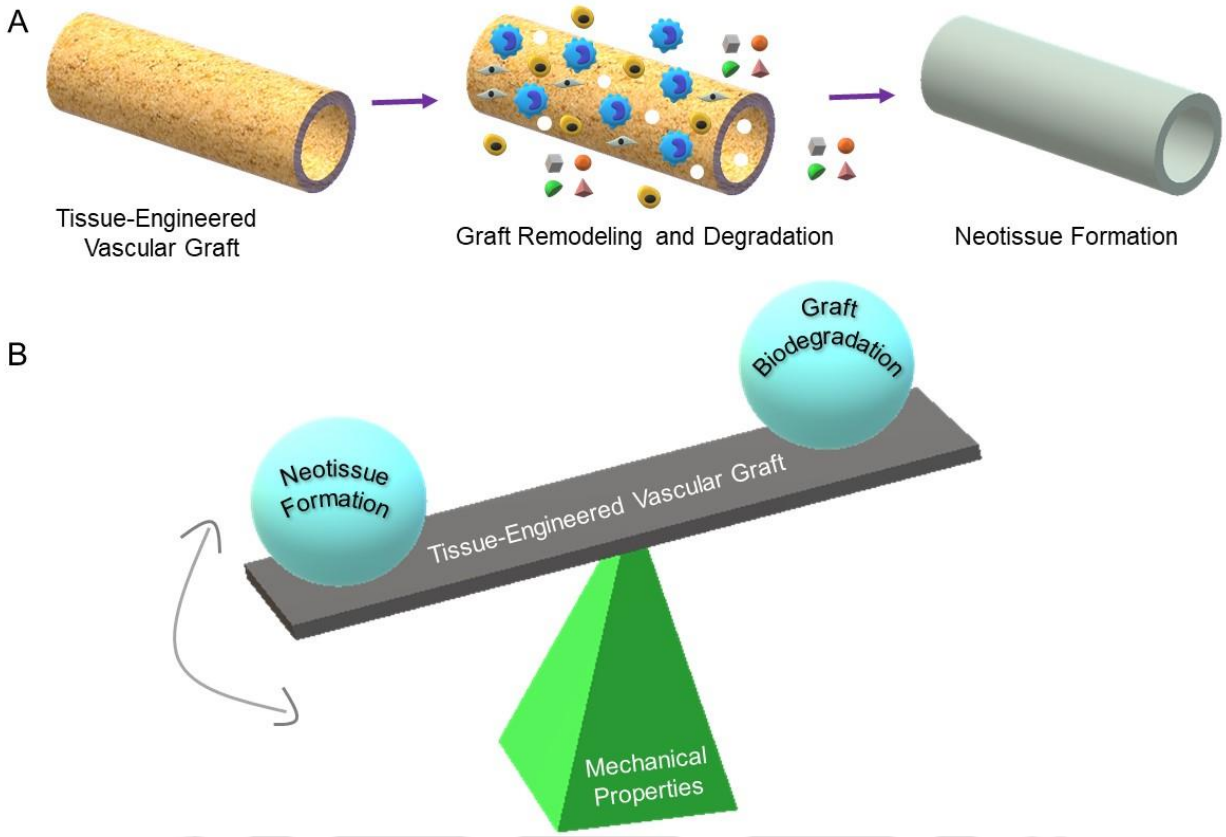

Figure 1.6. *(A) Model of biodegradable tissue-engineered vascular graft remodeling. Host cells infiltrate the graft, initiate its biodegradation, proliferate, secrete their own extracellular matrix proteins and eventually replace the graft material with neotissue. (B) A critical balance between biodegradation, graft mechanics and rate of neotissue formation is required for constructive graft remodeling.*

Native silk fibers are comprised of hierarchical structure; hence their degradation is slower than regenerated silk fibroin [147]. The latest scientific advancements indicate that the degradation rate of BM silk could be varied from days to months depending on their structural conformation [146, 147]. While molecular weight and crystallinity of SF regulate the degradation pattern, researchers are delving into more innovative ways that can control the SF degradation based on implantation site with high fidelity. The disparity among *in vitro* and *in vivo* degradation of silk matrices led researchers to investigate the degradation of biomaterials directly at the implantation

site for more reliable outcomes. For instance, BM silk membranes implanted in the rat dorsal skin demonstrated slower degradation as compared with skeletal muscle implantations [148]. Exploration of mechanistic insights suggests that *in vivo* degradation of SF matrices relies on the presence of proteolytic enzymes and macrophage activity [147]. After recruitment at the implantation site, macrophages secrete multiple proteolytic enzymes (e.g., MMPs, collagenase, gelatinase) in addition to other acid hydrolases and lysozymes [149, 150]. Notwithstanding the availability of an array of proteolytic enzymes in the close vicinity of implanted silk material, the scarcity of enzyme cleavage sites orchestrates a slow degrading status to SF biomaterial [151]. While classical approaches for manipulation of SF degradation rely on structural and molecular weight alterations, advanced approaches are focusing on imparting degradation susceptibility by means of incorporating enzyme catalytic sites. For example, an MMP cleavable peptide (PLCL) was incorporated in the genome of silkworms, producing a fast degrading SF protein interspersed with MMP susceptible sites conjugated in H chain using transgenic technology [152]. Other methods of manipulating the SF degradation profile includes chemical cross-linking, exploitation of scaffold porosity and blending with other polymers [147]. Overall, the literature suggests that tunable biodegradability of silk biomaterials would provide remarkable opportunities to vascular tissue engineers for the fabrication of a TEVG having ideal degradation properties with an existing set of tools.

1.2.5.2.3 Interaction of silk matrices with vascular cells

SF protein has long been used in medical science as suture material and is known to be biocompatible for various cell types [10]. Without exception, the growth of vascular cells is also supported by various SF matrices. Electrospun nanofibrous BM silk scaffolds support the growth and proliferation of human aortic ECs and coronary artery SMCs [153]. While cultured SMCs represented the structural alignment and elongation, interconnected capillary-like structures were spotted after seven days ECs' culture with predominant expression of cell-specific functional markers. Other studies have also substantiated the favorable attributes of SF matrices towards supporting the growth of all three vascular cells [15, 60, 154]. Prior studies rationally validate the aptness of native and regenerated silkworm silk (both mulberry and non-mulberry varieties) for supporting the growth of vascular cells.

Endothelialization is of paramount importance for TEVG success. From pre-implantation seeding of TEVGs in the lumen of the vascular graft to relying on *in situ* endothelialization, a suitable surface is necessary, which could facilitate the stable adherence of ECs and maintain a confluent endothelium. Notwithstanding the optimal properties of SF-based matrices, researchers have further delved into the improvement of certain features by means of surface modification. Another emerging technology is to recapitulate the native-like cellular arrangement to manipulate the cell function in the best possible way. Silk biomaterials from mulberry and non-mulberry silkworms present numerous possibilities for vascular tissue engineering, as they support the culture and proliferation of all three vascular cell types. Inherent availability of RGD cell-binding tripeptide in non-mulberry silk orchestrates growth and functional attributes by facilitating firm adherence of seeded cells. RGD availability also plays a crucial role in the recruitment and infiltration of host cells post-implantation of a TEVG [155].

1.2.5.2.4 Hemocompatibility of silk biomaterials

Hemocompatibility of the biomaterial is the most fundamental property to be considered for designing a viable TEVG. Among other favorable properties, the hemocompatibility of SF protein remains comparatively elusive and lacks a general consensus in its native form. A few studies have shown the rapid coagulation of blood after exposure to silk-collagen scaffolds and soluble SF [156, 157]. On the contrary, the hemocompatibility of silk-based TEVGs has been validated in animal studies [158]. In a single parametric study, researchers have revealed elevated fibrin polymerization and adsorption of serum proteins on SF fibers than films, possibly due to format differences [159]. A co-relation of SF structure with platelet/THP-1 cell adhesion and activation and protein adsorption was further established. Silk films having high hydrophobicity and crystallinity showed lower protein adsorption upon treatment with human plasma, influencing platelet activation. Further investigation suggested that the differences in the protein adsorption were primarily attributed to chemotactic factors (e.g., C3a, C3b, and C5a); however, comparable fibrinogen adsorption was reported [160].

As most of aforementioned blood testing practices emphasize limited factors of blood-biomaterial interaction and predominantly using 2D silk films, the possibility of false-positive or negative results cannot be ignored. Investigation of APTT takes only the intrinsic pathway of blood coagulation into account, whereas PT estimates the prothrombin to thrombin conversion time

associated with the extrinsic pathway. Estimation of platelet adhesion and activation in response to biomaterial also unveils one aspect of the complex blood coagulation cascade. From a tissue regeneration perspective, investigation of whole blood interaction with 3D porous scaffolds using multiparametric assays would pragmatically produce more accurate results [161]. In order to parse these former concerns, researchers have resorted to investigating comprehensive thromboelastomeric (ROTEM®) response of non-mulberry (*Antheraea mylitta*: AM) 3D porous scaffolds followed by comparison with BM silk scaffolds and Uni-Graft® W (a clinically used graft) [162]. A comparison of altered ROTEM parameters revealed insignificant differences in hemocompatibility among silk scaffolds and reference material; however, some trivial alterations of *Antheraea mylitta* silk scaffolds were attributed to the inherent presence of RGD tripeptide. The existence of the former notion may facilitate the interaction of *Antheraea mylitta* silk with membrane glycoproteins (IIb and IIIa) on platelet surface, which could substantially manipulate the material thrombogenicity by triggering the platelet assisted initiation of blood coagulation cascade [163]. The overall hemocompatibility of silk scaffolds has although shown to be reasonably optimal and comparable to few clinically used reference materials, SF materials provide numerous possibilities of surface modification with various anti-thrombotic molecules to improve their blood compatibility.

Some of the frequently used approaches to improve silk hemocompatibility are the incorporation of heparin and sulfur modification. Electrospun silk scaffolds modified with heparin demonstrated superior antithrombogenicity and ECs' proliferation [164]. In addition to endowing antithrombogenicity, heparin modification of silk biomaterials has also shown to manipulate the VEGF release profile from silk films [165], inhibit SMCs proliferation (an important aspect to prevent intimal hyperplasia in TEVGs), and facilitate vascularization in 3D porous silk scaffolds [166], and promote elastogenesis [167]. Composite sulfonated silk films were prepared by adding sulfuric acid during SF processing, and their anticoagulant activity was investigated by means of APTT, PT, and TT estimation. Results revealed an increment in the former parameters, validating their superior blood compatibility. Restricted platelet adhesion further substantiated the effectiveness of sulfur modification of silk films endowing hemocompatibility, which was attributed to a change in negative charge density owing to the presence of sulfanilamide radical groups [168]. In addition to prevalently used heparin and sulfur modification, hemocompatibility of SF matrices can also be improved by means of modification with zwitterionic phosphobetaine,

poly(ethylene glycol), ferulic acid, and chlorosulfonic acid [161]. In a recent attempt, silk biomaterials were biofunctionalized perlecan via recombinant expression for developing blood-compatible surfaces [169].

1.2.5.2.5 Immune response to silk biomaterials

It is imperative for an aspiring biomaterial not to induce the adaptive immune response; however, a mild innate response is known to assist tissue regeneration [45]. Another considerable aspect is the interaction between immune cells with proteins adsorbed onto the implant surface. External surfaces of all implants are exposed to body fluids immediately after implantation, which results in the adsorption of several proteins onto the implant surface, forming a provisional matrix. Morphological characteristics and surface chemistry of the implanted material crucially regulate the former process [170]. Previous studies have shown that native SF conjugated with sericin protein elicits an exuberant adaptive immune response, whereas purified SF is surprisingly compatible [171, 172]. Native silk fibers induce allergic response (type I allergy), causing upregulation of IgE levels and asthma [173]. The pro-inflammatory and allergic reactions in response to native silk fibers were later found to be originating from its sericin component (containing glycoproteins prevalently comprised of serine) [172]. Different formats of SF matrices (porous scaffolds, nanofibrous electrospun scaffolds, thin films) have shown a characteristic impact on provoking an immune response. In fact, morphological features of silk scaffolds (porosity, pore size, etc.) considerably determine their immunogenicity [174]. *In vitro* macrophage response to BM silk using murine macrophage cells (RAW 264.7) substantiated the immunological compatibility of fibers; whereas, insoluble particles triggered the release of TNF, a proinflammatory cytokine. Moreover, while silk sericin treatment of macrophages was comparatively neutral, its cumulative impact along with bacterial lipopolysaccharide triggered the macrophage activation [175]. A six-week i*n vivo* investigation of autologous rat MSCs seeded films revealed comparatively higher inflammatory reactions for collagen and PLA films than the silk ones, corroborating their immune compatibility [176].

Implementation of most of the SF-based matrices has been shown to activate the complement system, which is eventually resolved over time [177, 178]. The activated complement cascade enacts the release of inflammatory cytokines and attracts other immune cells at the implantation site. Chemokines comprise a fraction of released cytokines, which facilitate the

recruitment of leukocytes, macrophages, and neutrophils by establishing a concentration gradient. While milder inflammatory activation has shown to render constructive remodeling of implanted grafts by means of assisting vascularization and ECM accumulation, an exuberant response leads to negative systemic effects by activating the adaptive immune system [46, 179]. The innate immune response is also categorized in acute (resolves in 7-14 days) and chronic (lasts up to months/years). Cytokines released in the acute phase (IL-4 and IL-13) are responsible for activating the chronic immune response, which is typically characterized by the presence of multinucleated FBGCs. These cells are originated as a result of the fusion of activated macrophages [170]. The primary job of FBGCs is to clear the foreign material that is escaped from phagocytosis. FBGCs are found in close vicinity of the implanted materials and release an array of proteases. In cases where the implanted device is practically bigger in size and cannot be cleared from the system, multiple layers of activated macrophages and FBGCs encapsulate the foreign body, forming granulation tissue. It finally forms a fibrous capsule (a process called 'fibrosis') by developing new vasculature and concerted efforts of activated macrophages and fibroblasts [180]. The latest literature also suggests the rational involvement of diverse macrophage phenotypes in regulating the new ECM assembly and tissue remodeling [179, 181]. Ideally, an implanted tissue-engineered graft would follow a constructive remodeling if it triggers a regulated inflammatory response while avoiding fibrosis.

In vivo implantation of BM silk matrices have been shown to trigger the release of IL-4 and IL-13, which asserts their ability to profoundly assist in FBGCs formation [182]. However, the inflammatory response has been observed to eventually subside without forming a fibrous capsule, substantiating the activation of remodeling cascade for tissue-engineered silk grafts [183, 184]. The ability of silk to circumvent the formation of fibrous capsule makes it an immune-compatible biomaterial from a tissue engineering perspective. With currently available knowledge, it is apparently sufficient to state that SF-based materials are prevalently immunocompatible as they do not elicit an exuberant immune chronic response. Similar to other tunable properties of SF, the immune response can also be modulated by means of manipulating degradation rate, producing a plethora of formats, functionalizing with bioactive molecules, which would orchestrate not only immune compatibility but also ensure constructive remodeling. In addition, more advanced state-of-the-art, multidisciplinary immune engineering approaches are emerging,

which could pre-determine the immune response by means of fabricating 'immune-informed' tissue-engineered grafts.

1.2.5.3 An update on pre-clinical implications of silk-based TEVGs

Silk has a long history in medical science for its use as suture material. Notably, regenerated BM silk-based scaffolds have acquired FDA approval for their use in human subjects. Sofragen developed 'Silk Voice,' a 3D silk scaffold for medialization of the vocal fold, which is the first and only FDA cleared composed of regenerated SF protein (https://www.sofregen.com/). A list of BM silk products currently in different stages of human clinical trials is provided in our previous review [13]. SERI silk scaffolds are already in the market for various regenerative medicine applications (https://seri.com) [185]. Its application has further been extended to treat various dermatological pathologies, breast and abdominal wall reconstruction [186, 187]. As of now, only BM silk products are clinically validated for tissue regeneration purposes, whereas the progress of other silk varieties remains in infancy and needs further attention. Moreover, none of the silk-based TEVGs has entered the human clinical trials phase. While silk grafts have shown remarkable long-term regeneration potential in small animal models, their performance in larger animals remains concerning and in an infancy stage. We provide a detailed list describing the implementation of silk TEVGs in various pre-clinical small animal models for vascular regeneration in **Table 1.3**.

Table 1.3. *Performance of silk TEVGs in various pre-clinical animal models.*

Scaffold type	Animal model used	Implantation site	Overall graft performance	Ref.
Gel spun silk tubes	Sprague-Dawley rats	Abdominal aorta	• Resistant to acute thrombosis. • Progressive infiltration of host SMCs and ECs.	[158]
Gel spun silk tubes	Sprague-Dawley rats	Abdominal aorta	• Improvement of graft porosity results in accelerated remodeling by means of neo-tissue formation and cellular infiltration. • Well-developed neo intima and adjacent matured SMC layer at one month, preferably at the luminal side.	[188]

			• Highly porous grafts although showed better remodeling but their compromised strength, which potentially reduced their *in vivo* feasibility. • Only low molecular weight SF grafts were mechanically stable till six months.	
Plaiting and winding of silk fibers	Sprague-Dawley rats	Abdominal aorta	• No observed acute thrombosis for silk grafts. • Silk graft showed superior patency rates than PTFE grafts over 1 year. • Silk grafts showed early arrangement of intimal and medial layer. 12-week explants revealed almost confluent endothelium. • Organization of medial layer was assisted by bone marrow derived cells. • Presence of vasa vasorum like capillaries were detected. • No sign of aneurysm formation. • Macrophage assisted graft degradation over extended time.	[189]
Braiding and winding of natural and recombinant silk fibers	Sprague-Dawley rats	Abdominal aorta	• Excellent patency (85%). • Signs of neo-tissue formation along the lumen. • Presence of organized SMC layer and mature endothelium. • Recombinant grafts (modified to express collagen active sites) showed faster transanastomotic ingrowth of CD31 positive cells compared with control grafts comprised of domestic BM silk fibers.	[190]
Transgenic SF braiding grafts	Sprague-Dawley rats	Abdominal aorta	• Signs of thrombus formation in occluded grafts. • No sign of intimal hyperplasia. • Superior endothelialization in central portion of transgenic SF grafts than wild type.	[191]

Double-raschel knitted silk TEVGs	Sprague-Dawley rats	Abdominal aorta	• Tunable elasticity and thickness of scaffold wall by manipulating knitting pattern. • Suitable patency and no sign of intimal hyperplasia. • PGDE crosslinking and aqueous SF coating endow adequate permeability comparable with medical grade PTFE grafts. • No significant difference in tissue ingrowth after 2 and 8 weeks, signifying slower degradation of scaffold.	[192]
Fibroin sponge coated double-raschel knitted silk TEVGs	Beagle dogs	Common carotid artery	• No acute thrombosis. • Sonography observation of 1-year implant suggested signs of intimal plaque formation at the middle and proximal anastomotic portion of the graft. • Sponge layer was completely replaced with fibrous tissue in 1-year explants. • Minimal detection of foreign body giant cells, substantiating immune compatibility.	[193]
Fibroin sponge coated double-raschel knitted silk TEVGs	Sprague-Dawley rats	Abdominal aorta	• Silk grafts coated with lower SF concentration (1-2.5% w/v) sponge facilitate constructive remodeling and prevent intimal hyperplasia/stenosis. • Significantly improved tissue infiltration in 1-2.5% SF coated grafts. • Complete degradation of sponge and replacement with host tissue.	[194]
Double-raschel knitted TEVGs (SF and PE splice grafts)	Beagle dogs	Abdominal aorta	• SF coating assist in rapid endothelialization and prevent medial thickening. • Thrombus formation in gelatin coated grafts. • SF coated grafts had thinner luminal layer compared with gelatin coated ones. • Higher ECs observed in SF coated silk fiber grafts.	[195]

Elastin modified double-raschel knitted SF grafts	Rats	Abdominal aorta	• Elastin coating facilitates ECs' attachment while prevent platelets adhesion. • Very good patency. • No sign of excessive immune response or fibrous capsule formation. • Rapid endothelialization within 2 weeks of implantation.	[196]
Plaited silk fibers and cocoon filaments coated with SF solution	Beagle dogs	Carotid artery	• Dismal patency possibly due to lost mechanical strength by virtue of degradation. • Limited remodeling in large animals. • 3-months data revealed superior endothelialization of silk graft compared with PTFE ones.	[197]
Braided SF threads	C57BL/6 mice	Right carotid artery	• ~13% (4/30) patency after 6 months. • 2-week explants showed presence of SMA and CD31 positive cells in neointimal. • Complete endothelialization at 4 weeks. • Significant presence of collagen and elastin fibers after 4 weeks. • Signs of SF degradation at 6 months.	[140]
Silk fabric core layer embedded in a porous scaffold	Rabbits	Common carotid artery	• No sign of stenosis and aneurysmal dilation. • Complete endothelialization in 3 months. • Blood flow profile was comparable with native artery. • Organized medial layer comprising of SMCs substantiating constructive graft remodeling.	[198, 199]
Double-raschel knitted silk TEVGs	Sprague-Dawley rats	Inferior vena cava	• 95% patency for silk grafts, 80% patency for ePTFE grafts over 4 weeks. • Full lumen coverage by ECs in 4 weeks. • Podoplanin-positive mesothelial cells were traced on the outer surface of graft.	[200]
Electrospun silk TEVG	Lewis rats	Abdominal aorta	• No sign of thrombus formation. • Good short-term patency. • Infiltration of host vascular cells observed in explant.	[201]

			• Newly developed elastic lamina along the graft lumen. • Notable presence of vasa vasorum at the outer scaffold surface.	
Electrospun silk TEVGs	Sprague-Dawley rats	Abdominal aorta	• Graft survival at 24 weeks: 95% (20/21) silk grafts, 73% (16/22) ePTFE grafts. • Rapid endothelialization in 6 weeks. • Regression of neointimal was also observed. • Constructive remodeling over time in terms of new ECM deposition, minimal number of inflammatory cells and reduction in granulation tissue.	[202]
Tri-layered SF/PCL composite electrospun TEVGs	Sprague-Dawley rats	Right carotid artery	• Good patency. • Significant infiltration of host vascular cells.	[203]
Bi-layered SF/PLCL composite electrospun TEVGs	Rabbit	Carotid artery	• Good patency. • Graft remodeling and infiltration of host vascular cells. • Loss of mechanical strength over time.	[204]
Electrospun silk TEVGs (aqueous and HFP based)	Sprague-Dawley rats	Abdominal aorta	• HFP grafts performed better than aqueous grafts. • No sign of aneurysm formation. • Neointimal regression over time. • HFP grafts facilitated faster contractile phenotype transition of SMCs. • Increased ECM production in HFP grafts.	[205]
Tri-layered silk TEVG (inner/outer electrospun layer, an intermediate woven layer)	Minipig and Sheep	Carotid artery	• The study identified that sheep would be suitable option for a long-term pre-clinical trial. • Grafts were easy to handle during surgery and showed adequate suture retention. • Pre-seeding of cells is not required for SilkGraft.	[154]
Composite electrospun	Rabbit	Left carotid artery	• Graft degradation and neo-tissue formation.	[206]

PLCL grafts coated with silk/heparin			• Remarkable patency. • No sign of intimal thickening. • Minimal inflammation resulting from biomaterial degradation. • Discontinuous endothelialization after 2 months.	
Composite silk-polyurethane (Silkothane) graft for haemodialysis	Sheep	Arteriovenous shunt	• Implantation between external jugular vein and common carotid artery. • No graft related complications. • 8/9 sheep: 100% primary patency. • Signs of initial inflammation and infiltration of ECs. • Overall 100% patency.	[207]

While prior literature suggests the predominant use of *Bombyx mori* silk for vascular tissue engineering applications, present thesis work explores the non-mulberry silk varieties. In addition, various innovative approaches are demonstrated to improve the *in situ* remodeling and clinical feasibility of silk-based TEVGs.

MOTIVATION AND OBJECTIVES

OF THE PRESENT INVESTIGATION

MOTIVATION AND OBJECTIVES OF THE PRESENT INVESTIGATION

A major proportion of cardiovascular diseases is originated from the occlusion of vital blood vessels carrying oxygenated blood to the target organ. Aberrant blood flow leads to ischemia and organ failure. One of the most predominant examples is the occlusion of the coronary artery causing myocardial infarction and eventual heart failure. Balloon angioplasty, laser angioplasty, and placement of stents are some of the effective clinical options but concomitantly are associated with secondary complications requiring follow-up surgical interventions. Autologous bypass grafting remains the gold standard for the past six decades but faces several limitations, including a shortage of healthy donor vessels. Small diameter (<6mm) blood vessels pose further challenges owing to their high failure rates. Tissue-engineered vascular grafts are currently the best-suited option, wherein a bioresorbable biomaterial is used to harness the body's regeneration capability. While synthetic biomaterials release toxic byproducts upon degradation, the implementation of natural polymers is promising in regeneration.

A substantial research impetus in the field is now focused on using natural ECM proteins as building blocks to manufacture TEVGs. In this regard, some of the prevalently explored natural polymers in tissue engineering are collagen, fibrin, elastin, gelatin, and silk fibroin. Collagen scaffolds are biologically active and predominantly contain cell-binding sites; however, the recapitulation of native-like fibril assembly conferring alpha-helix structure is a formidable challenge. As a result, collagen-based grafts succumb to physiological blood pressure owing to poor mechanical properties. Similarly, fibroblast embedded fibrin gel-based grafts require long-term maturation in a simulated dynamic environment. On the other hand, the fibrin gel provides a congenial structural framework to cells as they secrete their own ECM, providing a mechanically resilient implantable TEVG. Inadequate *in situ* elastin production and lamellar organization in implanted TEVGs is one of the persisting limiting factors. Incorporating either smooth muscle cells generated elastin or engineered synthetic elastin in vascular grafts before implantation is one prospective solution. While some of these natural biomaterials offer outstanding bioactivity, their questionable mechanical properties have limited direct implementation of such polymers. Moreover, their large-scale production is time-intensive and expensive.

Silk is a natural, versatile protein biopolymer produced by various insects (silkworms, spiders, scorpions, mites, and flies). This ancient textile material has long been used as sutures in surgery owing to its biocompatibility and remarkable tensile strength. Considering an array of favorable inherent properties, the past few decades have witnessed silk use as a potential biomaterial for various tissue engineering applications. Among other variants, regenerated silk fibroin obtained from *Bombyx mori* silkworm cocoons is widely explored for regenerative medicine. Lately, a few of the silk-made bioengineered products were approved by FDA for clinical implementation, including SERI surgical scaffold® and Silk Voice®. Few characteristic properties that make silk a suitable choice for tissue engineering applications are: 1) biocompatibility, 2) tunable biodegradation, 3) minimally immunogenic, 4) ability to adapt various formats (3D scaffolds, thin films, nanofibers, microspheres, nanoparticles, hydrogels, etc.), 5) extraordinary mechanical strength, 6) easy accessibility, 7) cost-effective, 8) easy green processing. Without exception, silk biomaterials are under active investigation to explore their potential for vascular tissue engineering applications. Notwithstanding the remarkable promise of silk in various regenerative medicine fields, its involvement in creating tissue-engineered vascular reconstruction products has witnessed a comparative scarcity. Moreover, a significant proportion of prior literature suggests the predominant application of silk fibroin obtained from domesticated *Bombyx mori* silk variety, possibly due to the geographically restricted distribution of many silk types. Nevertheless, lately, researchers are actively investigating silk-based TEVGs prepared by diverse fabrication methodologies in pre-clinical settings and have shown very encouraging outcomes.

We first identified various parameters, which are of utmost importance for the clinical translation of TEVGs. The anti-thrombogenic property of biomaterial is crucial to allow blood flow through the scaffold lumen without coagulation. The fabricated graft should sustain the physiological blood pressure without failure while concomitantly allowing the formation of neo-tissue. A controlled innate immune response facilitates graft remodeling. From a clinical perspective, readily available or fast fabricating grafts would be suitable. In addition, a cell-free graft would have a better chance of regulatory clearance. Affordability is another essential aspect for the broader applicability of tissue-engineered grafts. In this thesis work, we have explored the potential of mulberry (*Bombyx mori*) and Indian endemic non-mulberry silk (*Antheraea assama*) for vascular tissue engineering applications. The additional advantageous aspect of non-mulberry

silk is their inherent presence of RGD (Arg-Gly-Asp) cell binding tripeptide, which is envisaged to facilitate cell adhesion and growth. Moreover, poly-alanine repeats in the heavy chain of non-mulberry silk render remarkable mechanical strength, which remains one of the vital prerequisites while developing vascular grafts.

Considering the enormous scope of silk biomaterials, we have used various progressive strategies to fabricate small-diameter vascular grafts. We first show the favorable cell-material interaction and implications of surface patterns to induce native-like unidirectional alignment resulting in functional improvement. We further report a novel facile methodology to develop bi-layered biomimetic grafts, which were investigated either in cell-seeded format (adipose stem cells) or cell-free platform (functionalized with human Wharton's jelly). We have shown the superior performance of non-mulberry silk-based TEVGs in rat and rabbit implantation models through various defined objectives. Finally, we provide a TEVG platform having the potential to locally deliver the desired bioactive cargo towards improving clinically viable acellular grafts. These grafts could be fabricated in a highly reproducible manner and are potential candidates for ready availability. Different hypothetical strategies are analyzed through the following defined objectives:

1. Combinatorial analysis of silk films' innate physicochemical properties and surface topography on the functional behavior of vascular cells.
2. Development of small-diameter vascular grafts using patterned silk films recapitulating native arterial structure.
3. Development of bi-layered tubular silk scaffolds consisting of inner porous freeze-dried layer coated with outer dense electrospun layer and their functional analysis in a rat aortic interposition model as cell-seeded vascular grafts.
4. Acellular silk-decellularized human Wharton's jelly extracellular matrix composite tubular scaffolds and their functional analysis in rabbit jugular vein as interposition graft for vascular tissue engineering applications.
5. Acellular silk lyogel conduits impregnated with bioactive polymeric microparticles as potential substitutes for vascular tissue engineering applications.

CHAPTER 2

Combinatorial analysis of silk films' innate physicochemical properties and surface topography on the functional behavior of vascular cells

This chapter investigates the effect of intrinsic physiological properties of silk substrates on the functionality of vascular cells. *Bombyx mori* and *Antheraea assama* substrates present distinct surface characteristics (hydrophobicity/hydrophilicity, chemical composition owing to structural dissimilarities). In addition, unidirectional alignment influences vascular cell functionality in terms of phenotype switch and physical contraction. Understanding cell-material interaction provides valuable insights for designing a translatable tissue-engineered product.

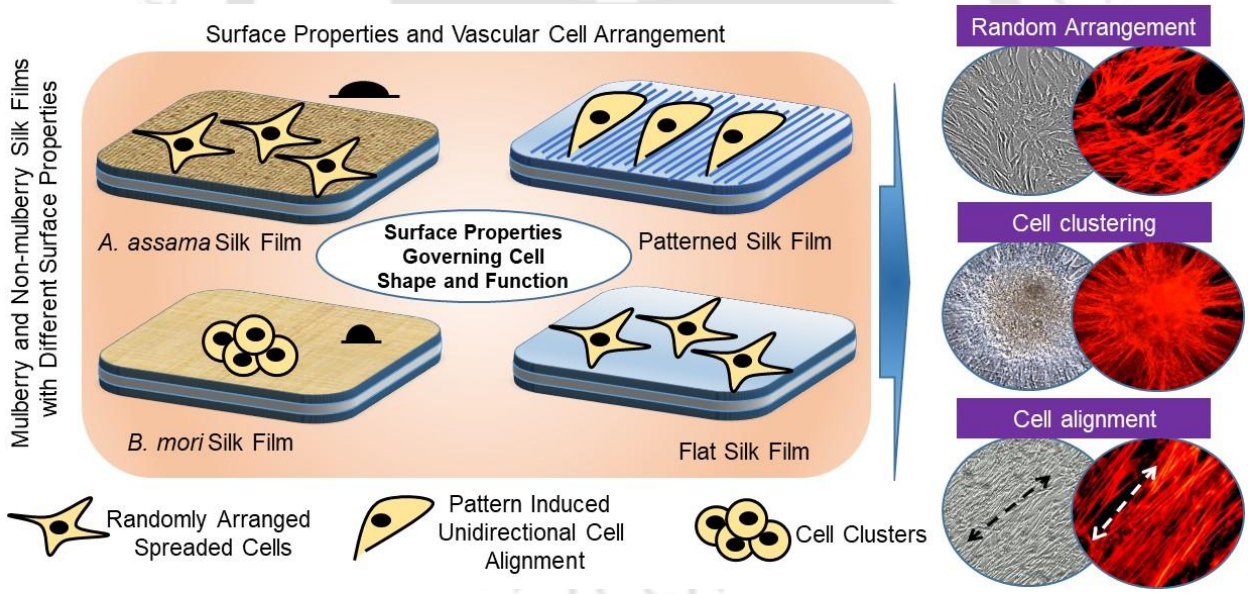

Publication:

Prerak Gupta, *Joseph Christakiran Moses and Biman B. Mandal. Surface patterning and innate physicochemical attributes of silk films concomitantly govern vascular cell dynamics.* ***ACS Biomaterials Science & Engineering.*** *2019; 5:933-49.*

ABSTRACT

Functional impairment of vascular cells is associated with cardiovascular pathologies. Recent literature clearly present evidences relating cell microenvironment and their function. It is crucial to understand the cell-material interaction while designing a functional tissue engineered vascular graft. Natural silk biopolymer has shown potential for various tissue-engineering applications. In the present work, we aimed to explore the combinatorial effect of variable innate physico-chemical properties and topographies of silk films on functional behavior of vascular cells. Silk proteins from different varieties (mulberry *Bombyx mori* – BM and non-mulberry *Antheraea assama* – AA) possess unique inherent amino acid composition that leads to variable surface properties (roughness, wettability, chemistry and mechanical stiffness). In addition, we also engineered the silk film surfaces and printed a microgrooved pattern to induce unidirectional cell orientation mimicking their native form. Patterned silk films induced unidirectional alignment of porcine vascular cells. Irrespective of alignment, endothelial cells (ECs) proliferated favorably on AA films; however, it suppressed nitric oxide (NO) production – an endogenous vasodilator. Unidirectional alignment of smooth muscle cells (SMCs) encouraged contractile phenotype as indicated by minimal cell proliferation, increment of quiescent (G0) phase cells and upregulation of contractile genes. Moderately hydrophilic flat BM films induced cell aggregation and augmented the expression of contractile genes (for SMCs) and endothelial nitric oxide synthase - eNOS (for ECs). Functional studies further confirmed SMCs' alignment improving collagen production, remodeling ability (matrix metalloproteinase - MMP-2 and MMP-9 production) and physical contraction. Altogether, this study confirms vascular cells' functional behavior is crucially regulated by synergistic effect of their alignment and cell-substrate interfacial properties.

2.1 Introduction

Cell microenvironment influences their behavior and functionality. It may be various soluble factors present in the close vicinity or the surrounding matrix that triggers multiple signaling pathways [208, 209]. All living tissues consist of a diverse population of cells embedded in specialized extracellular matrix (ECM) in a very intricate manner. This ECM provides the structural framework and determines cell polarity and arrangement. Biochemical composition and topographical organization of ECM are two key determining factors regulating cellular behavior and functionality. Hence, a lot of research has been focused on modulating cell-surface interactions by tuning surface topography [209]. One of the arguments about studying the co-relation between cell distribution pattern and their function is discrepancy among 2D vs 3D microenvironments. However, the majority of studies have implemented 2D surfaces to study the fundamental principles of cell biology owing to its simplicity as compared to complex 3D microenvironments. Most recently, structural control of surface topography using micro/nano technology has paved the way to mimic the 3D complex microenvironments while preserving the easiness of working with 2D surfaces [210, 211].

At cell substrate interface, several factors (including topography, wettability, roughness, chemistry and mechanical properties of the substrate) play a crucial role in determining cell behavior. The majority of human adherent cell types are spatially arranged innately in a unique manner that helps them maintain their function and overall tissue dynamics [212, 213]. Of note, vascular cells, typically endothelial cells (ECs) in tunica interna and smooth muscle cells (SMCs) in tunica media of blood vessels follow a unique topographical arrangement. ECs are aligned along the direction of blood flow and maintain vascular homeostasis [214], whereas SMCs are aligned radially contributing to the mechanical robustness and vasoactive responsiveness of blood vessels [215]. These design parameters become important for tissue engineering of vascular grafts where the main focus for success is to engineer the scaffold wall surface in such a way so that it recruits the progenitor vascular cells and provides a congenial microenvironment for their growth and functionality. Recently, several studies have shown the co-relation between vascular cell morphology/organization and their functionality *in vitro* [216] and *in vivo* [217, 218].

A functional and continuous monolayer of ECs maintains un-interrupted blood flow in the blood vessels. Any damage in ECs' monolayer may lead to various pathological conditions like thrombosis, hyperplasia, stenosis and inflammation in the vessel wall, which alters the vascular

tone [219]. Besides that, cell morphology, shape, alignment and polarity are also other determining factors that regulate ECs' functionality [220]. Hence, mimicking a native-like physiological environment becomes a point of interest. ECs present in blood vessels' lumen lining are exposed to shear stress and cyclic circumferential strain due to continuous blood flow. Under these circumstances, these cells tend to adopt unidirectional alignment along the direction of blood flow. The adjacent multiple layers of SMCs in the vascular wall (tunica media) align themselves radially (perpendicular to the direction of blood flow) [215]. Recently, several researchers have reported the positive effect of unidirectional alignment on vascular cell functionality. Majority of them focused on either engineering the cell culture surfaces (by printing grooved pattern) or by exposing the cultured cells to the flow shear stress [79, 213, 215, 221].

Surface wettability is another important parameter that influences cell morphology affecting their functionality [213]. It is well proven fact that cells prefer to spread better on moderate hydrophilic surfaces [222, 223]. Limited cell adhesion and spreading was reported on highly hydrophilic surfaces because such surfaces do not allow long-term retention of cell adhesion molecules [224]. The biochemical composition of the cell culture matrix or surface chemistry also regulates cell morphology and spreading [225, 226]. For instance, surface bio functionalization with cell binding RGD peptide enhances the cell attachment and proliferation via integrin (cell adhesion receptor) mediated process [227]. Apart from surface patterning (guiding cellular alignment), surface roughness also determines the functionality of vascular cells. Cellular response to surface roughness at micro scale is a bit controversial owing to the inconsistency noticed throughout several reports. For instance, endothelial cells showed superior growth on rougher PU-PEG (Polyurethane-polyethylene glycol) surface irrespective of presence of surface cell adhesion peptides (RGD) [228]. On the contrary, smoother solvent casted poly (L-lactic acid) (PLLA) surfaces supported better ECs' functionality [229]. Nanostructured titanium surfaces favorably supported the adhesion of SMCs and ECs [230]. Such paradoxical behavior is generally attributed to undefined attributes of surface roughness and needs more specific definition that considers different nanostructured shapes, spacing between irregularities and sharpness of the peaks [224]. Among all cell-substrate interface properties, substrate rigidity is considered least important but recently it is identified as a very crucial factor in determining cells' fate. The phenomenon of change in cell's chemical microenvironment in response to mechanical signals is called 'mechanotransduction' [231]. Substrates with same chemical composition and different rigidity

have shown to modulate SMCs adhesion [224]. Studies have shown that substrates with low rigidity does not allow cellular spreading whereas cells spread better on stiffer substrates (depending on cell type) [232]. One of the plausible explanation of such cellular behavior might be related with imbalance between cell traction forces and corresponding extracellular matrix (ECM) response, a crucial parameter for assembly of cell-matrix adhesion complexes and cell spreading [224]. Several studies have reported the effect of individual factor on cellular functionality; however, in a native *in vivo* microenvironment, cells are exposed to multiple factors simultaneously. Hence, investigating the combinatorial effect of more than one factor becomes of great importance.

In the present study, we intend to explore the functionality of vascular cells (ECs and SMCs) when cultured on mulberry *Bombyx mori*-BM and non-mulberry *Antheraea assama*-AA silk films. Our selection of using different silk relied on following crucial parameters: (1) both proteins are highly biocompatible and have been explored for various tissue engineering applications [233, 234]; (2) their ability to be fabricated into myriad structural designs with nano level accuracy, allowing surface engineering to print any desirable pattern [14], and (3) structural variability in their native amino acid sequence and arrangement of secondary protein structures [235]. The molecular composition of these silk proteins is quite different. Heavy chain of both silk proteins consists majorly of Ala (44.5% vs 28.8% for AA vs BM) and Gly (30.1% vs 43.7% for AA vs BM), nonpolar amino acids [126]. The alanine methyl groups are usually exposed to external microenvironment because of their arrangement outside of protein backbone [236]. Owing to presence of different percentage of hydrophobic amino acid residues in BM and AA silk proteins, the surface wettability of films made of these proteins is expected to be dissimilar. The crystalline core of AA is made-up of poly-alanine motifs, which makes 37.4% of total Ala out of 44.5%. In contrast, BM protein have multiple repeats of AGSGAG comprising 55% of total crystalline core [237]. Differential amino acid composition and arrangement leads to formation of unique secondary structures. For instance, the poly-alanine motifs present in AA silk prefer to form anti-parallel β-sheets via non-covalent inter-molecular interactions, which confers tensile strength [238]. Besides, it also provides more hydrophobicity, forming stronger β-sheets as compared with AGSGAG repeats of BM silk. In general, alanine motifs provide tensile strength to silk fibers whereas glycine rich sequences are responsible for fiber elasticity. It has also been reported that even the short polyalanine stretches $(A)_6$ are able to confer remarkable tensile strength to AA

protein by forming strong β-nanocrystal, which is much higher than all other wild silk varieties [239]. Additionally, AA silk has intrinsic presence of RGD cell binding motif in its native amino acid structure making its surface chemically different from BM silk [126]. Owing to these aforementioned characteristics, surfaces of silk films obtained from different silks provide variable surface characteristics. Therefore, in the current endeavour, we cultured vascular cells on BM and AA silk films and looked into their functional behaviour in response to combinatorial effect of multiple physico-chemical factors acting at cell-substrate interface.

2.2 Materials and methods

2.2.1 Fabrication of silk films

Mulberry silk (*Bombyx mori* - BM) and non-mulberry silk (*Antheraea assama* - AA) proteins were used for this study. Silk fibroin (SF) proteins were obtained by following previously described procedures [233]. BM silk was extracted by degumming the cocoons in 0.02M sodium carbonate followed by dissolution in 9.3M LiBr and dialysis against distilled water for 72h with frequent water changes. Non-mulberry AA silk was obtained directly from silk glands of mature 5^{th} instar larvae. The glandular protein was extracted using fine forceps and dissolved in 1% (w/v) sodium dodecyl sulfate (SDS). Protein solution was further dialyzed in milli-Q water at 4℃ for 4h. Percentage of silk protein was estimated using gravimetric method and SF protein solution was stored at 4℃ until use.

A 2% (w/v) SF solution was used for fabricating silk films. Both flat and patterned polydimethylsiloxane (PDMS) molds were prepared as per earlier described techniques. Flat molds were fabricated by blending PDMS substrate (Dow Corning Corporation, Midland, MI USA) with its cross-linker (10:1 w/w ratio) and baking at 60℃ for 4h. Soft lithography technique was used to prepare microgrooved patterned molds (distance between ridges: 3 μm; groove depth: 200 nm) [240]. 4 x 4 cm^2 PDMS molds were used to fabricate films by spreading 2 mL of 2% SF protein solution and allowed to dry at ambient flow conditions overnight. The dried silk films were exposed to water vapor annealing in a vacuum desiccator for 6h at 37℃. The water stabilized films were detached further from the PDMS molds and stored at 4℃ sterile conditions until further use. The following abbreviations are used henceforth for designating different experimental groups: standard tissue culture plate (TCP), BM flat films (BMF), BM patterned films (BMP), AA flat films (AAF) and AA patterned films (AAP).

2.2.2 Physico-chemical characterization of silk films

Water vapor annealed films were analyzed for their surface roughness and topography by atomic force microscopy (Agilent Model 5500, USA). All silk films were scanned in non-contact mode with a scanning area of 15 x 15 μm^2 at room temperature (RT). WSxM 5.0 Develop 7.0 software was used to calculate various parameters and plotting surface profiles of patterned silk films. Both flat and patterned silk films were observed under FESEM (Zeiss, Sigma) for analyzing their surface morphology. FESEM micrographs were captured after gold sputtering of silk films. Water contact angle of flat silk films was further investigated by sessile drop technique using contact angle goniometer (Holmarc, India). Water vapor annealed silk films of 2 x 2 cm^2 were used. An automated micro-syringe extruded 3 µL of milli-Q water droplet onto silk film and captured images were processed to determine the contact angle of both flat and patterned silk films. Patterned silk films were characterized parallel (PAR) and perpendicular (PER) to the direction of microgrooves. A scheme of directions of these analyses is shown in **Figure 2.1**. For each film, at least three different spots were used for calculating the contact angle.

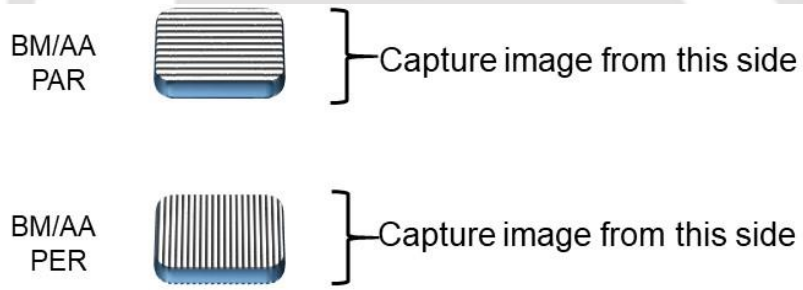

Figure 2.1. *Schematic representation of contact angle measurement for patterned silk films. BM/AA PAR is representing that the image was captured parallel to the direction of pattern and BM/AA PER is representing that the image was captured perpendicular to the direction of pattern.*

Silk films were further analyzed to explore their mechanical properties. Only water vapor annealed flat films were subjected for this analysis owing to their stability in hydrated conditions in which the analysis was performed. Silk film strips (length: 3 cm and width: 1 cm) were used for tensile testing under hydrated conditions using Universal Testing Machine (UTM, Instron 5944, USA) in a BioPuls bath (with PBS as immersion buffer) at 37°C. Stress-strain curves were obtained at a crosshead speed of 1 mm/min until sample failure. Modulus of films was calculated as slope of stress-strain curves. Silk films were also subjected for cyclic testing until 10 cycles (5% deformation strain) value at a rate of 1 mm/min. Mechanical analysis of silk films was performed for at least n=4 specimens.

Infrared spectra of regenerated silk fibroin solutions (BM and AA) and water vapor annealed silk films of the same were characterized using Fourier transform infrared spectrometer (Shimadzu, Model: IR Affinity-1S WL) in attenuated total reflectance (ATR mode) with germanium internal reflection element. Each measurement consisted of 30 scans averaged to yield the spectra (4000 – 400 cm^{-1}) with a resolution of 2 cm^{-1}. The amide-I spectra (1700 – 1600 cm^{-1}) was further deconvoluted by taking second derivative of the spectra and fitting Gaussian peaks to determine the secondary structures present in the regenerated silk fibroins and its water vapored annealed films. Band assignments for secondary structures were given as follows: α-helices (1650 – 1658 cm^{-1}), β-sheets (1620 – 1640 cm^{-1}), anti-parallel β-sheets (1670 – 1695 cm^{-1}), disordered structures (1640 – 1650 cm^{-1}), loops (1660 – 1680 cm^{-1}) following previous reports [241, 242]. The deconvoluted spectra were area normalized and subsequently used to determine the percentage of secondary structures present in the samples investigated.

2.2.3 Isolation and culture of vascular cells

Smooth muscle cells (SMCs) and Endothelial cells (ECs) were isolated from descending porcine aorta following our previously described protocol [243]. In brief, porcine descending aorta was collected from local slaughterhouse and transported in ice cold sterile phosphate buffered saline (PBS). Tissue was processed within 1h of collection. Associated fat was removed and the aorta was cut into 1 cm^2 pieces followed by digestion with collagenase type 1A (1 mg/mL, Sigma-Aldrich, USA) keeping luminal side in contact with the plate surface. These tissue sections were further incubated in a humidified incubator (95% humidity) at 5% CO_2, 37°C for 1h. Post incubation, the luminal surface was scraped to harvest ECs. From the remaining tissue, a medial layer containing SMCs was isolated from the adventitial layer and digested further in 0.5% collagenase for 8h. Digested tissue was filtered through a cell strainer (70 µm pore size, BD Biosciences, USA) and cultured in high glucose Dulbecco's Modified Eagle's medium (DMEM, Gibco, USA) supplemented with 10% (v/v) fetal bovine serum (FBS, Gibco, USA) and 1% (v/v) antibiotic-antimycotic solution (Himedia, India) in a humidified incubator. After 24h of cell adherence, media was changed to ECGS (endothelial cell growth supplement, recommended concentration in DMEM culture media, Sigma-Aldrich, USA) for ECs and SMGS (smooth muscle cell growth supplement, 2% w/v in DMEM culture media, Life Technologies, USA) for SMCs.

2.2.4 Immunostaining for vascular cell identification

Vascular cells isolated from porcine aorta were subjected to immunostaining for cell specific marker expression. ECs were stained for vWF (Von Willebrand factor) and SMCs were stained for calponin and αSMA (alpha- Smooth muscle actin) markers. Cells cultured on standard TCP (tissue culture plate) were fixed in neutral buffered formalin (NBF, Sigma-Aldrich, USA) overnight and permeabilized with 0.1% (v/v in PBS) TritonX-100 for 15 minutes. Cells were further treated with blocking solution (2% w/v bovine serum albumin-BSA in PBS) to prevent any non-specific binding. Rabbit primary antibody solution was prepared in blocking solution with the following dilutions: vWF (1:400), calponin (1:250) and αSMA (1:100). Cells were treated with primary antibody for 1h at 37°C followed by FITC tagged anti rabbit secondary antibody treatment (1:500) for 1h. Cell nucleus was stained with Hoechst 33342 (1:1000, Sigma-Aldrich, USA) and the cellular cytoskeleton was stained with rhodamine phalloidin (1:40, Life technologies, USA). Cells were given three PBS wash after each successive step. Stained cells were imaged under a fluorescent microscope (EVOS FL, Life Technologies, USA).

2.2.5 Proliferation of vascular cells cultured on silk films

Silk films from each experimental group were cut into circular discs (ϕ 15 mm) and placed in a 24 well tissue culture plate. Films were further sterilized followed by conditioning overnight with culture media (DMEM with 10% FBS). Vascular cells (both ECs and SMCs) were seeded carefully onto these discs at a density of 10^5 cells/cm^2 suspended in minimal volume (~20 µL) of culture media to avoid spillage from the films. After initial cell adherence onto silk films, 1 mL of culture media was added into each well and plate was kept in humidified incubator (5% CO_2, 37°C). AlamarBlue (Thermo Fisher Scientific, USA) dye was used to monitor the cell activity and proliferation following manufacturer's protocol and as described previously [234]. Cell growth was determined at three different time points and represented as normalized value of percentage reduction of AlamarBlue.

2.2.6 Cell distribution profile and orientation analysis

Phase contrast microscopic images of vascular cells (both ECs and SMCs) cultured on silk films were captured using microscope (EVOS FL, Life Technologies, USA). These images were further processed using MBF ImageJ software (model 1.52a, National Institute of Health, USA). Cell

orientation was calculated by OrientationJ plugin, which is available online (http://bigwww.epfl.ch/demo/orientation/). Briefly, captured phase contrast images were converted to 32-bit greyscale type and orientation distribution plugin was used to plot the cell distribution profile with 5% minimum coherency level. Moreover, in order to visualize the distribution of actin cellular filaments, cells cultured on silk films were stained with rhodmine-phalloidin fluorescent dye as described previously and observed under a fluorescent microscope (EVOS FL, Life Technologies, USA).

2.2.7 Cell cycle analysis

Circular discs of silk films (ϕ 3 cm) were sterilized, conditioned in culture media and placed in 6-well tissue culture plate. ECs and SMCs were seeded onto silk films with a cell density of 10^5 cells/cm^2. After 4 days of culture, cells were harvested from silk films using trypsin-EDTA (Himedia, India) and analyzed for cell cycle profile. Briefly, cell suspension was fixed in ice cold ethanol followed by 2 washes with PBS. Cells were further treated with 200 µg/mL RNase A (Sigma-Aldrich, USA) for 1h to avoid any false positive signal from RNAs. Cells suspension was treated with 40 µg/mL propidium iodide (PI, Thermo Fischer Scientific, USA) and kept on ice for an additional 10 min prior to flow cytometry date acquisition. Cell cycle data was acquired in FL2 channel using BD Accuri C6 plus flow cytometer machine equipped with blue laser (488 nm). Data was analyzed on inbuilt BD Accuri™ C6 software to calculate the percentage of cell population present in each phase of cell cycle.

2.2.8 Analysis of functional gene expression using qRT-PCR

Vascular cells cultured on topographically different silk films were investigated for the expression of functional genes. For this, we studied the expression of endothelial nitric oxide synthase (*eNOS*)/angiopoietin 1 (*ANGPT1*) for endothelial cells and alpha smooth muscle actin (*αSMA*)/smooth muscle myosin heavy chain (*SM-MHC*) contractile markers for smooth muscle cells. After 4 days of culture, cells were lysed using TRIzol reagent (Sigma-Aldrich, USA) to isolate the RNA. The cell lysate was centrifuged for 10 min at 13,000 rpm at 4°C followed by transfer of supernatant to fresh tubes containing chloroform. After 15 min, three distinct layers were observed and tubes were centrifuged again at 13,300 rpm. Upper aqueous layer containing RNA was transferred to fresh tubes and RNA was eluted and purified by repeated washing with

ethanol. RNase free water was used to re-suspend the RNA pallet. The extracted RNA was quantified and processed for reverse transcription using high efficiency reverse transcription kit (Applied Biosystems, Invitrogen) and thermal cycler (Takara, Japan). Gene expression profile was further quantified using Power SYBR Green PCR master mix (Applied Biosystems, Life Technologies, USA) and real-time PCR machine (Applied Biosystems, Quant Studio 5) following manufacturer's instructions. Primer sequences of the target genes are mentioned in **Table 2.1**.

Table 2.1. *Primer sequences of target genes.*

Gene	Primer Sequence
Porcine eNOS	**F:** 5′- TTCCGGGGATTCTGGCAGGAG -3′ **R:** 5′- GCCATGGTGACGTCGCCGCAG-3′
Porcine ANGPT1	**F:** 5′- CTTCCTCGCTGCCATTCTGA-3′ **R:** 5′- GACAGTTCCCGTCGTGTTCT-3′
Porcine αSMA	**F:** 5′- GGCCGAGATCTCACTGACTA-3′ **R:** 5′- AGTGGCCATCTCATTTTCAA-3′
Porcine SM-MHC	**F:** 5′- CTGCAGCTTGGAAATATCGT-3′ **R:** 5′- GAGTGAGGATGGATCTGGTG-3′
Porcine GAPDH	**F:** 5′-TCGGAGTGAACGGATTTGG-3′ **R:** 5′-CCAGAGTTAAAAGCAGCCCT-3′

2.2.9 Functional studies

2.2.9.1 NO production by endothelial cells

Production of NO (nitric oxide) by endothelial cells was quantified as per previously described protocol [244]. Circular silk film discs were placed in 12 well tissue culture plate, sterilized and conditioned with culture media prior to cell seeding. A higher cell number (~5 x 10^5) were seeded into each well to obtain a uniform cell monolayer. After day 1 of culture, 1 mL of media was pooled out and replaced with same volume of fresh media. The experiment was terminated after 4 days of culture and spent media was collected in fresh vials. Collected media was stored at -20°C until further use. Nitrite was quantified by using Griess reagent (Sigma-Aldrich, USA) which is a stable degradation product of NO. Spent media was centrifuged to remove any possible cell debris or particles and 100 µL of supernatant was incubated with equal volume of Griess reagent in a 96 well plate at RT under dark conditions for 15 min. The mixture was read at 540 nm and readings were fitted into standard curve equation (obtained using sodium nitrite) to quantify the amount of NO produced by endothelial cells.

2.2.9.2 Collagen production by smooth muscle cells

In order to determine the amount of collagen secreted by SMCs, cells were seeded on different silk films placed in 6 well plates at a density of 5 x 10^5 cells/well. After 4 days of culture, the experiment was terminated and Sirius red dye based assay was used to quantify the total collagen content following previously published protocol [245]. Silk films with cultured SMCs were digested using pepsin digestion buffer (1 mg/mL pepsin-Sigma-Aldrich, USA, 0.5M NaCl and 0.1M acetic acid, pH 3.0). 100 µL from each digested sample was aliquoted in 96 well plate and allowed to dry overnight at 37°C. The dried sample layer was further treated with Sirius red dye (1 mg/mL) followed by fixation with saturated picric acid for 1h. Fixed sample coatings were washed with 0.01 normal HCl and dissolved in 0.1 normal NaOH. Optical density (O.D.) readings were taken at 550 nm using multiplate reader (Tecan infinite M 200 pro). A standard curve was plotted using rat tail collagen (Sigma-Aldrich, USA) to determine the total collagen content secreted from SMCs cultured on silk films. Furthermore, secreted collagen was normalized with total DNA content quantified using Quant-iT™ PicoGreen™ dsDNA Assay Kit (Thermo Fisher Scientific, USA) following manufacturer's instructions.

2.2.9.3 Gelatin zymography

To detect the activity of secreted matrix metalloproteinase (MMP - 2 and 9) porcine SMCs at cell density of 6000 cells/cm^2 were seeded on different films and cultured in SMC growth media supplemented with 10% (v/v) FBS. After cells attained confluency, these cell seeded films were incubated in SMC growth media without FBS supplementation for 14h. The serum starved conditioned media was collected to assess the MMP activity through gelatin zymography following previously published protocols [245]. Briefly, 40 µg of protein from serum starved conditioned media from each group were loaded in each lane and separated in non-reducing conditions using 7.5% (w/v) polyacrylamide separating gel with 4 mg/mL gelatin. After resolving the gel was incubated in renaturation buffer [50 mM Tris-HCl, pH 7.5, 1% (w/v) triton X-100 (Sigma-Aldrich, USA), 5 mM $CaCl_2$ (Sigma-Aldrich, USA) and 1 mM $ZnC_4H_6O_4$ (Sigma-Aldrich, USA)] overnight at 37°C. The gel was then stained with 0.5% (w/v) Coomassie Brilliant Blue R-250 (Himedia, India) and destained to visualize the gelatinolytic bands which appeared as clear bands in dark background. The densiometric profiling was done using Image-J software (NIH, USA).

2.2.9.4 Collagen gel contraction assay

The functional contractility attained by porcine SMCs with respect to biophysical cues presented by different films were assessed using collagen gel contraction assay, following previously published protocols [246]. Briefly, porcine SMCs were seeded on different films at a seeding density of 6250 cells/cm^2 and cultured for 4 days in SMC growth media supplemented with 10% (v/v) FBS. Thereafter, the cells were detached using trypsin and resultant cell suspension was seeded on to preformed collagen gels (collagen-I, rat tail, Gibco, USA) following the manufacturer's protocol in 96 wells plate at density 10^5 cells/mL. After 24h, the extent of collagen gel contraction was assessed using Image-J by measuring the area of gel before contraction and after contraction.

2.2.10 Statistical analysis

All of the statistical analyses were performed using OriginPro 8 (Origin lab Corporation, USA) following one-way analysis of variance (ANOVA) and Tukey's test. All the experiments were performed at-least for n=3, unless otherwise specified. Significant levels were analyzed at 95% and 99% confidence and represented as #$p<0.05$ and ##$p<0.01$. All data is represented as mean ± standard deviation.

2.3 Results

2.3.1 Physico-chemical properties of silk films

Cell substrate interaction influences the cells' functionality. Surface topography is one of the factors that cells experience when cultured on any substrate. Therefore, we performed AFM scanning of silk films (**Figure 2.2A**). A considerably higher surface roughness was noticed for AAF films ranging 57.52 ± 3.89 nm, approximately 1.6 times more than BMF films. Reported values are representative of 3 different scanning spots. When calculated for patterned silk films (BMP and AAP), no such roughness difference was observed and the patterning (microgroove pattern) dominated the nano range roughness difference. The surface plot of patterned silk films demonstrated smoother ends of microgrooves for BMP whereas irregular edges were observed for AAP films. Distance between consecutive microgroove ridges was recorded to be ranging from 2.8 – 3.0 µm for both type of patterned films. Similar features were observed when these films

were visualized under FESEM (**Figure 2.2B**). AA films showed rougher surface whereas smoother surface and edges were observed for BM films.

Another crucial determining factor is surface contact angle or surface hydrophobic/hydrophilic nature that governs cellular adhesion, spreading and functionality. We further investigated the water contact angle for both of silk protein types. Both silk films were hydrophilic owing to the fact that their water contact angles were well below 90°; however, their degree of hydrophilicity was significantly different. BMF films showed approximately 1.43 times higher contact angle as compared to AAF films, making it moderately hydrophilic than AAF type (**Figure 2.2C**). We further analyzed the contact angles for patterned silk films along and perpendicular to the direction of microgrooves. Again, a similar trend was observed and AAP films showed relatively higher degree of hydrophilicity with less contact angle. The contact angle values for various silk films are summarized in **Table 2.2**.

Table 2.2. *Contact angles of silk films.*

Sample	Contact angle (in degrees)
BMF	66.92 ± 1.75
AAF	46.76 ± 1.39
BMP PAR	68.41 ± 1.28
BMP PER	64.98 ± 1.56
AAP PAR	40.93 ± 1.02
AAP PER	39.58 ± 1.87

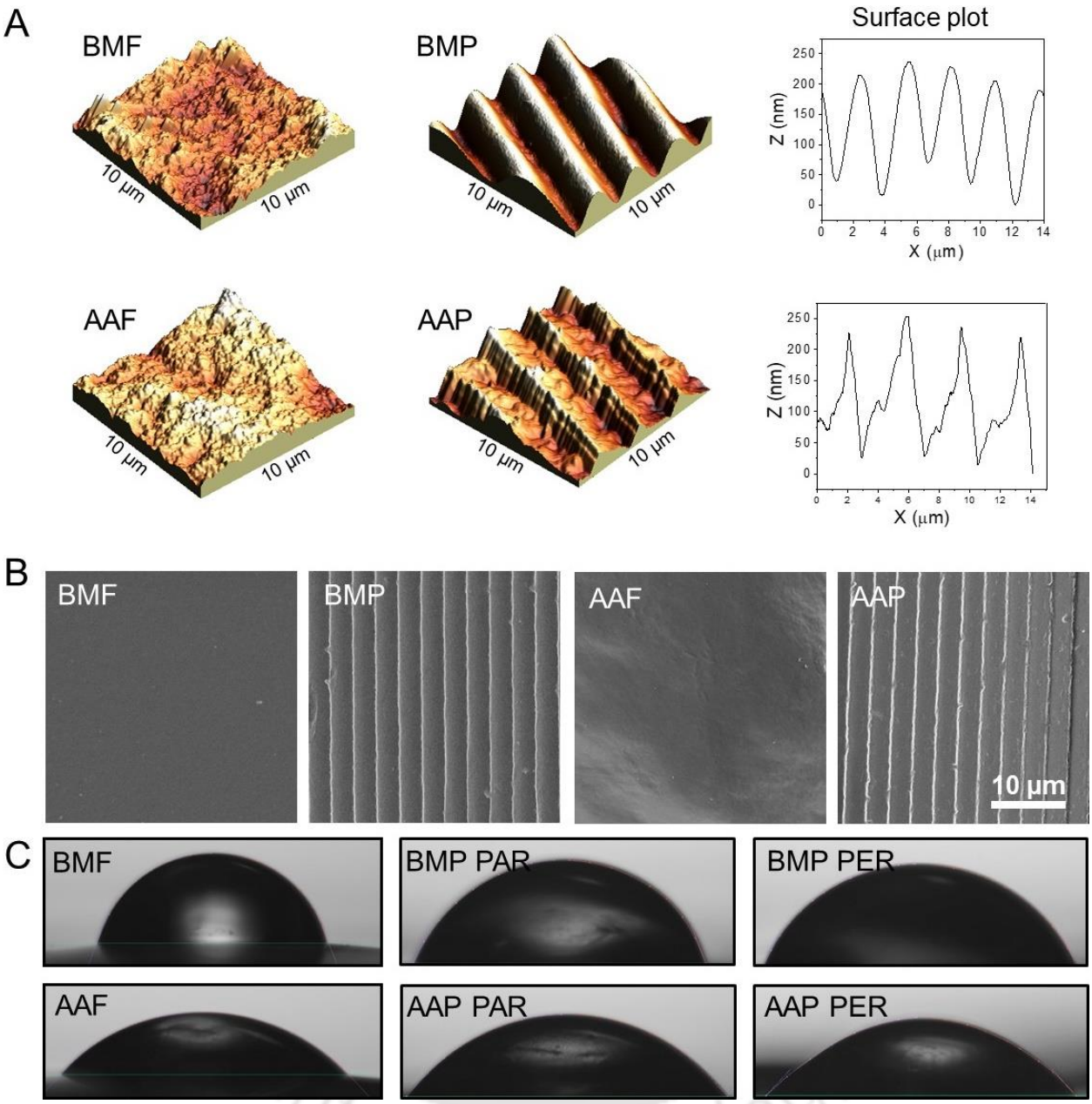

Figure 2.2. *Surface characterization of silk films. (A) Atomic force microscopic images of flat and patterned silk films showing surface roughness. Surface plot profile of patterned films is also illustrated indicating the groove depth and peak-to-peak distance. (B) FESEM micrographs of silk films demonstrating surface topography and patterning. (C) Water contact angles of flat silk films (BMF and AAF) and patterned silk films (BMP and AAP in both parallel (PAR) and perpendicular (PER) to the microgroove direction). Images are showing droplet micrographs in contact with silk films. Contact angle values mentioned in the table are representative of at least three different spots onto silk film surfaces.*

Furthermore, mechanical properties of silk films were analyzed. Only water vapor annealed flat silk films were subjected for this analysis. Stress-strain curves suggested higher slope of AAF

films as compared with BMF (**Figure 2.3A**). The representative load-displacement curves are also shown in **Figure 2.4**. AAF films were stronger/stiffer and showed ~2-fold higher modulus (32.54 ± 9.51 MPa) than BMF films (16.79 ± 0.51 MPa) (**Figure 2.3B**, $p<0.01$). A similar trend was observed for stress at failure (3.09 ± 0.65 MPa vs 8.54 ± 1.04 MPa for BMF vs AAF films respectively) (**Figure 2.3C**, $p<0.01$); however, no significant difference was observed for strain at failure (0.25 ± 0.08 MPa vs 0.30 ± 0.12 MPa for BMF vs AAF films respectively) (**Figure 2.3D**). Tensile cyclic testing of silk films was also performed to obtain hysteresis behavior. BMF films did not exhibit much of energy loss between first and last cycle (**Figure 2.3E**); however, strain hardening and energy gain was observed for AAF films until fifth cycle followed by plateau for last five cycles (**Figure 2.3F**).

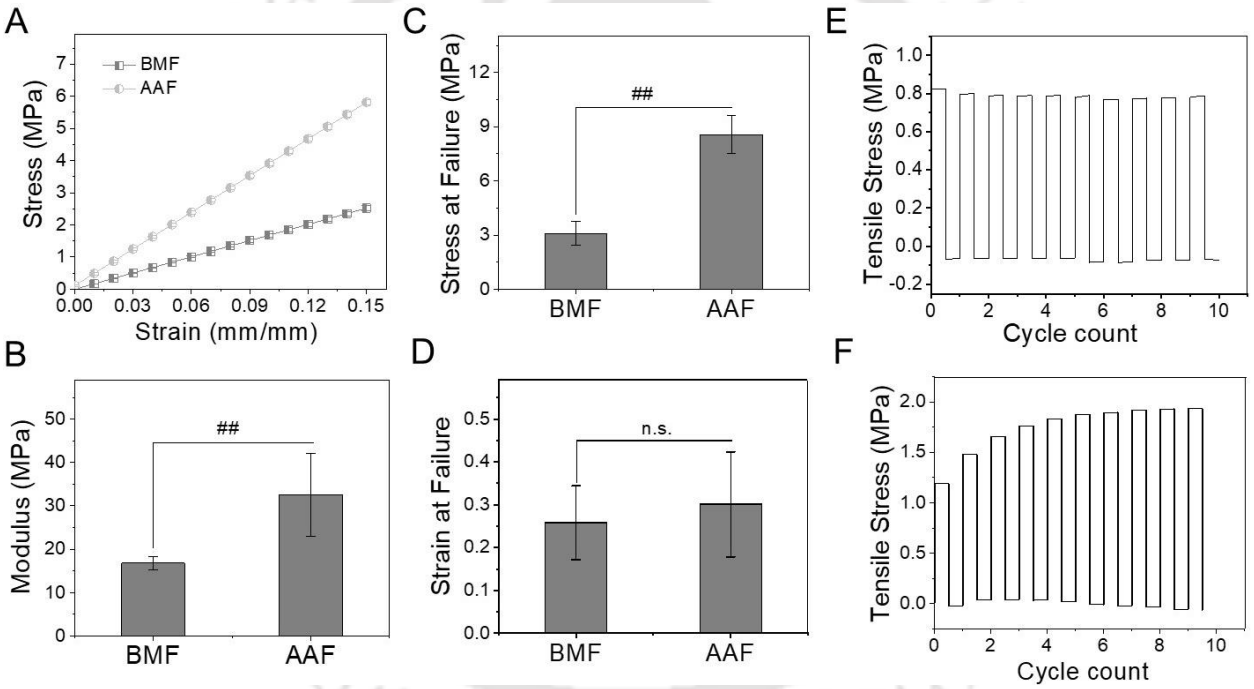

Figure 2.3. *Mechanical properties of silk films. (A) Representative stress-strain curves showing the slope of BM and AA flat hydrated films. (B) Modulus of silk films calculated from stress-strain curve slope. (C) Comparison of stress at failure values for both silk films. (D) Comparison of strain at failure values for both silk films. (E) Representative tensile cyclic analysis of BM silk films. (F) Representative tensile cyclic analysis of AA silk films. (##p<0.01, n.s.=not significant)*

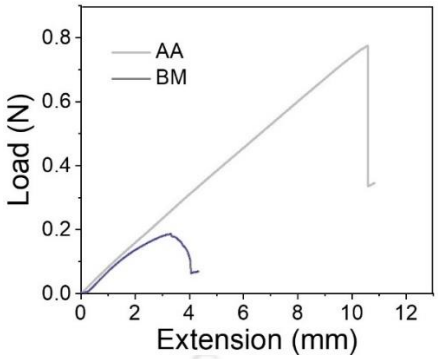

Figure 2.4. *Representative load-displacement curves of hydrated silk films.*

Chemical structure analysis was further performed to investigate the secondary structure composition of silk films (**Figure 2.5A**). Silk fibroin solution (AAS and BMS) and water vapor annealed films (AAF and BMF) were subjected for this analysis. All specimen showed characteristic peaks in amide-I (1610-1660 cm^{-1}), amide-II (1510-1560 cm^{-1}) and amide-III (1210-1260 cm^{-1}) regions [247]. On comparing the samples before (AAS, BMS) and after (AAF, BMF) water vapor annealing, a blue shift was observed in amide-I region. Alternatively, amide-II and amide-III regions demonstrated a red shift, a characteristic of β-sheet transition after water vapor annealing, making silk films water stable [247]. In order to quantify the secondary structure composition in silk solution and water stable silk films, we de-convoluted the amide-I region between 1600-1700 cm^{-1} region (**Figure 2.5B**). The percentage of secondary structures after water vapor annealing is summarized in **Table 2.3**. The blue shift noticeable in the amide-I spectra of water annealed films meant an increase anti-parallel β-sheet and cumulative β-sheet content was much higher than in fibroin solution indicating water stability of films consistent with previous reports. The higher percentage of β-sheet in non-mulberry silk is attributed to the poly-alanine present in AA.

Table 2.3. *Effect of water vapor annealing on silk secondary structure composition.*

Secondary structures	**Percentage (%)**			
	BMS	**AAS**	**BMF**	**AAF**
β-sheets	44.7	58.1	29	33.2
α-helices	7.7	23.1	-	1.7
Loops	36.2	5.9	16.3	-
Antiparallel β-sheets	-	1.7	34.9	61.9
Disordered structures	11.3	11.2	19.8	3.2

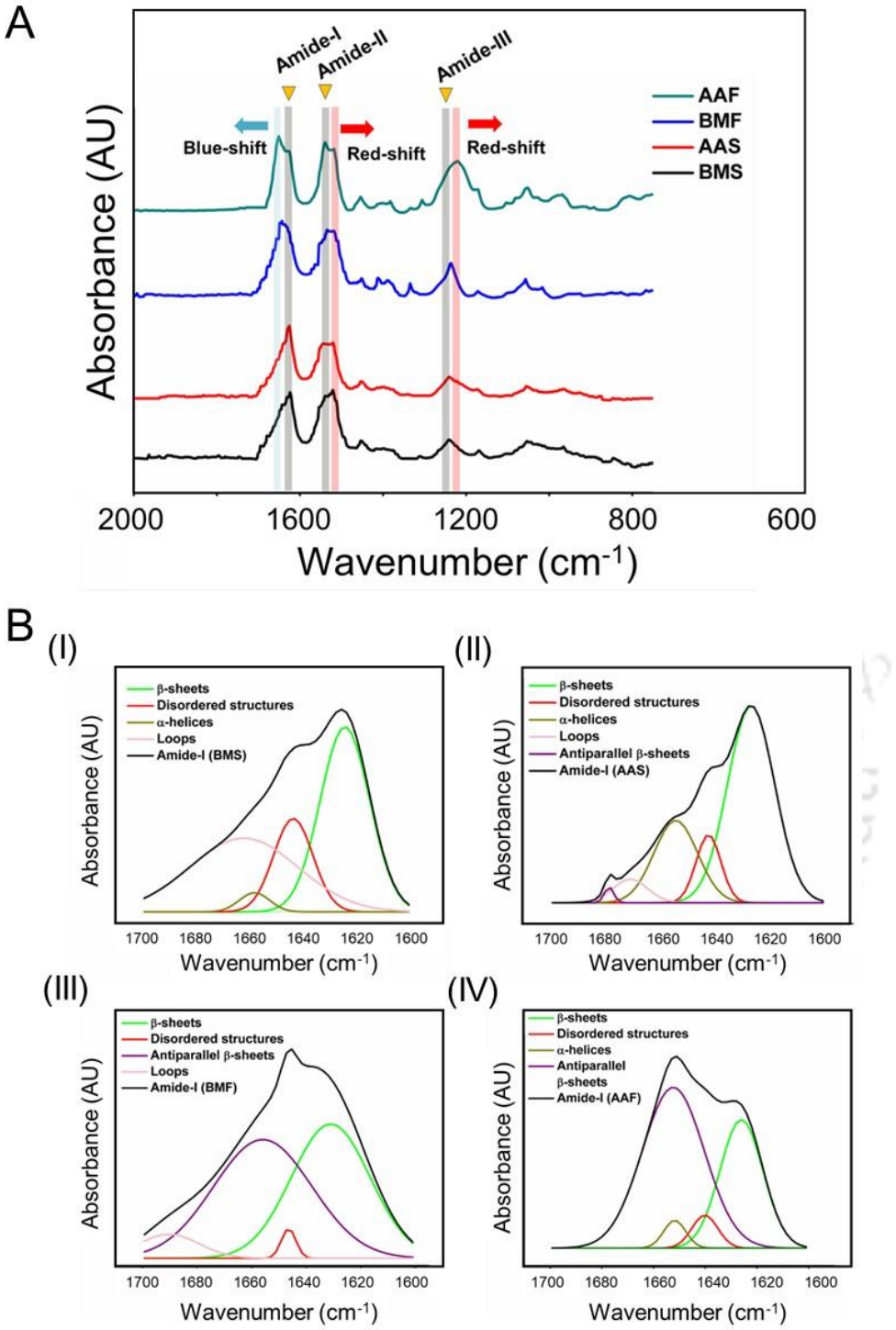

Figure 2.5. *Fourier transform infrared (FTIR) spectra of silk films.* ***(****A) Spectrographs showing peak shifts in amide-I, II and III peaks before and after β-sheet induction: BM solution (BMS). AA solution (AAS), films after β-sheet induction (BM film (BMF), AA film (AAF)). (B) Deconvolution of amide-I peaks to determine secondary structure through second order derivative of amide-I spectra for i) BMS, ii) AAS, iii) BMF and iv) AAF.*

2.3.2 Marker analysis of vascular cells and their proliferation on silk films

Vascular cells isolated from porcine descending aorta were identified based on expression of cell specific markers. ECs expressed uniformly distributed typical dotted pattern of von Willebrand Factor (vWF) in cytosol – a glycoprotein produced by endothelial cells. SMCs on the other hand showed expression of two signature protein markers: αSMA (alpha smooth muscle actin – early differentiation marker) and calponin (mid differentiation marker) (**Figure 2.6**). Presence and predominant expression of specific markers confirmed the vascular cell identity.

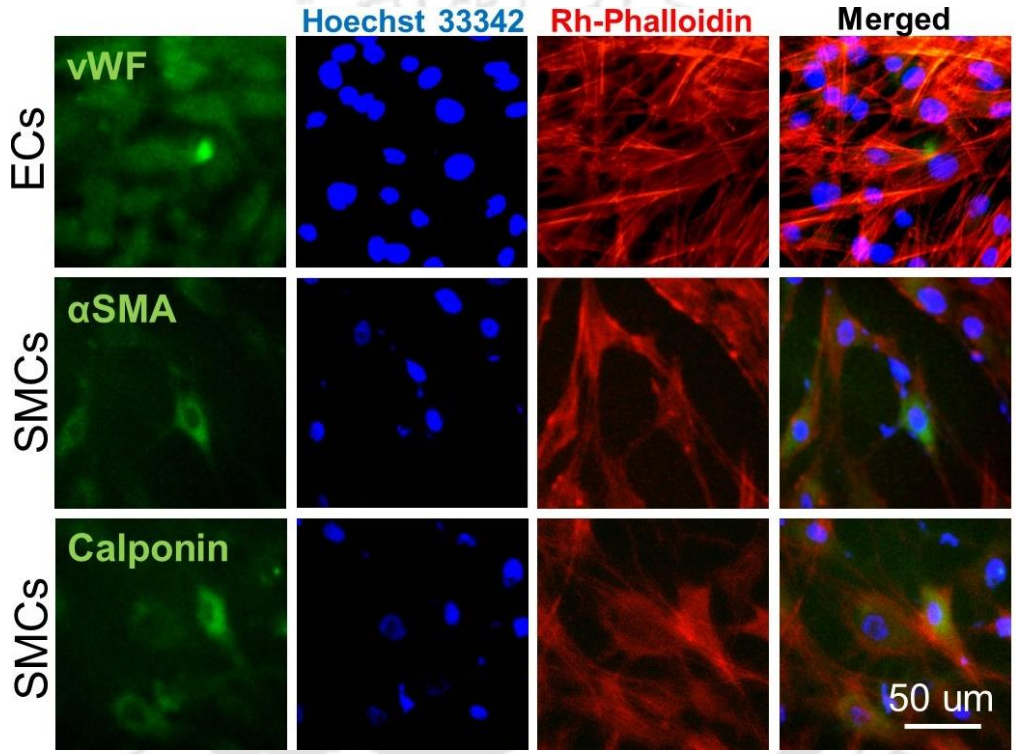

Figure 2.6. *Vascular cells' (ECs and SMCs) marker specific identification. Vascular cells isolated from porcine aorta were characterized based on specific marker expression. Cells were cultured on standard tissue culture plate (TCP) and labelled with marker specific antibodies (vWF for endothelial cells, αSMA and calponin for smooth muscle cells: green color), Hoechst 33342 (for staining nucleus: blue color) and rhodamine-phalloidin (for actin cytoskeleton: red color).*

We further investigated the vascular cell proliferation on silk films. Both SMCs and ECs were compatible with different silk film surfaces and they we metabolically active for whole examination period. In all experimental groups, normalized Alamar reduction value increased from day 1 to day 6 ($p<0.01$), attesting the active cell proliferation; however, variable growth patterns were observed for different silk films. Utmost growth of ECs on day 6 was observed on AA films irrespective of their surface topography, it was significantly higher than standard tissue culture

plate (TCP), and both of BM silk film types ($p<0.01$). ECs' proliferation on AAP was 1.52 times higher than BMP counterpart and 1.27 times higher than TCP (**Figure 2.7A**). SMCs exhibited a completely different growth profile on day 6 and patterning of these cells led to slower proliferation. No significant difference was observed among any of the flat surfaces (AAF, BMF, and TCP). SMCs proliferation on AAP and BMP was 1.15 and 1.58 times slower than flat surfaces respectively ($p<0.01$), a clear indication towards dominant effect of cell alignment (**Figure 2.7B**).

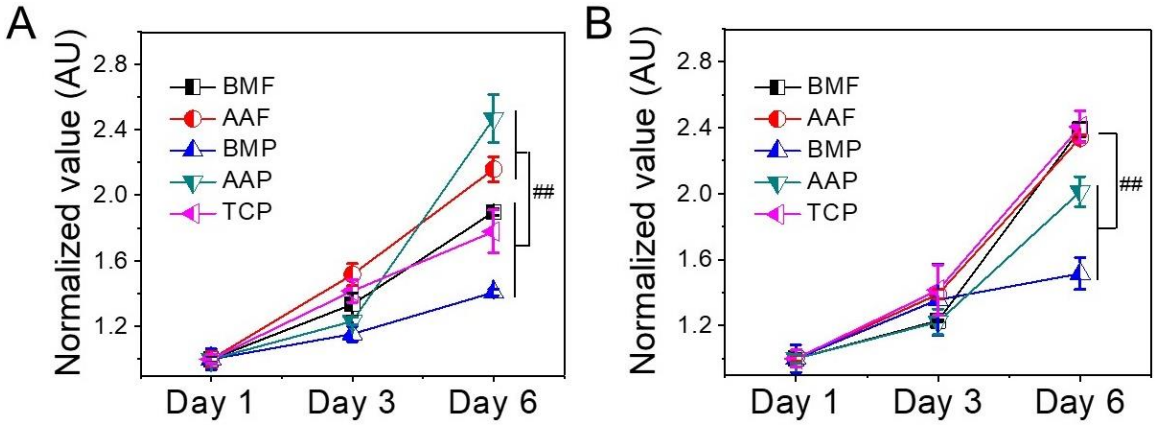

Figure 2.7. *Proliferation of vascular cells on silk films. Proliferation profile of (A) ECs and (B) SMCs cultured on silk films. (##p<0.01)*

2.3.3 Vascular cell distribution on different silk films

Multiple factors that affect the cellular distribution include surface roughness, surface hydrophilicity, surface patterning and extent of cell-cell/cell-surface interaction depending upon cell seeding density. All these factors concomitantly regulate the cell spreading and distribution; which ultimately determine cellular function. Here in this study we tried to analyze the vascular cell distribution pattern on topographically different silk films. ECs arranged themselves in their signature cobblestone morphology on TCP. When cultured on silk films, cell elongation was observed but still most of the cells were distributed uniformly and spread well on all silk films except BMF; where slight cell clustering was observed (**Figure 2.8A**). On a similar note, SMCs distribution followed the same distribution pattern and predominant clustering of cells was observed after 4 days of culture on BMF films (**Figure 2.8B**). Even in certain cases, where SMCs cultured on BMP film, clustering tended to dominate the cellular alignment. Cell orientation profile were also plotted to ensure unidirectional cell alignment. Both ECs and SMCs were able to align themselves following the surface patterning as their unidirectional pattern is attested by single peak on the orientation curve; whereas cells cultured on flat silk films and TCP exhibited a random

distribution and multiple peaks throughout the orientation angle range (**Figure 2.8A, B**). We further stained the cellular cytoskeleton with rhodamine-phalloidin fluorescent dye to analyze the actin filament distribution pattern. Actin filaments also followed the similar pattern and unidirectional alignment was observed on patterned silk films (**Figure 2.8C**). Representative lower magnification images of vascular cells cultured on various silk films are shown in **Figure 2.9**.

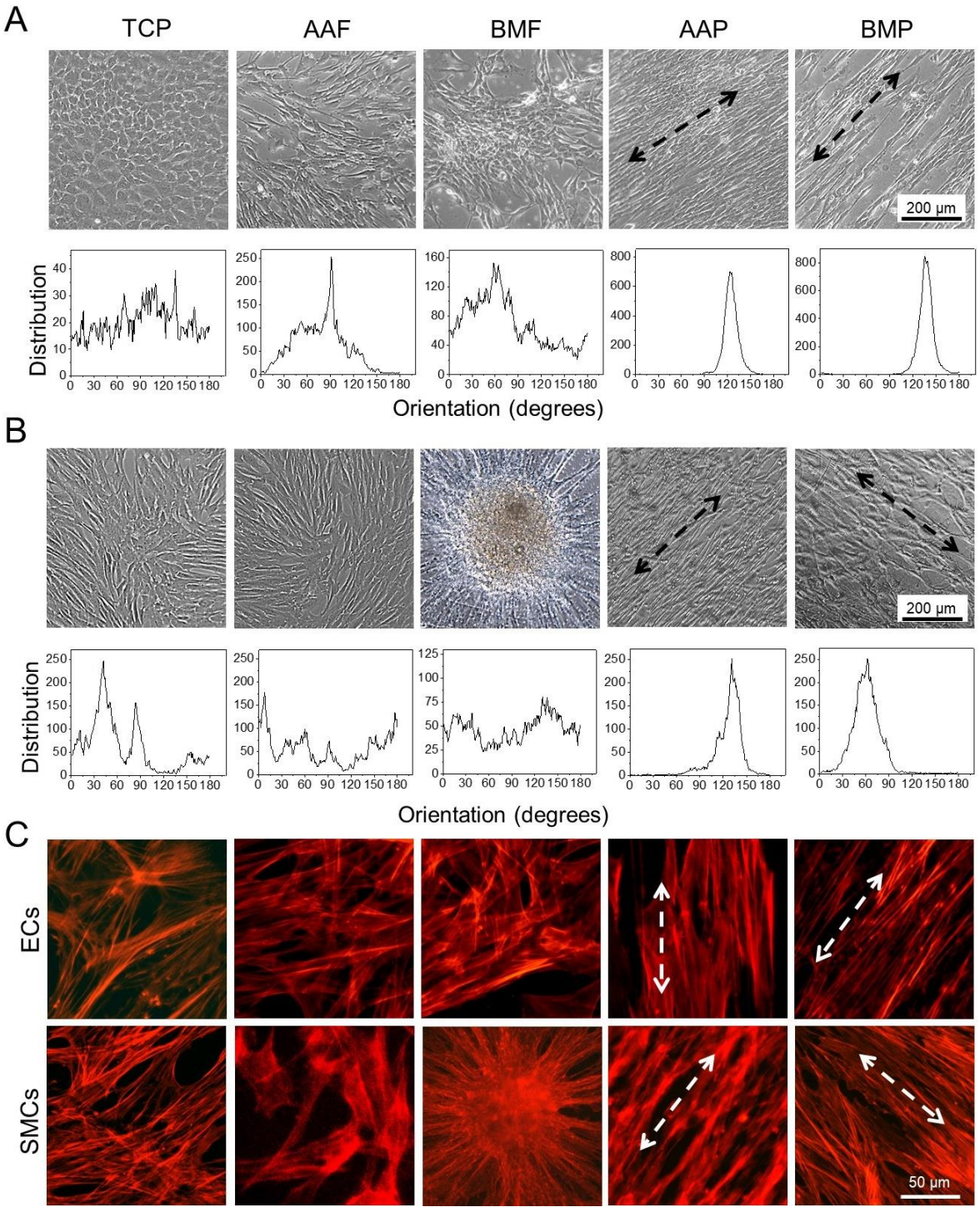

Figure 2.8. *Orientation profile of vascular cells cultured on silk films. Phase contrast microscopic images of (A) endothelial cells and (B) smooth muscle cells cultured onto tissue culture plate (TCP) and silk films after 4 days. Images were processed using ImageJ software to calculate the cell distribution/orientation profile. Black arrows are indicating the direction of cellular alignment, (C) Orientation of cytoskeletal actin fibers. Cells cultured onto silk films were stained with rhodamine-phalloidin to investigate the distribution of actin fibers. Unidirectional alignment of actin fibers was observed for cells cultured onto patterned silk films (AAP and BMP). White arrows are indicating the direction of cellular alignment.*

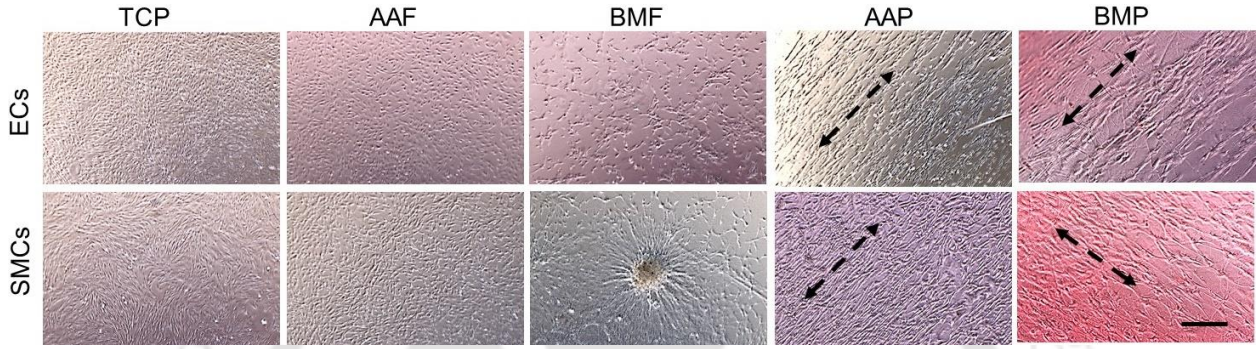

Figure 2.9. *Representative lower magnification of vascular cells cultured on silk films. Scale bar represents 500 μm. Black arrows represent direction of cell alignment.*

2.3.4 Cell cycle analysis

Earlier reports demonstrate the connection between expression of specific genes and cell cycle progression [248]. Hence, we looked further into cell cycle phases of vascular cells cultured on silk film surfaces with variable topographies. Cell cycle profile of ECs and SMCs is shown in **Figure 2.10A, B** respectively, indicating different cell cycle phases with assorted colors. On quantifying the percent population of vascular cells present in each phase, we did not observe any significant difference in G0 phase for ECs. However, on comparing the G1 phase population, higher percentage of cells was observed (**Figure 2.10C**). In contrast, on analyzing for SMCs, a significantly higher quiescent phase population (G0) was noticed for cells growing on patterned silk films irrespective of other surface properties ($p<0.01$). Approximately 30% and 38% of total cell population was trapped in G0 phase for BMP and AAP films groups respectively (**Figure 2.10D**).

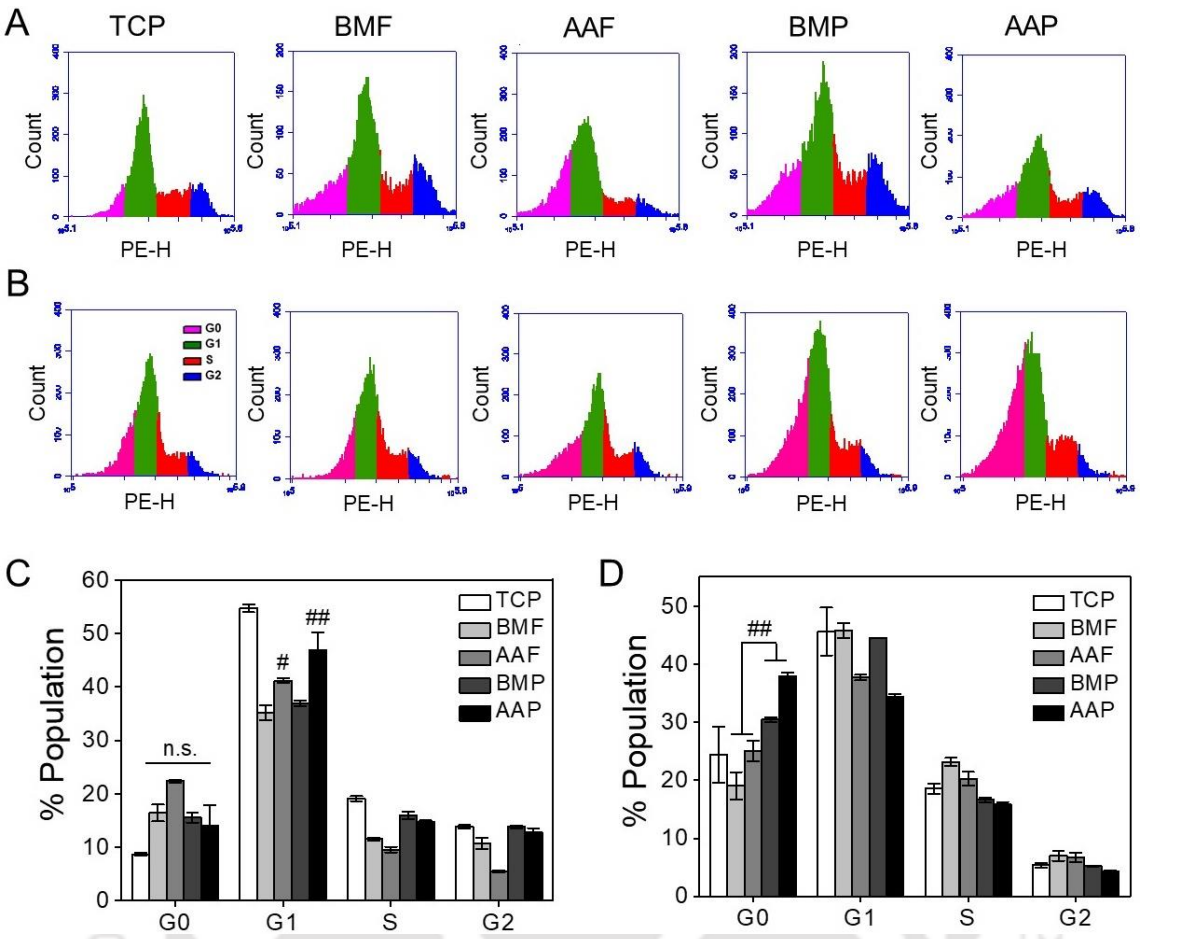

Figure 2.10. *Analysis of cell cycle. Vascular cells cultured on silk films were subjected for cell cycle analysis after 4 days. Cell cycle profile of (A) endothelial cells and (B) smooth muscle cells, showing four distinct phases (G0, G1, S and G2/M). Percentage population of cells in each phase is represented for (C) endothelial cells and (D) smooth muscle cells. (n.s.=not significant, ##p<0.01, #p<0.05)*

2.3.5 Real-time gene expression profile of vascular cells

The effect of cell morphology and distribution at gene level was analyzed by quantifying the real-time gene expression after 4 days of culture. We investigated ECs' function specific genes: eNOS (encodes for an enzyme involved in synthesis of NO; a key molecule determining the blood vessel dynamics) and angiopoietin 1 (crucial modulator of vascular development and angiogenesis). eNOS expression in ECs was surprisingly found to be boosted up for cells cultured on BMF (~19 times higher) as compared to all other experimental groups except TCP ($p<0.01$) (**Figure 2.11A**). Minimal expression of eNOS was observed for ECs cultured on AAP films. Expression profile of ANGPT1 gene was influenced by cellular patterning. Alignment of ECs on patterned silk films (BMP and AAP) downregulated the ANGPT1 expression by almost 50 times as compared to flat

films (BMF and AAF) and TCP ($p<0.01$) (**Figure 2.11B**). We further analyzed the gene expression profile of SMCs cultured on silk films. Two functional genes were selected for this study; αSMA – early differentiation marker and SM-MHC (smooth muscle myosin heavy chain) – late differentiation marker. Expression of these two genes is related with regulation of SMCs' phenotype and their contractile behavior. Expression of both genes was upregulated for cells cultured on BMF films. αSMA expression was almost 15 times higher as compared to flat AAF and TCP surfaces and approximately 5 times higher than patterned films ($p<0.01$). Patterning of SMCs clearly improved the αSMA expression (**Figure 2.11C**). Being the late differentiation marker, very minimal expression of SM-MHC was observed for flat surfaces (AAF and TCP) post 4 days of culture and relatively lower expression was noticed for patterned films (BMP and AAP), dictating the effect of cellular patterning on functional gene expression profile (**Figure 2.11D**).

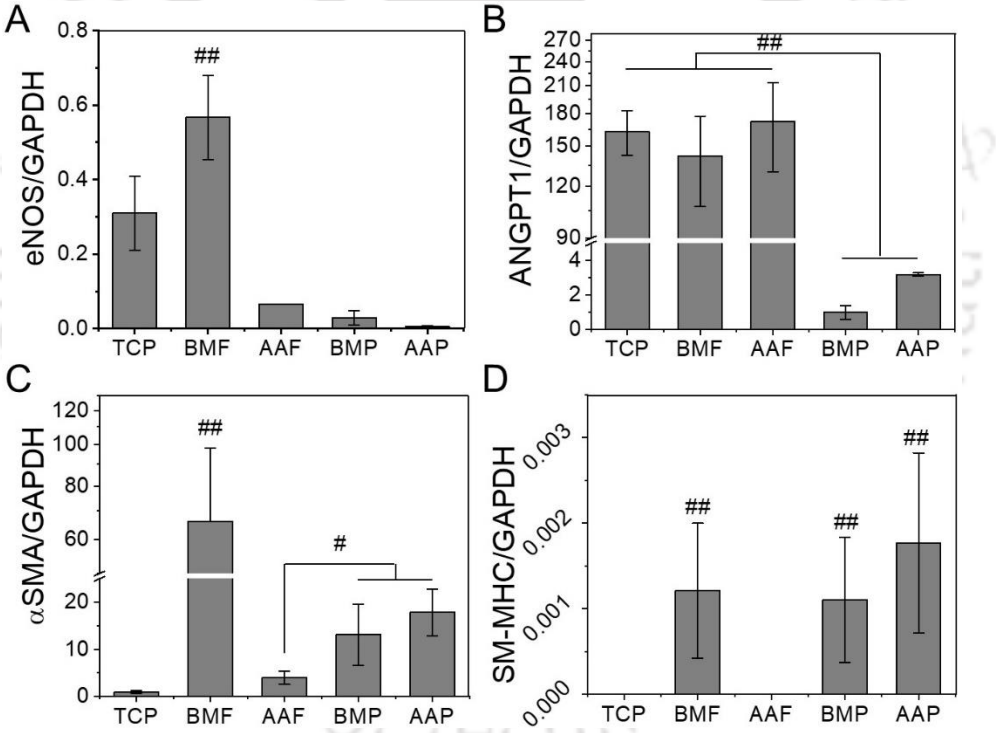

Figure 2.11. *Quantification of functional gene expression by qRT-PCR. Vascular cells cultured on silk films were investigated for functional gene expression after 4 days of culture. Endothelial cells were tested for (A) eNOS and (B) ANGPT1 expression whereas smooth muscle cells were tested for (C) αSMA and (D) SM-MHC expression. (#p<0.05, ##p<0.01)*

2.3.6 Functional assessment of vascular cells

Expression of functional proteins by tissue specific cells is one of the crucial requirements for maintaining healthy tissue dynamics. Vascular ECs produce nitric oxide (NO) by calcium-

calmodulin dependent enzyme eNOS; an essential regulator of vascular cell growth and protecting blood vessel from adverse effects of platelets [249]. Herein we quantified the production of NO from ECs cultured on different silk films on day 1 and day 4. On quantifying the NO production on day 1, cells cultured on TCP showed the maximum NO production significantly higher than other experimental groups ($p<0.01$). BMP cultured cells produced minimal NO after 4 days (**Figure 2.12A**). Interestingly, when we calculated the fold increase profile from day 1 to day 4, we observed the downregulation of NO secretion from aligned ECs ($p<0.01$). A paradoxical behavior was observed for TCP cells where NO production was in the range of aligned ECs (**Figure 2.12B**). Collagen secretion from SMCs is another parameter we considered for analyzing the cellular functionality. Majority of blood vessel's ECM is made-up of collagen and elastin, which help maintain tissue's mechanical integrity without compromising its elasticity [250]. Hence, we quantified the total collagen secreted from SMCs cultured on various silk films at different time points. No significant difference was observed for day 1 samples; however, on day 4, cellular alignment induced the collagen production as compared with flat surface cells (**Figure 2.12C**). In order to get more accurate idea about collagen secretion, we normalized the total collagen content with DNA. SMCs cultured on AAP produced the maximum collagen and it was significantly higher than its counterpart AAF ($p<0.01$). However, we did not observe any difference among BMP and BMF cultured SMCs (**Figure 2.12D**).

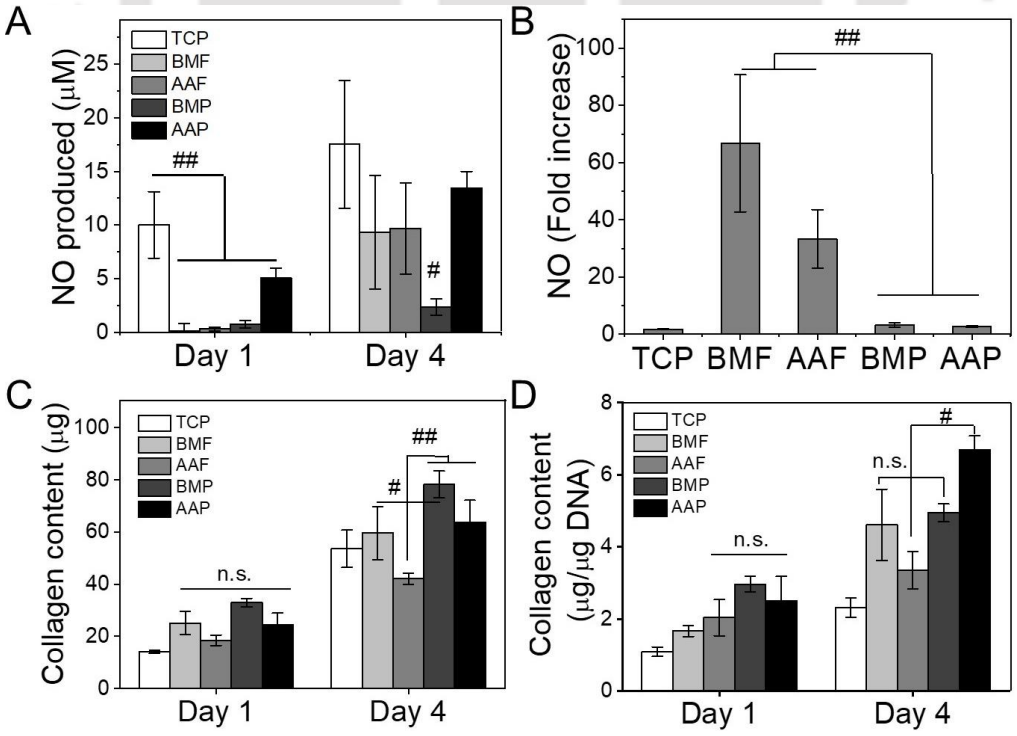

Figure 2.12. *Production of functional moieties by vascular cells cultured on silk films. (A, B) Endothelial cells were tested for production of NO (Nitric oxide) from day 1 to day 4. (C, D) Total collagen content produced by smooth muscle cells was also quantified which was further normalized with DNA content. (n.s.=not significant, #p<0.05, ##p<0.01)*

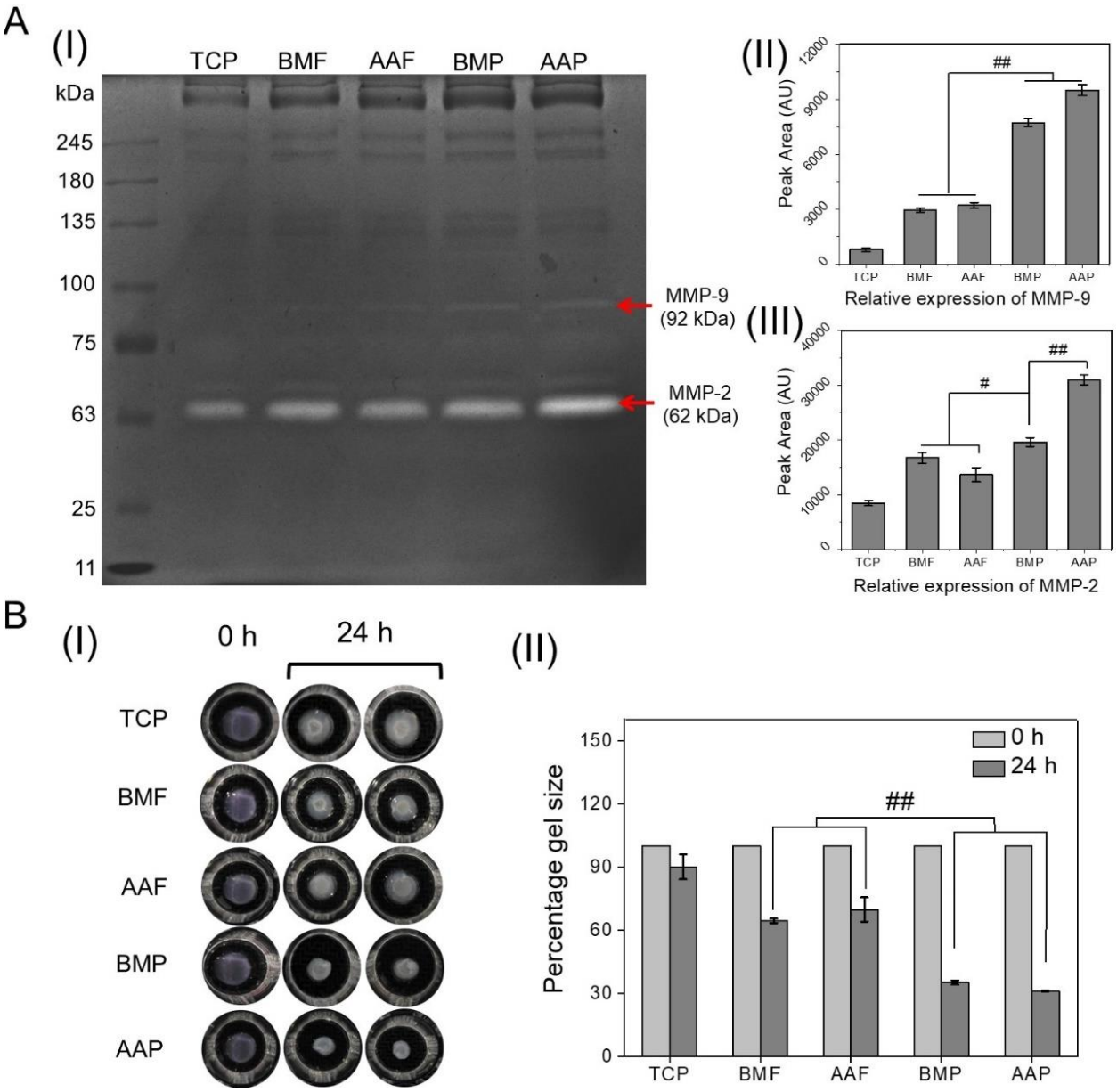

Figure 2.13. *Functional analysis of smooth muscle cells. (A) Representative gelatin zymography profile of SMC media collected after 4 days of culture period showing the expression of MMP2 and MMP9 enzymes. (i) Image showing MMP bands in different groups. Quantification of band intensity of (ii) MMP-9 and (iii) MMP-2 representing relative expression. (B) Collagen gel contraction assay of smooth muscle cells. (i) SMCs were entrapped in collagen gel and images were captured at different time points. (ii) Quantification of gel contraction by measuring the gel size after 24h. (##p<0.01)*

Apart from providing mechanical robustness to the blood vessels by secreting the structural components, SMCs also contribute to tissue remodeling by secreting ECM degrading enzymes-MMP-2 (matrix metalloproteinase-2) and MMP-9. Considering this, we explored the effect of surface topography and hydrophilicity on matrix remodeling capability of SMCs. Our gelatin zymography results suggested that cellular alignment on patterned silk surfaces boost the secretion of MMP-2 and MMP-9 irrespective of cell surface hydrophilicity. Very bright and sharp gel bands were spotted for MMP-2 (at 62 kDa) as compared with MMP-9 (92 kDa) (**Figure 2.13A-i**). On quantifying the relative band density for MMP-9, TCP cultured cells showed minimal secretion followed by flat films (3 times higher) and patterned films (8-9 times higher) (**Figure 2.13A-ii**). Similarly, SMCs cultured on TCP showed minimum MMP-2 production and AAP with maximum production of MMP-2 (3 times higher) (**Figure 2.13A-iii**).

Blood vessel walls are always exposed to continuous contraction and relaxation; hence the most important aspect for SMC functionality is their contractile behavior. In order to speculate about the impact of different surface topography and hydrophilicity on SMCs contractile behavior in 3D culture conditions, we encapsulated SMCs in collagen hydrogels post 4 days of 2D culture on silk film surfaces (**Figure 2.13B-i**). Gel contraction was quantified in terms of its size after 24 h culture. Maximum contraction was observed for BMP and AAP groups (~60%); which was significantly higher than flat film surfaces (~30%) and TCP (~10%) ($p<0.01$) (**Figure 2.13B-ii**). SMC contraction was solely found to be affected by cellular patterning and no effect was observed for variable surface hydrophilicity.

2.4 Discussion

There is great interest on the effect of physical factors (including surface topography, hydrophilicity and shear stress) on vascular cell functionality [79, 213, 215]. Published reports clearly assure that chemical factors are not the only regulator for cells' functional modulation rather physical cues are of equal importance. In this study, we investigated the functional behavior of vascular cells cultured on films fabricated using different silk (AA and BM). Both silk proteins have unique amino acid sequences; hence, different structural arrangement conferring variable surface properties. Our selection of using silk protein also relied on its remarkable biocompatibility and its ability to acquire any topographical shape even at micro and nano scale, which provides another dimension to add one more variable at cell-substrate interface apart from their natural

traits. By using proteins from different variety of silk worms (either mulberry or non-mulberry), we fabricated surfaces having different properties without any chemical modification. These inherent physico-chemical properties of BM and AA silk films owing to the compositional difference of the silk fibroins, provided surfaces with variable roughness, wettability, chemistry (presence of RGD motif on AA film) and stiffness (BMF and AAF). Moreover, we also engineered the silk surfaces by printing a microgroove pattern to induce unidirectional alignment of porcine primary vascular cells.

Several studies have recently reported the unidirectional alignment of SMCs [79, 213, 221, 251-253] and ECs [214, 220, 254-257]. The rationale behind using such specifically designed topographical surfaces is to improve the cell functionality. SMCs are capable of adopting two contrasting phenotypes: contractile and synthetic. Cell behavior in both of these phenotypes differs drastically. Under healthy physiological conditions, SMCs remain in the contractile phenotype. However, a phenotype switch (towards synthetic) leads to development of multiple pathological conditions including atherosclerosis, intimal hyperplasia and restenosis after angioplasty. Unidirectional alignment of SMCs is primarily aimed to induce contractile phenotype in order to prevent the diseased condition [258]. In blood vessels, ECs' monolayer in the lumen works as barrier between blood and underlying tissue. It also acts as natural anticoagulant surface that allows uninterrupted channeling of blood. Because of direct contact with bloodstream, ECs are regularly exposed to fluid shear stress. It induces their alignment along the direction of blood flow and ultimately help them maintaining their function [220, 256].

In order to assess the cumulative effect of surface physico-chemical properties and unidirectional cell alignment, we used flat and micro grooved silk films from both silk varieties. Surface roughness of AA films was superior to BM counterparts as depicted by AFM analysis. The higher surface roughness might be attributed to distinct presence of inherent amino acid stretches and their arrangement [126, 236]. In contrast, for patterned films, no significant difference was observed between two silk types; possibly due to dominance of microstructural surface features over nanostructures. By convention, any surface with a water contact angle less than 90 degrees is considered hydrophilic. BMF and AAF films showed different degrees of hydrophilicity (water contact angle 69.92 ± 1.75 and 46.76 ± 1.39 degrees respectively). AAF surfaces were more hydrophilic than BMF surfaces. One plausible justification for AA surfaces being more hydrophilic might be related with the presence of higher percentage of Ala amino acid

residues, which is more hydrophobic than Gly. When in aqueous solution, the non-polar amino acids tend to form hydrophobic core, leaving polar amino acid residues in contact with outer environment, hence more hydrophilic surface. This hypothesis was further substantiated from our FTIR deconvolution data, wherein we observed higher β-sheet content in AA groups in comparison to BM groups. The β-sheet rich crystalline region in silk fibroin forms the intact hydrophobic core. The predominantly higher β-sheet content noticed in AAF contributes for more polar groups exposed outwards, which favored the relatively hydrophilic surface of AAF. We further analyzed the contact angle for patterned silk films. For more precise measurement, we recorded the contact angle from both directions; i.e. parallel and perpendicular to the microgrooves. A similar hydrophilicity trend was recorded for patterned silk films with no significant difference between the contact angles from two different directions. Silk films' hydrophilicity range is also relevant for this study owing to better EC adhesion on surfaces with a contact angle 40-45 degrees as compared to surfaces with a contact angle of 60-65 degrees' surfaces [259, 260]. Although these prior studies report the cell adhesion percentage on surfaces with different wettability, the functional behavior of ECs was not investigated. On further analysis of mechanical properties of silk films, both film types showed significant difference. AA films were mechanically stiffer and showed higher tensile modulus. Load-displacement curves also suggested significantly higher elongation of AA films at the breaking point. The higher tensile strength and elongation of AA silk is because of presence of distinct polyalanine stretches in its native structure; conferring formation of higher amounts of anti-parallel β-sheet structures [238].

We further evaluated the biological reaction of vascular cells in response to variable cell-substrate interface features of silk films. We first looked into the proliferation of vascular cells. Surface pattern induced ECs' alignment is reported to enhance the cellular proliferation [261, 262] but in the present study, irrespective of surface patterning, ECs cultured on AA films showed significantly higher proliferation than BM films in a 6 days experiment ($p<0.01$). As mentioned earlier, interactions at cell-substrate interface determine the cell behavior; therefore, superior proliferation of ECs on AA films might be attributed to either surface wettability (allowing better cell adhesion) [259, 260], presence of inherent RGD cell binding motifs on the surface of AA films (improving cell adhesion and proliferation) [126, 263] or substrate stiffness (stiffer substrates are reported to support better ECs proliferation) [264]. As suggested by AFM data, AAF and AAP films' surface roughness showed no significant difference, eliminating influence of roughness

factor on ECs' proliferation. These findings suggest that favorable substrate chemistry, wettability and stiffness of AA films cumulatively dominate the influence of surface patterning and subsequent cell alignment on ECs' proliferation. When compared between BMF and BMP films, surface patterning altered the ECs' proliferation profile. ECs cultured on BMP films showed comparatively lesser proliferation. This contrasts with a few prior reports, where ECs' alignment was found to improve cellular proliferation [261, 262]. The plausible reason for such cellular behavior might relate with the size of grooves (depth and peak distance) that might alter cell adhesion and proliferation. On the other hand, the proliferation profile of SMCs showed a contrasting behavior than ECs and surface pattern induced alignment was observed to be the dominating factor over other surface properties**.** In line with the previous reports, SMCs' alignment suppressed the proliferation rate, one of the features observed during phenotype transition from synthetic (high proliferation index) to contractile (low proliferation index) [258]. The underlying mechanism of alignment-induced switch of SMCs' contractile phenotype has not been explored in details but several studies suspect the possible role of integrin for signaling across the plasma membrane. The two downstream signaling molecules FAK (focal adhesion kinase) and ERK (extracellular signal regulated kinase) might be involved with proliferation alteration of SMCs cultured on flat and patterned surfaces [251].

The progression of cell cycle is directly co-related with cell proliferation [258, 265]. On that account we further investigated the cell cycle profile of vascular cells under the influence of various surface properties. In native blood vessels, SMCs remain in a non-proliferative quiescent state (G0 phase) and maintain a contractile phenotype [266]. Hence, we evaluated the percentage cell population in G0 phase only. SMCs cultured on patterned silk surfaces (BMP and AAP) showed increment in quiescent phase (G0 phase) cell population when compared with flat surface counterparts ($p<0.01$). Based on these results, it may be inferred that unidirectional alignment of SMCs induce the non-proliferative (contractile) phenotype via induction of quiescent phase cells. On the other hand, no significant difference was observed for G0 phase cell population for ECs in response to variable cell-substrate interfacial properties. However, in line with proliferation data, a higher G1 phase cell population was recorded for ECs cultured on AA films, irrespective of their surface patterning. It suggests that on AA films, more number of cells are entering in cell cycle leading to higher proliferation. Important to note here is that under *in vivo* conditions, ECs are exposed to a very dynamic microenvironment where they are attached as a monolayer on basement

membrane (topographical factor) and remain in direct contact with blood flow (dynamic mechanical loading) [267]. Both of these factors synergistically modulate the ECs' cell cycle progression. It is evidenced by a previous report where three-fold reduction (compared to randomly aligned cells) in Ki67 expression (a proliferation associated protein expressed during cell cycle phases but absent from G0 phase) was observed for endothelial cells cultured on aligned nanofibers and exposed to orthogonal shear stress [268]. Such observations clearly indicate that modulation of cell-substrate interface might not be enough to recapitulate the *in-vivo* like microenvironment rather fluid shear stress is equally important.

Functional aspect of vascular cells is further assessed by investigating the expression of functional genes and proteins. A healthy monolayer of ECs is needed to maintain the vascular homeostasis by releasing nitric oxide (NO), which regulates vasodilation and suppress platelet activation and aggregation [269]. The NO molecule is synthesized by nitric oxide synthase (eNOS) enzyme. On analyzing the eNOS expression by ECs cultured on different silk films, we observed that BMF group showed the maximum expression while the patterned surfaces were found to suppress the eNOS expression**.** In order to further verify at the protein level, we quantified the production of NO by ECs. TCP cultured ECs produced maximum NO, but in order to normalize these values we calculated fold increase in NO production from Day 1 to Day 4. In agreement with the gene expression data, BMF group observed maximum fold increase ($p<0.01$). This is in contrast with previous reports where shear stress was observed to induce eNOS expression and NO production [254]. In a previous report it was observed that substrate compliance induced modulation of ECs' NO production is mediated by fluid shear stress [270]. Surface microgroove induced alignment of ECs has also shown to influence the production of NO. As suspected in a previous report, microgroove size also matters when it comes to alignment induced functional manipulation of ECs. Microgrooves measuring 5 μm suppressed the eNOS expression significantly as compared to higher dimensions [271]. In addition, eNOS expression remained unchanged on flat and microgrooved surfaces [271, 272]. In yet another report, researchers have shown the effect of ratio of groove to ridge width influencing the ECs' cytokine and chemokine profile related with remodeling and inflammation [254]. It is obvious from the prior studies that microgroove dimension also affects ECs' functionality crucially. The suppressed expression of eNOS and downregulation of NO production from ECs cultured on patterned silk surfaces might be related with the microgroove width of patterned silk films used in this study. However, an in

depth investigation on effect of microgroove dimensions on silk films is needed to ascertain any such possibility. Angiopoietins are another class of proteins that regulate the vascular homeostasis. Angiopoietin-1 (ANGPT1) stabilizes the vascular endothelium by activating Tie2 receptor whereas Angiopoietin-2 (ANGPT2) acts as an antagonist for the former protein [273]. Considering the importance of ANGPT1 for the maintenance of healthy vascular endothelium, we further enquired if its expression is affected by surface physico-chemical cues of silk films. A drastic downregulation of ANGPT1 was observed on patterned silk films**.** As per our best understanding, there is no such report investigating the effect of biophysical factors on ANGPT1 expression. A detailed molecular analysis is needed to justify these observations. Such paradoxical behavior might be related to the fact that ECs' alignment and other substrate properties (roughness, wettability and chemistry) are not the only determining factors of cell functionality; dynamic microenvironment created by blood flow shear stress is also of crucial importance.

SMCs present in tunica media primarily hold the mechanistic responsibility by maintaining their contractile phenotype and producing extracellular matrix (ECM) proteins – collagen and elastin. Therefore, we further aimed to investigate the expression of contractile phenotype related genes and collagen synthesis in response to variable cell-substrate interfacial properties. Expression of two contractile genes is studied – αSMA and SM-MHC. Cellular alignment on patterned surfaces (BMP and AAP) upregulated the expression of contractile genes, which is in agreement with previous reports [215]. However, BMF group (having a comparatively less hydrophilic surface, lesser surface roughness and without any presence of RGD cell binding motifs) also exhibited the enhanced expression of both of these genes. Such behavior of SMCs might be related to the cell clustering and self-assembly of cells on BMF films. Owing to the inferior hydrophilicity of BMF films, after reaching an optimal cell density, SMCs favored more cell-cell interaction compared to cell-substrate interaction and started forming cell clusters mimicking 3D micro tissues that might be one of the plausible justifications for improved contractile gene expression on BMF films [274-276]. A similar trend is observed with the collagen quantification analysis. Including patterned silk films (BMP and AAP); SMCs cultured on BMF films showed enhanced collagen production. Increased collagen production from SMCs expressing upregulation of contractile genes is in agreement with a previous report [277]. The underlying mechanism for such cellular behavior relies on increased gap junction communication mediated by Wnt3a and subsequent modulation of Wnt signaling [277]. Our findings suggest that

although surface patterning induced cellular alignment is sufficient to induce SMCs' contractile phenotype and collagen production but other surface properties cumulatively might also lead to a similar cellular response.

The functional aspect of SMCs is further elaborated and investigated in terms of their matrix remodeling capability (production of matrix metalloproteinase – MMP-2 and MMP-9) and physical contraction ability using collagen gels. For any tissue engineered vascular graft (TEVG), matrix remodeling is very crucial. In this regard, SMCs are known to produce MMP-2 and MMP-9 in blood vessels undergoing remodeling post injury [278]. Increased expression of MMP-2 and MMP-9 is observed for BMP and AAP groups independent of other surface properties. Cell alignment induced upregulation of MMPs might relate to the SMCs' contractile phenotype [277]. We further looked into the contraction ability of SMCs cultured on different silk films by encapsulating them in collagen hydrogel [246]. SMCs cultured on patterned surfaces showed better contraction capability. However, the superior expression of contractile genes for BMF group is not reflected here. It indicates that SMCs' alignment and cell-cell gap junction mediated communication is important for their functional contractile behavior. These outcomes indicate that predominant unidirectional alignment of SMCs lead to induction of their contractile phenotype, allows more collagen and MMP production and shows better contraction capability when compared with cells cultured on flat silk films growing in random orientation. Another key observation is that SMCs' contractile phenotype and ECM production might also be altered depending on synergistic effect of surface wettability, surface chemistry and substrate stiffness, as observed in case of BMF group.

Our findings in this work suggest that depending on cell type, surface properties of silk films synergistically determine cellular functionality. Most of the prior research is focused on extrapolating the effect of a single factor at the molecular level in a highly controlled microenvironment, however unveiling the effect of complex dynamic environment is of much clinical relevance. Although this study is limited to few standard substrate properties of silk films without any consideration of dynamic mechanical microenvironment (due to blood flow shear stress) but a detailed molecular and functional analysis by mimicking the complex native-like microenvironment is much needed to understand the vascular cell dynamics under various physio pathological conditions.

2.5 Significant findings

1. Vascular pathologies are majorly associated with malfunction of vascular cells under the influence of dynamic microenvironment. Understanding the functional aspect of these cells under *in vitro* conditions demands the recapitulation of native-like environment involving multiple physico-chemical factors.
2. In this work, we evaluated the functionality of vascular cells (SMCs and ECs) cultured on engineered silk film surfaces having different wettability, roughness, chemistry and mechanical stiffness owing to variable inherent characteristics of BM and AA silk.
3. Our findings suggest that surface pattern induced alignment solely is not adequate for maintaining ECs' functionality; however other surface properties play a crucial role. For instance, ECs' showed superior proliferation on AA films irrespective of their surface patterning.
4. Gene expression profile and NO quantification data evidenced the negative impact of surface pattern induced cellular alignment.
5. In contrast, SMCs were more responsive when cultured on patterned surfaces in terms of proliferation, expression of contractile genes, remodeling capability and physical contraction. Surface patterning favorably induced the unidirectional cell alignment and modulated their function.
6. Together with surface patterning, other surface properties of flat silk films (BMF) also influenced the contractile gene expression and ECM production favorably.
7. Altogether, this study demonstrates that surface physico-chemical properties of silk films synergistically determine the functional behavior of vascular cells.

CHAPTER 3

Development of small-diameter vascular grafts using patterned silk films recapitulating native arterial structure

This chapter demonstrates the development of silk films-based multilayered small-diameter vascular grafts recapitulating native blood vessel architecture. Vascular cells cultured and aligned onto silk films via contact guidance were assembled in a tubular structure implementing a customized rolling device. Following this methodology, a patient-specific TEVG can be obtained using autologous cells, eliminating the possibility of immune rejection post-implantation.

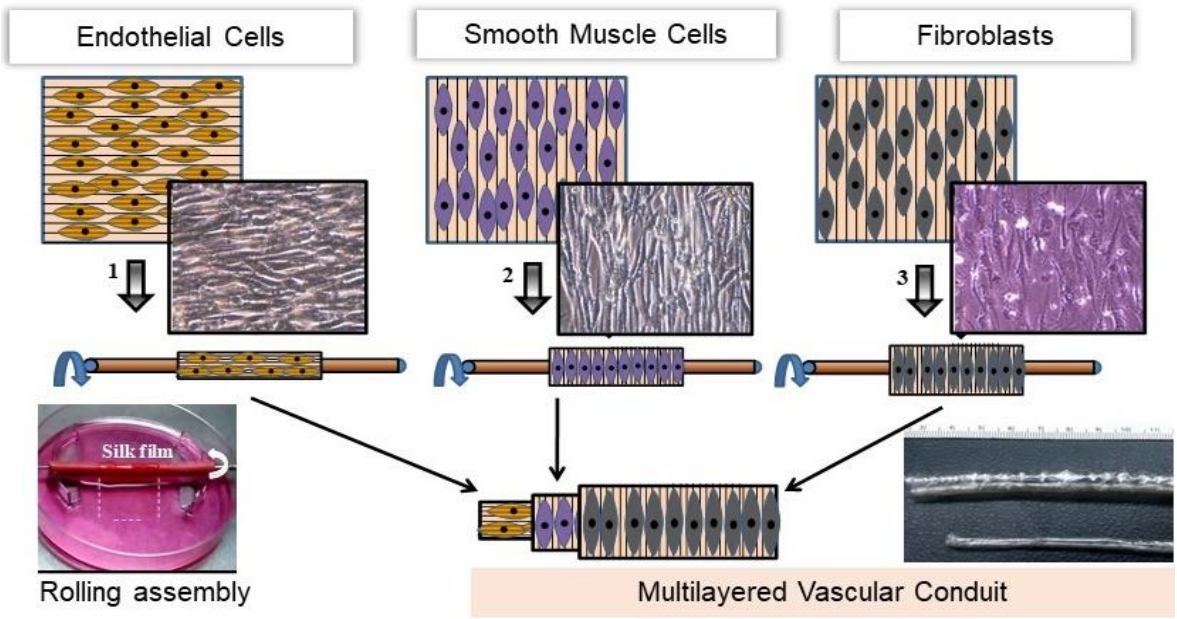

Publication:

***Prerak Gupta**, Manishekhar Kumar, Nandana Bhardwaj, Jadi Praveen Kumar, CS Krishnamurthy and Biman B. Mandal. Mimicking form and function of native small diameter vascular conduits using mulberry and non-mulberry patterned silk films. **ACS Applied Materials & Interfaces**. 2016; 8:15874-88.*

ABSTRACT

Autologous graft replacement as a strategy to treat diseased peripheral small diameter (<6mm) blood vessel is often challenged by prior vein harvesting. To address this issue, we fabricated native-tissue mimicking multilayered small diameter vascular graft (SDVG) using mulberry (*Bombyx mori*) and Indian endemic non-mulberry (*Antheraea assama* and *Philosamia ricini*) silk. Patterned silk films were fabricated on microgrooved PDMS mold, casted by soft lithography. The biodegradable patterned film templates with aligned cell sheets were rolled onto an inert mandrel to mimic vascular conduit. The hemocompatible and mechanically strong non-mulberry films with RGD motif supported ~1.2-fold greater proliferation of vascular cells with aligned anchorage. Elicitation of minimal immune response on subcutaneous implantation of the films in mice was complemented by ~45% lower TNF-α secretion by *in vitro* macrophage culture post 7 days. Pattern induced alignment favored functional contractile phenotype of smooth muscle cells (SMCs), expressing the signature markers- calponin, α-smooth muscle actin (αSMA) and smooth muscle myosin heavy chain (SM-MHC). Endothelial cells (ECs) exhibited typical punctuated pattern of von Willebrand factor (vWF). Deposition of collagen and elastin by the SMCs substantiated the aptness of the graft with desired biomechanical attributes. Furthermore, burst strength of the fabricated conduit was in the range of ~915-1260 mmHg, a pre-requisite to withstand physiological pressure. This novel fabrication approach may eliminate the need of maturation in a pulsatile bioreactor for obtaining functional cellular phenotype. This work is thereby, an attestation to the immense prospects of exploring non-mulberry silk for bioengineering multilayered vascular conduit similar to native vessel in 'form and function', befitting for *in vivo* transplantation.

3.1 Introduction

Cardiovascular malfunctioning is one of the leading causes of death globally and India is now being called 'the world capital of cardiovascular diseases'. It is pertinent to mention that coronary artery occlusion incidences are more prominent (~50% of total cardiovascular patients). A recent report from World Health Organization (WHO) states that 17.3 million people died of cardiovascular diseases in 2008 and this number is expected to reach 23.3 million by 2030 [1]. Current surgical treatment methods require an adequate supply of native or native like vascular constructs so as to replace the diseased vessels. Autologous vessels, including saphenous and umbilical veins and mammary arteries serve as 'gold standard' for coronary replacement but almost one-third of patients do not have their veins appropriate for grafting due to pre-existing vein stripping, vascular disease and prior vein harvesting [4, 279]. The associated surgical cost and significant morbidity rate pose additional limitations.

Considering these limitations, there exists an urgent need to find a suitable alternative. Tissue engineering, in this regard could serve as important tool for preparation of readily available, functional and biocompatible vascular grafts through scaffold based biomimetic approach. Synthetic materials like polyethylene terephthalate (Dacron) and expanded polytetrafluoroethylene (ePTFE) are apt choice for large diameter (>6mm) vascular grafts and have been implanted successfully in thoracic and abdominal aorta [189, 280]. On the contrary their use for small caliber vessels has shown to cause thrombosis, anastomotic intimal hyperplasia and subsequent occlusion (reduced patency) due to compliance mismatch and inflammation [281]. This necessitates the selection of a suitable biomaterial that could withstand the continuous shear and vascular wall stretches with minimal energy loss and supports the growth of vascular cells. Among others, silk represents its potential candidature for vascular tissue engineering owing to its easy accessibility, ease in processing, morphology control with immense modification options, extraordinary mechanical properties with flexibility, tunable degradability and hemocompatibility [114]. Further, amenability for fabrication into various forms like film, fiber, gel, sponge and particles broadens its usefulness and opens new portal of applications [165].

It is important to know that blood vessel is a layer by layer assembly of vascular cells arranged in a unique fashion so as to sustain the shear forces induced via blood flow. Recent endeavors implementing the use of silk for vascular tissue engineering application demonstrated the fabrication of porous silk microtube using layer-by-layer deposition and gel spinning methods

[158, 281, 282]. Such grafts although provides control over porosity but major drawback with these grafts is randomly arranged cells and their inability to maintain functional cellular phenotype. Electrospun nanofibrous silk tubes certainly improved the prior fabrication approach but maintenance of long term mechanical compliance and poor control over mechanical and degradation properties imposed further limitations [283]. Silk composite were then investigated for their supposedly improved properties. In this regard, tri layered vascular grafts composed of elastin, polycaprolactone, silk and collagen were developed to match the required mechanical properties [284]. Silk micro-tube encapsulating heparin have been used as carrier for vascular endothelial growth factor (VEGF) sustained release, with concomitant hemocompatibility and endothelialization, thereby reducing the chance of thrombosis [165, 285]. A recent study projected the use of hybrid protein polymers containing silk and human recombinant tropoelastin to provide better tissue elasticity and extensibility [286]. These 'top down approaches' are based on the use of spongy scaffold as a template for engineering tubular construct followed by cell seeding in order to recapitulate compact and organized tissue. However, limitations in terms of long term mechanical compliance can be easily comprehended in situations that demand stretchable tube like structure with millimeter range wall thickness. Developing native like cellular arrangement and maintaining tissue integrity and complexity still remains a challenge in the field of vascular tissue engineering. Further limitations include co-culture of vascular cells, remodeling capability, long reproducible time and associated high cost.

Scaffold free approaches later came into existence that allows mimicking native cellular alignment and tissue integrity with higher fidelity. Cell sheet engineering is a good example of aforesaid technique. More than a decade ago, L'Heureux *et al.* successfully demonstrated the fabrication of human blood vessel using cell sheet engineering [287]. They have shown the subsequent rolling of sheets of SMCs and fibroblast cells over an inert mandrel followed by endothelial cell seeding in the luminal surface. The concept is although completely bio-based where one can precisely control the cellular and extracellular matrix (ECM) alignment; the rolling of the highly delicate cell sheets itself is tedious. In order to implement the concept of cell sheet engineering for preparing vascular graft and making the rolling process more feasible, recently people have tried to combine the principle of cell sheet engineering with the electrospinning technique [288, 289]. In this approach, aligned electrospun mat is used as a platform for cell seeding and after getting a confluent cell sheet, mat is rolled over the mandrel. This combined

approach made the rolling process more facile but require cellular infiltration during the maturation process. Limited infiltration of cells in electrospun scaffolds due to lesser pore size and inadequate surface properties need additional measures for graft success [283, 290].

Several reports have attested the applicability of *Bombyx mori* silk for vascular tissue engineering applications however non-mulberry silk varieties like *Philosamia ricini* and *Antheraea assama* are quite unexplored [189, 281, 282]. We have previously reported that non-mulberry silk varieties (e. g., *Antheraea mylitta*) support better cell attachment and proliferation owing to intrinsic presence of RGD motif (cell binding site) [291]. Recently, presence of similar cell binding motif was reported in *A. assama* [292]. Additionally, unique molecular architecture (polyalanine repeats without any intervening amino acid) of *A. assama* silk is reported to improve its mechanical properties- a considerable aspect of vascular tissue engineering [239, 293]. Hence, we attempted to explore the suitability of Indian endemic non-mulberry silk varieties (PR and AA) for vascular tissue engineering application.

In the current endeavor, we project an alternative approach by combining the cell sheet engineering and patterned silk films to overcome the above mentioned limitations. A schematic representation of our methodology to fabricate small diameter vascular graft is shown in **Figure 3.1.** Several reports have attested the applicability of *B. mori* silk for various tissue engineering applications but other non-mulberry silk varieties like *P. ricini* and *A. assama* are quite unexplored. In this study, we used the latter in comparison with *B. mori* silk. This approach would serve as a suitable cell sheet platform simultaneously inducing the functional contractile phenotype of SMCs (alignment induced phenotypic transition). Also, it may be envisaged that cellular platform (silk film) would make the rolling process more facile and would not require long term maturation in pulsatile bioreactor to obtain sufficient mechanical strength and functionality. This consecutive rolling assembly is expected to exactly mimic the native cellular alignment (EC aligned longitudinally along the blood flow direction, SMCs and fibroblasts in the concentric arrangement improving mechanical contractility).

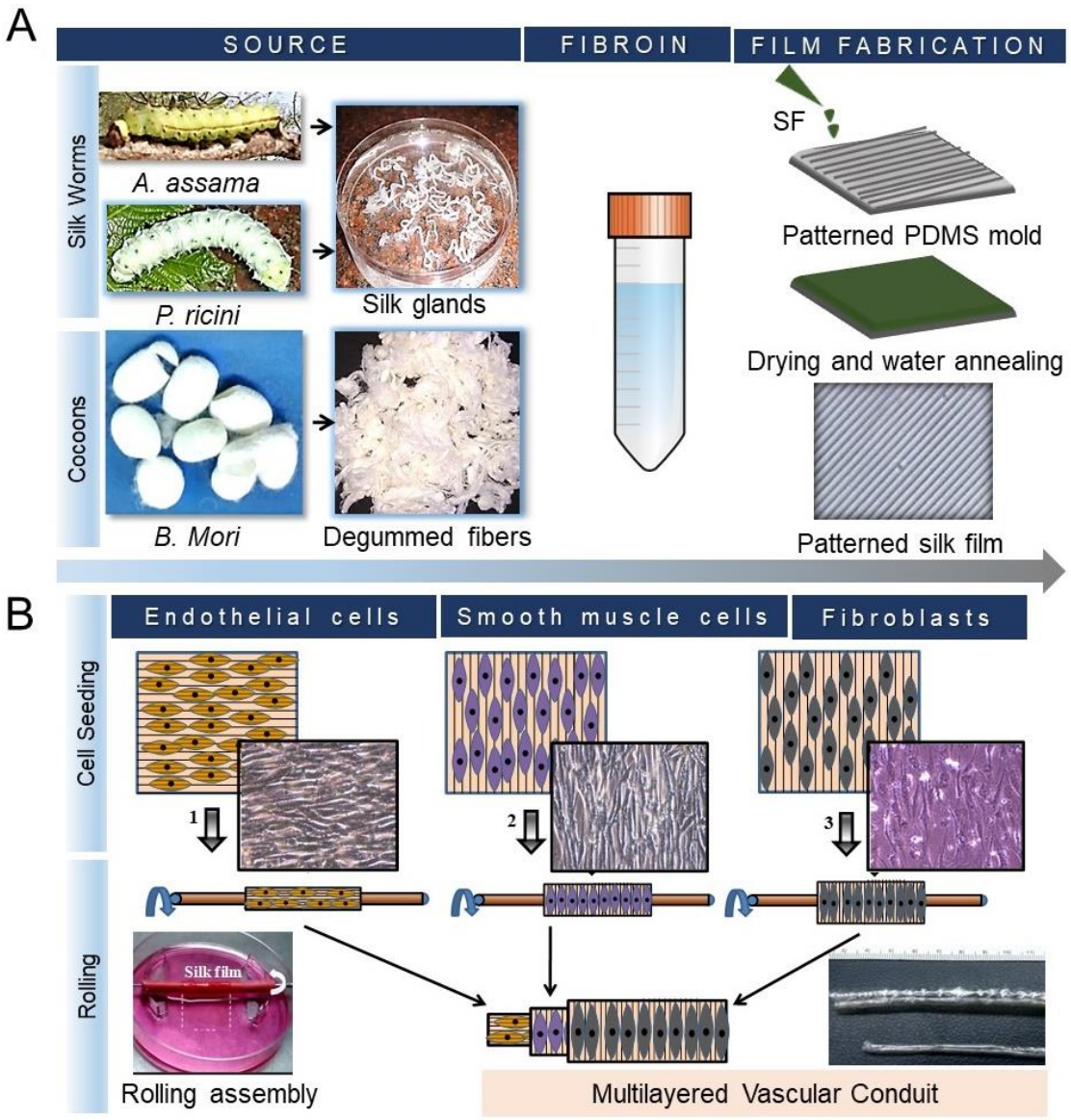

Figure 3.1. *(A) Schematic representing the fabrication of patterned silk films and (B) rolling process of vascular cell sheets to obtain tri-layered biomimicking tissue engineered small diameter blood vessel.*

3.2 Materials and methods

3.2.1 Preparation of aqueous silk fibroin (SF) solutions

SF protein was obtained from both mulberry (BM) cocoons and non-mulberry (AA and PR) silk glands as previously described procedures [118, 294]. Briefly, small cocoon pieces were degummed in boiling 0.02M sodium carbonate, washed properly with distilled water and dried overnight at room temperature (RT). Dried and degummed silk fibers were than dissolved in 9.3M

LiBr and dialyzed against milli-Q water using dialysis membrane (MWCO 1200) for 3 days with successive water change. On the other hand, non-mulberry silk protein was isolated from silk glands of fully-grown fifth-instar matured larvae of *A. assama* and PR. Obtained protein was dissolved in 1% (w/v) sodium dodecyl sulfate and dialyzed against milli-Q water. The concentration of regenerated silk solution obtained was determined by gravimetric method.

3.2.2 Fabrication of silk films

Patterned (microgroove) silk films were fabricated by using grooved PDMS substrates (Dow Corning Corporation, Midland, MI USA) prepared by previously described soft lithography technique [240, 295]. 1.5 mL of 1% (w/v) extracted aqueous silk solution was poured onto 4 x 4 cm^2 PDMS platforms and spreaded uniformly. Casted SF solution was allowed to dry at RT overnight. Resulting 4-5 µm thick films were subsequently subjected to water vapor annealing in a vacuum drying oven for 6h, 37°C in order to induce β-sheet transition and making them water insoluble. After that films were taken out from PDMS molds carefully and kept under sterile conditions till further use.

3.2.3 Physical characterization of silk films

3.2.3.1 Atomic force microscopy

Surface roughness of water vapor annealed patterned and flat silk films was measured in non-contact mode using atomic force microscope (Agilent Model 5500, USA) with tips mounted on triangular cantilevers (spring constant 40 N/m, as specified by manufacturer). All the measurements were performed at room temperature by selecting scanning area range of 20 µm x 20 µm. Acquired data was processed to calculate RMS roughness, roughness average and average height using WSxM 5.0 Develop 7.0 software.

3.2.3.2 Mechanical properties of silk films

Silk films were analyzed for their mechanical properties using Universal testing machine (Instron 3342). 100 Newton (N) load cell was used to carry out the experiment. Silk films (3 cm x 1 cm) were cut keeping the longest dimension parallel to the direction of patterned grooves. For calculating the thickness of silk films, Field Emission Scanning Electron Microscope (FESEM, Zeiss, Sigma) images were captured after gold sputtering. FESEM images were further processed

through MBF ImageJ software to calculate film thickness. The data were acquired at a rate of 0.5 mm/min at 25°C for n=6 samples from each group. Results were reported as Young's modulus and percentage elongation at break.

3.2.3.3 Fourier transform infrared (FTIR) spectroscopy

Fourier transform infrared (FTIR) spectroscopic analysis of water vapor annealed and untreated films was performed using an FTIR Spectrophotometer (Nicolet iS 10) in ATR mode in the spectral region from 1100-1800 cm^{-1} under absorbance mode. All spectra were obtained with a resolution of 4 cm^{-1} and 32 scans per spectra.

3.2.3.4 Wide angle X-ray scattering

The crystallinity of water annealed silk films was analyzed by X-ray diffraction spectroscopy (Bruker D2 Phaser) under Cu radiation (30 KV, 40mA current having Ni filtered) with a scanning rate of 1° per min. All scans extended from 5° to 50° in 2θ with Lynexeye detector system.

3.2.3.5 Thermal analysis of silk films

Water content of water vapor annealed dried silk films was detected using thermogravimetric analysis (TGA, Pyris Diamond TG-DTA). 5 mg of sample was used to carry out analysis in nitrogen atmosphere. Sample was heated at constant rate of 10°C/min in aluminum crucibles from 50°C to 700°C and % weight loss was recorded as a function of time. A differential scanning calorimeter (Perkin Elmer Pyris Diamond DSC) was used to study phase changes in silk films at higher temperatures. 3 mg of sample was heated in aluminum crucibles from 50°C to 400°C with a dry nitrogen gas flow at a constant heating rate of 10°C/min.

3.2.4 Swelling properties

Swelling properties were estimated by gravimetric method used conventionally [296]. Silk films of pre-determined weight prepared of 1% (w/v) SF were immersed completely in phosphate buffer saline (PBS, pH 7.4) at 37°C. At pre-defined time points, swollen films were weighed after soaking the excessive residual PBS using filter paper. The dry weight (W_d) and wet weight (W_s) of silk films was recorded and swelling ratio was calculated implying the following equation:

$$\text{Swelling (\%)} = [(W_s – W_d)/W_d] \times 100$$

3.2.5 *In vitro* enzymatic degradation

In vitro enzymatic degradation profile of silk films was studied in presence of protease XIV isolated from *Streptomyces griseus* (enzymatic activity 3.5 U/mg, Sigma-Aldrich, USA). Initial dry mass of all films was recorded. Silk films were than immersed in 2 mL of PBS (pH 7.4) with and without 2 U/mL protease at 37°C. At predefined time points films were taken out of the enzymatic solution and dried at 60°C for 24h. Enzyme treated dried films were weighed and compared with the initial dried weight. For every 72h, enzyme solution was replaced with freshly prepared enzyme solution. Remaining mass fraction was calculated as:

$$\% \text{ Mass remaining} = (\text{Mass at time t}/\text{initial mass}) \times 100$$

3.2.6 Isolation and culture of primary vascular cells

Small portion of descending porcine aorta was obtained from a local slaughterhouse and kept in sterile, ice cold Dulbecco's phosphate buffered saline (PBS) for transportation. All three vascular cell types were harvested as per the previously reported protocols [243, 297]. Briefly, small part (~1 cm) of aortic tube was cut. The outermost adventitial layer containing fibroblasts was scraped followed by 0.018% (w/v) collagenase digestion (collagenase type IA from *Clostridium histolyticum*, lyophilized powder ≥125 CDU/mg solid, Sigma-Aldrich, USA) for 12h. Fibroblasts extruded from the tissue were plated on standard tissue culture plate. Remaining part containing endothelial cell layer at the luminal side and SMCs' in the middle layer (embedded in extracellular matrix) was cut open to expose the luminal surface. Endothelial cells were harvested by scraping the inner part. SMCs' were harvested following the similar protocol as described for fibroblasts. All three cells were maintained in high glucose Dulbecco's Modified Eagle's Medium (DMEM; Gibco, USA) supplemented with 10% fetal bovine serum (v/v, FBS, Gibco, USA) and 1% antibiotic-antimycotic (v/v, Himedia, India) at 37°C in a humidified incubator at 5% CO_2 level. Media was replenished on regular basis to remove the tissue debris and non-adhered cells. Primary cells were passaged twice after 60-80% confluency and used at early passages (P4 to P8) for carrying out further experiments.

3.2.7 Proliferation of vascular cells on SF films

SF (1% w/v) films from different silk varieties were evaluated for their ability to support the proliferation of vascular cells. Films were conditioned with Dulbecco's Modified Eagle Medium

(DMEM, Gibco, USA) overnight prior to cell seeding. Equal number (~10^4 cells/cm^2) of EC, SMC and fibroblasts were seeded on each film (n=4). Cell proliferation was assessed using AlamarBlue dye (Invitrogen, USA) reduction assay following the manufacturer's instructions at 1, 4 and 7 days. Briefly, cell seeded silk films were incubated with 10% (v/v) dye in culture media for 3h. Post incubation, 100 µL of culture media from each sample was read at 570/600 nm using a multiplate reader (Tecan infinite M 200 pro). Results were reported as normalized value of % AlamarBlue reduced at various time intervals.

3.2.8 *In vitro* hemocompatibility of silk films

3.2.8.1 Platelet adhesion onto silk films

Hemocompatibility of silk films and their antithrombogenic property was checked by checking the amount of platelet adhesion as reported by Cutiongco *et al.* [298]. Whole blood was taken out from healthy porcine and primed with 8 U/mL heparin (Sigma-Aldrich, USA). Platelet rich plasma (PRP) was isolated by centrifuging the whole blood at 100g for 20 min at 20°C. Supernatant was collected and used fresh for further studies. Briefly, 200 µL of PRP was incubated on silk coated coverslips for 1h at RT. Coverslips were kept on orbital shaker during incubation at 60 rpm. Collagen (1.5 mg/mL) coated coverslips were considered as positive control. Silk coated coverslips were washed subsequently thrice with PBS (pH 7.4). Adhered platelets were further fixed by Neutral Buffered formalin (NBF, Sigma-Aldrich, USA) for overnight followed by permeabilization with 0.1% Triton X-100 (v/v, Sigma-Aldrich, USA) for 15 min. Permeabilized platelets were stained with rhodamine-phalloidin (1:40, Life Technologies, USA) and visualized under inverted fluorescent microscope (EVOS FL, Life Technologies, USA).

3.2.8.2 Activity of adhered platelets

For analyzing the activity of adhered platelets, 24 well plate was coated with silk protein. 500 µL of PRP was incubated in each well for 1h, 37°C on shaker (60 rpm). Adhered platelets were washed with PBS (pH 7.4) three times and lysed with 1% Triton X-100 for 1h at 37°C. Cell lysate was centrifuged at 10,000 rpm at 4°C and supernatant was analyzed for lactate dehydrogenase (LDH) activity using LDH assay kit (Sigma-Aldrich, USA) following the manufacturer's instructions. Assay was performed in quadruplet and LDH activity was reported in milliunits/mL.

3.2.9 Immunogenicity of silk films

3.2.9.1 Macrophage stimulation assay

Immunogenic response of SF films prepared using *B. mori* cocoons and AA/PR silk glands protein was assessed by estimating the tumor necrosis factor alpha (TNF-α) release profile as previously reported [175, 299]. TNF-α is a cell signaling cytokine that is released primly from macrophages as a foreign body response causing inflammation. RAW 264.7, a mouse macrophage cell line, was used to analyze the immunogenic response of silk films. Equal no. (~50,000 cells/well) of cells were seeded on sterile protein coated 12 well tissue culture plate. Uncoated wells with same cell density were considered as negative control whereas wells containing 1000 ng/mL lipopolysaccharide (LPS, from *Escherichia coli*, Sigma-Aldrich, USA) were taken for positive control. Culture media was collected at day 1 and day 7 for estimation of TNF-α production.

3.2.9.2 Determination of TNF-α release

Amount of released TNF-α was quantified using mouse TNF-α ELISA kit (Life Technologies, sensitivity <3 pg/mL) as per the manufacturer's instructions. Briefly, cell culture supernatants were collected at pre-defined time points. For standard curve preparation, 100 µL of Ms TNF α (0-1000 pg/mL) was added in duplicate in 96 well antibody (against mouse TNF-α) coated plate. Cell supernatant was diluted 2 fold with standard diluents buffer and added in same manner as for standard. 50 µL of biotinylated secondary antibody was added into each well followed by 90 min incubation at RT. After four subsequent washing, wells were added with 100 µL streptavidin-HRP working solution. Post 30 min incubation period, wells were washed and incubated with 100 µL stabilized chromogen solution. Reaction was stopped after 20 min by adding 100 µL of stop solution and absorbance was measured at 450 nm using multiplate reader (Tecan infinite M 200 pro). Amount of TNF α released was calculated using standard curve values.

3.2.9.3 *In vivo* response to silk films

The animal experiments were performed following an ethical committee approved protocol in accordance with institutional animal ethical committee (IAEC), West Bengal University of Animal and Fishery Sciences (WBUAFS), West Bengal, India (Permit No. Pharma/IAEC/36 dated 30.6.2014) in accordance with "Principles of laboratory animal care". Swiss (I.B.) mice of 30-35 g body weight and either sex were used to carry out the study. Animals were undergone surgery

under isoflurane (1-3% in oxygen and up to 5% for initial induction), using a precision vaporizer. Patterned silk films of all three varieties were cut in to 2 x 2 cm^2 pieces and sterilized properly under UV radiation exposure. Sterile silk films were implanted through a 0.5 cm incision in subcutaneous pocket of lateral side of thoracic-lumber region and protected using a non-absorbable nylon suture stitch. The healing process was continuously monitored for any infection at the incision. No death was recorded during the entire experimental duration. The animals were sacrificed after 4 weeks by cervical dislocation. Implanted films were collected along with the surrounding tissue and stained with hematoxylin and eosin for histological examination.

3.2.10 Cellular alignment and immunostaining

Vascular cells were seeded onto the patterned silk films at a density of 2 x 10^4 cells/cm^2. Media was replenished every 2^{nd} day. Cell growth was continuously monitored under phase contrast microscope. After almost 80% confluent cell monolayer maturation, cells were washed twice with phosphate buffer saline (pH 7.4) followed by Neutral Buffered formalin (NBF, Sigma-Aldrich, USA) fixing for 24h. NBF was removed with 3 subsequent PBS washes. Formalin fixed cells were permeabilized with 0.1% TritonX-100 (v/v, in PBS, Sigma-Aldrich) for 15 min. In order to reduce the chances of non-specific binding, cells were incubated with blocking buffer (1% w/v bovine serum albumin and 0.3M glycine) for 1h at RT. After three subsequent PBS washes, corresponding primary antibodies developed in rabbit against anti vWF (Abcam, 1:100 dilution) for endothelial cells, anti α-smooth muscle actin (α-SMA, Abcam, 1:300 dilution), anti calponin (Abcam, 1:100 dilution), anti-elastin (Abcam, 1:300 dilution) for smooth muscle cells were used for cell specific marker detection. FITC conjugated Goat anti rabbit IgG H&L (Abcam) secondary antibody was implied for fluorescent imaging. Cells were than counterstained with Hoechst 33342 (1:1000, Sigma-Aldrich, USA) and rhodamine-phalloidin (1:40, Life Technologies, USA) for nucleus and cytoskeleton respectively followed by imaging under an Inverted Fluorescent Microscope (EVOS FL, Life Technologies, USA). Cells were washed properly with PBS before imaging in order to reduce the background noise. Pattern direction and cytoskeleton alignment was observed for cellular patterning.

3.2.11 Quantitative real-time polymerase chain reaction (qRT-PCR)

For analyzing the alignment induced contractile phenotype of SMCs cultured on patterned *A. assama* silk films, smooth muscle myosin heavy chain (SM-MHC) and α-smooth muscle actin (α-SMA) expression were checked after 10 days. SMCs cultured on flat films were taken as control. After 10 days culture, one mL TRIzol reagent (Sigma-Aldrich, USA) was added to the cultured cells on silk films and incubated at 25°C for 30 min. Films were scraped and solution was centrifuged at 13,000 rpm (10 min, 4°C). Supernatant was transferred to fresh tubes and incubated with chloroform for 15 min. These tubes were centrifuged at 13,000 rpm (15 min, 4°C) and upper aqueous layer was transferred to new tubes. RNA was further eluted, purified using ethanol and finally re-suspended in RNAse free water (Sigma-Aldrich, USA). RNA was reverse transcribed using High Capacity Reverse Transcription Kit (Applied Biosystems, Invitrogen, USA) in a thermal cycler machine (TaKaRa). Expression level of contractile genes (SM-MHC and α-SMA) was quantified using Power SYBR Green PCR Master Mix (Applied Biosystems, life technologies) in a real-time PCR machine (Applied Biosystems 7500) with 7500 Software v2.0.6. Primers with the following sequences were used: SM-MHC (Forward 5′-AGGACCAGTCCATTTTGTGC-3′, Reverse 5′-CCTGGTCCTTCTTGCTCTTG-3′), α-SMA (Forward 5′-GGGAATGGGACAAAAAGACA-3′, Reverse 5′-ATGTCGTCCCAGTTGGTGAT-3′) and GAPDH (Forward 5′-TCGGAGTGAACGGATTTGG-3′, Reverse 5′-CCAGAGTTAAAAGCAGCCCT-3′). The gene expression was normalized with corresponding GAPDH expression and fold change was calculated by $2^{-\Delta\Delta Ct}$ method.

3.2.12 Extracellular matrix (ECM) secretion by SMCs on 2D silk film

Cells (~10^4 cm^{-2}) were seeded onto patterned *A. assama* silk films to quantify ECM production (collagen and elastin). Cell seeded silk films were stained for collagen and elastin deposition at different time points. For elastin staining, samples were fixed with neutral buffered formalin (NBF, Sigma-Aldrich, USA) overnight. Deposited elastin fibers were stained with elastic stain kit (Sigma-Aldrich, USA) following manufacturer's protocol. Briefly, fixed samples were washed with PBS thrice and incubated with working elastic stain solution for 10 min. Samples were further rinsed with 95% ethanol (v/v aqueous) followed by brief PBS washing. Elastin fibers were stained by incubating samples with Van Gieson solution followed by dehydration and mounting.

Collagen deposition over time was assessed using trichrome stain (Masson) kit (Sigma-Aldrich, USA). The total collagen content was also quantified by modified Hride Tullberg-Reinert method [300]. For staining, samples were fixed in Bouin's solution overnight at 25°C. Fixed samples were stained with Weigert's iron hematoxylin solution for 5 min after brief rinsing with running tap water. Samples were further incubated with biebrich scarlet-acid fucshin solution followed by working phosphosphotungstic-phosphomolybdic Acid solution for 5 min. Samples were subsequently transferred to aniline blue solution, incubated for 5 min and dipped in 1% acetic acid (v/v) for 2 min. Stained samples were rinsed briefly with deionized water and quickly dehydrated with graded ethanol. After clearing in xylene, samples were mounted in DPX mountant (Sigma-Aldrich, USA). Stained samples were imaged with bright field microscope (EVOS FL, Life Technologies, USA). For quantification of deposited collagen secreted by SMCs cultured on patterned mulberry and non-mulberry films, samples were digested with pepsin digestion buffer (0.1M acetic acid, 0.5M NaCl and 1mg/mL pepsin (from porcine gastric mucosa, Sigma-Aldrich, USA)). Digested samples were coated onto 96 well tissue culture plates and stained with direct red 80 (1 mg/mL aqueous solution, Sigma-Aldrich, USA). Dye was fixed with saturated picric acid solution. Samples were washed with 0.01N HCl thrice and red collagen granules were dissolved in 0.1N NaOH. Final solution was read at 550 nm using multiplate reader (Tecan infinite M 200 pro). Collagen content was estimated after plotting the standard curve prepared using collagen from rat tail (Sigma-Aldrich, USA).

3.2.13 Preparation of silk film-based vascular conduit

Silk films were sterilized under ultraviolet light prior to cell seeding. An optimal number of vascular cells (4 x 10^4 cells/cm) were seeded onto 4 x 4 cm^2 patterned film. Approximately 70% confluent silk films were used for rolling. At first, 2 layers of endothelial cell seeded film were rolled over the inert mandrel using custom designed rolling assembly. SMCs seeded silk film (4-6 layers) was rolled over the endothelial layer considering the concentric alignment. At last, fibroblast seeded silk film (3-4 layers) was used to cover the SMC layer. This specific arrangement was chosen to mimic the native structure of blood vessel. Such rolled films were held together onto the mandrel using a sterile silk thread. This assembly was further submerged in the basal culture medium (high glucose DMEM supplemented with 10% FBS (v/v) and 1% (v/v) antibiotic-antimycotic solution) and maintained at 37°C in a humidified incubator at 5% CO_2 for maturation

over 14 days. After maturation, thread was removed and the vascular construct was slide out of the mandrel.

3.2.14 Histological analysis of vessel structure

Immediately after harvesting (14 days), cell seeded vascular construct was cut into small pieces (~1 cm) and fixed in neutral buffer formalin (NBF) for at least 24h (4°C). It was than dehydrated using grading ethanol solutions (50, 70, 90, 95, 100% v/v) followed by paraffin embedding. 5 µm thick sections were cut and mounted onto glass slides. Cell distribution was assessed by imaging the Hoechst 33342 stained sections as per the standard protocol.

3.2.15 Burst strength of tubular construct

The burst strength of tubular construct was measured in hydrated conditions. Silk tube of approximately 4 cm in length was connected to 50 mL syringe at one end while other one was connected to traceable manometer pressure/vaccum gauge (Fisher Scientific™). This assembly created a closed channel (**Figure 3.2**). Syringe was fixed in a syringe pump and air was perfused at a constant flow rate of 1 mL/min. A continuous flow of air created positive pressure inside the construct. Maximum pressure point at tube failure was recorded and considered as burst pressure.

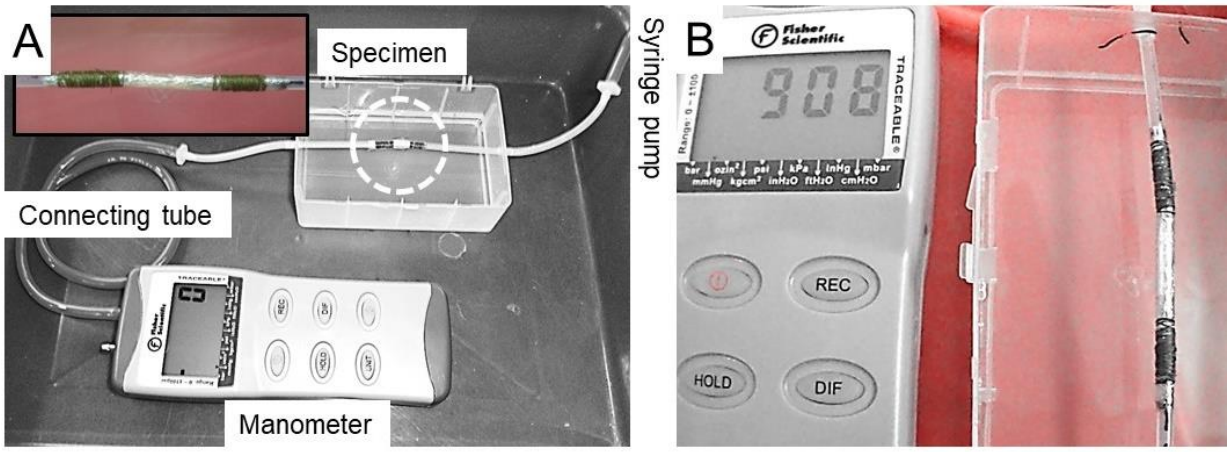

Figure 3.2. *(A) Set-up used to analyze the burst strength of vascular construct (In the inset is the enlarged image of tubular specimen) and (B) Representative image of vascular graft withholding the pressure of up to 908 mmHg.*

3.2.16 Statistical analysis

All the experiments were carried out for n=3 samples. For cell viability analysis (AlamarBlue reduction assay), n=4 samples were used. Data was reported as mean ± standard deviation (S.D.).

One-way analysis of variance (ANOVA) was performed to measure the significance level among different groups followed by tukey's test. All statistical analysis was performed using OriginPro 8 (Originlab Corporation, USA) at both 0.05 and 0.01 significance level.

3.3 Results

3.3.1 Surface morphology and mechanical properties of silk films

Surface morphology of the various silk films prepared using regenerated SF after water annealing was assessed by atomic force microscopy. Patterned silk films made up of non-mulberry silk exhibited sharp and distinct grooves whereas pattern on *B. mori* films showed plateau pattern**.** Moreover, on analyzing the flat silk films, we observed greater degree of roughness on non-mulberry silk films (**Figure 3.3A**). RMS roughness was 44.70 ± 3.42 nm with an average height of 331.18 ± 15.73 nm for *B. mori* film. On the other hand, RMS roughness values for *P. ricini* and *A. assama* films were 92.73 ± 7.91 nm and 94.53 ± 4.85 nm with average heights of 320.03 ± 16.98 nm and 278.45 ± 20.09 nm respectively, thereby representing greater extent of roughness for non-mulberry silk varieties.

Mechanical integrity of construct is an important parameter for vascular engineering. For mechanical property assessment, thickness of films was measured from FESEM images using ImageJ software (**Figure 3.4, Table 3.1**). Non mulberry films were found to be mechanically strong as compared to mulberry silk (BM). Young's modulus of former films ranged between 2.5 and 3.2 MPa. This was significantly higher (2 fold) than the latter (0.99 ± 0.14 MPa, $p<0.01$) (**Figure 3.3B**). Similarly, elasticity of *A. assama* silk films was also highest among the group with 16.13 ± 3.55% elongation at break point. *B. mori* films showed almost half (i.e. 8.98 ± 0.99% elongation) the extension of *A. assama* films before failure ($p<0.05$) (**Figure 3.3C**). There was no significant difference between *P. ricini* films and other two experimental groups. Results attest the mechanical superiority of non-mulberry silk films over mulberry counterpart.

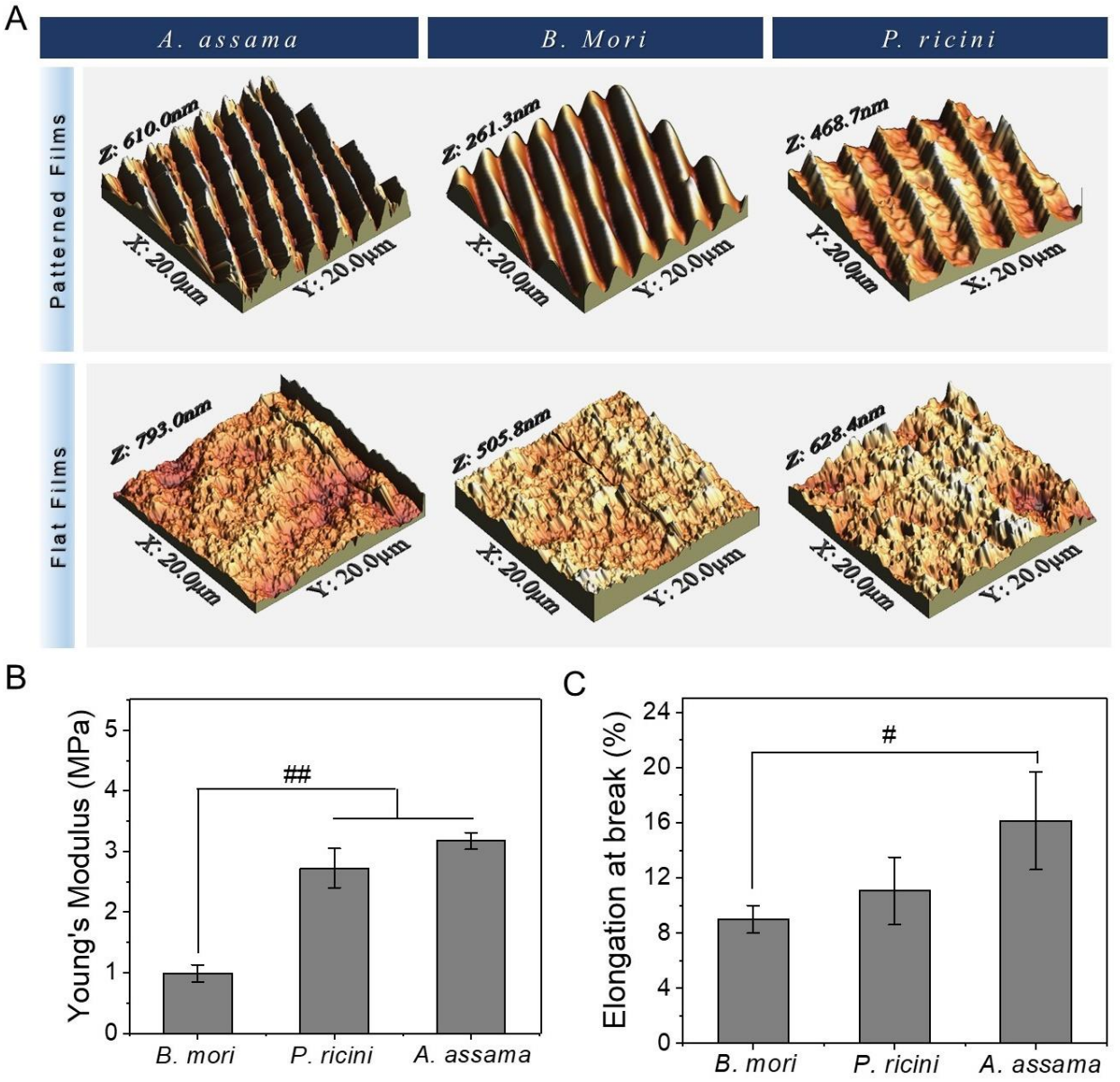

Figure 3.3. *(A) Atomic force microscopic images of water vapor annealed patterned and flat films of both mulberry and non-mulberry silk varieties. Mechanical properties of silk films (B) Young's modulus, and (C) elasticity showing percentage elongation at break. (#p<0.05, ##p<0.01)*

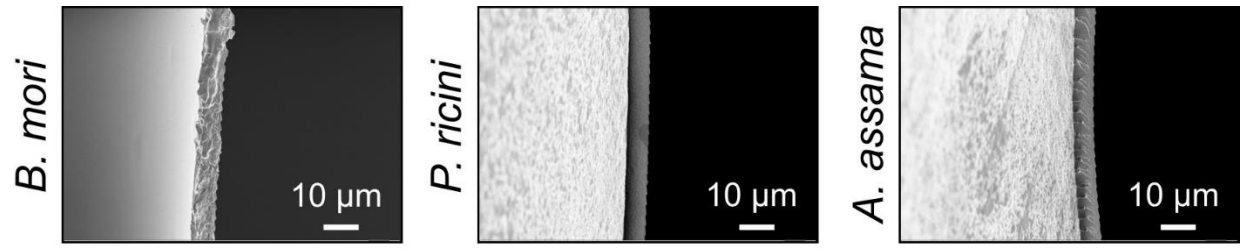

Figure 3.4. *Field emission scanning electron microscopy of patterned silk films.*

Table 3.1. *Thickness of patterned silk films.*

S. No.	Sample	Thickness (µm)
1	BM film	6.89 ± 0.18
2	PR film	6.45 ± 0.13
3	AA film	6.03 ± 0.24

3.3.2 Fourier transform infrared (FTIR) spectroscopy

Secondary structure-transition of regenerated SF films was studied by FTIR spectroscopy (**Figure 3.5A**). For all samples, characteristic vibration bands for peptide backbone between 1610-1660 cm^{-1} (amide I), 1510-1560 cm^{-1} (amide II) and 1210-1260 cm^{-1} (amide III) were observed corroborating the presence of C=O stretching, N-H bending and C-N stretching, respectively [301]. Specific vibration frequency corresponds to characteristic structural conformations (β-sheet and random coil/α-helix) for silk protein. Absorption at 1648-1554 (amide I) and 1535-1542 is indicative of silk I conformation whereas some studies report these values corresponding to random coil structure [302]. Regenerated SF from *B. mori* cocoon showed typical peaks at 1660 and 1549 cm^{-1} in the amide I and amide II region suggesting its α-helix/random coil conformation. A similar peak values were obtained for *P. ricini* Silk gland protein at 1660 and 1527 cm^{-1}. Water vapor annealing for 6h led to structural transition towards β-sheets conformation with signature peaks at 1630 and 1530 cm^{-1} in amide I and amide II regions. Peak values within 1610-1630 cm^{-1} (amide I) and 1510-1530 cm^{-1} (amide II) range are specific for silk II secondary structure [247]. Water vapor annealed *P. ricini* SF films represented the characteristic peak values at 1630 and 1529 cm^{-1} whereas for *A. assama* silk these peak values fall at 1626 and 1528 cm^{-1} suggesting β-sheet transition. A low intensity amide III band was also observed for all samples ranging from 1222-1240 cm^{-1}. The IR spectrum of regenerated silk protein confirms the transition from native predominant random coil structure in untreated state to β-sheet structures after water vapor annealing. Shifting of spectral peaks signifies the rearrangement of hydrogen bonds in the SF protein moiety that converts it in to more stable β-sheet secondary structures.

3.3.3 X-ray diffraction

Conformational transition and crystallinity of regenerated SF was further analyzed using wide angle X-ray diffraction study (**Figure 3.5B**). Previous studies suggest α-helix conformation of SF at 2θ values 11.8° and 22° whereas characteristic X-ray diffraction peaks at 16.5°, 20.2°, 24.9°,

30.9°, 34.59°, 40.97° and 44.12° demonstrate the presence of β-sheets [247, 303]. X-ray spectra of SF protein showed the characteristic peaks for 2θ values at 11.8° and 16.5°, after water vapor annealing for 6h. Minor peaks at 22.2° and 25.4° were also observed for all silk protein samples confirming the presence of β-sheet structure. Data suggested that water vapor annealing induces the conformational transition from silk I to silk II type. Significant influence of water on the silk I structure is also evident from the data. These results were consistent with prior reports where almost similar peaks were obtained for *Antheraea pernyi* silk, another member of non-mulberry silk variety [304].

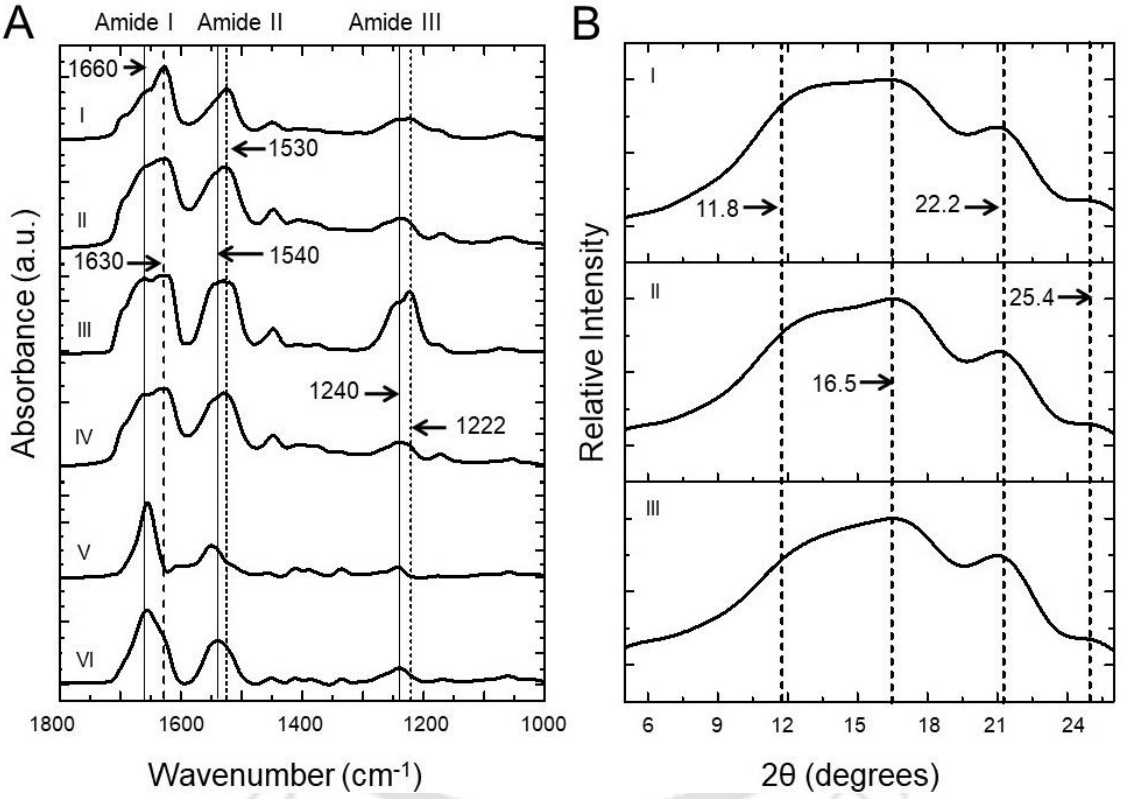

Figure 3.5. *(A) Fourier transform infrared spectra of water vapor annealed (II, IV, VI) and untreated (I, III, V) 1% (w/v) silk fibroin films from A. assama (I, II), P. ricini (III, IV), and B. mori (V, VI) silkworms, respectively. (B) X-ray diffractogram of water vapor annealed silk films (I) BM, (II) PR, and (III) AA.*

3.3.4 Thermal analysis

All the water vapor annealed SF films demonstrated three characteristic peaks (**Figure 3.6A**). The first endothermic glass transition (T_g) peak was formed at around 80°C, indicating the presence of water and the segmental movement of the SF protein molecules. The second exothermic peak

formed at around 224℃, indicates the movement of random coil and α-helix conformations and crystallization of SF influenced by heat. The third endothermic peak formed at around 300°C shows the thermal decomposition of ordered fibroin protein in all the silk films [247]. The decomposition temperatures of *B. mori* silk were slightly lower than *A. assama* and *P. ricini* films, a clear indication of improved thermal properties in the latter films. An endothermic peak at around 290℃ was obtained for *B. mori* silk whereas this peak was at around 360℃ for other two silk varieties. This signifies the induction of crystalline structure in silk films which require higher activation energy for the breakage of covalent bonds in β-sheet structures as compared to random coils structures.

The thermal behavior of *B. mori, A. assama* and *P. ricini* films was further studied by TGA (**Figure 3.6B**). The thermogram demonstrates four steps of weight loss with significant variation within the temperature range of 33-770℃. The initial weight loss step at around 100°C refers to the removal of absorbed water (loss of moisture). The second weight loss step ranging from 250 to 400℃ is imputed to the cleavage of peptide bonds and breakdown of side chain groups of amino acid residues [247]. The third weight loss step ranging from 400 to 770°C is the decomposition stage as described earlier from the DSC results. The TGA curves reveal that in the temperature region (400–770℃) for decomposition, the *A. assama* silk films shows slightly more thermal stability (400- 770℃) than *B. mori* and *P. ricini* treated films.

3.3.5 Swelling properties

Swelling behavior determines the structural integrity and stability. Rate of water uptake by 2D SF films was studied for extended periods. All films swelled rapidly in PBS and attained an almost plateau pattern within 2h owing to low protein concentration. Maximum swelling was observed during first 20 min with a swelling ratio of 420 for all silk varieties under consideration **(Figure 3.6C)**. Regenerated SF films of *P. ricini* and *A. assama* silkworms exhibited swelling ratio of around 700 and 650 respectively whereas this value was 550 for *B. mori* silk films. At later stages *P. ricini* films were found to uptake maximum amount of water and it was significantly higher from *B. mori* films ($p<0.05$). On the other hand, the swelling pattern of *A. assama* silk films did not vary from other two silk varieties.

3.3.6 *In vitro* enzymatic degradation

In vitro degradation profile of regenerated silk films in PBS with and without protease was studied till 28 days by monitoring the rate of weight loss. Results were reported as percentage mass remaining with time (**Figure 3.6D**). Films were degraded more rapidly in presence of protease whereas PBS alone did not impose such effect and silk films were found to maintain their integrity for prolonged periods. 2-6% weight loss was observed in PBS for different silk varieties. The differences in the degradation pattern were apparent in case of protease treated SF films. A continuous time dependent degradation was observed for all silk film varieties. In particular, *B. mori* silk film degraded maximally and lost up to 95.97 ± 0.31% after 21 days and 97.85 ± 1.20% weight after 28 days. Also rate of degradation was highest for *B. mori* silk films. Non-mulberry silk films were found to resist protease treatment till certain extent. Weight loss of 43.05 ± 1.97% (2.27-fold decrease) and 66.70 ± 3.78% (1.46-fold decrease) was observed for *P. ricini* and *A. assama* silk films respectively after 28 days. However initial rate of degradation was much less for these two silk varieties. *P. ricini* silk films retained 85.45 ± 1.17% mass of the initial weight after 14 days whereas this value was 73.46 ± 0.50% for *A. assama* silk film.

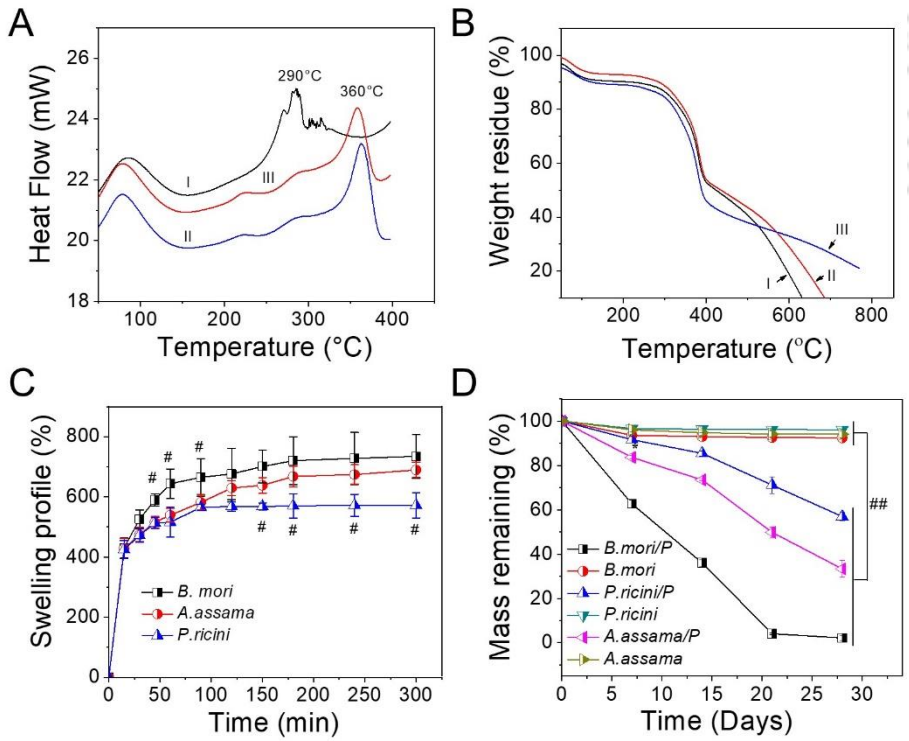

Figure 3.6. *Thermal analysis of silk films. (A) Differential scanning calorimetry (DSC) and (B) thermogravimetric analysis (TGA) studies. Swelling (%) (C) and degradation profile (D) of water vapor annealed silk films. (/P) indicates the presence of protease (#p<0.05, ##p<0.01)*

3.3.7 Proliferation of vascular cells on silk films

AlamarBlue cell viability assay was used to investigate the proliferative index of vascular cells on different variety of silk films. Percentage reduction of AlamarBlue dye corresponds to cell viability and metabolism that is directly co-related with the number of live cells. Regenerated SF coated and uncoated wells were analyzed for cellular proliferation at day 1, 4 and 7. Growth profiles of vascular cells at day 7 clearly demonstrated better cell attachment and proliferation on silk films from non-mulberry (*P. ricini* and *A. assama*) silk varieties and ~1.3-fold increase for SMCs, ~1.1-fold increase for fibroblasts, ~1.15-fold increase for ECs was observed as compared to *B. mori* silk (**Figure 3.7A-C**). In particular, vascular adventitial fibroblasts exhibited higher dye reduction on *P. ricini* and *A. assama* films than normal tissue culture plate. Although *P. ricini* films outperformed during initial time periods (day 1 to day 4) for all three cultured vascular cells but at day 7, proliferation values of vascular cells seeded on *A. assama* films almost overlapped with *P. ricini* values ($p>0.05$).

3.3.8 Antithrombogenic activity of silk films

Antithrombogenic activity on silk films was evaluated by observing number of platelets adhered within a predefined time interval while incubating with PRP. LDH assay was performed to determine the activity of adhered platelets. Results were in accordance with platelet adhesion test and followed a similar trend where maximum LDH activity (5.9 ± 0.42 milliunits/mL) was observed for collagen coated coverslip (**Figure 3.7D**). Platelets adhered onto silk films exhibited minimal values and these values lied in between 0.01-0.10 milliunits/mL for both mulberry and non-mulberry silk films. Although a broad range of LDH activity was detected for mulberry silk, however no significant difference was observed among different silk varieties. Extent of adhered platelets on to *A. assama* and *P. ricini* films was comparable with *B. mori* silk films. Collagen coated coverslip was considered as positive control where considerably higher population of adhered platelets was observed (**Figure 3.7E**). Fluorescence microscopic images depicted more extended and comparatively spreaded morphology on collagen coated coverslips while almost rounded morphology was observed onto silk films.

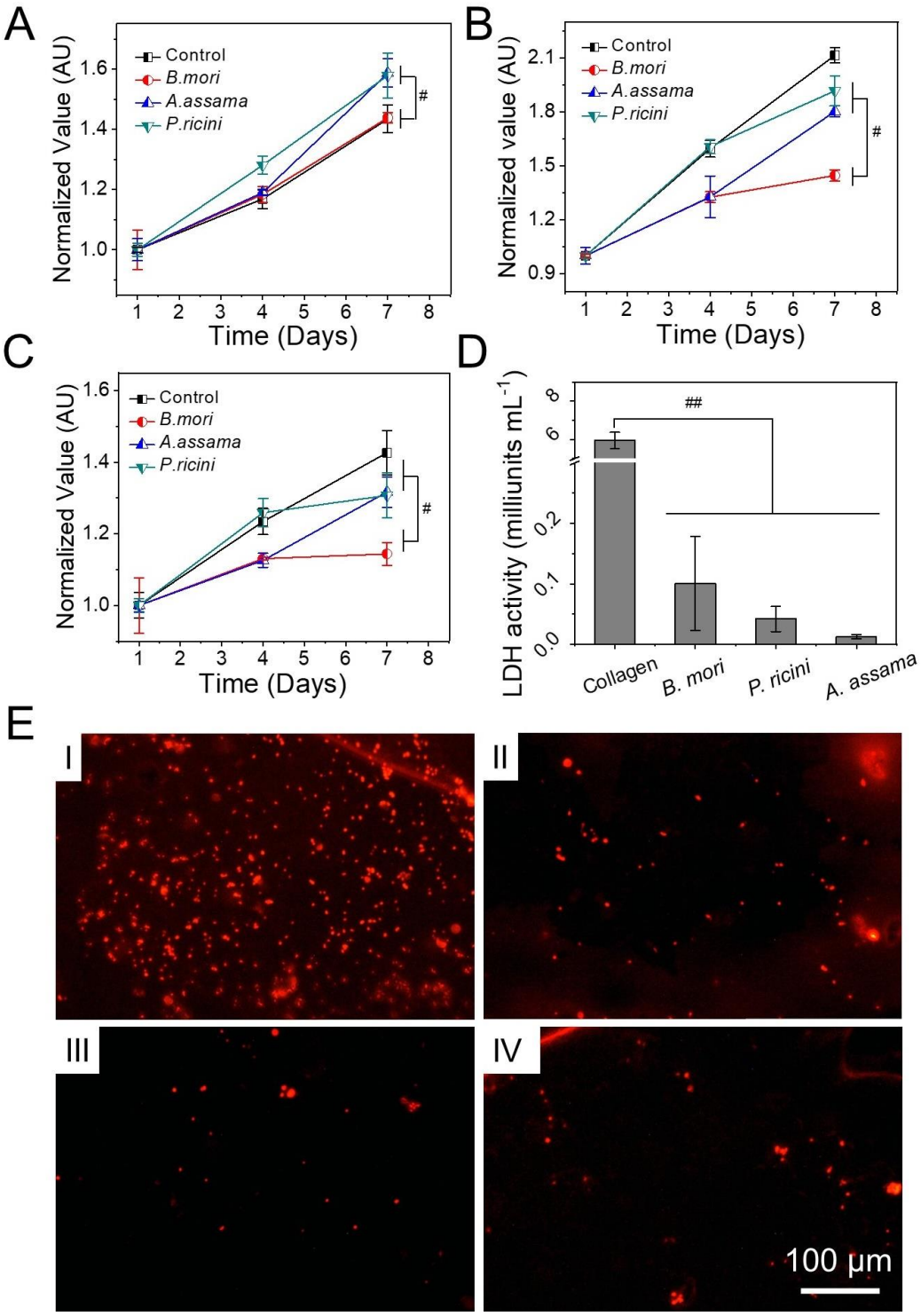

Figure 3.7. *In vitro cyto and hemocompatibility assessment of silk films. Growth profile of (A) fibroblasts, (B) smooth muscle cells and (C) endothelial cells cultured on silk films of different varieties obtained using alamar blue dye reduction assay. (D) Lactate dehydrogenase (LDH) activity of adhered platelets on different silk films. (E) Adhesion of platelets on silk films; (I) Collagen coated coverslips-positive control, (II) B. mori film, (III) A. assama film, (IV) P. ricini film. Platelets were stained with rhodamine phalloidin (red color). (#p<0.05, ##p<0.01)*

3.3.9 Immunogenicity of silk films

3.3.9.1 *In vitro* response of mouse macrophages to silk films

Immunogenicity of silk films was assessed by investigating the amount of TNF-α released from mouse macrophages (RAW 264.7 cell line) cultured in presence of different variety silk membranes (**Figure 3.8**). Both short and long term stimulatory effect was studied from day 1 to day 7. Very low levels of TNF-α were observed at day 1 for different silk film varieties and these values were comparable with polystyrene tissue culture plate. Slightly elevated TNF-α levels were obtained for positive control (samples with LPS, $p<0.05$). Moreover, at day 7, TNF-α release was increased 4 folds and ranged between 1100 pg/mL-1600 pg/mL for different silk varieties. At this point also, these values were comparable with polystyrene tissue culture plates. A rapid increase was although observed with positive control. Response of macrophage to silk films of all three varieties was found to be in acceptable range. These findings suggest the low immunogenicity of silk films in terms of TNF-α release that enables their applicability as biomaterial for various tissue engineering applications.

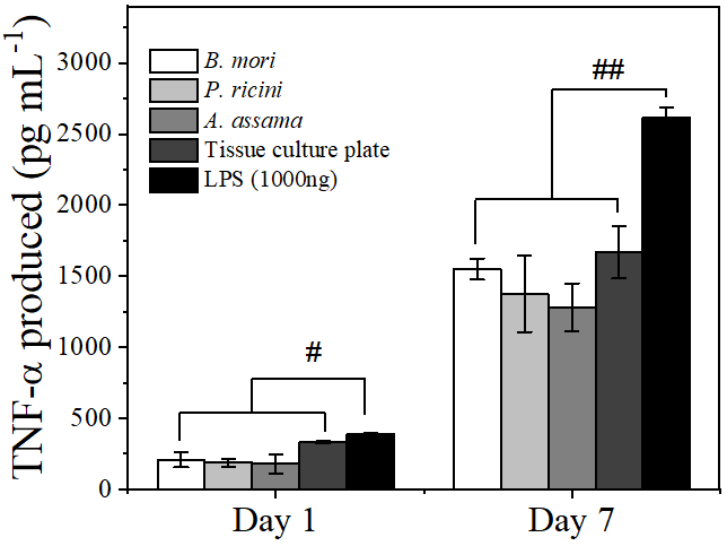

Figure 3.8. *Production of TNF-α by RAW 264.7 mouse macrophage cells in response to silk films. Cells were stimulated by 1 wt% patterned silk films from different variety silk. Standard tissue culture plate was considered as negative control whereas for positive control, 1000 ng/mL lipopolysaccharide from E. coli was used. Amount of TNF-α released was calculated quantitatively from the standard curve plotted using recombinant TNF-α. (#p<0.05, ##p<0.01)*

3.3.9.2 *In vivo* response to silk films

In order to better understand the immunogenicity of silk films and to assess the implant integration, films were implanted in the dorsal subcutaneous pocket of mice. Implanted material was retrieved

after 4 weeks. Post retrieval, implanted films were stained with H&E stain as per the standard protocol (**Figure 3.9**). Occasional occurrence of immune cells was observed nearby the film implants. 5-6 layers of fibroblast cell sheets were observed along with milder immigration of macrophages for all silk films. Macrophages were limited to film-tissue interface. *A. assama* film section depicted well organized adipose and muscular tissue which retained their structural integrity without involving any inflammatory reaction. The material attached to the dermal and subdermal tissues showed no infiltration of giant cells, macrophages and mononuclear cells. Analysis of *B. mori* film suggested normal cellular proliferation and angiogenic reaction in muscular and hypodermal tissues. The material revealed mild inflammatory reaction consisting of few lymphocyte and macrophages. Orientation to the structural portion is quite normal. Results were in accordance with previous reports stating the immune-compatibility of pure silk films that has shown to induce lower immune response as compared to collagen films [176]. A comparative immune response of non-mulberry silk varieties with FDA approved *B. mori* silk validates the applicability of former for various tissue engineering purposes.

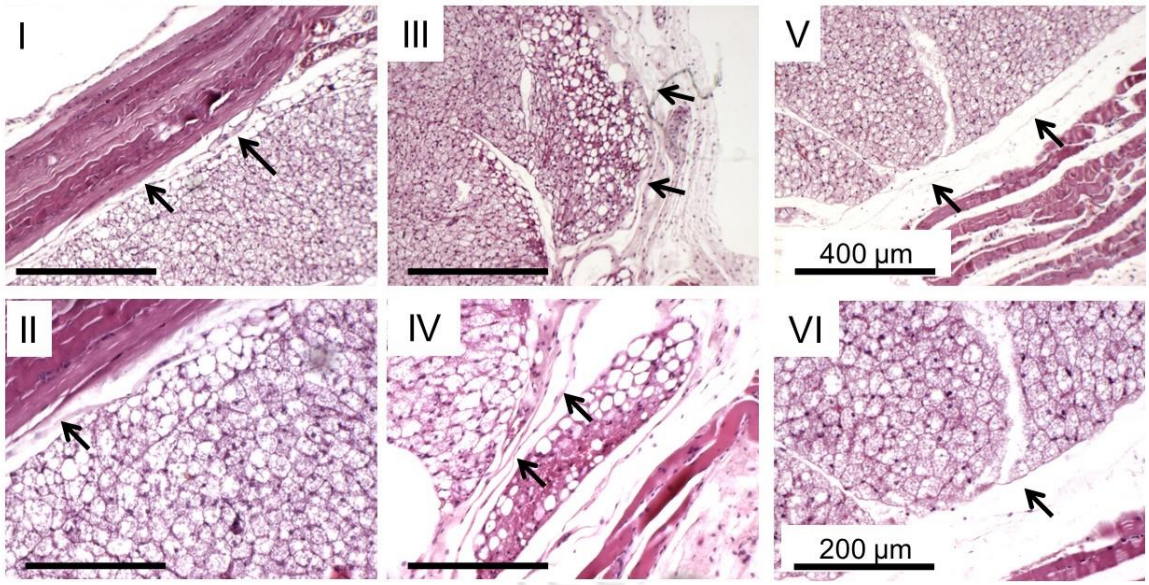

Figure 3.9. *Bright field microscopic images of H&E stained sections showing in vivo immunological response of silk films, B. mori (I, II), P. ricini (III, IV) and A. assama (V, VI) retrieved 4 weeks post implantation from subcutaneous pocket of mice. (Black arrows are indicating the location of film).*

3.3.10 Cellular alignment and expression of cell specific surface marker on patterned silk films

Phase contrast microscopic images after one week of culture exhibited unidirectional alignment of vascular cells on patterned silk films. Elongated cell morphology along the direction of groove axis was observed. Smooth muscle cells responded comparatively faster than other two cell types and aligned themselves parallel to groove direction within 24h. Over extended period of time, a confluent monolayer culture of vascular cells was established on all three varieties of silk films (**Figure 3.10**). Magnified images demonstrated very low angle between direction of pattern and major axis of cell. Elongated geometry of cells on pattern silk films confirmed that microgroove imprinted silk films guide the cellular alignment concomitantly maintaining cellular proliferation.

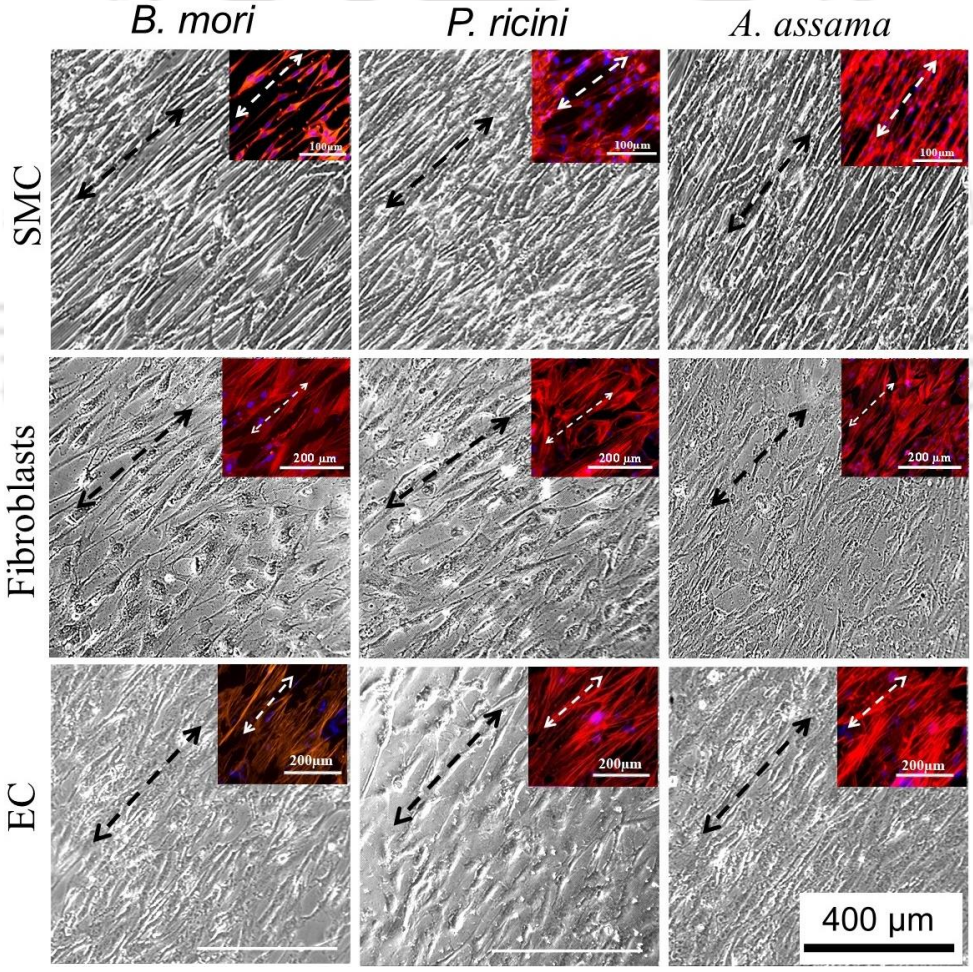

Figure 3.10. *Phase contrast microscopic pictograph of confluent monolayer of vascular cells aligned unidirectionally on patterned silk films. Inset images demonstrating rhodamine-phalloidin stained (red color-alignment of actin cytoskeleton) and Hoechst 33342 stained (blue color) fluorescent microscopic pictograph of vascular cells. White and black arrows are indicating the direction of alignment.*

Cell type and specific phenotype was confirmed by presence of cell specific marker protein expression using immunocytochemistry. Cells were plated on patterned silk films of all three varieties, keeping the initial cell density same (~1x10^4 cells/cm^2). After 7 days of culture, an almost confluent layer of vascular cells was observed. Fluorescent microscopic images exhibited expression of calponin and α-SMA (early and mid-differentiation marker of SMC) marked the functionality of SMCs (**Figure 3.11A-D**). Furthermore, distinguishable presence of cytoplasmic distribution of vWF, a phenotypic marker for endothelial cells (**Figure 3.11E-F**) suggested that patterned silk films support the growth of vascular cell types while maintaining the cellular phenotype. Maintaining contractile phenotype of SMCs is one of the major challenges in the field of vascular tissue engineering. In order to assure the maintenance of functional cellular phenotype onto patterned silk films, we checked for expression level of contractile phenotype markers (SM-MHC and α-SMA). SMCs cultured on both flat and patterned *A. assama* silk films were analyzed using RT-PCR. Expression of SM-MHC and α-SMA by SMCs cultured on patterned silk film was found to be elevated by 10.6 fold and 1.85 fold respectively as compared to flat films after 10 days of culture (**Figure 3.11G**). Results suggested that alignment of SMCs on to patterned silk films helps maintaining contractile phenotype of SMCs.

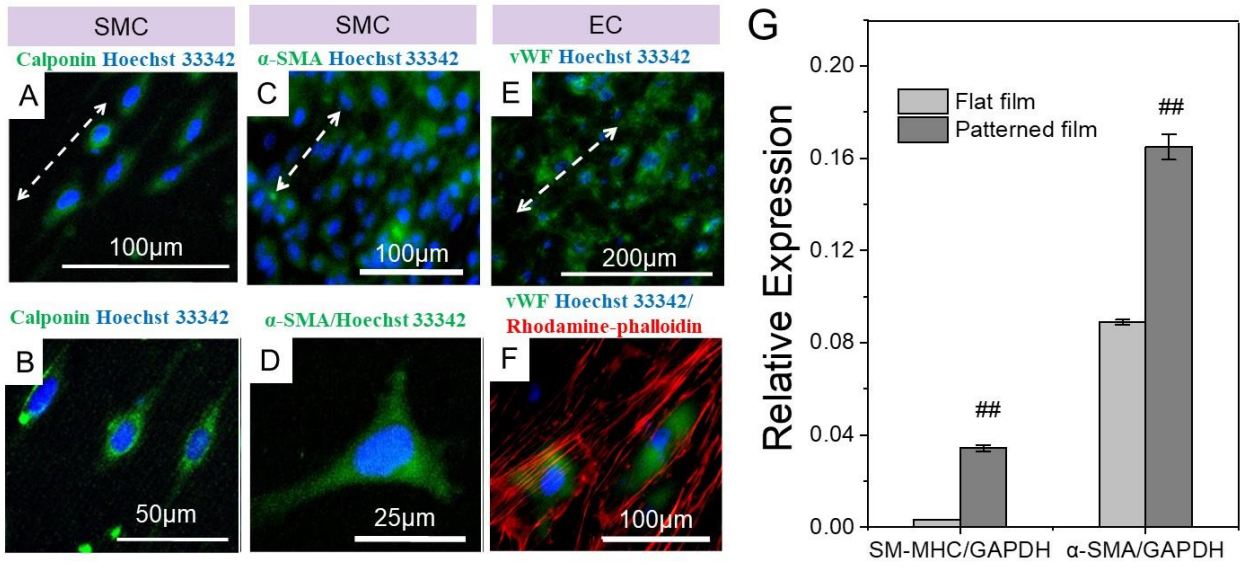

Figure 3.11. *Representative fluorescent microscopic images depicting phenotypic marker expression and functionality of vascular cells cultured on A. assama patterned silk films. SMCs were stained with phenotype markers: calponin (A, B) and α-SMA (C,D). EC's functionality was confirmed by visualizing the vWF expression (E, F). All phenotypic markers are stained with FITC tagged secondary antibody (green fluorescence). Cells were further counterstained with rhodamine-phalloidin (red) and Hoechst 33342 (blue color) to visualize actin cytoskeleton and*

nucleus respectively. White arrows are indicating the direction of alignment. (G) Real time gene expression analysis showing upregulation of contractile phenotype markers (SM-MHC and α-SMA) in SMCs cultured on patterned A. assama silk films for 10 days. (##p<0.01)

3.3.11 ECM deposition by SMCs cultured on patterned silk films

Collagen and elastin are two major constituents of ECM present in the artery medial layer. These proteins are mainly responsible for imparting elasticity and mechanical stability to the vessel. Elastin production was analyzed by staining intracellular soluble tropoelastin of SMCs cultured onto patterned silk films. Although we had not observed the prominent fibrous elastin in the ECM of SMC culture but a distinct punctuated pattern in the cellular cytoplasm proves elastin biosynthesis (**Figure 3.12A**). In order to further verify the elastin deposition by SMC, samples were stained with Van Gieson stain. Bright field microscopic images demonstrated presence of unorganized elastin fibers in SMCs cultures after 10 days whereas no such presence was observed at earlier time points (**Figure 3.12B**). Elastin fibers were arranged in the form of mesh and found to connect adjacent cells in the confluent culture. Collagen deposition was also visualized (blue color) by Masson's Trichrome staining (**Figure 3.12C**). Significant and uniform deposition of collagen was observed in confluent SMC culture after day 10 as compared to earlier time point. Total content of collagen secreted by SMCs was quantified on both mulberry and non-mulberry silk films at different time points. Collagen deposition on to different silk films was independent of SF type and no significant difference was observed among different groups. On the other hand, time dependent increment of collagen content was observed. Before solubilization in 0.1N NaOH, dye stained red globules were clearly visible indicating the presence of collagen deposition. Collagen content in the various samples increased from 30-49 µg/mL after day 1 to 93-107 µg/mL on 10^{th} day (**Figure 3.12D**). Almost 2-3 fold increase was recorded in collagen content after 10 days as compared to day 1 ($p<0.05$).

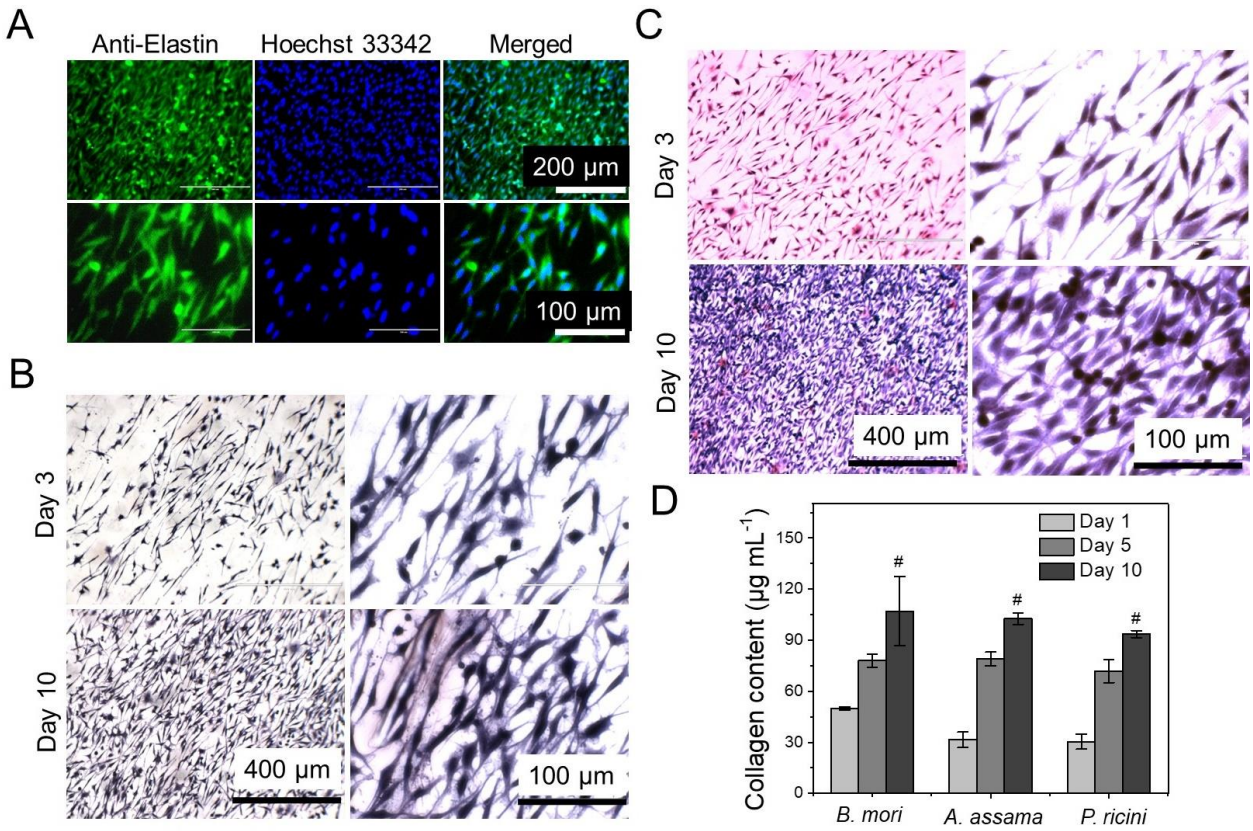

Figure 3.12. *Representative images of ECM deposition by SMCs cultured on A. assama patterned silk films. (A) Intracellular localization of soluble tropoelastin (green color) and nucleus (blue color) in SMCs. Images were captured after 10 days of culture. (B) Van Gieson's staining at different time points showing deposition of immature elastin fibers (black color) network. (C) Masson's trichrome staining showing collagen deposition (Blue color). (D) Quantification of collagen deposition by SMCs cultured on mulberry and non-mulberry patterned silk films at different time points. (#p<0.05)*

3.3.12 Histology assessment of 3D vascular construct for cellular distribution and burst strength analysis

Gross morphology of matured vascular graft is shown in **Figure 3.13A-I**. Cross section of cell seeded construct after day 1 exhibited loosened multilayered structure (**Figure 3.13A- II**) whereas mature vessel construct after day 14 maintained a tubular morphology and cell seeded film layers remained cohesively bound (**Figure 3.13A-III**). Mature vascular conduit (after day 14) was assessed for cellular distribution by histology analysis. Deparaffinized sections were directly stained with Hoechst 33342 to locate cells in the mature rolled assembly. Fluorescent microscopic images revealed homogenous distribution of vascular cells throughout the circular tissue section

(**Figure 3.13A, IV-VI**). Retention of cells after rolling step verifies the applicability of this procedure.

Mechanical strength of the silk film based acellular vascular construct was determined in terms of burst strength so as to check if it sustains physiological blood pressure. Burst pressure ranged between 915-1260 mmHg for tubular constructs made up of different silk varieties under hydrated conditions and no significant difference was observed among different experimental groups (**Figure 3.13B**).

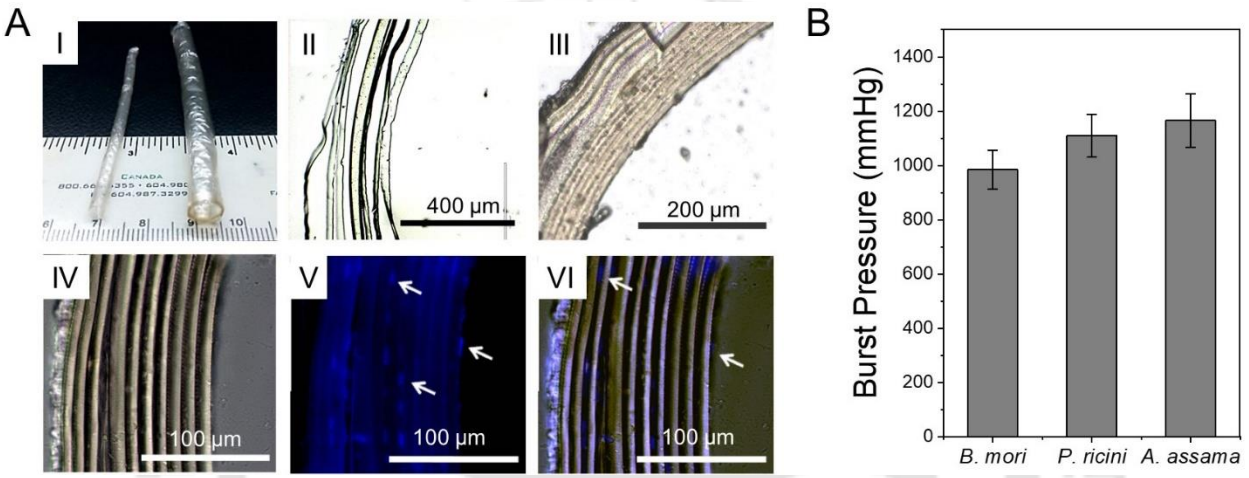

Figure 3.13. *(A) Histological analysis of mature small diameter vascular construct. (I) Gross view of vascular graft. (II) Bright field image of graft cross section after day 1 of cell seeding depicting loosened multilayer structure. (III) Cross-section of matured vascular graft after 14 days of cell seeding showing maintenance of graft integrity films due to ECM secretion. Deparaffinized sections of matured graft were stained with Hoechst 33342 to locate cellular distribution of vascular cells - (IV) Bright field unstained, (V) Fluorescent microscopic Hoechst 33342 stained (blue color) and (VI) Merged view of the graft cross section. (B) Burst pressure of silk film based acellular vascular tubes.*

3.4 Discussion

Silk, being the ancient material having superior mechanical properties has long been used as a suture material and still continues even after the availability of myriad of synthetic materials available in the market [10]. Apart from load bearing applications, silk is currently emerging as one of the most promising material in the field of tissue engineering. Ability of silk to support the growth of vascular cells projects it as a potential biomaterial for vascular tissue engineering applications [281, 282, 305]. Mimicking the native geometry of blood vessel is also a crucial aspect in the field of vascular tissue engineering. It requires directionally aligned cells to maintain the cellular phenotype. Ability of silk to obtain desirable patterns even at micro and nano level makes

it an apt choice for vascular tissue engineering application [306, 307]. Our overall aim for preparing SDVG is to biomimic the cellular geometry and architecture of native blood vessel. Herein we used pattern silk films from three different silk varieties in combination with all three vascular cells. Patterned silk films were used as template for cell sheet engineering which would be advantageous over latter in many aspects discussed previously.

Integration of implanted graft with native body tissue is crucial for its successful implementation into various tissue engineering aspects. Among other properties, it requires a controlled rate of degradation so as to maintain equilibrium with the growth and maturation of native tissue *in vivo*. In this regard, silk serves as an ideal material due to its controlled slow rate of degradation whereas simultaneously maintaining tissue integrity. *In vitro* degradation profile of silk films from all three silk varieties suggested structural integrity in PBS and only ~6-8% wt. loss was recorded even after 28 days. This long term integrity may be attributed to presence of β-sheet resulting from water annealing as evidenced by FTIR data. Structural integrity of silk logged in this study was in accordance with the prior reports. Moreover, lesser water holding capability of non-mulberry silk varieties is directly co-related with the presence of higher extent of hydrophobic amino acid residues [292, 308]. Hence, considering the structural inequity among different silk varieties, faster degradation of *B. mori* films might have resulted from its high water holding capability. It allows access to higher extent of proteolytic enzyme to interact with native structure. Enomoto *et al.* have demonstrated successful replacement of rat aorta with custom made silk based vascular graft with acceptable patency that was subsequently replaced by an artery like structure within 1 year tenure [189]. SF fibers retained more than 50% of initial mechanical strength two months after their *in vivo* implantation [309]. Degradation of biomaterials under *in vivo* conditions is a complex phenomenon that involves various synergistic pathways of biochemical and mechanical origin. *In vitro* enzymatic degradation may provide a clue regarding the functional interaction of biopolymer with the biological environment. Li *et al.* investigated the degradation response of porous silk films in the presence of protease XIV, collagenase 1A and α-chymotrypsin [310]. Study demonstrated maximum degradation in presence of protease XIV owing to non-specific activity of this enzyme towards chemical structure and amino acid sequence. Mimicking *in vivo* conditions more closely entails concurrence of several enzymes (chymotrypsin, collagenase, etc.) with specific amino acid sequence for their activity. Instead of using several enzymes in order to speculate about *in vivo* biodegradation of silk films, we opted for protease

XIV despite its absence in human body. Several reports also attest that non-specific proteolytic activity of protease XIV would show higher degradation and might simulate the synergistic effect of several enzymes with specific activity [303, 309, 311]. This would help to understand the stability of biomaterial under harsh enzymatic *in vivo* conditions. Non-mulberry silk films were comparatively more stable than mulberry silk in presence of protease. Outperformance of *P. ricini* and *A. assama* films may be attributed to differential molecular weight of heavy and light chains or amino acid content present as compared to *B. mori* silk. It has been reported that *B. mori* SF contains multiple repeats of AGSGAG that accounts for nearly 55% of total protein making the crystalline structure [237]. Moreover 30.2% alanine and 45.9% glycine make up majority of protein structure. The methyl groups of alanine are known to be arranged outside the protein backbone and exposed to external microenvironment [236]. On the other hand, the non-mulberry *P. ricini* SF's major constituent is poly alanine (47.9%) that remains in α-helix conformation and packed closely [308]. The differential composition of these two proteins might be the plausible reason for stability of non-mulberry silk owing to presence of greater percentage of hydrophobic amino acid residues leading to close packing and minimal exposure to external aqueous microenvironment. Additionally, AFM data suggested an increase in surface roughness of non-mulberry SF films that may contribute to better stability of these films [312]. Non- mulberry films (*A. assama*) also demonstrated superior mechanical properties and elasticity than that of mulberry silk. The distinctive feature of *A. assama* SF is presence of its poly alanine residues not intervened by any other amino acid. This feature makes it quite unique as compared to its other *Saturniidae* family members. Such characteristic properties mainly impart mechanical robustness to these films [239, 293].

An ideal biomaterial for any tissue engineering application should be minimally immunogenic. In this regard, we checked for mouse macrophage activity (in terms of TNF-α release) in response to silk films. The amount of TNF-α released in response to non-mulberry silk films were comparable with FDA approved *B. mori* silk [175]. Material safety was further confirmed by examining the *in vivo* immunogenic response (4 weeks) in a mice model for both mulberry and non-mulberry silk films. Tissue response towards silk films was assessed in terms of growing collagen fibrils orientation and fibroblast layers surrounding the silk films. Attached fibroblast layer and macrophages at tissue implant junction was observed for all silk varieties. Very mild response was observed (extent of macrophage infiltration) for non-mulberry silk that

was almost analogous with the *B. mori* silk which is known to be less immunogenic than collagen [176]. Moreover, degradation of silk produces small peptides and amino acids that are utilized by the surrounding cells to carry out their metabolic activities [146].

We further checked for cellular metabolic activity and attachment of vascular cells on silk films. Percentage AlamarBlue reduction, that directly co-relates with cell viability suggested better cellular proliferation on non-mulberry silk films. Results were in accordance with AFM data indicating superior proliferative capacity on rougher surface of *A. assama* and *P. ricini* films. It may also be attributed to availability of integrin binding RGD motifs present on surface of non-mulberry *A. assama* and *P. ricini* silk films [292]. More interestingly, growth pattern of adventitial fibroblasts profoundly favored silk films as compared to standard tissue culture plates that clearly indicate the importance of surface roughness and presence of RGD motifs on cell attachment and proliferation. Surface topography and chemistry is known to alter the cellular response. Cells with spread-morphology and well developed actin cytoskeleton survive better than cells with round morphology [313]. Staining of actin cytoskeleton of aligned vascular cells with rhodamine-phalloidin revealed strong color intensity hence well-developed actin fibers onto non-mulberry silk films. This may also be attributed to RGD availability and roughness. These findings were in agreement with previous reports [291].

Engineering of functional vascular tissue demands well grown endothelial cell layer to serve as the hemocompatible surface, reducing the chances of thrombosis [314]. Taking all these aforementioned limitations into consideration, fabrication of tissue engineered blood vessel primarily demands hemocompatibility of the biomaterial. Motivation of using silk to fabricate vascular construct was acquired by virtue of its antithrombotic properties [315]. We investigated latter by analyzing the reaction of silk films towards platelet adhesion and activation (LDH activity). Results showcased least activation of adhered platelets on to silk films. Also, further processing for stabilization of the silk films against water, we adopted water vapor annealing over other methods owing to its superior hemocompatibility [316]. In native artery, endothelial cells remain in quiescent state and aligned in the direction of blood flow hence form a continuous lining. These cells enter into the proliferative phase during an injury or diseased condition. One of the major hurdles in the field of vascular tissue engineering is proper endothelialization since most of the loosely attached cells detach under the influence of blood flow induced shear stress [317]. Under *in vivo* conditions after graft implantation, tissue engineered vascular grafts usually fail to

sustain the endothelial cell lining due to shear forces generated via blood flow [318]. Herein we have successfully shown a confluent monolayer of endothelial cells aligned along microgrooves on silk films. We hypothesize that parallel arrangement of cells along the flow direction might help them to resist shear forces and circumvent cell loss by presenting lesser surface area to the flow direction. Additionally, two layers of endothelial cell seeded films were wrapped to provide more congenial environment and reduce the chances of early stage thrombosis. Our findings of immunostaining also demonstrated strong expression of vWF in the cellular cytoplasm confirming the maintenance of endothelial cell phenotype on aligned silk film.

Another constraint of designing functional tissue engineered vascular graft is maturation of construct under pulsatile flow bioreactor for extended periods. Main aim behind this maturation is to align SMCs and extracellular matrix concentrically [319]. It also assists in transition from synthetic to contractile phenotype rendering superior strength and compliance of fabricated construct [320]. Major drawback of blood vessel maturation in a pulsatile bioreactor is that it requires long term (~3 months) maturation that reduces the chances of its clinical applicability. Also during the long span of construct maturation might cause cellular senescence [321]. Herein, we tried to explore whether SMCs in a confluent cell sheet cultured on patterned silk films exhibit contractile phenotype. Positive staining of SMCs for calponin and α-SMA (contractile genes) clearly suggested that cellular patterning on silk films substantially induces phenotype transition of SMCs towards contractile nature. Moreover, the contractile phenotype of SMCs was verified by upregulation of contractile gene expression (SM-MHC and α-SMA). Results were in accordance with previous reports [79]. Pre fabrication alignment was achieved in shorter span of time (~3-6 days) thus allowing rapid assembly of vascular construct making it apt choice for clinical applications.

Cross sectional analysis of tubular vascular construct after maturation exhibited evenly distributed cell population. Different silk film layers were found to stick together. This might be attributed to ECM formation responsible for keeping the silk films together and maintaining the tubular construct. For confirming the aforementioned, we checked the deposition of two major ECM constituents- Collagen and Elastin. Results exhibited a time dependent increment of ECM deposition by SMCs cultured on patterned silk films. Amount of collagen was found to be almost doubled within 10 days. Black *et al.* (2008) reported that incorporation of ECM proteins (collagen and elastin) improve the modulus and other mechanical properties of sheets [322]. Hence, it is

quite reasonable to assume that ECM deposition would not only help in maintaining graft integrity but also it would improve the mechanical compliance of fabricated graft.

To reduce the possibility of structural loss during washing and processing steps during H&E staining protocol, we opted for Hoechst 33342 staining that directly stains cell nucleus with minimal washing steps. Tubular constructs without cell was considered as control. Cross sectioning of the latter construct although exhibited consecutively arranged film layers but distinguishable gap was observed between film layers. These findings suggest that prolonged maturation (~14 days) of film based construct even under static condition helps maintaining the structure by holding the films together where secreted ECM acts as glue. On further analysis of burst pressure of mature tubular constructs, the pressure values were around 10 times more as compared to physiological pressure (120/80 mmHg) and around 5 times higher than above pathological pressure (180-220 mmHg) [323]. This attests the mechanical suitability of silk film based vascular grafts fabricated in the current endeavor.

A noticeable aspect that is usually considered as missing link while developing SDVG is engineering of internal elastic lamina (IEL). It is a fenestrated proteinaceous barrier that works as a basement membrane for luminal endothelial cell lining and allows the exchange of various soluble factors crucial for cell functioning. Most of the tissue engineered vessels were not able to synthesize sufficient elastin so as to maintain IEL type layer and it is usually neglected while fabricating any such graft [324]. Irregularity in the IEL layer might lead to various diseased conditions like atherosclerosis since it fails to restrict the infiltration of macrophages into the intimal layer of artery [325]. We hypothesize that strategy followed in this work might enable us to circumvent the aforestated issue considering the analogy of silk film present in between the cell sheet layers with IEL. We anticipate that methodology developed herein would be advancement towards cell sheet based engineering and improve the clinical applicability of fabricated SDVG.

3.5 Significant findings

1. In this work, facile approach is described to fabricate tissue-engineered vascular grafts for prospective application in coronary artery bypass surgery.
2. Coalescing of engineered cell sheet and patterned silk films through a simple rolling process is envisaged to assist the maintenance of graft integrity.
3. The mechanically robust constructs withstood physiological arterial pressure, forwarding the fabricated material for bypass grafting.
4. The patterned silk films supported unidirectionally aligned monolayer of metabolically active vascular cells, expressing functional phenotype.
5. This work attests better credentials to non-mulberry silk varieties (*A. assama and P. ricini*) in terms of stability, mechanical strength, vascular cell compatibility and minimal *in vivo* immunological response than the mulberry counterpart *B. mori* silk.
6. Future advancement in this direction may lead towards "off the shelf" clinical implementation of SDVG.

CHAPTER 4

Development of bi-layered tubular silk scaffolds consisting of inner porous freeze-dried layer coated with outer dense electrospun layer and their functional analysis in a rat aortic interposition model as cell-seeded vascular grafts

This chapter demonstrates a new fabrication methodology to develop a bi-layered tubular silk scaffold for vascular tissue engineering applications. The inner porous layer is designed to support cell growth and infiltration, while outer thin nanofibrous layer renders mechanical resilience. Human adipose derived SVF seeded TEVGs performed well in rat aortic implantation model. This approach is envisaged to provide a patient specific therapeutic option towards developing a clinically feasible vascular graft.

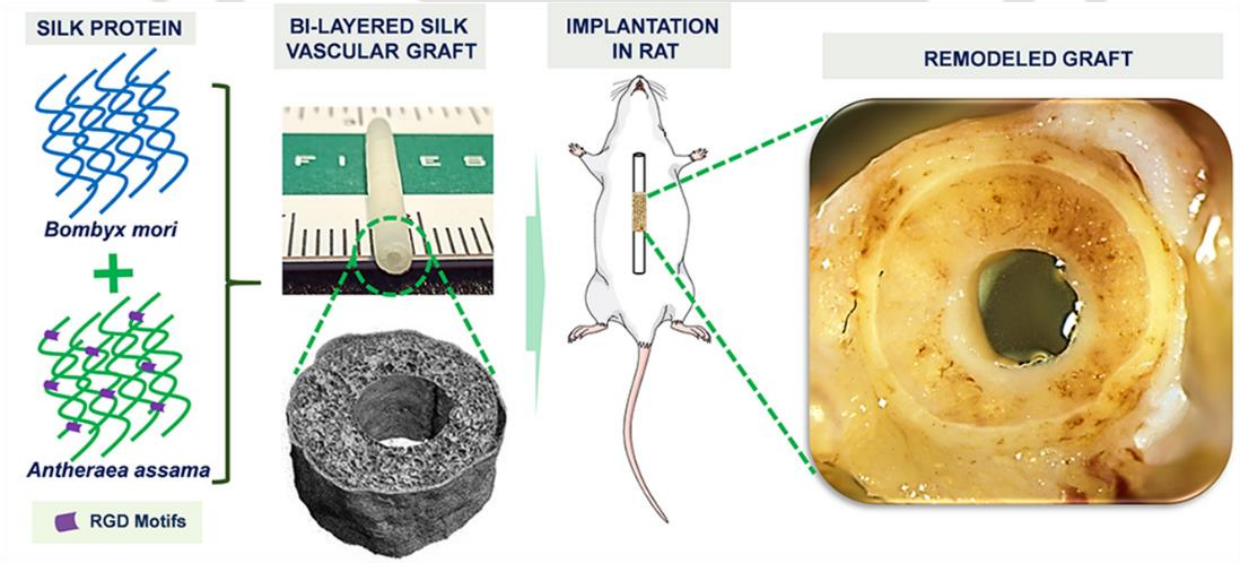

Publication:

***Prerak Gupta**, Katherine L. Lorentz, Darren G. Haskett, Eoghan M. Cunnane, Aneesh Ramaswamy, Justin S. Weinbaum, David A. Vorp and Biman B. Mandal. Bioresorbable silk grafts for small diameter vascular tissue engineering applications: In vitro and in vivo functional analysis. **Acta Biomaterialia**. 2020; 105: 146-158.*

ABSTRACT

The success of tissue-engineered vascular graft (TEVG) predominantly relies on the selection of a suitable biomaterial and graft design. Natural biopolymer silk has shown great promise for various tissue-engineering applications. This study is the first to investigate Indian endemic non-mulberry silk (*Antheraea assama*-AA) – which inherits naturally superior mechanical and biological traits (e.g., RGD motifs) compared to *Bombyx mori*-BM silk, for TEVG applications. We designed bi-layered biomimetic small diameter AA-BM silk TEVGs adopting a new fabrication methodology. The inner layer showed ideally sized (~40 μm) pores with interconnectivity to allow cellular infiltration, and an outer dense electrospun layer that confers mechanical resilience. Biodegradation of silk TEVGs into amino acids as resorbable byproducts corroborates their *in vivo* remodeling ability. Following our previous reports, we surgically implanted human adipose tissue-derived stromal vascular fraction (SVF) seeded silk TEVGs in Lewis rats as abdominal aortic interposition grafts for 8 weeks. Adequate suture retention strength (0.45 ± 0.1 N) without any blood seepage post-implantation substantiate the grafts' viability. AA silk-based TEVGs showed superior animal survival and graft patency compared to BM silk TEVGs. Histological analysis revealed neo-tissue formation, host cell infiltration and graft remodeling in terms of extracellular matrix turnover. Altogether, this study demonstrates promising aspects of AA silk TEVGs for vascular tissue engineering applications.

4.1 Introduction

Cardiovascular disease (CVD) remains the primary cause of death globally and coronary artery disease (CAD) is the most prominent form of CVD [1]. The main cause of CVD is occlusion of blood vessels, which restricts blood supply to vital organs. Current treatment options rely on surgical revascularization by either stent placement or implantation of an interposition graft to bypass the occlusion. In the case of coronary artery bypass surgery, surgeons commonly use the saphenous vein; however, removal of the vein causes significant donor site morbidity. Moreover, limited availability of autologous grafts restrict their application [4]. Therefore, an urgent need exists to identify a viable option for bypass of occluded small diameter vessels. Tissue engineered vascular grafts (TEVGs) have recently made remarkable progress. The fundamental difference between conventional vascular grafts and current approaches to graft development is the biodegradability of the polymer. In 1980s, Weinberg and Bell fabricated a collagen gel based tubular graft for vascular tissue engineering [9]. Since then, a number of biodegradable natural/synthetic polymers have been investigated as 'off the shelf' vascular grafts. Poly (lactic acid) [PLA] and poly (glycolic acid) [PGA], along with their various co-polymers, are a popular choice for vascular tissue engineering applications owing to their tunable mechanical and degradation properties [36]. Despite several advantages, these synthetic polymers have a number of drawbacks including their moderate biocompatibility and acidic degradation products [326].

Among several natural polymers used for tissue engineering applications, the structural protein silk has shown great potential. The advantages of using silk for vascular tissue engineering include its appropriate mechanical properties, tunable degradation producing non-toxic by-products and good biocompatibility [114, 116, 327, 328]. Lovett and colleagues first reported the fabrication of silk fibroin microtubes using dip coating method [281] followed by a gel spinning process to fabricate silk-based tubular grafts. In this study, the dip coating was not automated and therefore did not provide uniform wall thickness. However, the gel spun tubes demonstrated good patency and host cell infiltration at 4 weeks *in vivo* [158, 282]. Recent studies suggest that there are several scaffold design parameters – such as porosity, pore size and other properties, which determine the performance of TEVGs [329]. Hence, it becomes crucial that the graft design should be flexible in terms of these parameters. The major limitation with gel spun tubes is that they are minimally flexible with alteration of pore size owing to use of very high percentage of silk protein (~25-35%, w/v), leading to smaller pore size [282]. Braided silk fiber-based tubes have also shown

promising results but exhibit prohibitively slow degradation and remodeling *in vivo* [189]. Furthermore, they posed several other complications including sub-optimal anastomotic strength and tube permeability leading to blood leakage [194, 330]. Electrospun silk grafts are mechanically suitable but they are limited due to small pore size, which prohibits host cell infiltration and graft remodeling [283]. A recent study has demonstrated rapid endothelialization of electrospun silk vascular grafts in a rat model [202]. In Chapter 3, we have constructed silk vascular grafts based on layering patterned silk films with vascular cells. Although this method produced cell and fiber alignment that mimics the native vessel architecture, the mechanics (e.g. suture retention) were inadequate to evaluate these grafts *in vivo*. Prior literature clearly validates the use of silk fibroin as a natural biomaterial for vascular tissue engineering applications and suggests that further advancement is required in terms of flexibility with graft design parameters.

Despite being the common method for fabricating porous silk scaffolds, direct implementation of the freeze-drying (lyophilization) process alone has not been reported previously for preparing silk-based TEVGs. This is possibly due to the limitation of the lyophilization technique, which is suitable for nearly 1 cm working depth, posing scaffold length constraints. In the present study, we were able to overcome this limitation by using a specific 3D printed mold (**Figure 4.1**) and following a new facile fabrication methodology (**Figure 4.2**).

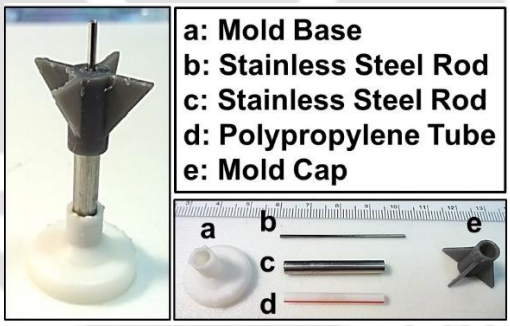

Figure 4.1. *Custom made 3D printed mold used for fabrication of inner porous layer of tubular silk scaffold. Polypropylene tube was inserted in the stainless steel tube, which helps in easy removal of silk scaffold post lyophilization.*

We adopt a molding approach followed by conventional lyophilization to obtain the porous tubular core, which is further coated with an outer electrospun layer to yield mechanically resilient, bi-layered silk fibroin conduits. Our approach provides several additional features over previously reported techniques including precise control over porosity, uniform wall thickness and reproducibility.

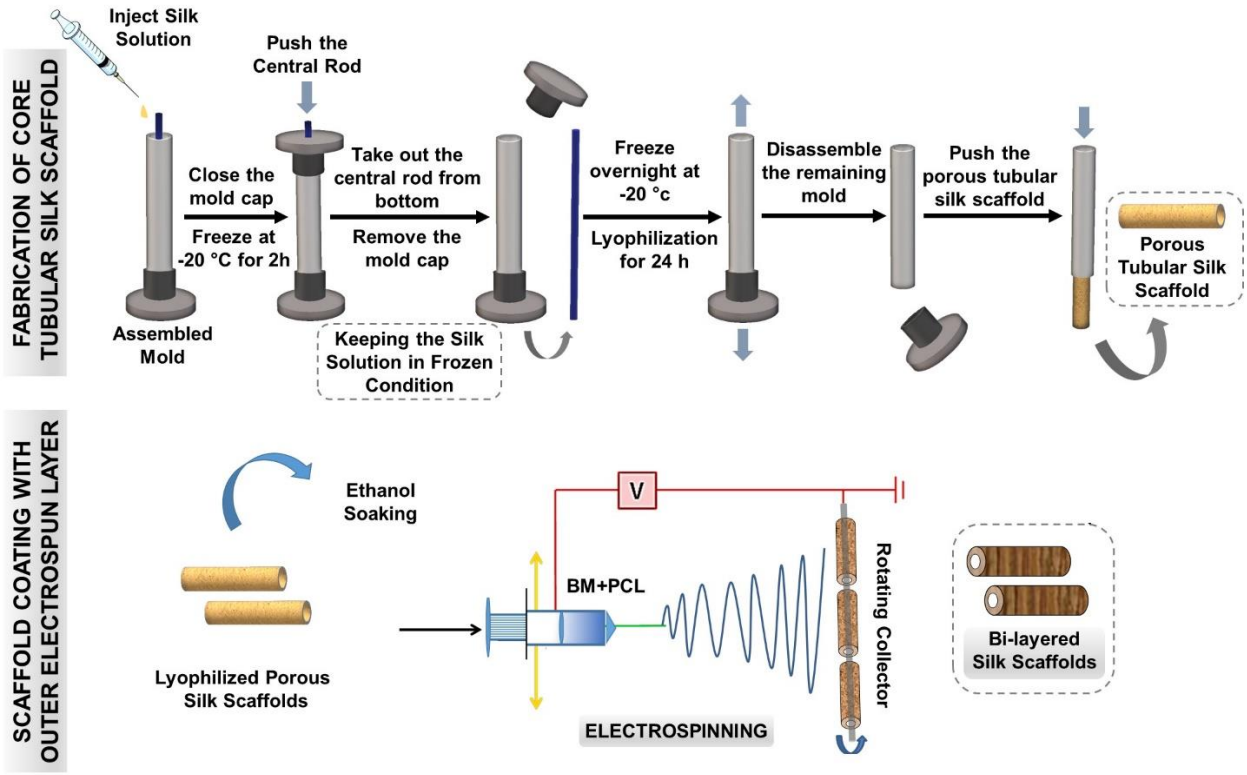

Figure 4.2. *Schematic representation of fabrication methodology of bi-layered small diameter silk scaffolds. The inner porous layer is prepared by molding and lyophilization based approach followed by coating with an outer nanofibrous electrospun layer.*

Bi-layered silk grafts fabricated in the present study are morphologically biomimetic having inner porous layer similar to tunica media and outer fibrous electrospun layer mimicking adventitia. It may also provide flexibility with various graft design parameters (e.g. tunable degradation and mechanical properties). Moreover, all prior studies report the use of mulberry *Bombyx mori* (BM) silk in various formats; but non-mulberry Indian endemic *Antheraea assama* (AA) silk is unexplored in the field of vascular tissue engineering. Our previous *in vitro* studies using 2D films suggest that AA silk supports vascular cell growth and functionality (described in Chapter 3); moreover, it has superior mechanical/elastic properties owing to its unique molecular architecture (polyalanine repeats without any intervening amino acid) [331]. Another unique advantage of AA silk is the natural presence of RGD (Arginine-Glycine-Aspartic acid) peptides, which have been shown to reduce acute thrombosis *in vivo* [155]. In the present study, we adopted a new facile methodology to fabricate silk TEVGs and attempted to explore the use of AA silk in combination and compared with BM silk *in vitro* and *in vivo* in a rat aortic interposition graft model over eight weeks.

4.2 Materials and methods

4.2.1 Isolation of silk protein

Silk fibroin (SF) protein was obtained from two different sources: mulberry *Bombyx mori* (BM) silk cocoons and non-mulberry *Antheraea assama* (AA) silk glands following previously described protocols [332]. Silk worms and cocoons were procured from a local farmhouse. BM cocoons were chopped into small pieces, degummed in 0.02M Na_2CO_3, dissolved in 9.3M LiBr (Sigma-Aldrich, USA) and dialyzed against distilled water to obtain regenerated SF protein. In contrast with BM silk, the aqueous AA silk was obtained directly from silk glands because AA silk fibers are insoluble in LiBr [118]. AA SF was obtained from silk glands and dissolved in 1% sodium dodecyl sulfate (SDS, Sigma-Aldrich, USA) followed by dialysis at 4°C against milli-Q water. SF protein solutions were stored at 4°C until use.

4.2.2 Scaffold fabrication

Two variants of bi-layered silk scaffolds were fabricated consisting of an inner lyophilized porous layer and outer electrospun layer. For the first scaffold type, we used only BM protein (6% w/v) to fabricate the inner lyophilized porous layer. The higher concentration (>3-4%, w/v) of AA silk forms hydrogel at physiological temperature. Hence, for the second scaffold type, we used a combination of BM and AA proteins (1:1 ratio of 10% BM protein and 2% AA protein (w/v) keeping 6% final protein concentration). In a previous report, we have shown that the aqueous solutions of BM and AA silk forms homogenous solution, which could be used for fabrication of blend scaffolds [333]. Tubular scaffolds were fabricated using custom-made 3D printed molds as illustrated in **Figure 4.1** and **Figure 4.2**. Our mold consisted of 3D printed base/cap, a polypropylene tube (3 cm long), stainless steel rod (1.1 mm diameter, 4 cm long) and a stainless steel cylinder (2 mm internal diameter, 3 cm long). Silk fibroin (SF) solution was injected into the void space between the central rod and polypropylene tube using a syringe followed by freezing in a -20°C freezer for 2h. The central rod and cap were removed rapidly (avoiding any possible melting of SF) to expose the lumen of the frozen SF solution. The mold was kept at -20°C overnight and lyophilized for 24h. The lyophilized porous SF tubular scaffolds were pushed out from the mold and soaked in 80% (v/v) ethanol to induce water stability.

The outer electrospun layer was coated onto the wet (ethanol soaked) lyophilized inner layer. The electrospinning solution consisted of 1:1 (v/v) ratio of 10% w/v polycaprolactone

(average Mn 80,000, Sigma-Aldrich, USA) and 10% (w/v) BM silk in 1,1,1,3,3,3-Hexafluoro-2-propanol (HFP, Sigma-Aldrich, USA). The ethanol soaked tubular scaffolds were mounted on a stainless steel mandrel (diameter 0.8 mm). The outer electrospun layer was fabricated using a custom-made electrospinning set-up described previously [334]. The following parameters were used for electrospinning: flow rate (100 µL/min), tip to collector distance (10 cm), applied voltage difference (15 kV), rotational speed (200 rpm), translational speed (50 mm/sec), temperature (~25°C) and humidity (~47%). Two scaffolds were coated per cycle with 300 µL electrospinning solution. Bi-layered scaffolds were stored in 80% ethanol until use at 4°C. Scaffold variants are designated as follow: 1) BM: inner porous layer made up of BM protein, without electrospun layer; 2) BMES: BM scaffold with outer electrospun layer; 3) BA: inner porous layer made up of 1:1 v/v ratio of 10% (w/v) BM protein and 2% (w/v) AA protein, without electrospun layer; 4) BAES: BA scaffold with outer electrospun layer.

4.2.3 Scanning electron microscopy (SEM) and micro-CT analysis

Vertical and horizontal sections of bi-layered silk scaffolds (exposing lumen and cross-section) were sputter coated (Sputter Coater 108 auto, Cressington Scientific Instruments, Cranberry Township, PA) and imaged under scanning electron microscope (SEM, JEOL JSM-6510LV/LGS). Scaffold dimensions (inner and outer diameter, thickness of porous and electrospun layer) were measured using ImageJ (National Institute of Health, USA). A total of 10-15 measurements were recorded for n=3 samples of each scaffold variant. Silk scaffolds were further subjected to micro-CT imaging on a Scanco microCT 50 (Scanco Medical, Bassersdorf, Switzerland) scanner at a nominal resolution of 1.2 µm and a beam energy of 45Kvp (high contrast conditions). The scaffolds were scanned individually without a liquid medium. 3D volumes were reconstructed from the raw data using the Scanco software, which also performs an automatic calibration of the images for mineral density using built-in algorithms for the particular scanning conditions. The Scanco 3D Bone Morphometry software was used to define the scaffold region and subsequently process the 3D volume. A 0.3 g/cc global threshold was used for segmentation of the strut material from the background. The geometric properties reported are pore volume fraction inside the scaffold, means and distribution of pore size. Each of these properties were calculated individually for inner freeze dried porous and outer electrospun nanofibrous layers.

4.2.4 Analysis of mechanical properties

4.2.4.1 Uniaxial (longitudinal and circumferential) tensile testing

All of the mechanical data for silk scaffolds was obtained using phosphate buffered saline (PBS) soaked wet scaffolds. Uniaxial tensile tests were performed using a tensile testing device with pneumatic grips (Instron, model 5543A). For longitudinal tensile testing, 3 cm long scaffolds (n=6) were cut open through the lumen to form a strip and both ends were clamped between pneumatic grips leaving ~2 cm gauge length. While clamping, precautions were taken to keep both of the scaffold ends flat in order to ensure uniform load distribution throughout the scaffold wall. Specimen length and width were recorded using a digital caliper (Thermo Fisher Scientific, Waltham, MA); whereas effective thickness of specimens was calculated by processing SEM images using ImageJ software. Load-displacement curves were obtained at room temperature with a crosshead speed of 2 mm/min until failure. For circumferential tensile testing (ring test), scaffold rings (n=12 each) were cut (2 mm length) and a previously described protocol was followed with minor modifications [335]. Elastic modulus of bi-layered silk scaffolds in both directions was calculated as the slope of the stress-strain curves in the low and high stress regions and is represented as low and high modulus respectively as described previously [336]. The transition point between low and high stress regions was defined as the point having maximum normal distance from the global secant. Maximum stress and strain values were also recorded at the failure point.

4.2.4.2 Suture retention strength

Suture retention strength of silk scaffolds was determined following American National Standard Institute–Association for the Advancement of Medical Instruments (ANSI/AAMI) VP20 standards [337]. Scaffolds were cut open longitudinally to obtain rectangular strips (n=6, length=20 mm). A single 7-0 polypropylene (SURGIPRO™ II, Syneture) suture was used to create a single loop ~2 mm away from the end. The free ends of the suture were first secured using laboratory labeling tape (Fisher Scientific) keeping scaffold at the center of the loop and the tape was further clamped in the upper pneumatic grip of tensile testing device (Instron model 5543A). Another end of the scaffold strip was secured in the lower grip and any slack was removed prior to recording the data. Load-displacement curves were obtained at a crosshead speed of 2 mm/min until failure. The maximum load prior to scaffold tear-off is reported as suture retention strength. Suture retention

tension was calculated by dividing the suture retention force by scaffold thickness as previously reported [337].

4.2.4.3 Dynamic compliance

A custom-made vascular perfusion system was used to analyze dynamic compliance of the silk scaffolds as described previously [337]. In brief, the perfusion system consisted of a flow loop and a centrifugal pump (Biomedicus) that provides pulsatile flow and induces physiologically relevant intraluminal pressure (120/80 mmHg). A He–Ne laser micrometer (Beta LaserMike, Dayton, OH) was used for real time measurement of the scaffold's outer diameter under the influence of pulsatile flow. The silk scaffolds (n=6) were mounted in a testing chamber and both ends were secured to stainless steel mounts using a 3-0 silk suture. The flow loop and testing chamber were filled with DI water. The intraluminal fluid was maintained at 37°C. A pulsatile flow was induced in the flow loop using the centrifugal pump and a physiological intraluminal pressure of 120 mmHg over 80 mmHg was maintained with minimal or no leakage from scaffold wall. Pressure and outer diameter of the scaffolds were recorded for 7h. For calculating the dynamic compliance, measurements of scaffold inner diameter (ID) were derived by assuming incompressibility of the scaffold wall under dynamic flow conditions as follows:

$$\text{Inner diameter } (\text{ID}_\text{P}) = 2 * \sqrt{\left(\frac{\text{OD}_\text{P}}{2}\right)^2 - \frac{\text{A}}{\pi}}$$

ID_P = Scaffold inner diameter at physiological pressure; OD_P = Scaffold outer diameter at physiological pressure recorded using laser micrometer; A = Cross-sectional area of the scaffold wall calculated by processing the SEM images using ImageJ software.

The inner diameter values were used to calculate the dynamic compliance of the silk scaffolds using the following expression:

$$\text{Dynamic compliance } (\text{C}) = \frac{(\text{ID}_{120} - \text{ID}_{80})}{\text{ID}_{80}} \frac{1}{\text{P}_{120} - \text{P}_{80}}$$

Where ID_{120} = Scaffold inner diameter at 120 mmHg intraluminal pressure; ID_{80} = Scaffold inner diameter at 80 mmHg intraluminal pressure; P_{120} = 120 mmHg; P_{80} = 80 mmHg

Scaffold dilation under dynamic pulsatile flow was also calculated in order to assess any possible plastic deformation with time. The recorded average outer diameter of the scaffold at the

end of 7h of pulsatile flow was divided by initial diameter to calculate creep. Furthermore, β-stiffness at the initial and final time point was calculated using the following expression:

$$\beta \text{ stiffness} = \frac{\ln\left(\frac{P_{120}}{P_{80}}\right)}{\left[\frac{(OD_{120} - OD_{80})}{OD_{80}}\right]}$$

4.2.4.4 Burst strength

The burst strength of silk scaffolds (n=6) was measured by recording the maximum pressure sustained without failure (bursting). A custom-made set-up was used as described previously [337]. Briefly, both ends of the scaffolds were secured on stainless steel tubes (fixed in the flow loop test chamber) using 3-0 silk sutures. One of the stainless steel tubes was connected to a syringe pump (Harvard Apparatus, Holliston, MA) and a digital manometer (pressure range 0-60 psi, Weiss), while the other tube was blocked making it a closed loop. The working chamber was filled with saline to submerge the specimen and scaffolds were infused with saline at a rate of 100 mL/min until failure. Maximum pressure before scaffold failure was recorded and considered as burst pressure.

4.2.5 *In vitro* degradation analysis of scaffolds

BMES and BAES tubular scaffolds (n=4, length: 1.5 cm) were further assessed for *in vitro* enzymatic degradation in the presence of protease XIV (Sigma-Aldrich, USA) following a previously described methodology [333]. Dry weight of the scaffolds was recorded initially and each scaffold was submerged in 1 mL of enzyme solution (2U/mL in PBS). In another set, scaffolds were submerged in PBS without the enzyme (negative control). Scaffolds were maintained at 37°C and enzyme solution was replaced every 72h to ensure proper enzyme activity throughout the experiment. In a similar parallel experimental set-up, smaller silk scaffold sections (~2 mm length) were kept in PBS and protease, which were subsequently subjected to SEM imaging. At pre-defined time points, the scaffolds were washed with de-ionized (DI) water, frozen at -20°C overnight and lyophilized. The dry weight of the scaffolds at each time point was recorded followed by continuation of enzymatic treatment. Scaffold weight was recorded for 28 days (excluding freezing and lyophilization time) and percentage of mass remaining was calculated as:

$$\% \text{ mass remaining} = \frac{Mt}{M0} \text{ x } 100$$

Mt = Scaffold dry weight at time t, M0 = Initial dry weight of scaffold

4.2.6 Scaffold seeding with SVF cells and dynamic culture

SVF cells were isolated from nondiabetic female human patients, under the age of 40 years and undergoing liposuction following previously described protocols [338, 339]. Tubular bi-layered silk scaffolds were seeded with SVF cells using a custom-made rotational vacuum seeding device as described previously [337, 338, 340]. The intraluminal pressure was measured in real time and scaffolds showing high pressure (>25 mmHg) were not used for animal implantation. The seeded constructs were transferred to a 500 mL spinner flask (Kontes #Cytostir 882911-0250) containing 100 mL culture media and subjected to dynamic culture at 80 rpm for 48h. These scaffolds were further used for rat aortic implantation (see "*In vivo* implantation in rat and angiogram recording").

Viability and metabolic activity of SVF cells cultured on silk scaffolds was quantified in a time dependent manner for 15 days using AlamarBlue assay (Thermo Fisher Scientific, USA) [234]. Porous lyophilized silk scaffold discs (6 mm diameter, 2 mm thickness) were seeded with SVF cells (~10^5 cells) and analyzed for cell viability over time. At each time point, media was replaced and AlamarBlue dye was added at 1:10 (dye: media, v/v) ratio followed by 3h incubation. The resulting media was read at 570 nm and 600 nm and % Alamar reduction was calculated using an online colorimetric calculator. Data is reported as normalized values compared to day 1.

4.2.7 *In vivo* implantation in rat and angiogram recording

We used 23 adult Lewis rats (average weight ~200 g) and divided them in 4 groups. First and second groups (n=3 each) were negative control and received acellular BMES and BAES scaffolds respectively. The third group (n=9) received SVF seeded BMES scaffolds (BMES + SVF), and the fourth group (n=8) received SVF seeded BAES scaffolds (BAES + SVF). Two of the rats from the second group and 1 from the fourth group) were euthanized prior to completion of experimental period due to surgical error and excluded from the study. Other animals were sacrificed either after 1 week or after 8 weeks to retrieve the implanted silk graft. All animal surgical procedures were performed in accordance with a protocol approved by University of Pittsburgh Institutional Animal Care and Use Committee (IACUC). Ethylene oxide sterilization may negatively affect the cell proliferation [341]; therefore, silk scaffolds were sterilized using 70% ethanol (v/v) followed by washing with PBS and overnight conditioning with culture media. SVF seeded silk scaffolds (1

cm long) obtained after 48h dynamic culture were surgically implanted as abdominal aortic interposition grafts in male Lewis rats following previously described protocols [338, 339, 342]. Animals were sacrificed after either 1 week or 8 weeks. *In vivo* graft patency was analyzed by recording angiograms soon after animal sacrifice.

4.2.8 Histological analysis of explanted TEVGs

Explanted tissue engineered vascular grafts (TEVGs) were fixed in 4% paraformaldehyde and subjected to histological analysis to observe cell and ECM distribution. Samples were cut into proximal, middle, and distal tissue blocks determined upon explant. Sections from the middle portion were used for all IHC (Immunohistochemistry) and IFC (Immunofluorescence) analysis. Five micron TEVG sections were mounted on slides and processed for immunostaining using previously described protocols [338, 339]. Briefly, tissue sections were permeabilized using 0.1% Triton X-100 (v/v) followed by blocking in 1% fetal bovine serum (FBS, v/v). Primary antibodies used for this study include mouse anti-smooth muscle α-actin (α-SMA, 1:500 dilution, Abcam), rabbit anti-calponin (1:500, Abcam), fluorescein isothiocyanate (FITC) conjugated mouse anti-von Willebrand factor (vWF, 1:250, US Biological, Salem, Mass) and mouse anti-cluster of differentiation 68 (CD68, 1:250, Abcam). The corresponding secondary antibodies used were FITC-conjugated goat anti-rabbit IgG (1:1000, Rockland Inc) and Cy5 conjugated goat anti-mouse IgG (1:1000, Abcam). Cell nuclei were counterstained using DAPI (Sigma-Aldrich, USA). Each section was imaged for DAPI (blue) and cell specific markers (green) which were overlaid for clear visualization of positive staining.

TEVG explants and native rat aorta were also investigated for cell, collagen and elastin distribution using H&E, Picro-Sirrus-Red and Verhoeff van Gieson staining respectively. Staining was performed at Histology Core at the McGowan Institute for Regenerative Medicine using 5 μm TEVG sections. Stained sections were imaged using a Nikon 90i fully automated upright microscope.

4.2.9 Collagen and elastin quantification

The collagen and elastin contents of explanted patent silk scaffolds at both 1 and 8 weeks was determined using a hydroxyproline assay and ninhydrin assay respectively. Due to the limited patency of some groups, a maximum of 2 explanted grafts per group was analyzed, with n=3 tissue

samples per graft. The hydroxyproline assay indirectly measured the collagen content of each sample using acid hydrolysis followed by treatment with chloramine-T and p-dimethylaminobenzaldehyde (p-DMBA) solutions [343]. The same tissue sample was used to measure elastin, collagen and total protein using a previously published protocol [344]. Both collagen and elastin quantities are reported after normalizing to the total protein content of each tissue segment. A segment of native rat aorta was also processed as a positive control.

4.2.10 Image processing

Fiji-ImageJ (National Institute of Health, USA) software was used to process the IFC images. For calculating the total number of cells infiltrated in the scaffold at different time points, 15 randomly selected DAPI stained images (10X) obtained from different sections of the scaffolds (n=3) were processed. The number of nuclei was calculated using the preset 'analyze particles' plugin (ImageJ) which applied a threshold to the circularity range and average area parameters of the cell nuclei (eliminating silk scaffold auto fluorescence and background noise). Furthermore, in order to estimate the presence of CD68 positive cells (representing macrophages) at 1 and 8-week time points, we calculated the percentage of fluorescent area in the scaffold wall stained positive for anti CD68 antibody. A total of six fluorescence images per scaffold variant with randomly selected regions of interest were implemented for this analysis. Silk scaffold auto fluorescence was eliminated using the aforementioned thresholding plugin.

The lumen diameter and wall thickness of the silk scaffolds before and after implantation was also calculated. Scaffold images obtained from SEM prior to cell seeding were used to calculate the lumen diameter and wall thickness before implantation. Moreover, H&E stained images were processed for 1 week and 8 week explants. A minimum of six images per scaffold (n=3) were processed manually by a blinded investigator and results are represented as average value with standard deviation.

4.2.11 Statistical analysis

All experiments were performed for at least n=3 samples unless otherwise noted. All data is reported as mean ± standard deviation (SD). One-way analysis of variance (ANOVA) was performed following post hoc Tukey's test using Origin 8.0 software. p values are reported for all the experiments. Two groups with at least $p<0.05$ were considered significantly different.

4.3 Results

4.3.1 Morphometric analysis

SEM micrographs of scaffold cross sections validated the presence of two distinct layers: inner porous lyophilized layer and outer electrospun layer. Scaffolds had an inner porous layer thickness of 598 ± 53 μm and outer electrospun layer thickness of 119 ± 24 μm, totaling 718 ± 65 μm thickness for the bi-layered scaffold wall. The inner diameter of scaffolds was 918 ± 82 μm. The outer electrospun nanofibrous layer was firmly adhered to the core layer without any visible delamination. The SEM micrographs also demonstrated open interconnected pores at the scaffold cross-section and throughout the lumen (**Figure 4.3A**). Micro-CT data suggested heterogeneous pore size distribution for inner porous layer of BMES and BAES scaffolds ranging 53 ± 30 μm and 43 ± 24 μm respectively. Overall porosity of inner layer was 91.63 ± 1.25% and 87.83 ± 2.14% respectively for BMES and BAES scaffolds (**Figure 4.3B, C**) ($p<0.05$). The pore size of outer nanofibrous electrospun layer was 5 ± 2 μm **(Figure 4.3D, E)**. The porosity of outer electrospun layer was 41.5 ± 4.94 for both scaffold types, which was significantly lower than inner layer ($p<0.01$).

4.3.2 Mechanical properties

Stress-strain curves showed that the addition of an electrospun layer (BMES and BAES) alters the mechanical response curves of the scaffolds (**Figure 4.4A-D**). For longitudinal testing, higher stress at failure was noted for scaffolds with an electrospun layer (BMES and BAES, 0.34 ± 0.70 MPa and 0.36 ± 0.08 MPa respectively) as compared with BM and BA scaffolds (0.12 ± 0.02 MPa and 0.10 ± 0.01 MPa respectively) ($p<0.01$). However, BMES/BAES ($p=0.987$) and BM/BA groups ($p=0.986$) were comparable. BA scaffolds showed higher strain at failure than BM/BMES ($p<0.01$) (**Figure 4.5**). The addition of an electrospun layer increased the scaffold modulus in the low stress region and BAES showed a significantly higher values than BMES scaffold ($p=0.004$). No significant difference was observed in high modulus across any group ($p>0.01$) (**Figure 4.4E-F**). A similar trend was observed for circumferential tensile testing of scaffolds and the addition of the electrospun layer improved the stress at failure ($p<0.01$). In addition, no significant difference among the groups was observed for strain at failure ($p>0.01$) (**Figure 4.5D**). In contrast with the longitudinal testing, no significant difference was noted for scaffold modulus in the low stress regions among the groups ($p>0.01$); however, addition of the electrospun layer increased the

scaffolds' modulus in the high stress region. BMES scaffolds showed the maximum high modulus (0.31 ± 0.04 MPa) and was significantly increased compared to BAES (0.21 ± 0.04 MPa, p=0.0023), BM (0.05 ± 0.01 MPa, p<0.01) and BA (0.08 ± 0.02, p<0.01) scaffolds (**Figure 4.4G-H**).

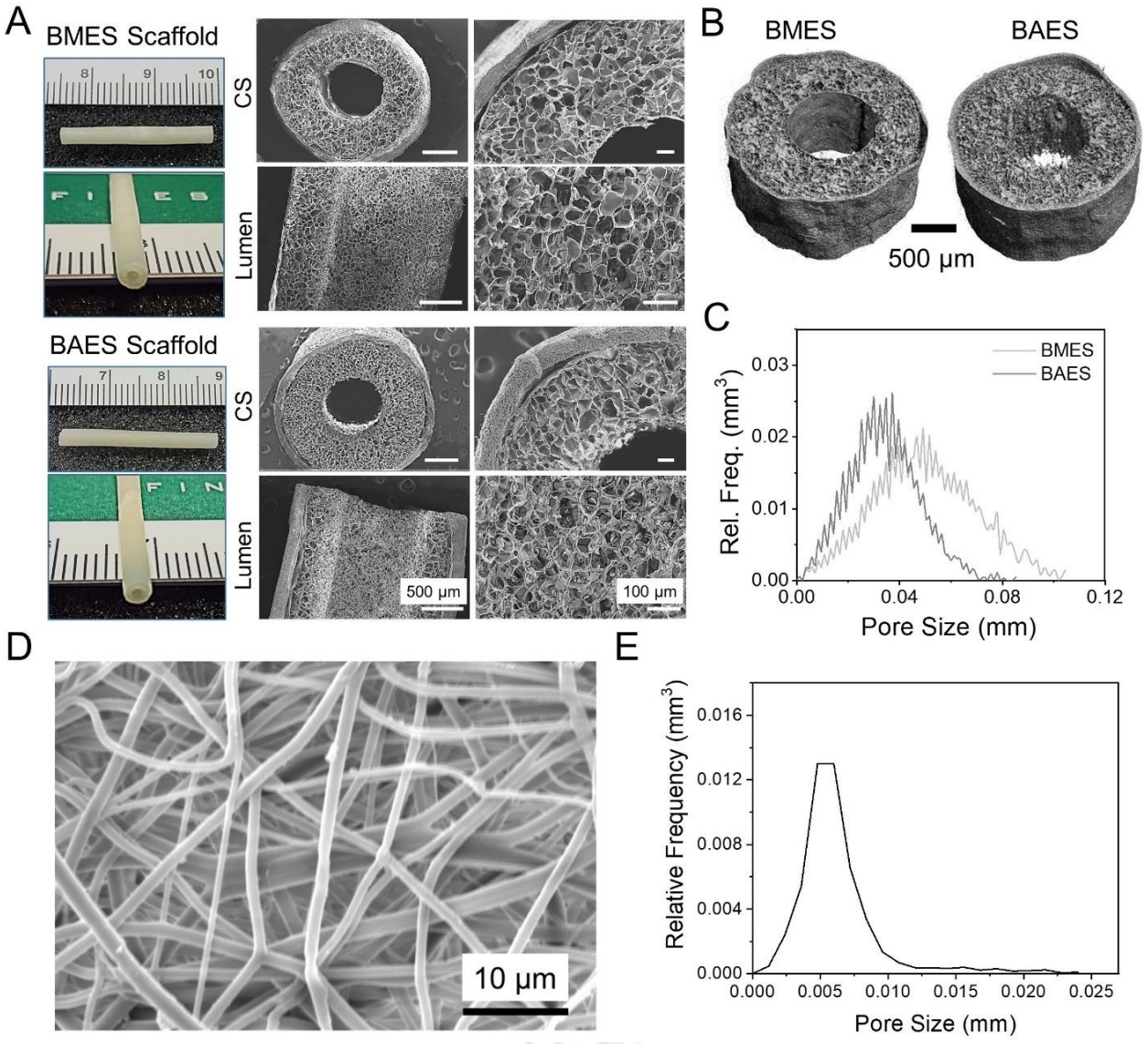

Figure 4.3. *Morphometric analysis of bi-layered silk scaffolds. (A) Representative images of tubular silk scaffolds and SEM micrographs showing internal porous architecture (CS: cross-section and lumen). Micro-CT analysis of tubular silk scaffolds representing (B) 3D scaffold models and (C) Distribution of pore size of inner porous layer. (D) SEM micrographs of outer electrospun layer representing porosity and nanofiber distribution, (E) Quantification of pore size distribution of outer electrospun layer calculated from micro-CT images.*

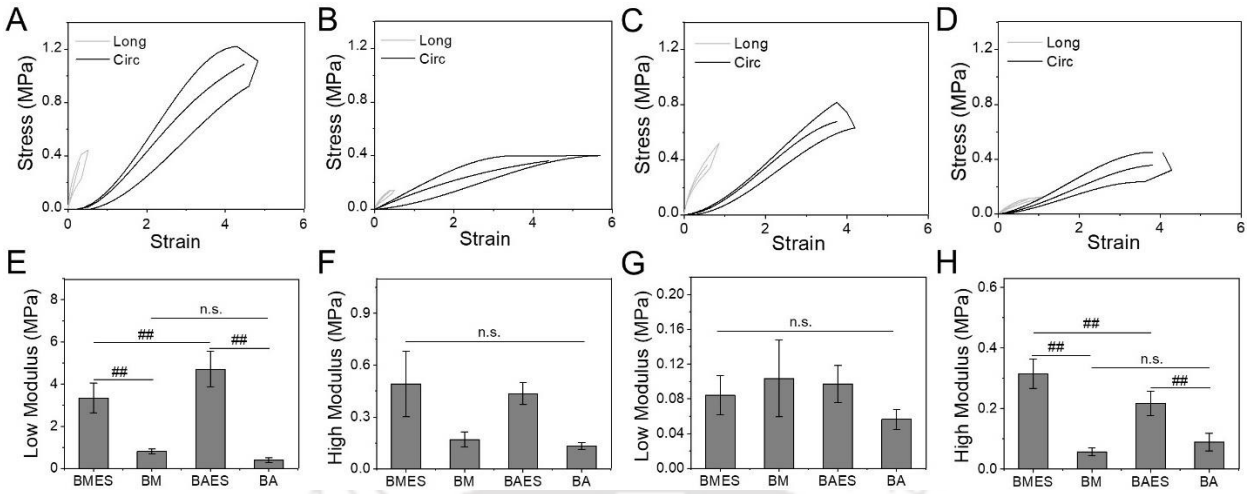

Figure 4.4. *Uniaxial tensile testing of silk scaffolds. Average stress-strain curves in longitudinal (Long) and circumferential (Circ) directions for (A) BMES, (B) BM, (C) BAES and (D) BA silk scaffolds. Comparison of scaffold average modulus in the low (E, G) and high (F, H) stretch regions in longitudinal (E, F) and circumferential (G, H) directions. (##p<0.01, n.s.=not significant)*

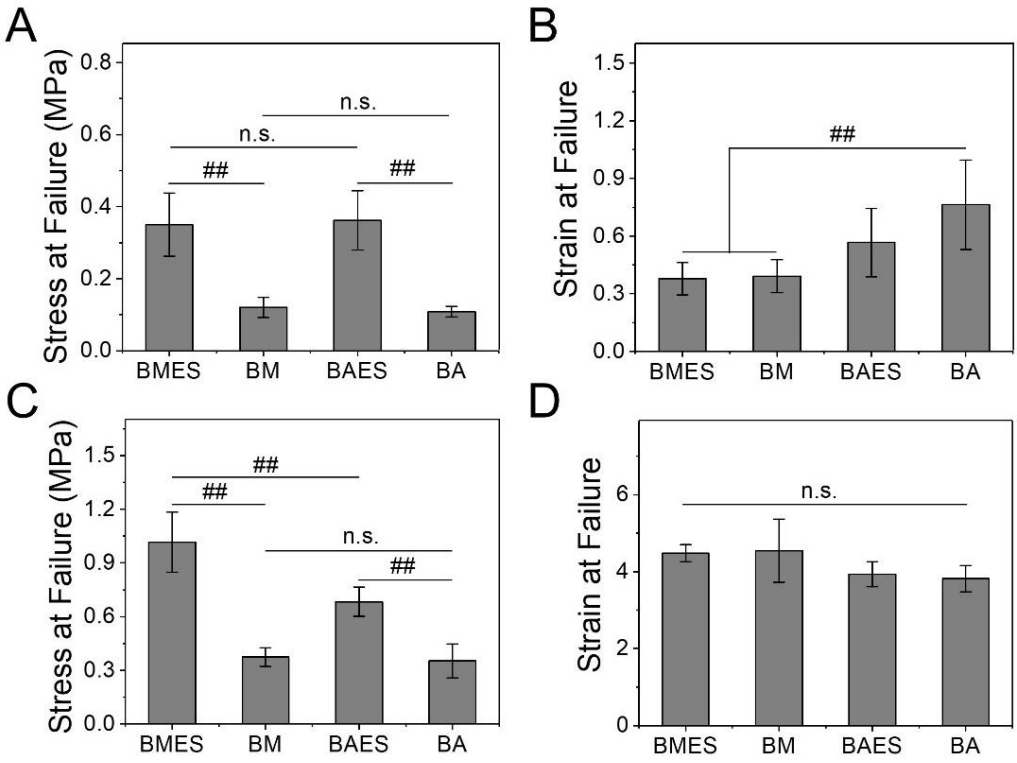

Figure 4.5. *Uniaxial tensile testing of silk scaffolds. Average stress values (MPa) at failure point (A, C) and corresponding strain at scaffold failure (B, D) in longitudinal (A, B) and circumferential (C, D) directions. (##p<0.01, n.s.=not significant)*

Suture retention force for tubular silk scaffolds was 0.38 ± 0.11 N for BMES and 0.46 ± 0.11 N for BAES scaffolds (p=0.290) (**Figure 4.6A**). Similarly, suture retention tension was not significantly different between BMES (520 ± 160 N/m) and BAES scaffolds (620 ± 150 N/m) (p=0.290, **Figure 4.6B**). No significant difference was observed for β stiffness at initial (150 ± 81 vs 205 ± 8) and final (207 ± 80 vs 214 ± 6) time points for BMES vs BAES scaffolds (p>0.01, **Figure 4.6C**). Dynamic compliance values were also non-significant at initial and final time points between the two silk scaffold variants (p>0.01, **Figure 4.6D**). Creep analysis for silk scaffolds over 7 hours suggests very low creep for both silk scaffolds (1.001 ± 0.005 vs 1.017 ± 0.017 for BMES and BAES) (p>0.01, **Figure 4.6E**). Moreover, burst pressure of silk scaffolds was comparable (827 ± 68 mmHg vs 798 ± 100 mmHg) for BMES vs BAES scaffolds (p=0.650, **Figure 4.6F**). In order to demonstrate the pressure-diameter relationship for silk scaffolds, we recorded scaffold diameter at physiologically relevant pulsatile pressure values at T=1h, showing consistency and insignificant distension of the scaffold wall. For both silk scaffold types, pulsatile behavior of pressure and scaffold diameter at 1h is shown in **Figure 4.7**.

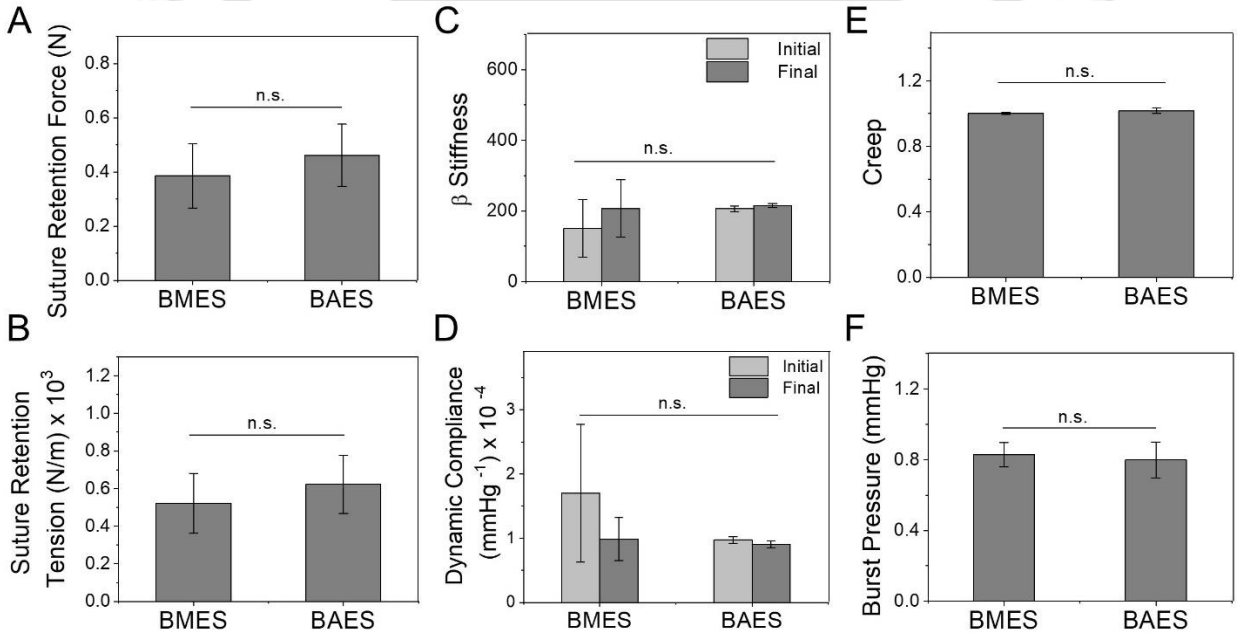

Figure 4.6. *Mechanical properties of bi-layered silk scaffolds. (A) Comparison of suture retention force and (B) Suture retention tension between the two silk scaffold variants. (C) Comparison of β stiffness and (D) Dynamic compliance of silk scaffolds at initial (T=0h) and final (T=7h) time points under the influence of physiologically relevant pulsatile flow. (E) Creep analysis of silk scaffolds after 7h physiologically relevant pulsatile flow. (F) Comparison of burst pressure of silk scaffolds. (n.s.=not significant)*

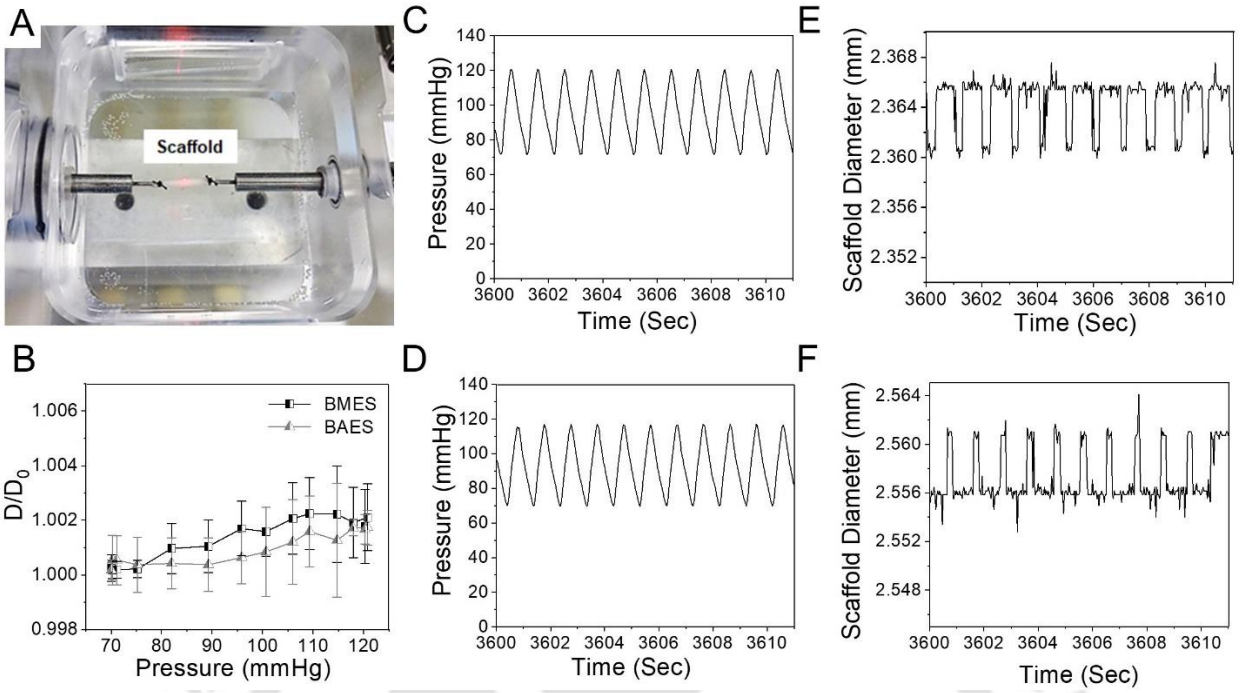

Figure 4.7. *Silk scaffold response to pulsatile flow. (A) Representative image showing silk tubular scaffold mounted in a testing chamber for pulsatile flow analysis. (B) Graph representing change in scaffold diameter under the influence of physiological pulsatile pressure post 1h testing. Representative graphs showing the pulsatile behavior of pressure with time for BMES (C) and BAES (D) scaffolds. Representative graphs showing the pulsatile behavior of scaffold outer diameter for BMES (E) and BAES (F) scaffolds.*

4.3.3 *In vitro* degradation profile

We performed both quantitative (by recording the mass loss with time) and qualitative analysis (by comparing the SEM images at different time points) to track the scaffold degradation. The effect of protease on the silk scaffolds is depicted in **Figure 4.8A**, representing the scaffold degradation pattern. Scaffolds kept in PBS alone, were smooth and did not show any visual structural alteration; whereas protease treated scaffolds were observed to be degrading with time. Images taken at higher magnification showed the formation of undefined pores in the scaffold struts after exposure to protease activity. All of the scaffolds maintained lumen diameter with no observed visual change with the exception of the BAES scaffolds treated with protease enzymes. Lumen diameter was quantified by analyzing the SEM images using ImageJ software. No significant change was observed for BMES/PBS, BMES/PRT and BAES/PBS groups ($p>0.01$), however the BAES/PRT group showed a significant decrease (~20% on day 8 and ~40% on day 15 when compared with day 0) in lumen diameter with time ($p<0.01$, **Figure 4.8B**). Both scaffold

types lost nearly 50% of their original weight within 15 days and nearly 70% at the end of 30 days in the presence of enzyme (**Figure 4.8C**). A significant difference was reported for protease treated and un-treated scaffold groups post 8 days onwards ($p<0.01$).

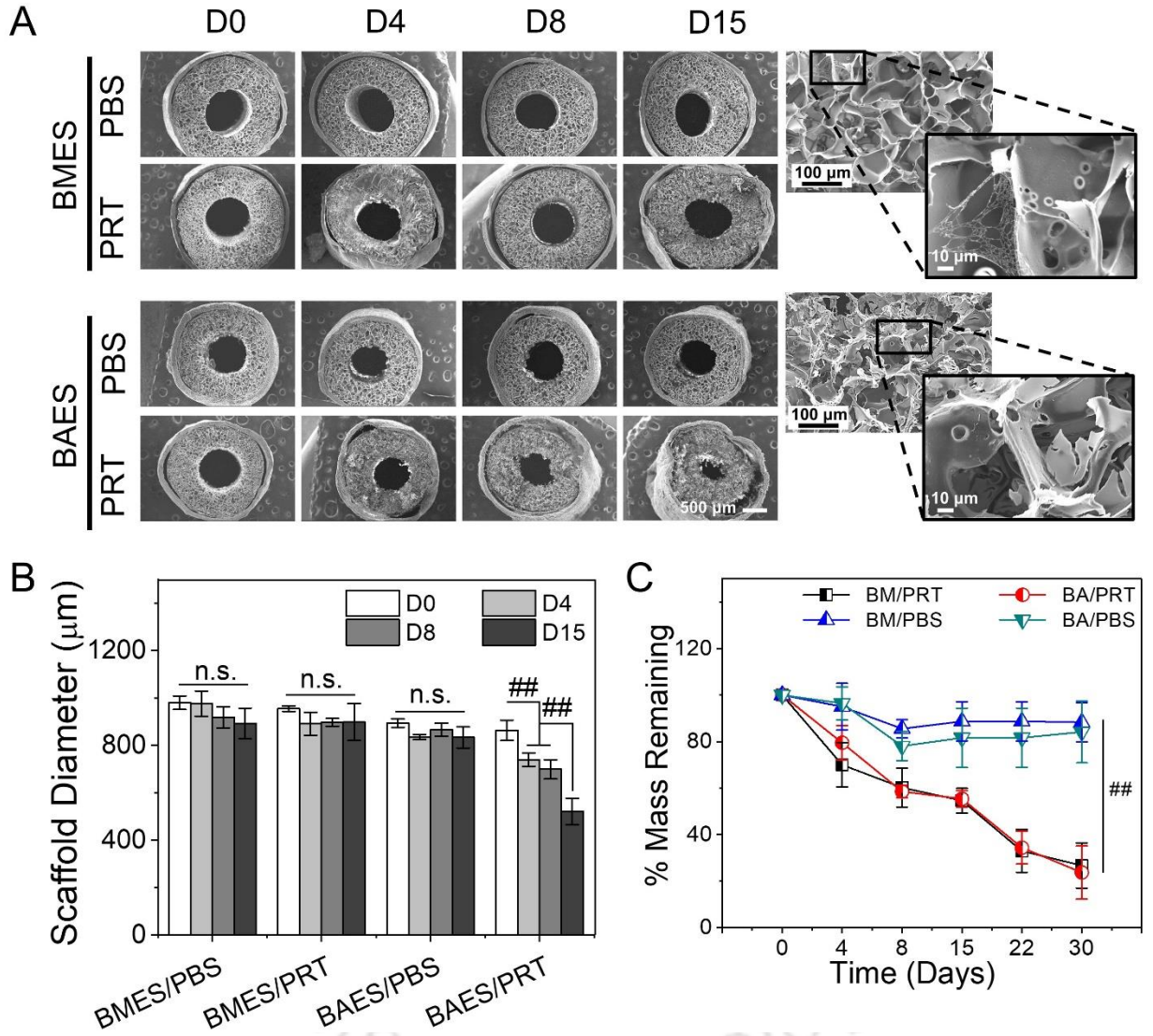

Figure 4.8. *In vitro degradation of tubular bi-layered silk scaffolds in the presence of protease XIV. (A) SEM micrographs showing the scaffold morphology and effect of protease treatment over time. The higher magnification images on the right represent the scaffold degradation pattern (pore formation in scaffold struts) after 15 days of treatment. (B) Quantification of scaffold diameter after 15 days. (C) Graph representing the degradation of silk scaffold (in terms of percentage mass loss) over time in the presence or absence of protease enzyme. ('/PRT' represents the presence of protease and '/PBS' represents the absence of protease) (##p<0.01, n.s.=not significant)*

4.3.4 Scaffold seeding and proliferation of SVF cells

The luminal pressure at the proximal end of the scaffold during the cell seeding remained between -10 mmHg and 10 mmHg **(Figure 4.9A)**. DAPI stained and ImageJ processed images showed uniform distribution of SVF cells along the scaffold wall (**Figure 4.9B**). Moreover, >90% cell seeding efficiency was achieved each time, as determined by calculating cell density in the perfused media. Silk scaffolds supported SVF cell viability and proliferation with time and results are reported as normalized values with respect to day 1. As shown in **Figure 4.9C**, both scaffolds supported SVF proliferation throughout the experimental time and no significant difference was recorded between the two groups after 15 days ($p>0.01$). Cells began proliferation after seeding into the silk scaffolds from day 1 onwards and a significant increase was observed at each successive time point with approximately 1.7-fold increase in cell population on day 15 ($p<0.01$).

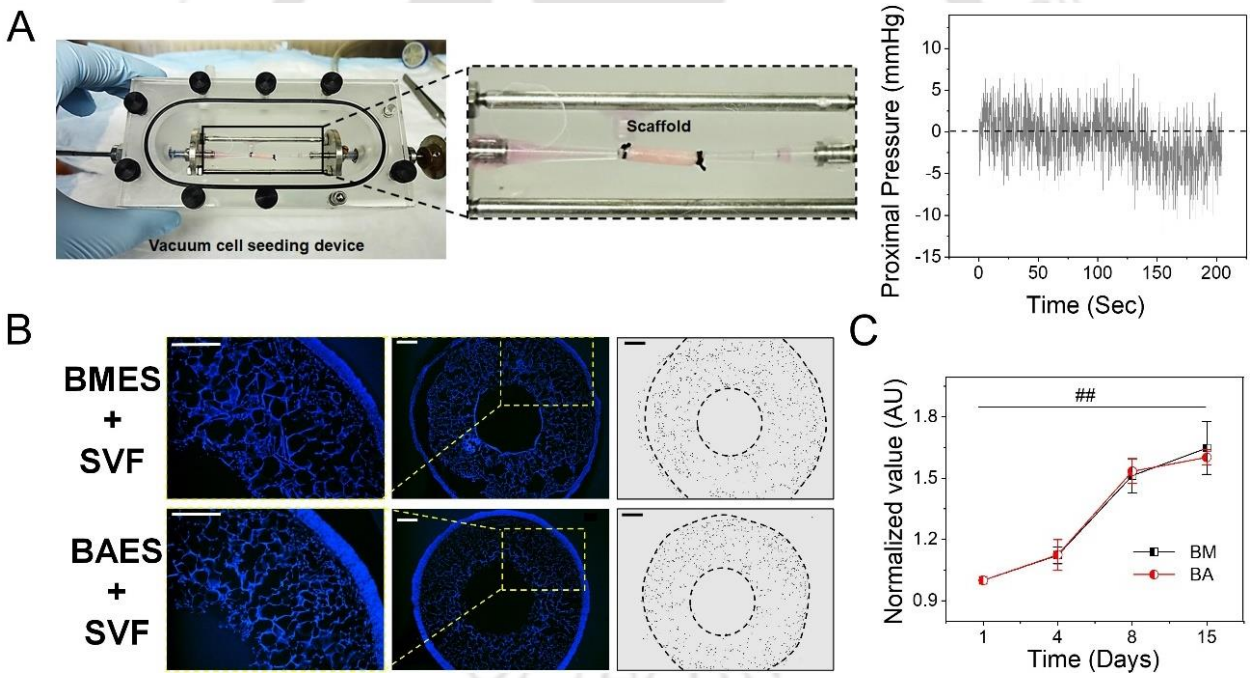

Figure 4.9. *Seeding tubular silk scaffolds with SVF cells and viability analysis. (A) Silk scaffolds were mounted into the rotational vacuum cell seeding device prior to cellular infusion. The graph on the right represents the recorded luminal pressure at the proximal end with time during infusion of cells. (B) SVF seeded scaffolds were exposed to 48h dynamic culture in a spinner flask and scaffold cross-sections were stained with DAPI (blue) indicating cell nuclei. ImageJ was used to map the cell distribution along the scaffold wall (representative images on the right side of the panel, dashed black line represents the scaffold wall); Scale bar: 200 µm. (C) Graph representing viability and proliferation of SVF cells cultured on silk scaffolds over 15 days under in vitro conditions. (##p<0.01)*

4.3.5 *In vivo* implantation and graft patency

Silk grafts were suturable and able to withstand the blood flow pressure (120 mmHg) and hemodynamic arterial microenvironment *in vivo*. Moreover, the electrospun silk/PCL layer prevented blood leakage. However, graft reddening was observed due to the infusion of blood cells in the inner porous layer of the silk scaffold instantly after micro clamp removal. A representative image of a silk graft after anastomosis and clamp removal is shown in **Figure 4.10A**. SVF seeded silk grafts were explanted at 1 week and 8 week time points. A gross morphological evaluation of silk explants suggested that 1 week explants demonstrated comparatively higher immune response as evidenced by accumulation of fibrin capsule surrounding the graft; whereas, 8 week explants showed better graft acceptance and dissolution of most of the fibrin capsule. A gross observation of the middle sections of the explanted scaffolds showed the presence of neotissue formation in the lumen of the 8-week explants (**Figure 4.10B, C**). Out of 21 implants, 3 BMES and 2 BAES grafts were implanted as control (without seeding SVF cells). All rats that received control grafts were observed for 8 weeks; unless impaired mobility of the hind limbs was observed requiring immediate euthanization. Graft performance was categorized into 4 groups and represented as: graft viability, patency, occlusion and acute thrombosis. Representative graph is shown in **Figure 4.10D** for SVF seeded silk scaffolds and **Figure 4.10E** for control explants. Graft patency was validated by recording angiograms (**Figure 4.10F**).

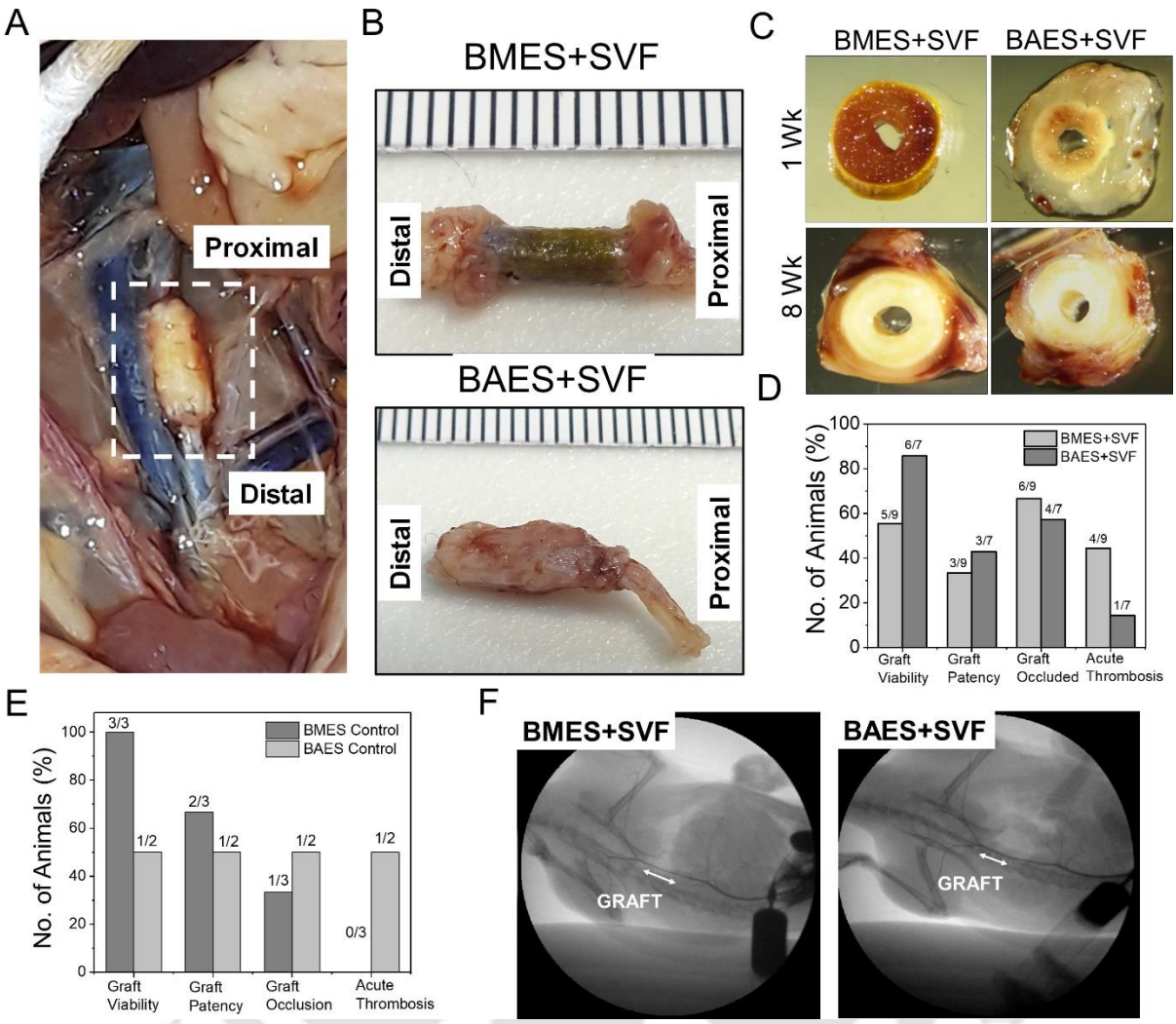

Figure 4.10. *In vivo implantation of silk scaffolds and graft patency. (A) A representative image of silk graft after aortic interposition implantation in a rat. (B) Representative images showing the explanted silk grafts after 8 weeks. (C) Representative images showing gross morphology of silk explants' cross-section post 1 week and 8-week time points. Black arrows are showing the presence of neo-tissue in the lumen of silk explants. (D) Quantitative data representing in vivo graft performance. (E) Viability and patency analysis of acellular control silk scaffolds. (F) Representative images of recorded angiograms showing graft patency after 8 weeks. White arrows represent the location of graft (infra-renal and above iliac bifurcation).*

Implanted silk scaffolds were determined to be 'viable grafts' in cases where no hind limb movement impairment was observed and the rat was bright, alert and responsive (BAR) until the completion of the experimental time. Graft patency was directly derived from angiogram data. 'Graft occlusion' include all the occluded grafts as a result of either intimal hyperplasia or acute thrombosis. The fourth category represents only the grafts with acute thrombosis within 48 h of surgery and confirmed by formation of a blood clot. All three of the control BMES grafts were

viable (1 occluded and 2 patent); whereas only one (out of 2) BAES scaffold was viable until 8 weeks (both occluded) (**Figure 4.11 and 4.12**). In the majority of cases, the reason for graft occlusion was either acute thrombosis or hyperplasia at the anastomosis site.

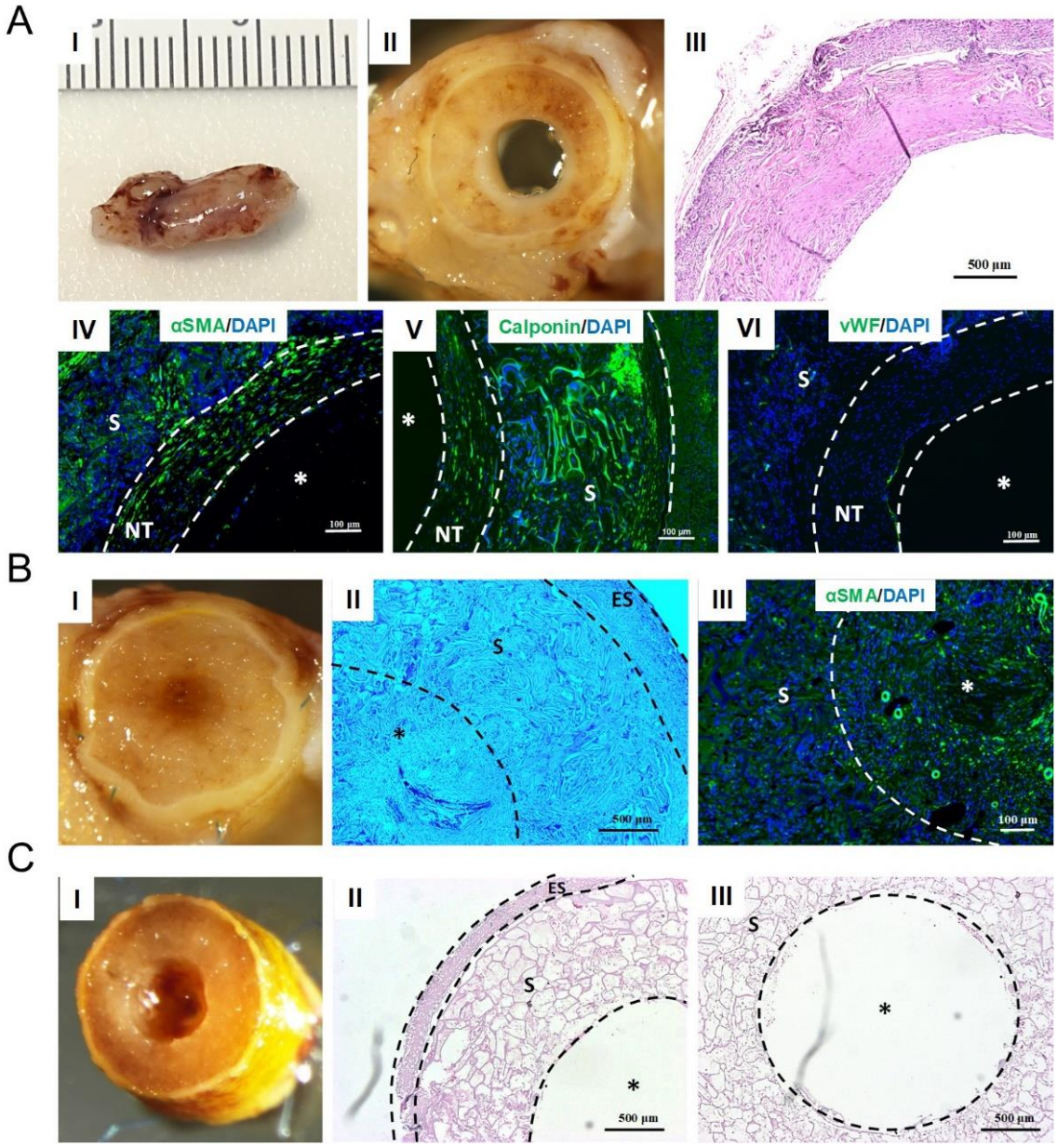

Figure 4.11. *BMES acellular (control) 8 weeks explant. (A) Patent BMES control explant. (I) Gross morphology of graft explant, (II) Cross section view of middle part of the explant showing neo-tissue formation, (III) H&E stained representative image of the explant (nucleus-blue, cytoplasm-red), (IV-VI) Representative immunofluorescence images showing expression of vascular cell specific markers (αSMA, calponin and vWF-green color). (B) Occluded BMES graft. (I) Cross section view of middle part of the explant showing occluded lumen, (II) H&E stained cross section, (III) Representative immunofluorescence image showing expression of αSMA (green color). (C) Patent BMES graft without any neo-tissue formation. (I) Cross section view of the*

explant showing patent lumen, (II, III) H&E stained sections showing absence of neo-tissue formation. ('' represents the lumen of the scaffold, 'S' represents the freeze dried scaffold part, 'ES' represents the outer electrospun layer, 'NT' represents neo-tissue, dashed lines and circle are separating the scaffold wall from lumen).*

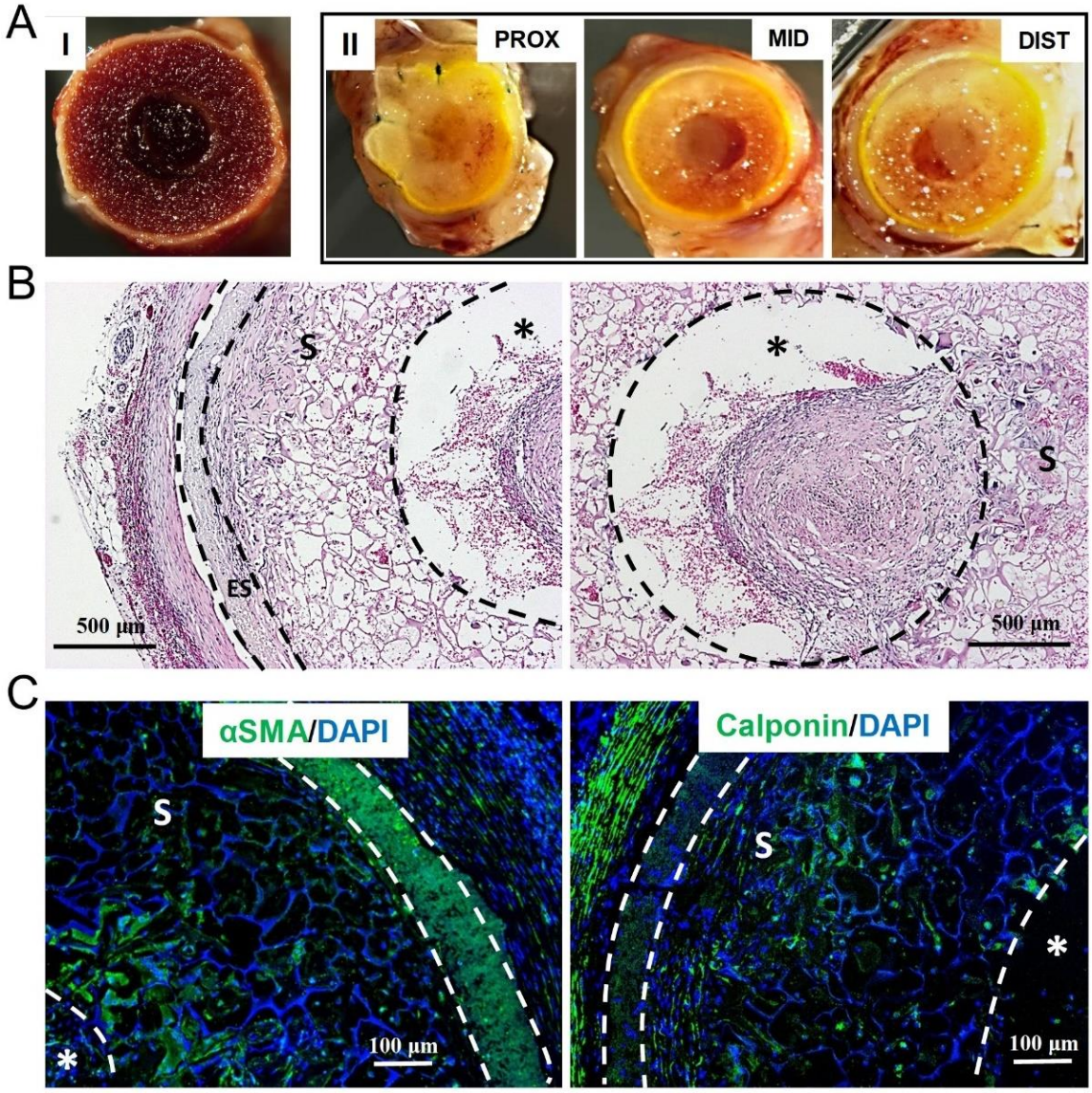

Figure 4.12. *BAES acellular (control) explant. (A) (I) Representative image of a 2-day explant occluded due to acute thrombosis, (II) Gross morphological analysis of 8 weeks explant showing complete lumen occlusion at the proximal end and partial occlusion at middle and distal end. (B) H&E staining of the partially occluded middle section of the 8 weeks explant. (C) Immunofluorescence images showing the expression of smooth muscle cell (SMCs) specific markers (αSMA and calponin- green color) in the middle part of partially occluded 8 weeks explant. ('*' represents the lumen of the scaffold, 'S' represents the freeze dried scaffold part, 'ES' represents the outer electrospun layer, dashed lines and circle are separating the scaffold wall from lumen).*

4.3.6 Host cell infiltration and graft remodeling

At the initial time point (after 7 days), many nucleated cells were present in both BMES and BAES scaffolds; however, limited expression of rat specific αSMA, calponin and vWF markers suggested minimal infiltration of host cells. Analysis of the 8 week explants revealed the presence of neo-tissue formation along the lumen of the scaffolds (for both BMES and BAES) and infiltration of host cells in the scaffold wall. A large population of αSMA and calponin positive cells was present in both the porous scaffold wall and lumen. In addition, a continuous layer of vWF^{+} cells at the scaffold-lumen interface marked the presence of mature endothelium. Notably, a distinct boundary was observed between the neo-tissue and the porous scaffold wall suggesting the initiation of neo-tissue formation over the scaffold followed by integration with the scaffold wall. In 8-week explants, SMCs in the neo-tissue were organized circumferentially. Scaffold remnants could still be visualized after 8 weeks. Considering the autofluorescence of silk protein, both merged and marker specific images are provided for clear representation (**Figure 4.13A**). BAES+SVF scaffolds potentially recruited more cells than BMES+SVF scaffolds ($p=0.0062$ for 1 week explant and $p=0.042$ for 8 week explants) (**Figure 4.13B**). A significantly lower no. of $CD68^{+}$ cells was observed at the 8 week time point ($p=0.022$ for BMES+SVF scaffolds and $p<0.01$ for BAES+SVF scaffolds) (**Figure 4.13C**). Comparing both scaffold variants, BAES+SVF scaffolds recruited higher numbers of CD68 positive cells at 1 week ($p=0.01$); however, 8 week explants showed no significant difference ($p=0.424$). The lumen diameter of both silk scaffolds was comparable with native rat aorta (~1.1 mm) (**Figure 4.13D**). A slight increase in scaffold lumen diameter was recorded post implantation. BMES+SVF and BAES+SVF explants showed ~1.5 and ~1.6 times increase respectively in lumen diameter at 1-week ($p<0.05$), which remained consistent at 8 weeks. In addition, no significant difference was observed for TEVG wall thickness over time (**Figure 4.13E**).

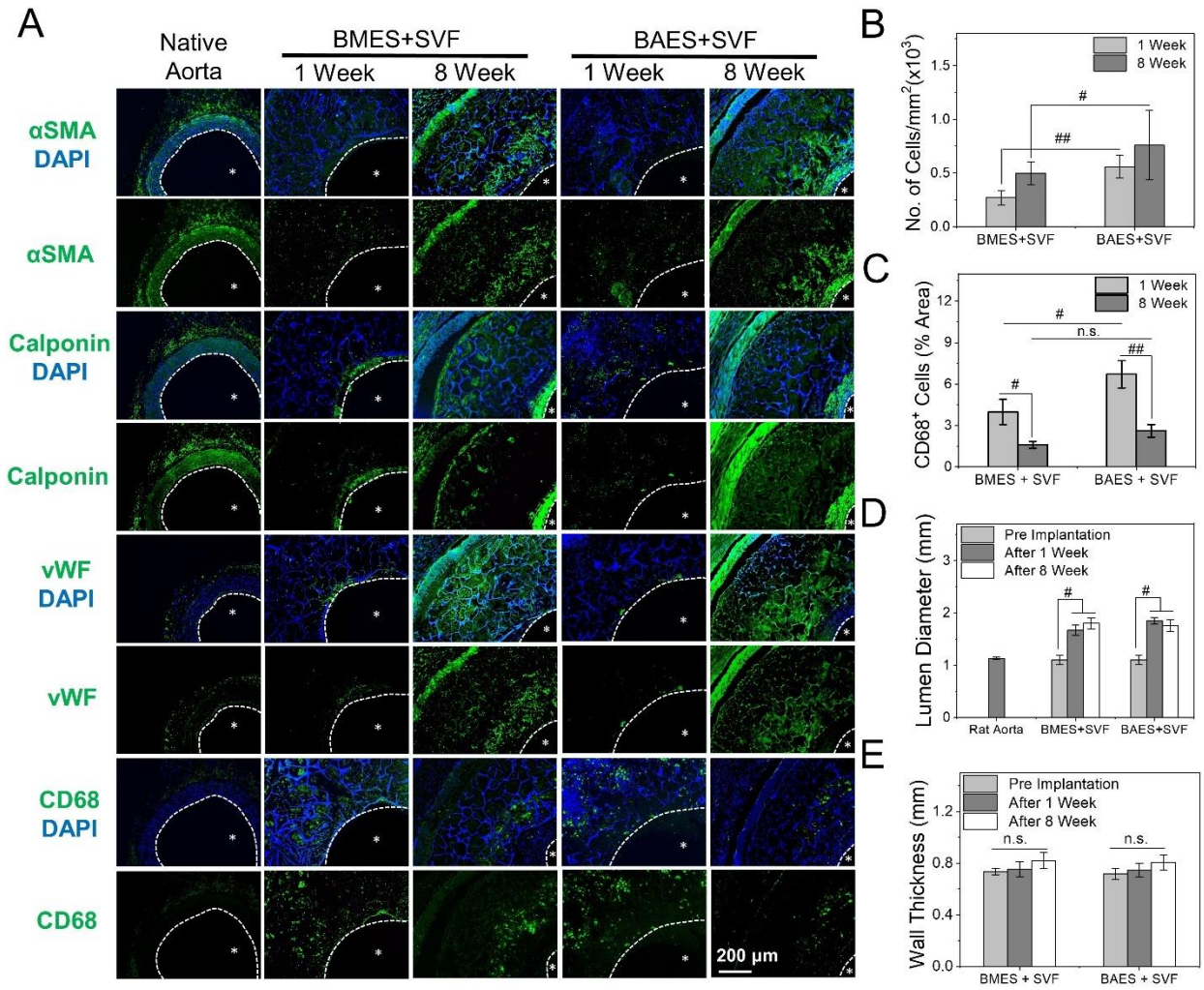

Figure 4.13. *Analysis of host cell infiltration, lumen diameter and wall thickness of explants. (A) Representative immunofluorescence images of the middle section of vascular explants at different time points showing the infiltration of host cells (αSMA and calponin: SMCs, vWF: ECs and CD68: macrophages). The lumen of the explants is labeled as '*' and marked with white dotted line. (B) Quantification of host cell infiltration in silk grafts. Graph representing (C) presence of $CD68^+$ cells in silk grafts, (D) lumen diameter and (E) Wall thickness of vascular explants. (#p<0.05, ##p<0.01, n.s.=not significant)*

Remodeling of the patent grafts was further reflected by deposition of ECM proteins (collagen and elastin) with time. In agreement with the immunofluorescence staining images, hematoxylin and eosin (H&E) stained explant sections showed cellular infiltration at earlier time point (1 week) in both scaffold variants. Cells were distributed uniformly along the scaffold wall with no specific alignment after 1 week. Picrosirius Red (PCRO) staining and Verhoeff-Van Gieson (VVG) staining of scaffold sections showed limited collagen and elastin deposition after 1 week. BAES+SVF scaffolds showed the formation of thick fibrin capsule covering the graft. The

neo tissue formation was evidenced by the presence of aligned collagen and elastin deposition. A visual analysis of stained histological sections suggested denser and more organized elastin deposition for BAES+SVF grafts after 8 weeks when compared with BMES+SVF counterpart (**Figure 4.14A**).

Quantification of collagen and elastin further substantiated the histological data. Higher collagen production was recorded at 1-week for BAES+SVF than BMES+SVF explants ($p<0.05$). Total collagen produced in both silk scaffolds after 8-weeks was comparable with native rat aorta ($p=0.06$) (**Figure 4.14B**). Elastin quantification showed limited presence of mature elastin at 1 and 8-week time points for both silk scaffold variants as compared with the native rat aorta ($p<0.01$) (**Figure 4.14C**). Moreover, both silk grafts showed no significant difference at 1 week ($p=0.321$); however, the elastin content of 8-week explant of BAES+SVF showed an increased value when compared with its BM counterpart ($p<0.05$).

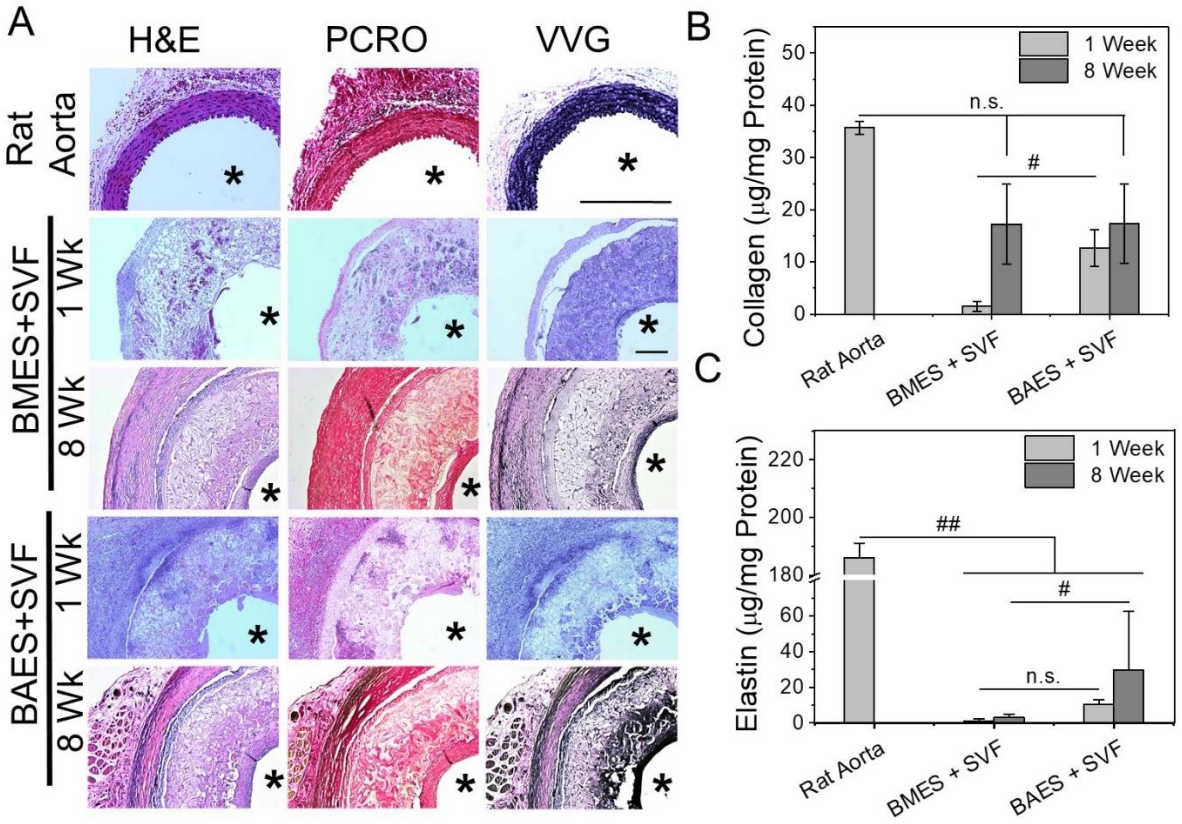

Figure 4.14. *Histological analysis of extracellular matrix (ECM) production and graft remodeling. (A) Representative histological images of the middle section of explanted grafts stained with H&E (hematoxylin and eosin) for cell infiltration, PCRO (picrosirius red) for collagen (red) and VVG (Verhoeff van Gieson) for elastin (black). Scaffold lumen is marked as '*'. (Scale bar: 500 μm) Quantitative analysis of (B) collagen (n=3) and (C) elastin (n=3) in silk grafts compared with rat aorta. (#p<0.05, ##p<0.01, n.s.=not significant)*

4.4 Discussion

A paradigm shift in the field of vascular tissue engineering has been observed since it was reported that the remodeling necessary for graft success is an inflammation mediated process [44]. Recent studies suggest that stem cells incorporated into vascular grafts play a paracrine role by recruiting endogenous inflammatory cells to the scaffold as well as providing anti-thrombogenic effects via signaling [104]. In addition, these cells tend to leave the scaffold within a week [44]. We have previously investigated TEVGs constructed with a synthetic biodegradable polymer-based tubular scaffold seeded with adipose derived stem cells or SVF [338, 339, 342, 345]. The potential advantage of using silk over other natural or synthetic polymers is its tunable biodegradability [146, 346], mechanical properties [182], remarkable biocompatibility and FDA acceptance [10]. Moreover, the degradation byproducts of silk protein polymer are fragments (peptides) or single amino acids, which may eventually be metabolized by cells without causing toxic effects [146]. In this study, we report for the first time the use of Indian endemic non-mulberry AA silk as a scaffold for small-diameter TEVGs.

Apart from graft material and composition, various design parameters should also be considered for success of any TEVG. With the latest computational modeling technologies, it is now possible to predict graft performance *in vivo* based on design parameters [329, 347]. Considering this, it is critical that TEVG scaffold fabrication methodologies confer controllable porosity, pore size, mechanical properties, degradation rate and other factors. No previous studies, to our knowledge, used the molding-lyophilization technique reported here to prepare porous silk scaffolds for small-diameter TEVGs. This is likely due to the freeze-drying process having limited working depth of ~1 cm due to the sublimation of water molecules from the surface. While preparing tubular scaffolds with submillimeter wall thickness and >1 cm tube length, it is crucial to keep the polymer solution in a frozen state. The typical molding technique only allows sublimation from both ends of the tube. In the present work, we designed custom 3D printed molds and a new fabrication methodology that keeps the silk solution in a frozen state, leaves behind a void space that becomes the scaffold lumen, and provides a large surface area (along the whole lumen) to sublimate with submillimeter working depth. Following this unique methodology, we achieved longer (~3 cm) silk scaffolds than what is possible using other methods, with submillimeter wall thickness. Silk tubes were further coated with a nanofibrous electrospun layer to provide enhanced mechanical stability. In contrast to a previous report, bi-layered silk grafts

fabricated herein are morphologically biomimetic where inner porous layer mimics tunica media and outer fibrous layer mimics adventitia [285]. Another added advantage of our fabrication methodology is that the inner porous layer can be fabricated by using a range of protein percentage (in contrast to gel-spun tubes where a very high percentage of silk protein is required). It may also allow (as per requirement) control over the scaffold porosity, pore size, degradation rate and mechanical strength by manipulating the silk protein percentage, freezing temperatures and thickness of both layers [348].

In general, for any tissue engineering scaffold, 10-μm pores have been shown to promote cellular infiltration which was observed in our model using *in vitro* cell seeding and *in vivo* host cell migration [349]. Pore size is also known to play an important role in governing macrophage mediated graft remodeling [350]. The silk scaffolds reported and used in this study are suitable for cellular infiltration; however larger pores might cause adverse effects during the course of graft remodeling [326, 351]. The pore size of inner freeze-dried layer could be reduced by using a higher percentage of silk protein [348].

Graft mechanics is a design parameter that needs to be regulated carefully. In a previous study, we reported the mechanics of human saphenous vein (hSV) and porcine internal mammary artery (pIMA) using a similar experimental design [337]. A comparative analysis of silk scaffolds with natural blood vessels (hSV and pIMA) is listed in **Table 4.1**. Circumferential modulus, suture retention force and burst pressure of silk scaffolds were comparable to either hSV or pIMA validating their suitability; however, silk scaffolds were stiffer leading to comparatively lower dynamic compliance that needs to be considered. In addition, minimal creep at physiological pressure validates the suitability of silk scaffolds. Burst pressure of scaffolds could also be improved by increasing the thickness of outer electrospun layer to match the ISO 7198 standard.

Table 4.1 *Comparison of mechanical properties of silk scaffolds with previously reported values for human saphenous vein (hSV) and porcine internal mammary artery (pIMA).*

	BMES scaffold	**BAES scaffold**	**hSV [337]**	**pIMA [337]**
Circumferential stress at failure (MPa)	1.01 ± 0.16	0.68 ± 0.08	3.7 ± 2.0	10.4 ± 7.1
Circumferential strain at failure	4.47 ± 0.22	3.92 ± 0.32	1.7 ± 0.7	1.5 ± 0.2

Circumferential modulus (MPa)	High: 0.31 ± 0.04 Low: 0.08 ± 0.02	High: 0.21 ± 0.04 Low: 0.09 ± 0.02	2.5 ± 1.0	0.4 ± 0.2
β Stiffness	207.2 ± 80.7	214.9 ± 6.03	40 ± 10	15 ± 10
Dynamic compliance ($mmHg^{-1}$)	$(0.98 \pm 0.33)*10^{-4}$	$(0.90 \pm 0.05)*10^{-4}$	$(3.4 \pm 2.0)*10^{-4}$	$(11.2 \pm 6.0)*10^{-4}$
Suture retention tension (N/m)	$(0.52 \pm 0.16)*10^{3}$	$(0.62 \pm 0.15)*10^{3}$	$(6.0 \pm 2.2)*10^{3}$	$(4.0 \pm 2.0)*10^{3}$
Suture retention force (N)	0.38 ± 0.11	0.46 ± 0.11	2.5 ± 0.8	1.0 ± 0.8
Burst pressure (mmHg)	827.43 ± 68.41	798 ± 100.9	1000.0 ± 400	2300 ± 100

Degradation of the graft after *in vivo* implantation determines the fate of graft remodeling and fast degrading polymers are now becoming the favored choice [326, 338, 339, 352]. Silk protein is biodegradable and showed a considerable mass loss *in vitro*. The degradation profile of both silk scaffolds represent their ability to integrate with host tissue without rupture or weakening due to rapid degradation [352]. Minimal structural deformation of silk scaffolds (in the presence of protease) further validated their suitability. In the protease treated groups, the diameter of BAES scaffold was observed to be reducing over time, which is in contrast with BMES scaffolds showing no significant difference; however, BA/PRT and BM/PRT were comparable when analyzed for mass loss over time. These different patterns may be resulting due to: (1) Delamination of inner and outer layers due to mechanical agitation, resulting in collapse of the inner layer and reduced scaffold diameter without changing the overall scaffold mass OR (2) Structural deformation during manual handling. Despite the fact that BAES grafts demonstrated lumen narrowing due to degradation *in vitro*, no such observation was made when implanted in rat aortae, which might be attributed to the hemodynamic pressure in the scaffold lumen. *In vivo* graft degradation is dependent on several factors including the site of implantation. A previous study suggests that macrophages play an important role in silk protein degradation *in vivo* [182, 353]. Higher infiltration of $CD68^{+}$ cells in BAES+SVF grafts might be suggestive of faster degradation and remodeling of these grafts post-implantation in the long term.

Preventing acute thrombosis is crucial for graft success. Conjugating anti-thrombotic molecules (e.g. heparin) is the most commonly used approach [352, 354]. However, recent studies make use of the dual activity of stem cells: (i) antithrombogenic property [104, 345] and (ii) ability

to recruit endogenous inflammatory cells by paracrine signaling for constructive tissue remodeling [44]. Adipose derived stem cells and stromal vascular fraction (SVF) cells have shown significant success in terms of preventing acute thrombosis and encouraging graft remodeling [338, 339, 342]. Hence, we used SVF seeded silk scaffolds for *in vivo* rat implantation. Both of the SVF seeded silk grafts showed fibrous capsule formation around the graft after 1-week *in vivo*, a sign of foreign body response (FBR) [355]. The BAES+SVF scaffolds showed formation of thick fibrous capsule at 1 week, possibly due to the intrinsic presence of integrin binding sites (RGD motifs) that subsequently might aid in recruiting macrophage/monocytes [170]. Unlike early stage explants, 8-week silk grafts showed minimal presence of surrounding fibrous tissue, a sign of graft remodeling and acceptance. Higher infiltration of $CD68^+$ cells in BAES+SVF grafts post 1-week might be attributed to the presence of RGD, which tends to influence thrombogenic response and graft remodeling by interacting with platelets and macrophages. These observations indicate that if we could prevent acute thrombosis in BAES silk scaffolds, they might have a better chance of host cell infiltration and graft remodeling. Despite the presence of SVF cells, BMES+SVF grafts (4/9) showed acute thrombosis, contrasting with previous reports with BM silk [158, 189, 202] and our poly (ester-urethane) urea (PEUU) based grafts [338, 339, 345]. The average pore size of BMES scaffold was higher than BAES scaffolds that might be one of the plausible reasons of acute thrombosis observed in BMES+SVF grafts. Moreover, another recent report stated that smooth surfaces present higher hemocompatibility [356], this might be related to the higher pore size, and therefore rougher surface, of BMES scaffolds leading to poor hemocompatibility. One week BMES+SVF scaffold explants also showed penetration of blood in the scaffold wall that might be attributed to larger pore size, leading to entrapment of clot inducing cells and ultimately resulting in blood clot formation. However, limited literature is available on direct assessment of scaffold pore size and hemocompatibility, which needs to be investigated exclusively. Acute thrombosis was not the only cause of silk graft occlusion, hyperplasia due to various factors was also observed. Occluded silk grafts showed the presence of αSMA and calponin positive cells, suggesting an overgrowth of SMCs in the lumen (hyperplasia) (**Figure 4.15 and 4.16**). BAES+SVF grafts showed occlusion predominantly at the anastomotic site, which might be attributed to damaged tunica intima during surgical anastomosis. Moreover, RGD bearing matrices have been shown to induce the re-expression of contractile phenotype of SMCs, therefore reducing the possibility of hyperplasia [357]. In addition, no significant change in TEVG wall thickness over time was

observed for patent explants, suggesting minimal possibility of hyperplasia. The graft-occluding pattern indicates that adopting a careful graft anastomosis protocol and avoiding possible damage to the tunica intima during surgery may increase the chances of BAES graft survival. The drug (e.g. rapamycin) eluting silk grafts may also be effective to prevent hyperplasia [358].

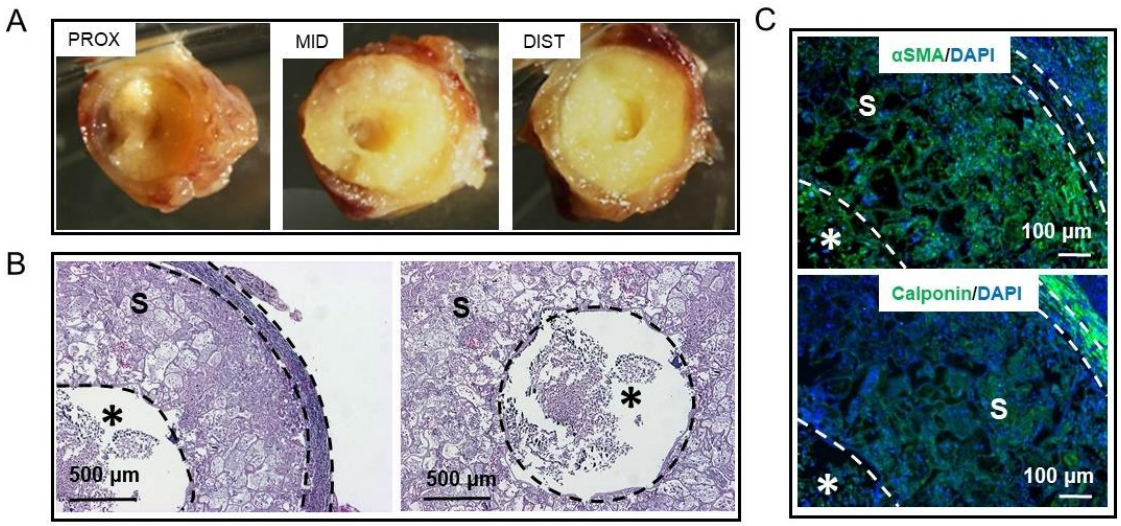

Figure 4.15. *BMES + SVF, 8 weeks occluded explant. (A) Gross morphological images of proximal, middle and distal cross sections of occluded explant. (B) H&E stained representative images of the middle section of explant showing the occluded lumen. (C) Representative immunofluorescence images of middle section of the explant showing the smooth muscle cell (SMCs) specific marker expression (αSMA and calponin, green color). ('*' represents the lumen of the scaffold, 'S' represents the freeze dried scaffold part, dashed lines and circle are separating the scaffold wall from lumen).*

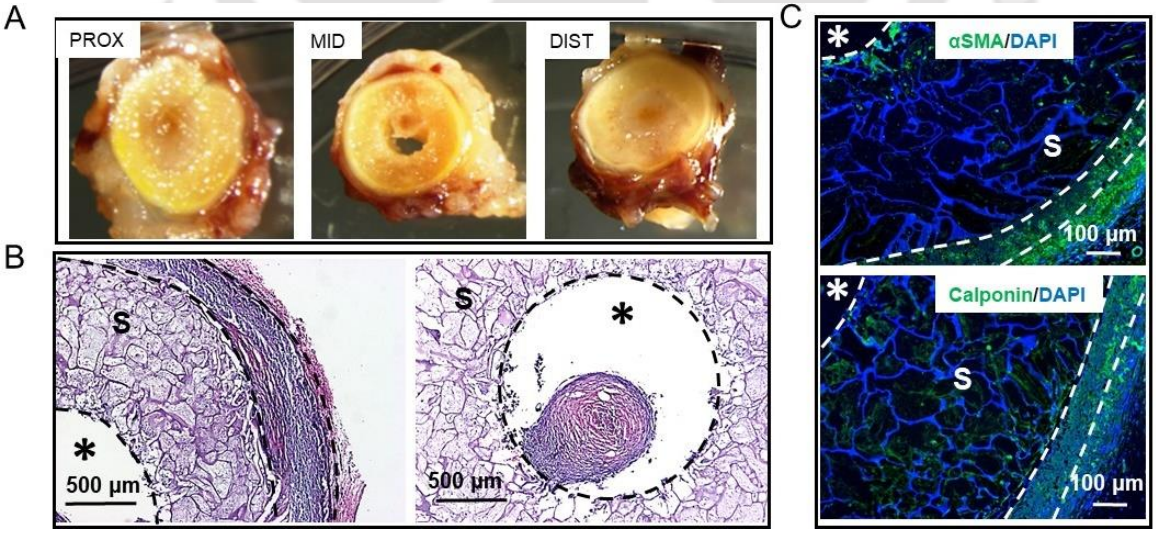

Figure 4.16. *BAES + SVF, 8 weeks occluded explant. (A) Gross morphological images of proximal, middle and distal cross sections showing graft occlusion at both ends and partial occlusion in the middle section. (B) H&E stained representative images of the middle section of*

explant showing partially occluded lumen. (C) Representative immunofluorescence images of middle section of the explant showing the smooth muscle cell (SMCs) specific marker expression (αSMA and calponin, green color). ('' represents the lumen of the scaffold, 'S' represents the freeze dried scaffold part, dashed lines and circle are separating the scaffold wall from lumen).*

Collagen and elastin present in the vessel wall maintain integrity under high-pressure conditions [326]. Furthermore, SMC distribution is directly related to the organization of ECM proteins and luminal pressure induces their radial alignment. Both scaffold types showed limited collagen and elastin after 1-week. However, radially aligned collagen and elastin fibers were evident in 8-week explants. Of note, the organization of ECM proteins was limited to neo-tissue; unorganized collagen and elastin were still present in the scaffold wall. Longer *in vivo* studies could explore the fate of unorganized collagen and elastin present in the scaffold wall but initiation of neo-tissue formation with aligned ECM protein fibers and its integration with the scaffold wall indicate initial graft remodeling. Interestingly, collagen content of both scaffold types after 8 weeks was comparable to the native rat aorta; however, production of mature elastin was an order of magnitude lower, which is one of the major challenges of vascular tissue engineering [324]. Comparatively higher elastin induced by BAES+SVF grafts might arise from the ability of these scaffolds to rapidly recruit host cells. The initial distention of the scaffold wall may result from luminal blood pressure after implantation. Notably, the angiogram data did not show any signs of graft aneurysm at any time point. The gradual increase in scaffold lumen diameter might be due to the compression of the inner lyophilized porous layer of the scaffold without changing the outer diameter. In addition, the possibility of vacuum seeding induced deformation should not be overlooked.

This work shows the *in vitro* and short-term *in vivo* performance of tubular bi-layered silk scaffolds as potential vascular grafts and suggests that using non-mulberry AA silk for this purpose is advantageous in multiple terms. Some future directions for this study may include optimizing the design parameters (pore size of inner scaffold layer and overall graft compliance) to improve the graft's *in vivo* performance. Reducing the wall thickness to match the native rat aorta may allow easier handling of graft during suturing and reduce the possibility of intimal hyperplasia. Moreover, this study is limited to using a rat model up to 8 weeks. In order to investigate complete neo vessel formation, graft remodeling and elastin production/rearrangement, long-term implantation studies are needed.

4.5 Significant Findings

1. In this study, we demonstrate a new approach to fabricate bi-layered scaffolds using mulberry (*B. mori*) and non-mulberry Indian endemic (*A. assama*) silk.
2. The bi-layered silk grafts are morphologically biomimetic with inner porous layer mimicking tunica media and outer fibrous electrospun layer mimicking adventitia.
3. TEVG fabrication methodology may also provide control over porosity, pore size, biodegradation and mechanical properties, which can be achieved by manipulating protein percentage, freezing temperatures and thickness of both layers. The flexibility of graft designing parameters is crucial and provides a substantial improvement over existing methodologies.
4. Both BMES and BAES silk scaffolds showed comparable physical, morphological and mechanical properties with the exception of average pore size and distribution.
5. *In vivo* rat aortic implantation of these scaffolds validated their suturability and strength.
6. Eight weeks of implantation in rat model revealed the superior performance of BAES+SVF TEVGs compared to BMES+SVF grafts (in terms of graft viability, recruitment of host cells and new extracellular matrix); possibly due to presence of intrinsic RGD cell binding motifs in AA silk protein.
7. Moreover, BAES+SVF grafts showed better remodeling than BMES+SVF in terms of host cell infiltration, neo-tissue formation and integration within scaffold wall, production of ECM proteins (collagen and elastin) and their arrangement.
8. None of the implanted scaffolds showed any sign of aneurysm formation.
9. Overall, this study highlights the feasibility of TEVG fabrication methodology and potential of non-mulberry silk bi-layered scaffolds for vascular tissue engineering applications.

CHAPTER 5

Acellular silk-decellularized human Wharton's jelly extracellular matrix composite tubular scaffolds and their functional analysis in rabbit jugular vein as interposition graft for vascular tissue engineering applications

This chapter demonstrates the fabrication of a cell-free tissue-engineered vascular graft functionalized with decellularized human Wharton's jelly matrix. Immunomodulatory and other bioactive factors secreted by Wharton's jelly stem cells are hypothesized to be preserved in the matrix, partially recapitulating the effect of cell-seeding. This approach is envisaged to provide a readily available cell-free option towards developing a clinically feasible vascular graft with high fidelity.

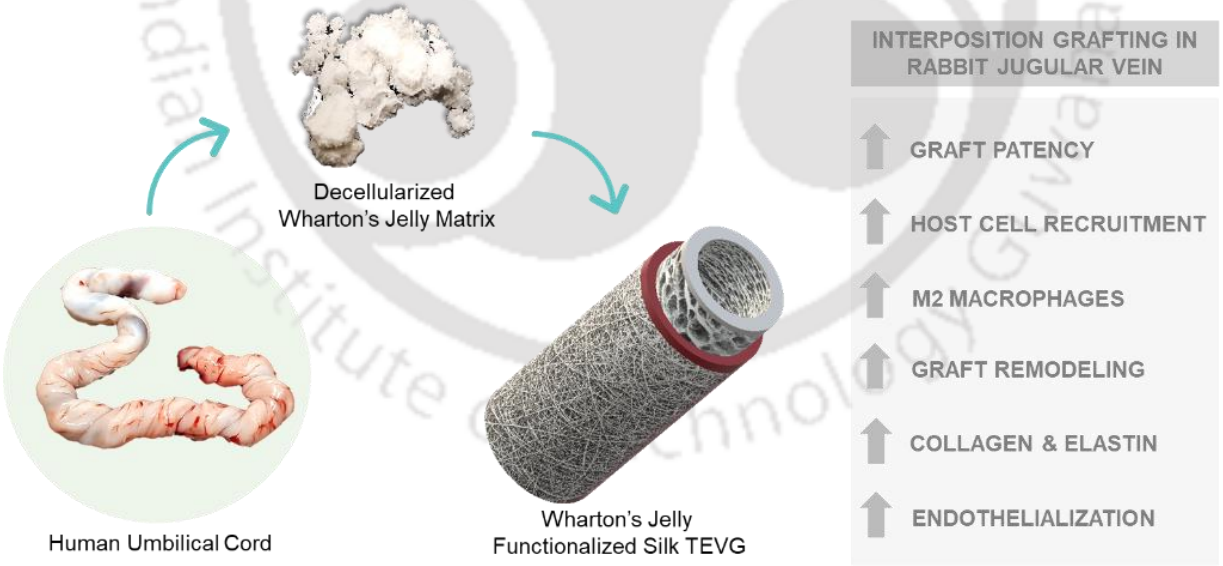

Publication:

Prerak Gupta[#], *Gaurab Ranjan Chaudhuri*[#], *G. Janani, Manoj Agarwala, Debaki Ghosh, Samit K. Nandi, Biman B. Mandal. Functionalized Silk Vascular Grafts with Decellularized Human Wharton's Jelly Improves Remodeling via Immunomodulation in Rabbit Jugular Vein. (# Co-First Authors) (Revision submitted to '**Advanced Healthcare Materials**')*

ABSTRACT

Cell-free polymeric tissue-engineered vascular grafts (TEVGs) have shown great promise towards clinical translation; however, their limited bioactivity and remodeling ability challenges this cause. Here, a novel cell-free bioresorbable small diameter silk TEVG system functionalized with decellularized human Wharton's jelly (dWJ) matrix is developed and successfully implanted as interposition grafts into rabbit jugular vein. Implanted TEVGs remain patent for two months and integrate with host tissue, demonstrating neo-tissue formation and constructive remodeling. Mechanistic analysis reveals that dWJ matrix is a reservoir of various immunomodulatory cytokines (IL-8, IL-6, IL-10, IL-4, and TNF-α), which aids in upregulating M2 macrophage-associated genes facilitating pro-remodeling behavior. Besides, dWJ treatment to human endothelial cells upregulates the expression of functional genes (CD31, eNOS, and VE-cadherin), enables faster cell migration, and elevates NO production leading to the *in situ* development of endothelium. The dWJ functionalized silk TEVGs support increased host cell recruitment than control, including macrophages and vascular cells. It endows superior graft remodeling in terms of a dense medial layer comprising smooth muscle cells and elevates production of extracellular matrix proteins (collagen and elastin). Altogether, these findings suggest that dWJ functionalization imitates the usefulness of cell seeding and enables graft remodeling.

5.1 Introduction

Remodeling of tissue-engineered vascular grafts (TEVGs, all synthetic and natural grafts except native cellular blood vessels) predominantly relies on scaffold bioactivity, which is orchestrated by either incorporating diverse cell types or bioactive molecules [359]. Developing viable TEVGs using patient-specific vascular cells is a time-consuming process. It requires long-term *in vitro* expansion of autologous cells, scaffold seeding, and *in vitro* maturation under physiologically relevant dynamic culture conditions, thus limiting their clinical translation [5]. Alternatively, bone marrow mononuclear cells (BM-MNCs) can be harvested in a time-efficient manner, which brings down the fabrication time from days to hours. BM-MNCs have the inherent ability to recruit endogenous vascular cells, which facilitates *in situ* endothelialization and neo-tissue formation after transplantation [37, 39, 44]. Prior studies suggest that BM-MNCs seeded in the vascular scaffolds assist in remodeling via paracrine communication [37, 44]. Monocyte chemoattractant protein-1 (MCP-1) secreted from mesenchymal stem cells (MSCs) was identified to be one of the signaling molecules involved in the former process [44]. Functionalization of acellular (cell-free) vascular scaffolds with MCP-1 revealed comparable outcomes to BM-MNCs-seeded scaffolds [44]. From a translational perspective, acellular vascular grafts are expected to follow a shorter path than cell-seeded grafts. Hence a lateral shift is observed lately towards cell-free vascular grafts to expedite their clinical translation [5, 359].

Acellular TEVGs have shown promising outcomes in animal models and human clinical trials [35, 37, 359]. Among biological grafts, autologous decellularized vessels (internal mammary artery [360] and umbilical artery [361]) are favored due to their regenerative potential and patency, but their sparsity limit clinical feasibility. Moreover, acellular xenografts pose the risk of immune rejection and disease transmission [362]. On the other side, polymeric grafts can be manufactured with high fidelity, which could be readily available for the patients and bypass the possibility of disease transmission. Prior reports show encouraging results for acellular polymeric grafts [108, 352, 363, 364]. For example, human acellular vessels (HAVs) are the most advanced acellular vascular grafts that are developed by seeding allogenic human smooth muscle cells (SMCs) on to a biodegradable polymeric scaffold, followed by their long-term maturation in dynamic conditions. Eventually, the graft polymer degrades while concomitantly allowing the extracellular matrix (ECM) deposition from seeded cells. The developed graft was decellularized to prevent immune rejection, and these HAVs showed promising results in human clinical trials [35, 90, 359]. One

ostensible setback of acellular vascular grafts is their limited bioactivity, which is generally addressed by functionalizing them with specific bioactive molecules. The functionalization aims to prevent acute thrombosis and stenosis, allow faster endothelialization, and mitigate intimal hyperplasia. Notably, studies showing the immobilization of bioactive molecules onto polymeric vascular scaffolds focus on the singular aspect of graft remodeling. For example, heparin functionalization of poly(glycerol sebacate) (PGS) grafts helps in preventing thrombosis [352, 365]. Researchers have also demonstrated improved endothelialization of dimethyloxalylglycine (DMOG) functionalized polycaprolactone (PCL) grafts by enabling hypoxia mimicking response [366]. Vascular endothelial growth factor (VEGF) improves graft endothelialization by capturing the circulating progenitor cells and prevent acute thrombosis [367, 368]. Other approaches include functionalization with integrin-binding ligand [369], microRNAs [370], nitric oxide (NO) [371], fibronectin [372], CD133 antibody [373], heparin [368, 371], etc. Scaffold functionalization with a specific bioactive molecule improves the graft performance, but it is surmised not to mimic the efficacy of cell seeding. BMMNCs and other MSCs confer therapeutic efficiency by secreting important chemokines and cytokines, including immunomodulatory, angiogenic, and anti-apoptotic factors [374]. MSCs derived extracellular vesicles (EVs) hold a plethora of signaling molecules, including cytokines and microRNA [98]. Few recent studies have ventured into exploring EVs' incorporation in acellular polymeric grafts with great success [375-377]. Loading of EVs in PCL-based vascular grafts significantly improved their patency in the hyperlipidemic rat and mitigated calcification. Mechanistic analysis revealed the immunomodulatory ability of MSC-derived EVs, as they induced phenotype transition of macrophages from M1 pro-inflammatory to M2c anti-inflammatory type [375]. MSC-derived exosomes also facilitated capturing endothelial progenitor cells (EPCs), assisting in faster endothelialization [376].

Among three potential sources of MSCs, bone marrow [40, 44] and adipose tissue-derived cells [378] have been widely explored in the field of vascular tissue engineering. By contrast, human Wharton's Jelly (WJMSCs) derived MSCs have shown limited application. Human Wharton's jelly ECM is a rich source of structural proteins (fibronectin, hyaluronic acid, collagens I, III, VI, XII, and tenascin-C) [379] and peptide growth factors (IGF-I, PDGF, FGF, TGF-β, EGF, VEGF, TIMP1, etc.) [380, 381]. The matrix also contains the WJMSCs derived exosomes [382]. The human umbilical cord is a medical waste and could be made available in large quantities; hence, recent studies have ventured into investigating the Wharton's jelly (WJ) matrix for tissue

engineering applications [381, 383-386]. The surface coating of glass coverslips with WJ matrix improved the growth and retention of vascular cells and MSCs [381]. Interestingly, the secretome of WJMSCs has been reported to posses a higher amount of angiogenic factors than the secretomes derived from bone marrow (BMMSCs) and adipose-derived mesenchymal stem cells (ADMSCs) [387]. Moreover, WJMSCs produce higher MCP-1 than their counterparts [388], which is crucial for TEVG remodeling. WJMSCs secreted bioactive factors might facilitate *in situ* endothelialization, host cell recruitment, and constructive graft remodeling [389].

Herein, aiming towards creating an acellular, clinically viable TEVG, silk-based vascular scaffolds are functionalized with decellularized human Wharton's Jelly (dWJ) matrix, for the first time. We hypothesized the preservation of WJMSCs secreted bioactive molecules in the Wharton's jelly matrix, which might improve the performance of acellular TEVGs. In this work, we followed a modified protocol to obtain dWJ matrix from human umbilical cords, avoiding any harsh chemical (e.g., detergents) or enzyme treatment, which presumably prevents the loss of bioactivity of bioactive molecules in the matrix. Our previously reported bi-layered silk scaffolds (described in Chapter 4) are functionalized with dWJ matrix in this study, and *in vivo* graft performance is investigated in the rabbit jugular vein as an interposition grafting model.

5.2 Materials and methods

5.2.1 Preparation and characterization of decellularized Wharton's jelly (dWJ) matrix

Discarded human umbilical cords (n=5) were obtained post-delivery from the Guwahati Neurological Research Centre (GNRC) hospital, Guwahati, after due institutional approval (reference no.: Inst/AS/2015/RR-2018/EC-103) and informed patient consent. Cords were transported in sterile ice-cold PBS and processed within 2-3h of procurement. The dWJ matrix was obtained following a previously described protocol with modifications [381, 382]. A schematic representation of the process is shown in **Figure 5.1A**. Briefly, the cord tissue was washed thoroughly with sterile Milli-Q water to remove any remaining blood. Post washing, ~2 cm tissue pieces were treated with red blood cells (RBC) lysis buffer (Sigma-Aldrich, USA) for 30 min at room temperature. The amnion membrane was cut open to remove umbilical arteries and a vein from each tissue piece. Wharton's jelly was scraped and transferred in sterile Milli-Q water (5 tissue pieces in 20 mL water) and kept at 4°C overnight on a shaker for dissolution. The obtained solution was filtered through a 70 µm strainer to remove any undissolved tissue chunk.

The filtrate at this stage contains water solubilized Wharton's jelly matrix components and MSCs. To obtain the dWJ matrix, cells were removed by centrifugation at 5000 rpm/10 min/4°C. The supernatant (dWJ matrix) was lyophilized and stored at -20 °C for further use. The DNA content in native and processed tissue was quantified to validate optimal decellularization using Pico green™ DNA kit (Molecular Probes, USA) following the manufacturer's protocol. Furthermore, the dWJ matrix solution (1 mg/mL) was prepared in filtered Milli-Q water and subjected for cytokine analysis using a human Bio-Plex ProTM Assay kit (Bio-Rad Laboratories, Inc, USA). The kit detects the following human cytokines: GM-CSF, IFN-γ, IL-2, IL-4, IL-6, IL-8, IL-10, and TNF-α. The analysis was performed according to the manufacturer's protocol.

5.2.2 Assessment of viability and functionality of dWJ treated vascular cells

5.2.2.1 Cell viability

The dWJ matrix was assessed for its compatibility with human umbilical vein endothelial cells (HUVECs) and human dermal fibroblasts (HDFs) at variable concentrations ranging from 0-1mg/mL. HUVECs (ScienCell Research Laboratories, USA) and HDFs (HiMedia Laboratories, India) were cultured following prescribed protocols and used between P1-P5. dWJ matrix stock solution (5 mg/mL) was prepared in PBS and sterilized under UV for 20 minutes. Cell viability analysis in the presence of dWJ matrix was performed using Live-cell staining and measurement of cell metabolic activity (AlamarBlue assay) following established protocols [390, 391]. Briefly, cells were seeded in a 12-well tissue culture plate (10,000 cells/well) for 24 h, followed by dWJ matrix treatment. Live cell imaging was performed using Calcein AM and visualized under a fluorescent microscope (EVOS FL, Life Technologies, USA). In a parallel experiment, the metabolic activity of cells was measured using AlamarBlue assay to quantify the cell viability in the presence of dWJ matrix post 1 and 3 days of treatment. Quantification of cell viability was represented after normalizing with Day 1 value.

5.2.2.2 Expression of functional genes (qRT-PCR)

Based on the outcome of the biocompatibility assessment of dWJ matrix, we used 1 mg/mL dWJ for all further *in vitro* 2D experiments. The effect of dWJ matrix treatment on HUVECs was further evaluated by investigating the expression profile of functional genes (CD31, eNOS, vWF, and VE-Cadherin). Cells were cultured in a 6-well plate and treated with dWJ matrix (1 mg/mL) for 24h.

Post-treatment, cells were processed for RNA isolation following TRizol based method as described in our previous study [392]. The cDNA was prepared from extracted RNA (200 ng/µL and 260/280 ratio=1.99-2.01) using a high-efficiency reverse transcription kit (Applied Biosystems, USA) and a thermal cycler. SYBR based standard RT-PCR was performed for target genes using Power SYBR Green PCR master mix (Applied Biosystems, USA) and real-time PCR machine (Applied Biosystems, Quant Studio 5, USA). The primer sequences of the target genes are listed in **Table 5.1**. Relative expression of genes was quantified by $2^{-\Delta Ct}$ method. Human β-actin was used as a housekeeping gene.

5.2.2.3 Cell migration assay

The migration of endothelial cells under the influence of dWJ matrix was analyzed by creating a circular wound in cell monolayer using a polydimethylsiloxane (PDMS) disc (diameter: 2 mm, thickness: 1 mm). A PDMS disc was kept at the center of each well of the 6-well plate, followed by seeding and culture of endothelial cells (10^6 cells/well) in complete growth media until confluence. The PDMS disc was then removed gently without disturbing the cell monolayer, leaving behind a circular blank space (without cells) at the center of the wells. Detached cells were removed by thorough washing with sterile PBS. Culture media (1% v/v FBS) was replenished in each well, and initial wound images were captured in a phase-contrast microscope. Experimental wells were treated with 1 mg (200 µL aqueous stock) of the sterile dWJ matrix. Images were captured again after 30h culture. Parallelly, HDF migration images were captured following standard scratch assay [377]. Images were processed using ImageJ to calculate the wound area following the Phase wound plugin (http://dev.mri.cnrs.fr/projects/imagej-macros/wiki/Wound_Healing_Tool). Percent wound closure with time was reported for cell migration analysis.

5.2.2.4 Nitric oxide (NO) quantification

Production of nitric oxide (NO), a functional molecule responsible for maintaining vascular tone, from HUVEC in response to dWJ treatment was investigated in 2D culture after 6h and 30h following the previous report [244]. A high cell density (3×10^5 cells /well) was cultured in 6 well tissue culture plates, which achieved confluency within a day. After 24h culture, fresh media was added to each well. The Control group was left untreated, while in the experimental group, 200 µL

of dWJ stock (1 mg matrix) was added. The culture was incubated for 6h and 30h, and spent media was collected, centrifuged to remove any cell debris, and processed for NO quantification using Griess reagent kit (Thermo Fisher Scientific, USA) following manufacturer's protocol. Fresh cell culture media with and without dWJ matrix was considered as a negative control. The NO concentration is reported after normalization with cell number.

5.2.3 *In vitro* assessment of dWJ treated human monocytes (THP-1)

5.2.3.1 Cell viability

THP-1 (human monocyte cell line) was procured from National Centre for Cell Science (NCCS), Pune, India, and maintained in suspension culture in RPMI 1640 media (Sigma-Aldrich, USA) following standard culture protocol. THP-1 cells (10,000 cells/well) were cultured in a 96-well tissue culture plate and differentiated to adherent macrophages (M0) by 100 ng/mL (162 nM) phorbol 12-myristate 13-acetate (PMA) (Sigma-Aldrich, USA) treatment for 16h. Cytotoxicity of dWJ matrix at variable concentrations (0-1 mg/mL) was studied using standard MTT assay following 24h treatment. The viability of THP-1 cells after dWJ treatment (1mg/mL) was further investigated by fluorescent live-dead imaging by staining cells with Calcein-AM and ethidium homodimer-1 dyes (Invitrogen, USA) following the manufacturer's instructions.

5.2.3.2 Immunomodulation analysis

Considering the presence of immunomodulatory cytokines in dWJ matrix, we looked into its ability to modulate macrophage polarization. THP-1 cells were differentiated into adherent macrophages followed by dWJ treatment (1 mg/mL) for 24h. Qualitative analysis of immunomodulation was studied by immunofluorescent staining of cells with CD68, CCR7, and CD163 (1:100, Abcam) primary antibodies, and corresponding AlexaFlour 488, FITC tagged secondary antibodies (1:200, Abcam) following standard protocol. Images were captured using a fluorescent microscope. Fluorescence images (n=6 per group) were further processed to quantify the expression of specific markers using ImageJ software following our previously reported methodology [378]. Expression of phenotype-specific genes (TNFα, CCR7, IL-6, MCP1, and IL-10) was further quantified using qRTPCR following the protocol, as mentioned earlier, to ascertain the effect of dWJ treatment on human macrophage phenotype modulation. Primer sequences of genes are listed in **Table 5.1**.

5.2.4 Fabrication and characterization of silk TEVGs

The aqueous silk fibroin (SF) protein was obtained from *Bombyx mori* (BM) cocoons and *Antheraea assama* (AA) silk glands following established protocols [233, 332]. Tubular bi-layered silk scaffolds were prepared using 3D printed molds following our previous methodology (described in Chapter 4). Scaffold variants used in this study are composed of different inner porous layers as follows: 1) BM-6% (w/v) *Bombyx mori*, 2) BA: 1:1 ratio of 10% (w/v) *Bombyx mori* and 2% (w/v) *Antheraea assama*, 3) BAW: BA + 3 mg/mL dWJ matrix. The choice of using a blend of BM and AA was motivated considering the limitation associated with AA silk, which forms hydrogel at higher concentrations (>3%, w/v). To maintain the structural similarity among different experimental groups, the same final concentration (6%, w/v) was used to fabricate the inner porous layer. The inner layer of all three scaffold types (BM, BA, BAW) were coated with same outer nanofibrous electrospun layer, following our previous study [378]. The electrospinning solution was consisted of 1:1 (v/v) ratio of 10% (w/v) BM silk and 10% (w/v) polycaprolactone (PCL, Mn 80,000, Sigma-Aldrich, USA) dissolved in 1,1,1,3,3,3- Hexafluoro-2-propanol (HFP, Sigma-Aldrich, USA). BAW scaffolds were crosslinked using EDC/NHS prepared in 80% (v/v) ethanol for 12h [385]. The crosslinked scaffolds were washed in sterile water on a shaker for 12h and stored at 4°C until further use. Similarly, stable crosslinking of dWJ matrix component (collagen I) was investigated in scaffold cross-sections by immunofluorescence analysis following standard protocol. Histological sections of bare scaffolds (without cells, after crosslinking step) were treated with anti-human Col-I primary antibody (1:100, Abcam) followed by fluorescent tagging with secondary antibody (Alexa Fluor 488, 1:500, Abcam). Images were captured using a fluorescent microscope.

For morphological analysis, scaffold cross-sections were obtained using a fine blade, preventing any morphological alteration. The surface morphology of silk scaffolds was analyzed under a field emission scanning electron microscope (FESEM, Zeiss, Sigma) after gold sputtering. Captured FESEM images were further processed using ImageJ software to calculate pore size distribution and wall thickness (n=6 images processed per experimental group). *In vitro* scaffold degradation in the presence and absence of protease enzyme was quantified following our previously published protocol (described in Chapter 4). Scaffold discs were prepared as described in "*In vivo immunomodulation analysis of 3D silk scaffolds"* and investigated for swelling and protein release profile in accordance with previous study [333]. Briefly, protein release from silk

scaffolds was assessed following the Bradford method. Silk scaffolds of uniform dry weight (approximately 10 mg, n=6 for each experimental group) were incubated in 1 mL PBS at 37℃. At predefined time-points, releasates (20µL) were incubated in 200 µL Bradford reagent for 20 min, followed by spectrophotometric analysis at 525 nm. The following standard formula was implemented to calculate the protein release over time:

$$\text{Protein release (\% w/w)} = (C_2/C_1)*100$$

C_1 represents the initial dry weight (mg) of the scaffold and C_2 represents protein content (mg) released over time.

The biocompatibility of 3D silk scaffolds with HUVEC cells was analyzed. Scaffold discs (2 mm thickness, 6 mm diameter) were prepared for all three variants. Sterilized scaffolds were conditioned with the culture media overnight in a 24-well plate and seeded with 10^5 cells (HUVEC) per scaffold. At predefined time points, the cellular metabolic activity was assessed using AlamarBlue assay [234]. The percentage Alamar reduction value was quantified at each time point, and results are reported after normalization with day 1 value. HDF migration was also checked in 3D porous scaffolds. Rectangular scaffold strips (length: 8-10 mm, width: 1 mm, height: 1 mm, n=3 each) were seeded with ~10,000 HDF cells at each longitudinal end and cultured for up to 7 days. At predefined time points, scaffolds were treated with MTT [3-(4,5-dimethylthiazol-2-yl)-2,5-diphenyltetrazolium bromide] for 4h following the previously described protocol [393]. The resulting blue formazan crystals indicated the boundaries of cell growth. The macroscopic images were captured and processed using ImageJ software to calculate the % area coverage over time.

5.2.5 *In vivo* immunomodulation analysis of 3D silk scaffolds

All animal studies were performed post approval from the animal ethical committee (IAEC), West Bengal University of Animal & Fishery Sciences, Kolkata vide permit no. Pharma/IAEC/163. Female adult New Zealand rabbits (1500-2000 g of body weight) were used for subcutaneous implantation of silk scaffolds. 3D silk scaffolds (BM, BA, and BAW, a composition similar to inner layers of silk TEVGs) were prepared by molding the aqueous solution in plastic molds, keeping a 2 mm solution height. Molds were kept at -20℃ overnight and lyophilized for 24h. Circular discs were cut using a biopsy punch (6 mm diameter, 2 mm thickness). Sterilized scaffold discs were soaked in PBS and implanted subcutaneously on the rabbit's dorsal side for five days

and one month (n=3 for each group). Scaffolds were explanted at predefined time points. Half a portion of each explant was fixed in neutral buffered formalin (NBF, Sigma-Aldrich, USA) and incubated with 30% (w/v) sucrose for 2h followed by cryosectioning to obtain 5 µm sections. Histological sections were stained with hematoxylin & eosin (H&E, Merck, USA) following standard protocol. In addition, the immunohistological analysis was performed by staining samples with anti CD68, anti CD163, and anti CCR7 primary antibodies (1:100 dilution, Abcam) followed by treatment with AlexaFlour 488 and DyLight 594 tagged corresponding secondary antibodies (1:200, Abcam). All sections were counterstained with DAPI, mounted and imaged using a fluorescent microscope. The remaining half of each sample was stored in RNA later (Sigma-Aldrich, USA). Tissue samples were homogenized and processed for qRTPCR for the following genes: β-actin, IL-1β, IL-6, IL-10, TNFα, and TGFβ. Primer sequences of genes are listed in **Table 5.1**.

Table 5.1. *qRT-PCR primer sequences*

S.No	Gene	Primer Sequence	Accession No.
1	Human β-actin	**F** 5′- CACAGGGGAGGTGATAGCAT-3′ **R** 5′- CTCAAGTTGGGGGACAAAAA-3′	NM_001101.5
2	Human PECAM (CD31)	**F** 5′-TCCGATGATAACCACTGCAA-3′ **R** 5′-TGGTGGAGTCTGGAGAGGA-3′	NM_000442.5
3	Human eNOS	**F** 5′-TTCCGGGGATTCTGGCAGGAG-3′ **R** 5′-GCCATGGTAACATCGCCGCAG-3′	NM_000603.5
4	Human vWF	**F** 5′-TCTTCCAGGACTGCAACAAG-3′ **R** 5′-TCCGAGATGTCCTCCACATA-3′	NM_000552.5
5	Human VE-cadherin (CD144)	**F** 5′-ACCCCCACAGGAAAAGAATC-3′ **R** 5′-GACTTGGCATCCCATTGTCT-3′	NM_001795.5
6	Human TNFα	**F** 5′-GAGGCCAAGCCCTGGTATG-3′ **R** 5′-CGGGCCGATTGATCTCAGC-3′	NM_000594.4
7	Human CCR7	**F** 5′-AAGCCTGGTTCCTCCCTATC-3′ **R** 5′-ATGGTCTTGAGCCTCTTGAAATA-3′	NM_001301718.1
8	Human MCP1	**F** 5′-CAGCCAGATGCAATCAATGCC-3′ **R** 5′-TGGAATCCTGAACCCACTTCT-3′	NM_002982.4
9	Human IL-10	**F** 5′-GACTTTAAGGGTTACCTGGGTTG-3′ **R** 5′-TCACATGCGCCTTGATGTCTG-3′	NM_000572.3
10	Human IL-6	**F** 5′-ACTCACCTCTTCAGAACGAATTG-3′ **R** 5′-GTCGAGGATGTACCGAATTTGT-3′	NM_000600.5

11	Rabbit β-actin	**F** 5′-AGGAGAAGCTGTGCTACGTG-3′ **R** 5′-CAGGAAGGAGGGCTGGAACA-3′	NM_001101683.1
12	Rabbit IL-1β	**F** 5′-TTGAAGAAGAACCCGTCCTCTG-3′ **R** 5′-CTCATACGTGCCAGACAACACC-3′	NM_001082201.1
13	Rabbit IL-6	**F** 5′-GAACAGAAAGGAGGCACTGG-3′ **R** 5′-CTCCTGAACTTGGCCTGAAG-3′	NM_001082064.2
14	Rabbit IL-10	**F** 5′-CAAGCCTTGTCGGAGATGAT-3′ **R** 5′-TTTTCACAGGGGAGAAATCG-3′	NM_001082045.1
15	Rabbit TNFα	**F** 5′-CTGCACTTCAGGGTGATCG-3′ **R** 5′-CTACGTGGGCTAGAGGCTTG-3′	NM_001082263.1
16	Rabbit TGFβ	**F** 5′-CAGTGGAAAGACCCCACATCTC-3′ **R** 5′-GACGCAGGCAGCAATTATCC-3′	NM_001082660.1

5.2.6 Implantation of silk conduits in rabbit jugular vein as interposition graft

Female adult New Zealand rabbits (1500-2000 g of body weight) were used for silk scaffold implantation. A total of 9 rabbits were used for this study. Animals were divided into three groups (3 each), and each group received BM, BA, and BAW silk grafts, respectively. Scaffold lumen diameter was selected to match the diameter of the rabbit jugular vein. Anesthesia was induced using xylazine hydrochloride at 5mg/kg body weight and ketamine hydrochloride at 33 mg/kg body weight. The Neck portion of the animal was shaved, and an incision was made to expose the internal jugular vein (JV). It was further bisected using micro scissors between microvascular clamps. The silk scaffold was anastomosed with proximal and distal segments of the internal jugular vein in an end-to-end manner as an interposition graft with 10-0 Ethilon following microvascular anastomosis technique. Once the graft is secured and no blood leakage was observed at anastomotic sites, micro clamps were released. The restoration of blood flow was evaluated and confirmed by the appearance of the venous pulse. The skin and muscle layer were closed using 3-0 polyglactin sutures (McKesson, Richmond, Va). Post-surgery, animals were subcutaneously injected with buprenorphine hydrochloride (0.5 mg/kg) every 12h until three days.

Post-operatively, graft patency was monitored by color Doppler imaging after day 12 and day 60 (at the time of graft retrieval). The middle portion of explants was used for histological analysis, whereas ~1mm tissue section from the proximal, middle and distal portion from each explant were subjected for extracellular matrix (ECM) proteins (collagen and elastin) quantification. To assess host cell infiltration in silk grafts, 5 µm cryosections were stained for H&E staining. Furthermore, tissue cryosections were also stained with DAPI (Sigma-Aldrich,

USA) to visualize the cell nucleus. Brightfield images of H&E stained sections and fluorescent images of DAPI stained sections were captured using a fluorescence microscope. Infiltrated cells were quantified by processing the DAPI stained images using ImageJ software following our previously published protocol (described in Chapter 4).

5.2.7 Graft remodeling and deposition of ECM proteins

Histological sections of explanted TEVGs were mounted on coated slides and processed for H&E staining (for cellular distribution), Masson's trichrome staining kit (Sigma-Aldrich, USA) (for collagen), and Elastic stain kit (Modified Verhoeff Van Gieson Elastic Stain Kit, Sigma-Aldrich, USA) (for elastin) following manufacturer's protocols. Tissue explants were further processed for quantification of ECM proteins: collagen (Hride Tullberg-Reinert method) and elastin (Ninhydrin assay), as described in Chapter 4. Native rabbit jugular vein was also processed and considered as the positive control. The results of collagen and elastin quantification were presented after normalizing with initial wet tissue weight. Bare silk scaffolds were also processed as the negative control. Infiltration of host vascular cells into graft during remodeling was detected by immunostaining with cell-specific antibodies (calponin and αSMA for smooth muscle cells, CD31 for endothelial cells) (1:100, Abcam) using Vectastain Elite ABC Universal kit (Vactor laboratories) following manufacturer's protocol. Stained sections were imaged in the brightfield mode of the microscope (Nikon ECLIPSE Ti2). The presence of resident macrophages was further studied by immunofluorescence staining of explant sections using anti CD68, anti CD163, and anti CCR7 antibodies followed by counterstaining with corresponding secondary antibodies and DAPI. Stained microscopic images were processed per our previous report to quantify the percent area coverage (described in Chapter 4) and M2/M1 macrophage phenotype ratio.

5.2.8 Biomechanical analysis of silk TEVG explants

Uniaxial circumferential biomechanical testing of silk TEVG explants was performed in accordance with the previously described methodology (Chapter 4). Briefly, 2 mm long circular tissue rings were obtained from the proximal, middle, and distal part of TEVG explant (n=6), and mounted in two U-shaped stainless steel hooks (rod diameter: 0.5 mm) through the lumen connected to pneumatic grips of universal testing machine (UTM, Instron 5944, USA). Samples were pre-conditioned at 5% strain for 10 cycles, followed by recording load-displacement data at

2 mm/min crosshead speed until failure in hydrated conditions. Stress-strain curves, modulus at low (low modulus) and high stretch regions (high modulus), stress, and strain at failure points were further calculated as described previously in Chapter 4.

5.2.9 Statistical analysis

Statistical significance of all data was analyzed using Origin 8.0 software following one-way analysis of variance (ANOVA). Analysis of equal variance was performed using the Levene test and means comparison between groups was performed using post hoc Tukey's test. Two experimental groups were considered significantly different, having p-values less than 0.05. All experimental data were acquired for at least n=3 samples (both biological and technical replicates), unless otherwise noted, and reported as mean ± standard deviation (SD).

5.3 Results

5.3.1 Decellularization and cytokine profile of Wharton's jelly matrix

The Wharton's jelly matrix was obtained in the powdered form, post lyophilization, which was white in appearance and easily soluble in water without forming any clumps (**Figure 5.1A**). The aqueous solubility of dWJ matrix allowed it to mix with silk fibroin solution homogenously. A 5 mg of dWJ matrix was dissolved in 1 mL of silk solution (6% w/v) without showing any protein coagulation. However, on further increasing the dWJ concentration, silk protein coagulation was observed, resulting in lump formation. DNA quantification analysis revealed significantly less (10 times lesser) amount of DNA in dWJ matrix post decellularization (~40 ng/mg dry weight) as compared to native umbilical cord tissue (~400 ng/mg dry weight) ($p<0.01$). In accordance with a previous report, the DNA content of decellularized tissue was within the acceptable limit (50 ng/mg tissue) [394]. We further analyzed the presence of inflammatory cytokines in dWJ matrix. Among the investigated cytokines, IL-8 concentration was maximum (1190 ± 94 pg/mL), followed by IL-6 (469 ± 100 pg/mL). Remaining cytokines were present in minimal amount: TNF-α (3.53 ± 0.13 pg/mL), GM-CSF (3.09 ± 0.16 pg/mL), IL-4 (0.72 ± 0.08 pg/mL) and IL-10 (0.21 ± 0.04 pg/mL) (**Figure 5.1B**).

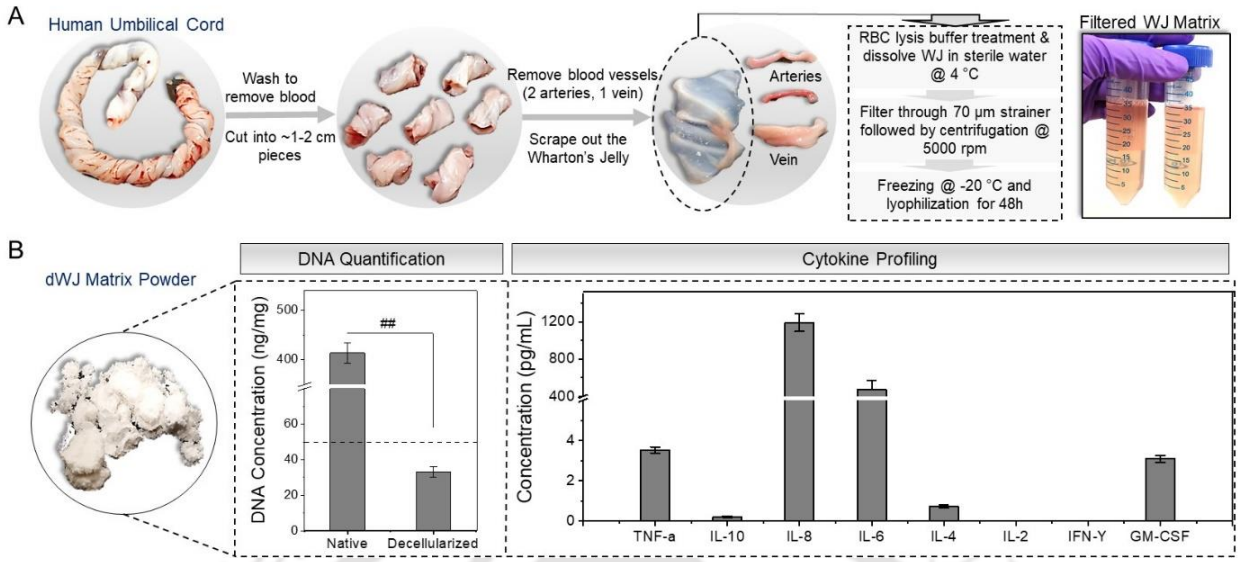

Figure 5.1. *Isolation and characterization of human decellularized Wharton's Jelly (dWJ) matrix. (A) Scheme showing the stepwise process to isolate dWJ matrix. (B) Aqueous dWJ solution was lyophilized to obtain powder form (white color) and re-dissolved in water to obtain the desired concentration. DNA quantification data are showing the decellularization of WJ matrix (n=5). The dotted line represents the allowed threshold limit of DNA for decellularized tissue. Cytokine profiling of dWJ matrix showing the presence of immunomodulatory cytokines (n=3). (##p<0.01)*

5.3.2 dWJ treatment improves performance of vascular cells in monolayer culture

Live-cell imaging suggested that even at higher concentrations (1 mg/mL), dWJ matrix did not significantly affect the viability of both vascular cells (human umbilical vein endothelial cells: HUVEC and human dermal fibroblasts: HDF). Viable cells were observed after three days at all investigated concentrations, and no morphological alteration was observed compared to the standard tissue culture plate (**Figure 5.2A-B, D**). Cell viability and proliferation were further quantified using the AlamarBlue assay. Cells proliferated ~1.2 folds over three days in control and dWJ treated groups, signifying no detrimental effect of dWJ treatment on cell viability (**Figure 5.2C, E**). Subsequent increment of aqueous dWJ concentration adversely affected the HUVEC cell viability. Considering the biocompatibility of dWJ matrix with human endothelial cells up to 1mg/mL, the same concentration was used henceforth for further *in vitro* analysis.

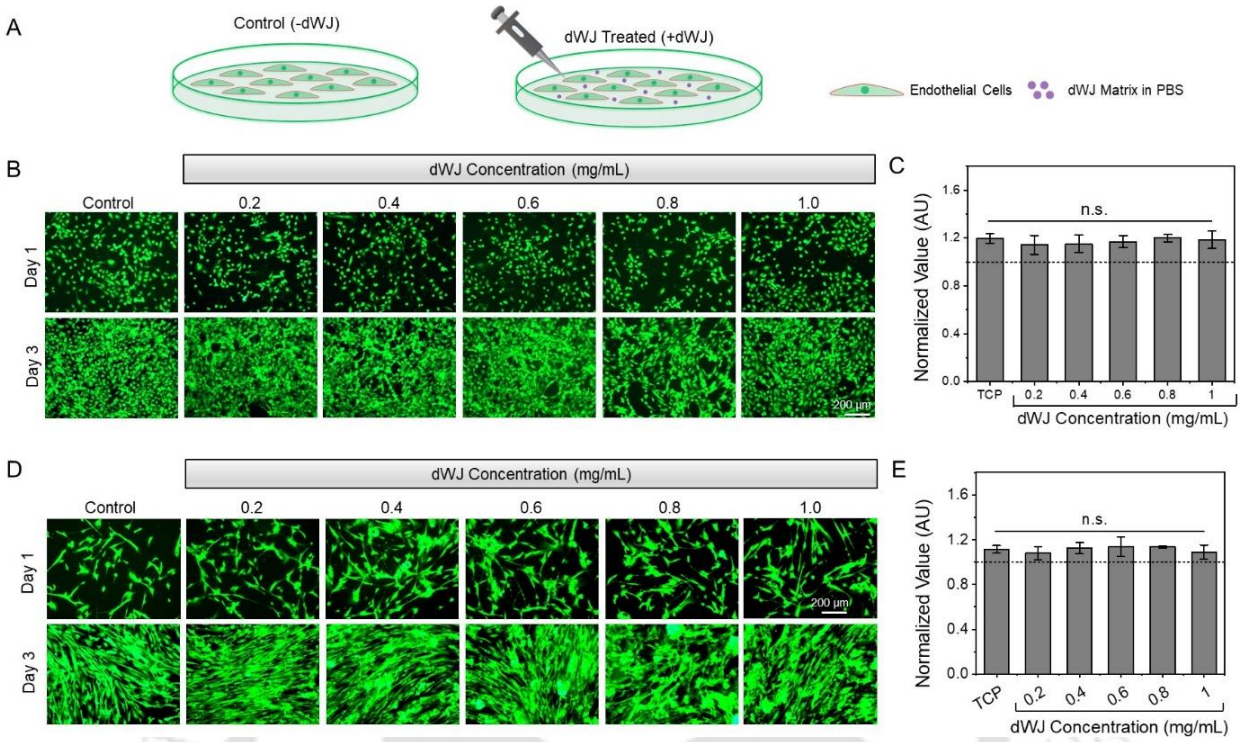

Figure 5.2. *Effect of dWJ matrix on vascular cell viability. (A) Schematic representation of aqueous dWJ matrix treatment on a 2D culture of vascular cells. Live cell imaging showing the viability of (B) HUVEC and (D) HDF cells after 1 and 3 days of aqueous dWJ treatment at varying concentrations (0-1 mg/mL). Quantitative assessment of metabolic activity of (C) HUVEC and (E) HDF cells at different dWJ concentrations. The dashed line is representing baseline metabolic cellular activity after 1 day of cell seeding. (n.s.=not significant)*

The expression profile of various endothelial functional genes (vWF, CD31, eNOS, and VE-Cadherin) by quantitative real-time PCR was investigated to assess the effect of dWJ matrix treatment onto cellular functionality. All of the studied genes play a crucial role in maintaining the overall blood vessel tone. Interestingly, endothelial cells showed significant upregulation of CD31 (~2000 fold), eNOS (~50 fold), and VE-cadherin (~1600 fold) genes after dWJ matrix treatment ($p<0.01$). However, vWF expression remained unchanged, and no significant difference was observed (**Figure 5.3**).

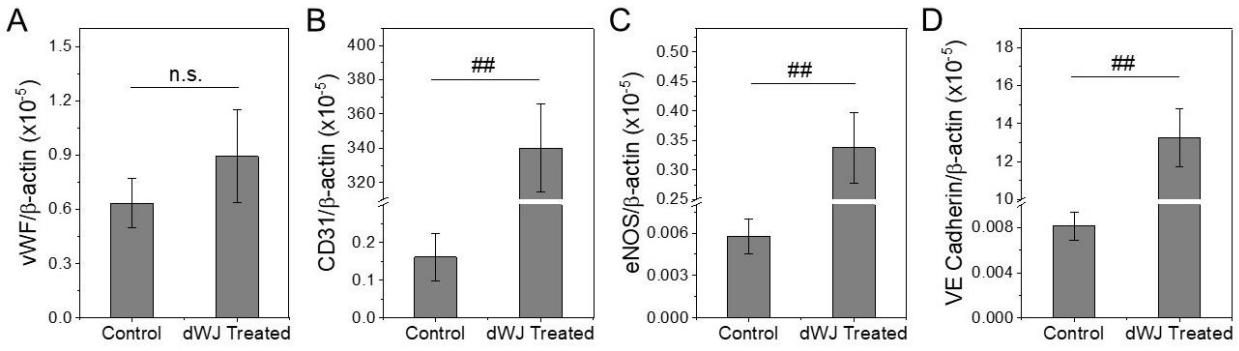

Figure 5.3. *Effect of dWJ matrix on HUVEC function. Real-time gene expression quantification for functional endothelial cell genes (D) vWF, (E) CD31, (F) eNOS and (G) VE-Cadherin after 24h aqueous dWJ treatment (1 mg/mL). (##p<0.01, n.s.=not significant)*

After implantation in animals, graft remodeling relies on the recruitment and migration of host cells from the surrounding tissue. We performed the cell migration assay as an indirect measurement of cell migration from the host tissue to the graft. Results suggested a faster migration of HUVEC and HDF cells in the presence of dWJ matrix (observed at 30h) (**Figure 5.4A-B, D**). Quantification of the wound area corroborated a similar pattern. dWJ matrix treated group covered ~85% wound area as compared to ~40% for the untreated group ($p<0.01$), signifying HUVEC migration at two times faster rate post dWJ treatment (**Figure 5.4C**). Similarly, approximately 2.5 times faster migration rate was recorded for HDF cells (**Figure 5.4D-E**). Furthermore, the amount of NO produced by endothelial cells was quantified, responsible for maintaining the vascular tone. At both time points (6h and 30h), endothelial cells treated with dWJ matrix produced a significantly higher (~47 and ~9 times, respectively) amount of NO than the control group ($p<0.01$) (**Figure 5.4F**). The NO concentration is reported after normalization with cell number.

5.3.3 Viability and immunomodulation of human THP-1 monocytes

With recent advancements in the vascular tissue engineering field, it is now established that the circulating cells, including monocytes, play a crucial role in the maturation and remodeling of vascular grafts [44, 367]. Hence, the effect of dWJ treatment on human monocytes was investigated (**Figure 5.5A**). The adherent THP-1 cells were subjected to various concentrations of dWJ matrix to analyze its cytotoxicity. MTT results showed no cytotoxic effect of dWJ matrix (0-1 mg/mL) on THP-1 cells (**Figure 5.5B**). The viability of the attached cells was further validated by live-dead fluorescence imaging. In both control and dWJ treated groups, mostly live cells

(fluorescing green) were present with the negligible presence of dead cells (fluorescing red). The results indicated that dWJ matrix does not show any cytotoxic effects on THP-1 derived macrophages at 1 mg/mL concentration (**Figure 5.5C**).

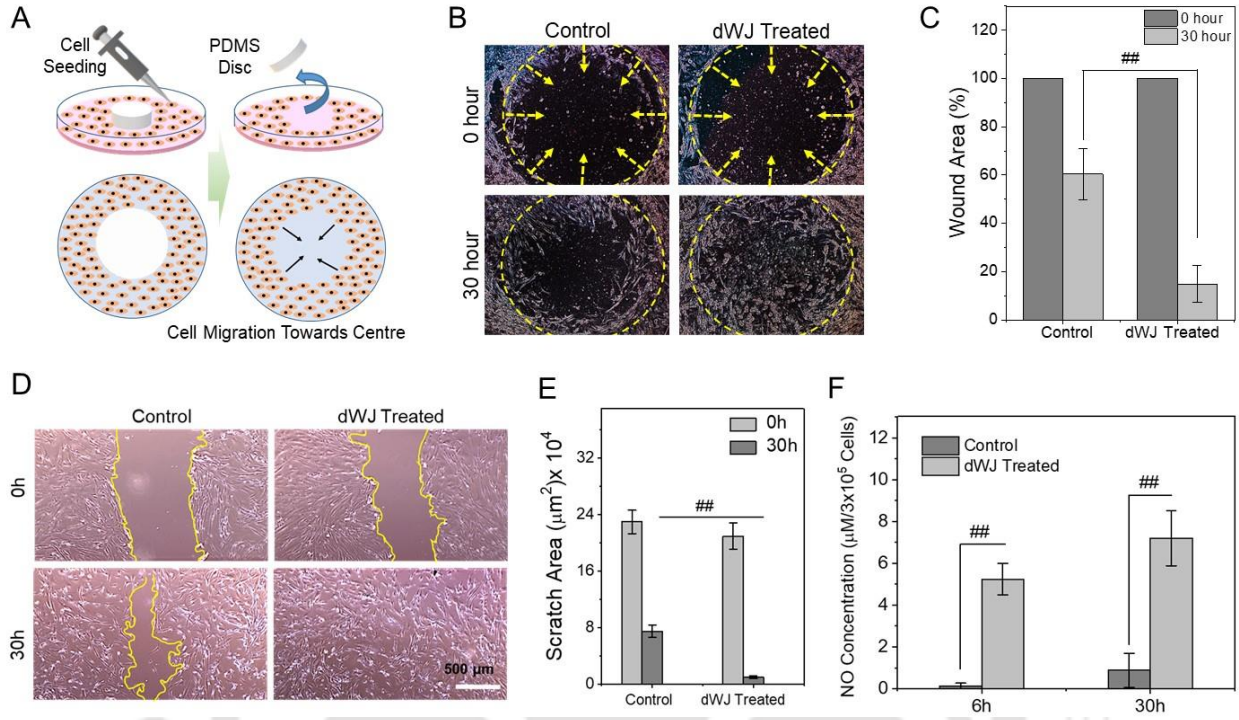

Figure 5.4. *Effect of dWJ matrix on vascular cell migration and HUVEC function. (A) Scheme representing the process followed for analyzing the migration of HUVEC under the influence of aqueous dWJ treatment. (B) Phase-contrast images of HUVEC processed using the 'Find Edges' function of ImageJ, showing the migration of cells inwards towards the center of the circle marked with a yellow dashed line. Dotted arrows are representing the cellular migration towards the center. (C) Quantification of cell migration in terms of percentage wound area over time. (D) Representative phase contrast microscopic images of scratch wound assay showing migration of HDF cells in control and dWJ treated groups. (E) Quantification of wound area covered over time. (F) Quantification of nitric oxide (NO) production from HUVEC after 6h and 30h aqueous dWJ treatment. (##p<0.01)*

Immunofluorescence imaging of control and dWJ treated THP-1 cells showed positive staining for CD68 and CCR7. However, THP-1 cells markedly stained positive for CD163 in dWJ treated group (**Figure 5.5D**). Quantitative real-time gene expression analysis revealed the downregulation of TNF-α, CCR7, and IL-6 genes, post 24h dWJ treatment. On the contrary, dWJ matrix induced the upregulation of MCP1, whereas no significant difference was observed for IL-10 (**Figure 5.5E-I**).

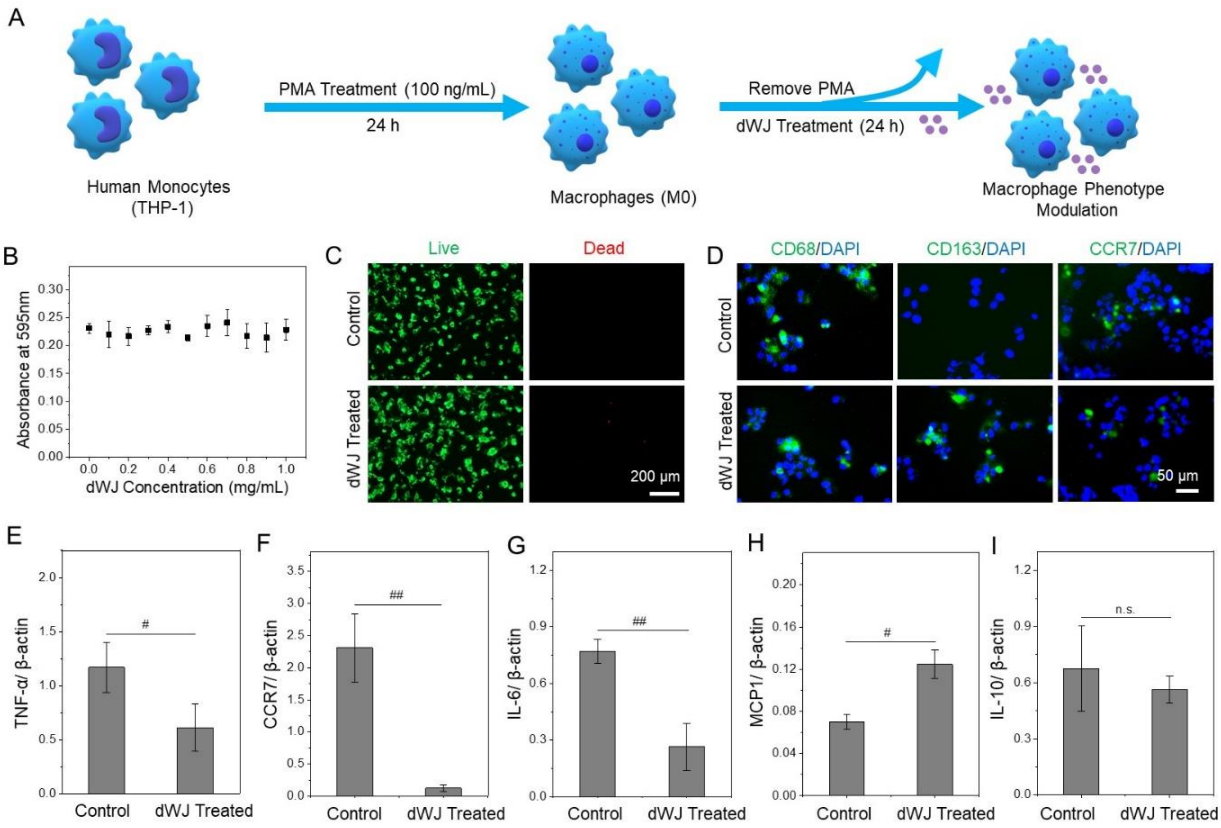

Figure 5.5. *In vitro analysis of the effect of aqueous dWJ matrix treatment on human monocytes (THP-1). (A) Scheme representing monocyte differentiation and aqueous dWJ treatment. (B) Quantification of THP-1 cells viability after 24h dWJ matrix treatment. (C) Live/Dead fluorescent microscopic images showing the viability of THP-1 cells. (D) Representative immunofluorescent images showing expression of CD68 (pan macrophage marker), CD163 (M2 marker), and CCR7 (M1 marker) in control and dWJ treated THP-1 cells. Real-time qPCR analysis quantifying the expression of (E) TNF-α, (F) CCR7, (G) IL-6, (H) MCP1, and (I) IL-10 genes in control and dWJ treated THP-1 cells. (#p<0.05, ##p<0.01, n.s.=not significant)*

5.3.4 Physical characterization of bi-layered tubular silk scaffolds and assessment of vascular cell viability and migration

Bi-layered composite silk scaffolds were fabricated, as shown in **Figure 5.6A**. The porous core layer supports the recruitment and growth of host cells. The outer electrospun layer provides mechanical resilience to the graft and prevents the transmural flow of blood through the scaffold wall post-implantation. SEM images of grafts' cross-sections showed the inner porous and dense outer layer. None of the grafts revealed any delamination among the two layers. The average thickness of the inner porous and the dense outer layer was 535 ± 38 µm and 51 ± 10 µm, respectively, resulting in 586 ± 48 µm total thickness of bi-layered scaffold wall. The core layer of all scaffold variants displayed the presence of interconnected pores (**Figure 5.6B**).

Quantification of pore size of the core layer revealed an overlapping distribution ranging 20-65 µm (mean value of 40µm) for BM, 20-72 µm (mean value of 40µm) for BA, and 10-55 µm (mean value of 32 µm) for BAW scaffolds ($p>0.05$) (**Figure 5.6C**). A minor, insignificant shift in porosity range for BAW scaffolds might be resulting from the presence of structural components of Wharton's jelly matrix.

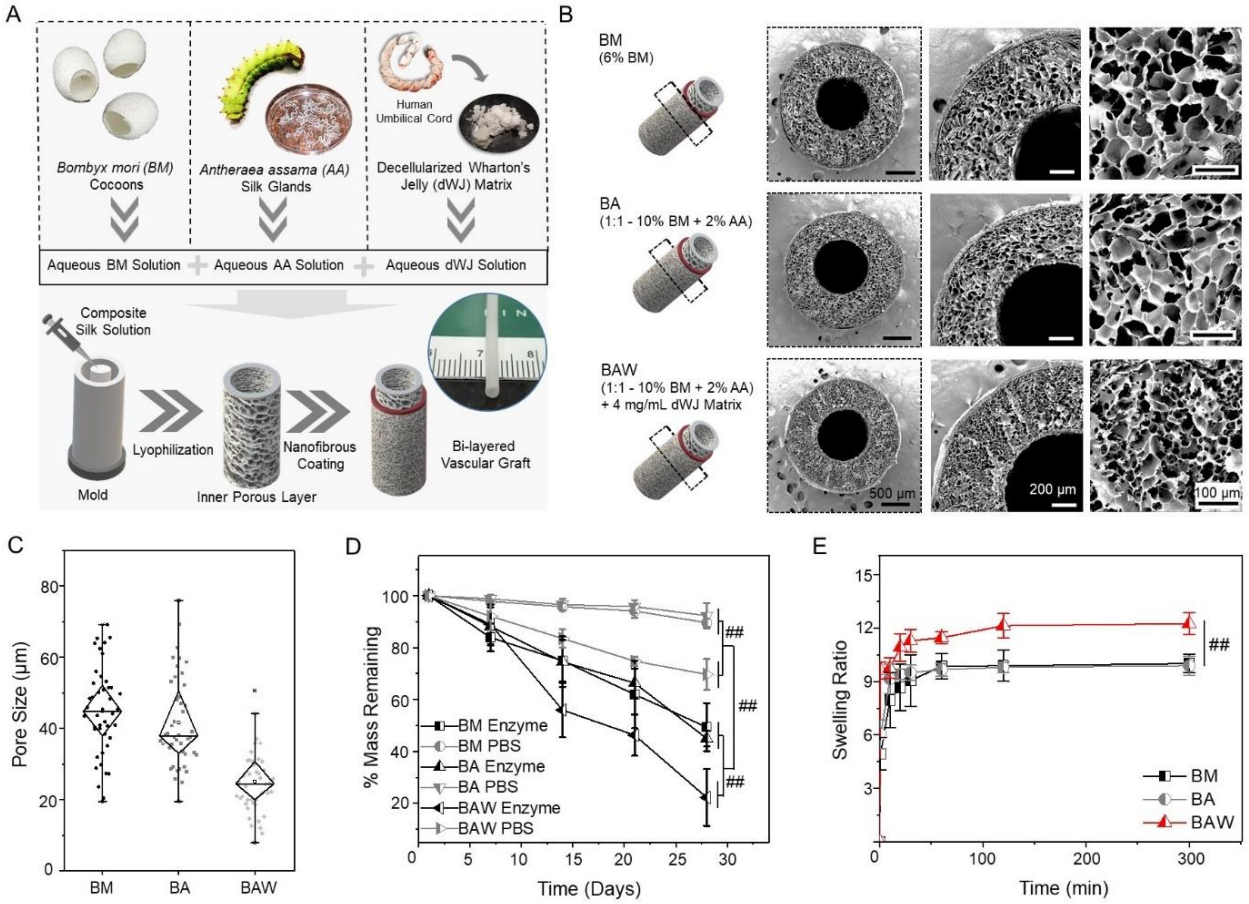

Figure 5.6. *Fabrication and physical characterization of tubular silk bi-layered vascular grafts. (A) Representative scheme showing the stepwise fabrication of bi-layered silk vascular grafts. (B) Scanning electron microscopic (SEM) images of cross-sections of grafts showing porosity and pore interconnectivity of the inner core layer. (C) Graph representing quantification of pore size of the inner porous layer for all three scaffold variants calculated by processing the SEM images (n=6, each group). (D) In vitro quantification of scaffold degradation in control (PBS) and treated (protease enzyme) groups over 28 days. (E) Graph representing water retention capability of silk scaffolds. (##p<0.01)*

In vitro scaffold degradation data revealed a faster degradation in the presence of protease enzyme for all variants ($p<0.01$). In both treated and untreated groups, BAW scaffolds showed a comparatively faster degradation profile than BM and BA scaffolds. Minimal scaffold degradation

(10.43 ± 1.58% and 7.70 ± 4.87% mass loss for BM and BA scaffolds, respectively, over 28 days) was recorded in the absence of enzyme; however, BAW scaffolds showed significantly higher mass loss (30.33 ± 5.94%) ($p<0.01$). A similar trend was observed for the enzyme-treated group over 28 days (50.68 ± 9.28% and 55.05 ± 2.96% vs. 77.78 ± 10.92% for BM and BA vs. BAW, respectively) ($p<0.01$) (**Figure 5.6D**). Further analysis of scaffold swelling property (water retention ability) revealed a superior swelling ratio for BAW scaffolds (12.25 ± 0.6) as compared with BM and BA scaffolds (10.01 ± 0.52 and 9.88 ± 0.5 respectively) post 300 mins ($p<0.01$). Early swelling data showed that all scaffold variants reached saturation after 30 minutes and followed the same trend at later time points (**Figure 5.6E**).

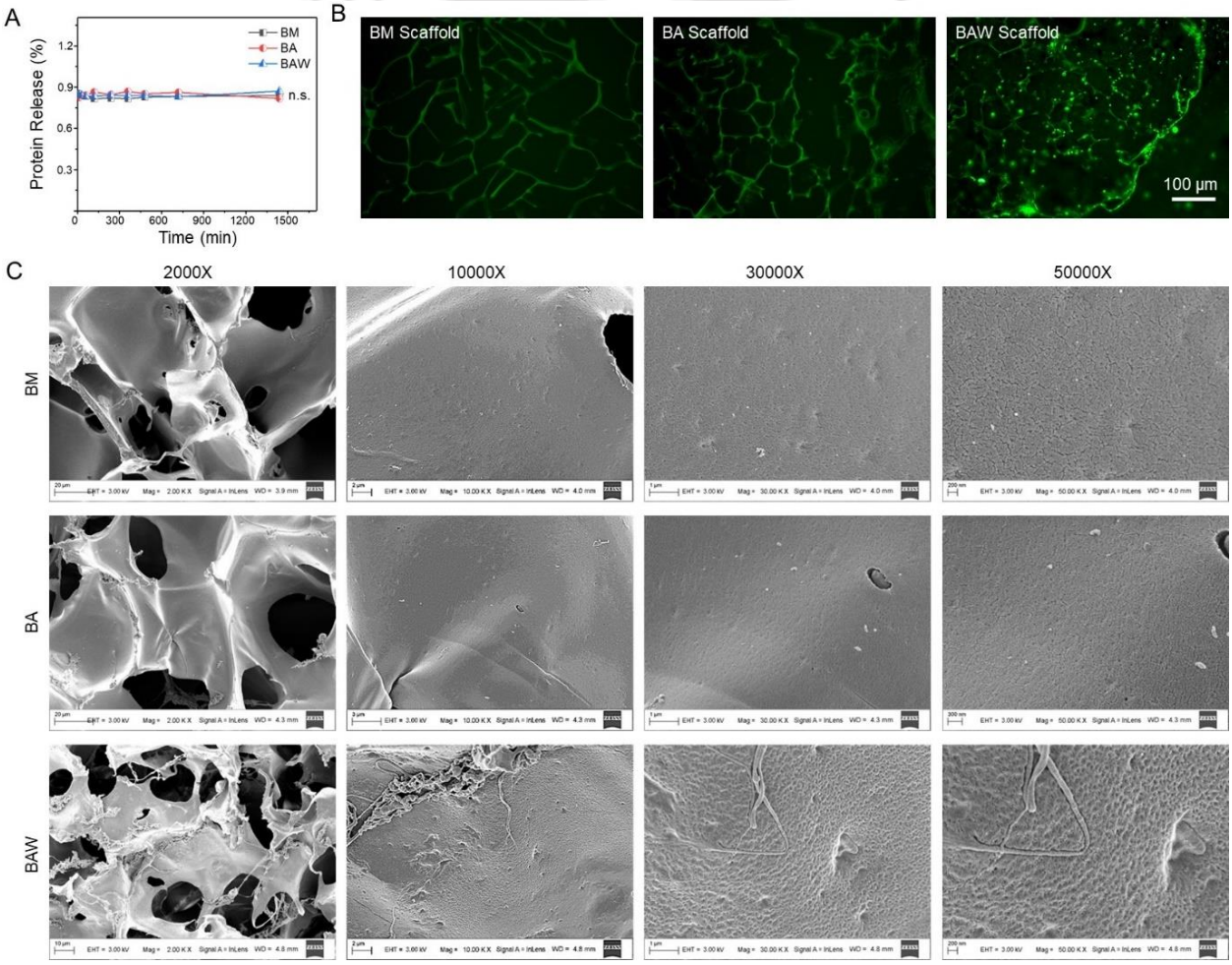

Figure 5.7. *Physical characterization of tubular silk bi-layered vascular grafts. (A) Quantification of protein release from silk scaffolds. (B) Fluorescent microscopic images of scaffold cross-sections stained with collagen-I antibody (green dots). Positive staining for BAW scaffolds substantiates their stable functionalization with dWJ matrix. (C) High magnification scanning electron microscopic (SEM) images of cross-sections of silk TEVGs. (n.s.=not significant)*

To analyze the scaffold integrity and ensure stable crosslinking, protein release from scaffolds was quantified for 24h. Results suggested less than 1% protein release for all scaffold variants corroborating their stability (**Figure 5.7A**). BAW scaffolds at the pre-implantation stage showed positive staining for collagen I (col-I), corroborating the stable integration of dWJ matrix components in the scaffold struts (**Figure 5.7B**). High magnification SEM images revealed a smoother surface of BM and BA scaffold struts; whereas, a significantly rougher surface for BAW. Notably, cross-sections of scaffold struts showed fibrous structures, substantiating the presence of dWJ matrix structural components in BAW scaffolds (**Figure 5.7C**).

The proliferation of endothelial cells on 3D BM, BA, and BAW scaffolds was analyzed by measuring the metabolic activity over 14 days. The result is reported after normalization with day one values (**Figure 5.8**). All three scaffold types supported the endothelial cell growth over 14 days, and no significant difference was observed in the growth rate among experimental groups. On day 14, a ~3 fold increase in cell number was recorded compared with day 1. The results suggest that in 3D porous silk scaffolds, the presence of dWJ matrix in BAW did not significantly affect the growth rate of endothelial cells. HDF migration analysis in 3D porous silk scaffolds revealed significant improvement in cell migration rate in BAW scaffolds on day 7, calculated in terms of % area coverage over time (**Figure 5.9A-C**).

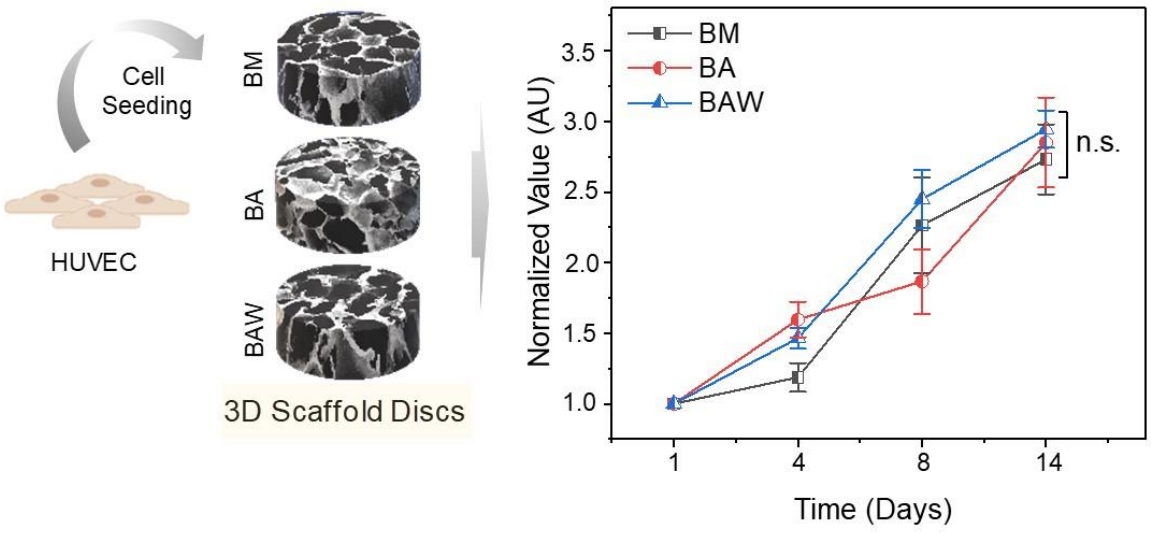

Figure 5.8. *In vitro HUVEC viability on 3D silk scaffolds. Analysis of viability and proliferation of HUVEC cultured on 3D scaffold discs (BM, BA, and BAW) over 14 days. (n.s.=not significant)*

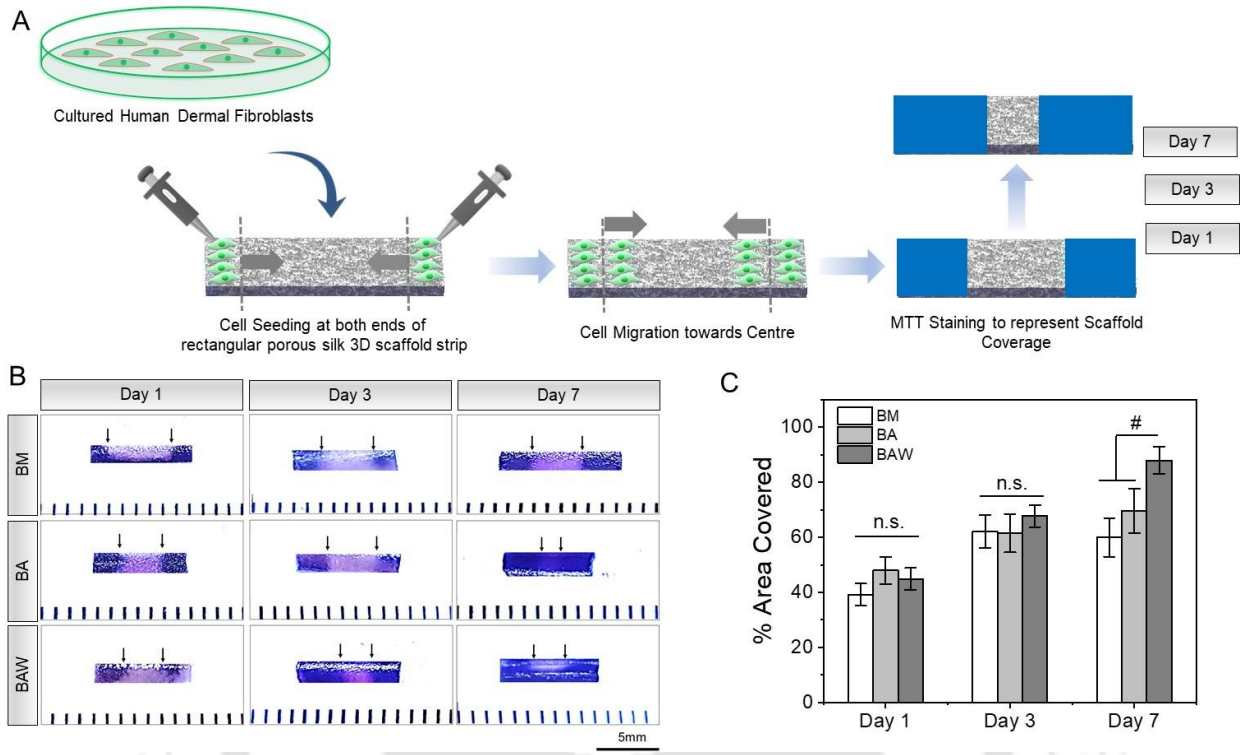

Figure 5.9. *Migration of HDF cell in porous 3D scaffolds. (A) Scheme representing the methodology adopted for cell migration analysis on silk scaffold strips. Cells were seeded on both longitudinal ends of strips followed by static culture. MTT staining was performed at predefined time points to visualize cell migration. (B) Cell-seeded MTT-stained silk scaffolds at different times. The presence of cells is represented in blue color. Black arrows are indicating the cell migration boundary. (C) Graph representing quantitative analysis of % area covered by cells over time. (n.s.=not significant, #p<0.05)*

5.3.5 Macrophage response and immunomodulation ability of dWJ functionalized 3D silk scaffolds implanted in rabbit subcutaneous pocket

As shown in **Figure 5.10A**, 3D silk scaffold discs were implanted in the subcutaneous pocket of rabbits followed by sample retrieval at five days and one month, post implantation. Qualitative assessment of H&E stained images showed a higher cellular infiltration at early point (five days) than one-month explants, signifying the host's initial inflammatory response followed by eventual graft acceptance. Interestingly, more cells were recruited by dWJ functionalized scaffolds (BAW) than other experimental groups after five days. In addition, cells were arranged along the scaffold struts suggesting their superior bioactivity (**Figure 5.10B**). Immunostaining of infiltrated cells showed positive staining for CD68, a pan macrophage marker, corroborating macrophage recruitment in all scaffold types following five days of implantation. In agreement with

histological data, considerably higher $CD68^+$ cells were observed in 1-month BAW explants. A similar trend was observed for $CD163^+$ cells (representing M2 anti-inflammatory phenotype). In contrast, all scaffolds showed a homogenous presence of $CCR7^+$ cells (representing M1 pro-inflammatory phenotype) at both time points (five days and one month) (**Figure 5.10C**).

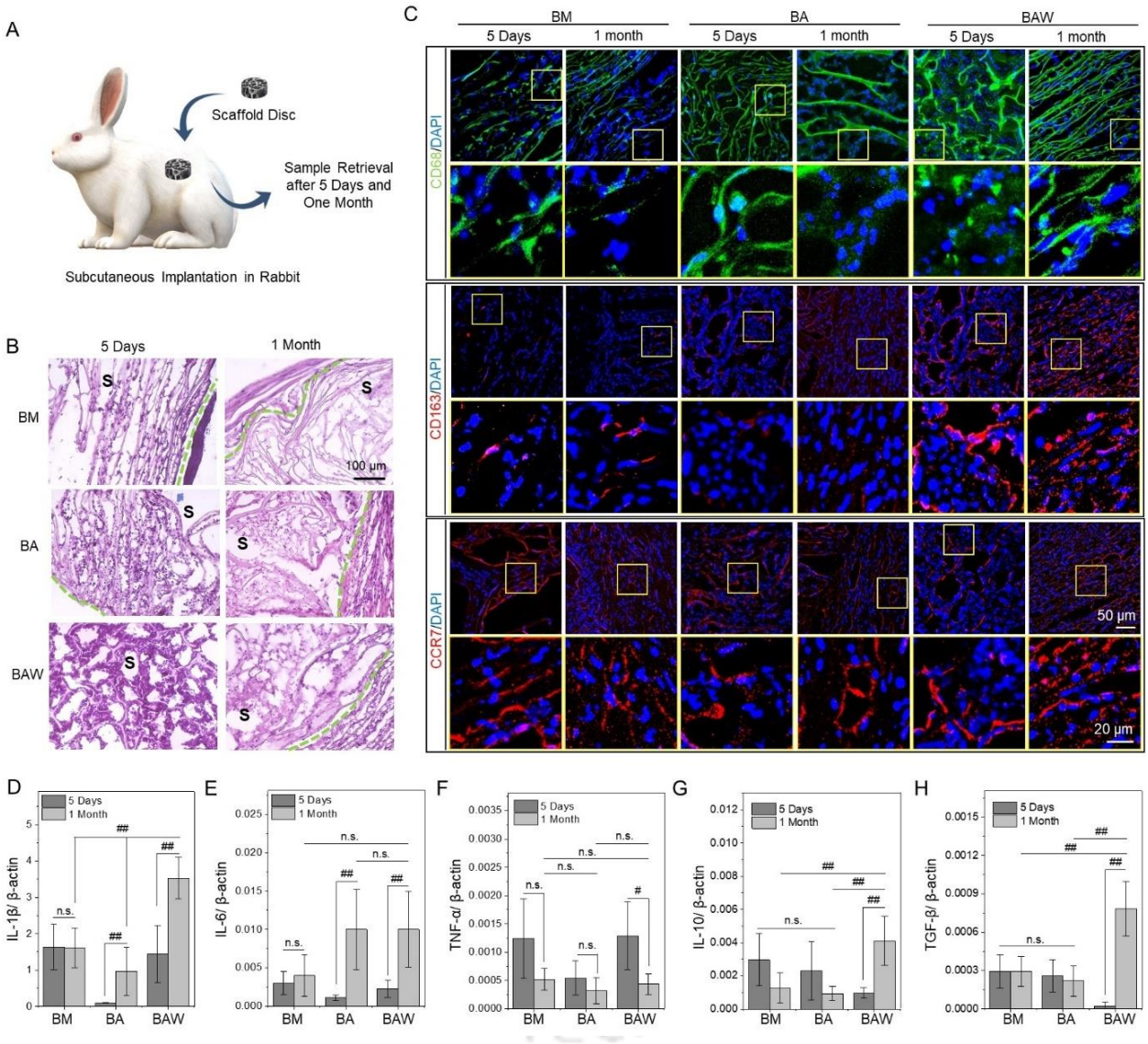

Figure 5.10. *In vivo immunomodulation analysis of dWJ functionalized silk scaffold discs in rabbit subcutaneous implantation model. (A) Schematic representation of subcutaneous implantation of silk/dWJ scaffolds in rabbit, followed by retrieval after five days and one month. (B) Hematoxylin & Eosin (H&E) stained histology sections of silk scaffold explants. The scaffold is marked as 's' and dotted green lines are representing the host tissue-scaffold interface. (C) Immunofluorescence staining of explanted silk scaffolds sections for CD68 (pan macrophage marker), CD163 (M2 macrophage marker), and CCR7 (M1 macrophage marker). For each specific antibody, the bottom row is the magnified image of the square labeled portion of the top row. (D-H) Quantification of real-time gene expression of M1 (IL-1β, IL-6, and TNF-α) and M2 (IL-10 and TGF-β) phenotypic*

markers in 5 days and 1-month explants of silk scaffolds (n=3). (n.s.=not significant, #p<0.05, ##p<0.01)

Quantitative expression of M1 (IL-1β, IL-6, and TNF-α) and M2 (IL-10 and TGF-β) phenotype-specific genes was further studied to analyze the impact of dWJ functionalization on macrophage polarization. Resident macrophages in BM scaffolds showed comparable expression of all genes at both time points. BA scaffolds showed an elevated level of pro-inflammatory genes after one month compared with five days ($p<0.05$), except for TNF-α, where no significant difference was observed among both the time points. Similarly, comparable expression of anti-inflammatory genes was evidenced at different time points for BA scaffolds. Interestingly, BAW scaffolds showed immunomodulatory activity. Upregulation of pro-inflammatory genes was observed over time (from day 5 to 1-month) ($p<0.01$), except for TNF-α, which was downregulated after one month ($p<0.05$). In addition, significant upregulation of anti-inflammatory genes was recorded for one month BAW scaffold explants ($p<0.01$). IL-10 and TGF-β expression for BAW explants were significantly higher than other scaffold variants at one month (**Figure 5.10D-H**).

5.3.6 Patency analysis and host cell infiltration in silk TEVGs

Silk TEVGs were implanted in rabbit jugular vein as interposition grafts by an end to end anastomosis (**Figure 5.11A**). The bi-layered silk scaffolds were easy to handle during the microsurgical procedure and withstood the intraluminal venous blood pressure without any sign of leakage. After removing surgical micro-clips, faint graft-reddening was observed, ensuring the recirculation of blood flow through the graft. After two months, the grafts were explanted, and an overall gross morphological overview suggested a resolved fibrotic response. Compared to BM and BA explants, BAW explant showed thicker fibrous capsule formation over the graft representing inflammatory response. Neo-tissue formation and the presence of microvessels over the graft surface indicate their integration with the native tissue. It was also corroborated by investigating the anastomotic graft site showing graft-native tissue (jugular vein) integration (**Figure 5.12A**). Graft patency was confirmed by color Doppler imaging after 12 and 60 days of implantation (**Figure 5.12B**). After 12 days of implantation, none of the grafts showed any sign of occlusion, precluding the possibility of acute thrombosis. However, color Doppler images of one of each BM and BA grafts after 60 days of implantation showed occlusion (**Figure 5.11B**). The

overall graft patency was 66.66% (2/3) for BM and BA grafts, whereas BAW grafts showed 100% patency (3/3) after two months without any sign of lumen narrowing (**Figure 5.12C**).

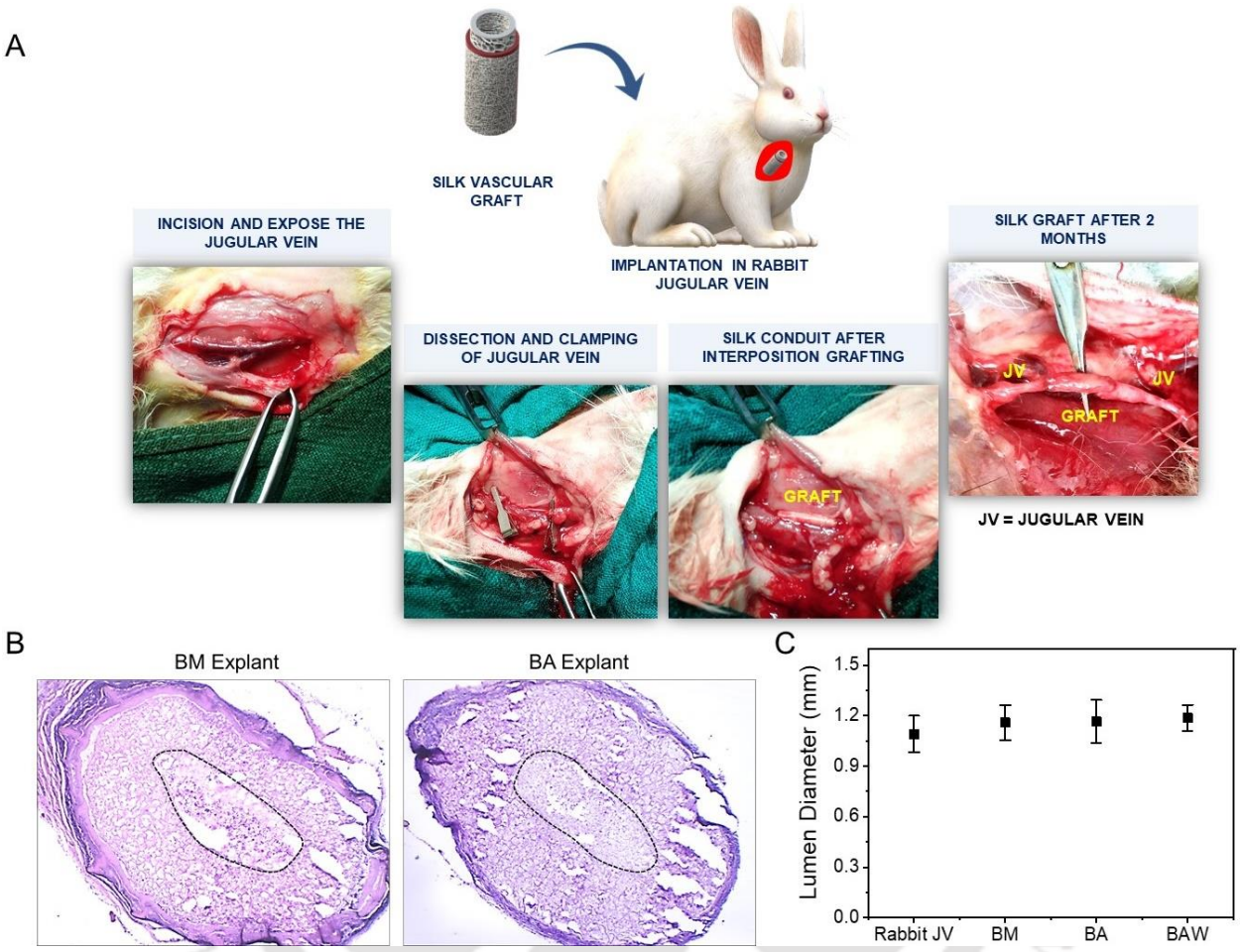

Figure 5.11. *In vivo implantation and characterization. (A) Representative images showing surgical implantation of silk vascular grafts in rabbit left jugular vein. (B) Representative H&E stained histological cross sections of 2 months' silk TEVG explants showing lumen occlusion. (C) Quantification of lumen diameter of explanted silk TEVGs compared with rabbit jugular vein (JV) showing no significant difference ($p>0.05$).*

The explanted silk scaffolds were further analyzed by investigating the histology cross-sections. H&E stained images of explants and native rabbit jugular vein are shown in **Figure 5.12D**. Histological images of patent grafts suggested that the lumen diameter of silk explants was similar to the native jugular vein (**Figure 5.11C**). Histological images revealed neo-tissue formation at luminal and ablumen surfaces covering the scaffold wall. Most of the scaffold struts were evident for BM and BA grafts; however, the cross-section of BAW explant exhibited comparatively lesser scaffold struts. The latter observation indicates the possibility of a higher

degree of graft remodeling over time for BAW grafts compared with other counterparts (BM and BA), which might be co-related with graft degradation rate suggesting a faster degradation rate of BAW grafts facilitating rapid neo-tissue formation [352]. We further investigated the host cell infiltration in the silk grafts, which revealed approximately 1.6 fold higher cells in BAW grafts than BM/BA grafts. Homogenous distribution of cells was observed in the scaffold walls radially (**Figure 5.12E-F**).

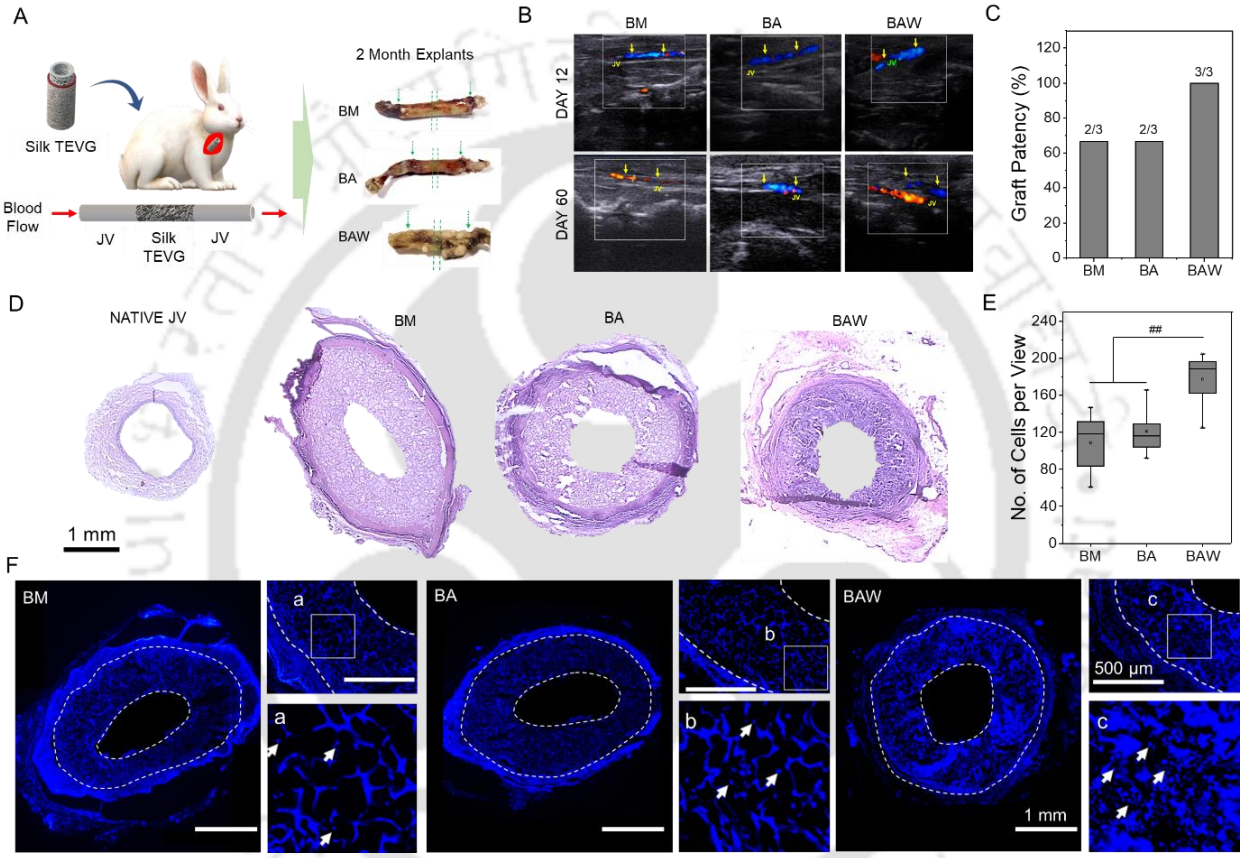

Figure 5.12. *In vivo implantation of silk TEVGs in rabbit jugular vein (JV). (A) Schematic representation of interposition grafting of silk TEVGs in rabbit JV. Grafts were explanted after 2 months. Dotted arrows are indicating the anastomotic point between TEVG and JV. Dotted lines in the middle portion of the graft represent the section used for histological analysis. (B) Representative color Doppler imaging of implanted TEVGs after 12 days and 60 days of implantation. Yellow arrows are representing the anastomotic site. (C) Patency analysis of silk TEVGs based on color Doppler data. (D) Hematoxylin & Eosin (H&E) stained histological cross-sections of native JV and silk explants, demonstrating host cell infiltration into silk TEVGs. (E) Quantification of host cells infiltrated into silk TEVGs. (F) DAPI stained fluorescent microscopic images of silk TEVG explants' cross-sections staining cell nucleus blue. White arrows are representing the presence of cell nuclei in each section. The square portions having white outline labeled as a, b, c are further magnified in the bottom images. (##p<0.01)*

5.3.7 *In vivo* remodeling of silk TEVGs

Remodeling of explanted silk TEVGs was monitored by qualitative and quantitative assessment of remodeled tissue. The immunohistological analysis for CD31 suggested homogenous endothelialization of BAW grafts along the lumen; however, BM and BA grafts demonstrated discontinuation of the endothelium (**Figure 5.13A**). A quantitative analysis of % area covered by $CD31^+$ cells revealed significantly higher endothelialization in BAW explants (**Figure 5.13B**). Smooth muscle cells (SMCs) in the developed neo-tissue were further substantiated by positive staining for αSMA and calponin (early and mid differentiation markers for SMCs). The qualitative assessment suggested densely packed SMCs in the scaffold wall for BA and BAW, whereas BM grafts showed a comparatively lesser density of SMC population. Overall, this data suggests that BAW grafts developed a superior neo-tissue comprising luminal ECs and medial SMCs over the experimental period than BM/BA grafts. BA grafts, although showed a predominant presence of SMCs in contrast with BM grafts, yet both BM and BA grafts performed poorly in terms of endothelialization as compared to BAW grafts (**Figure 5.13A**).

Two month silk explants were further analyzed for graft remodeling and ECM (collagen and elastin) deposition. In corroboration with DAPI staining data, H&E stained sections revealed the elevated host-cell infiltration in BAW scaffolds. The elastin content of the explants was stained by Verhoeff Van Gieson (VVG) staining, which revealed minimum elastin in BM scaffolds. On the other hand, a dense deposition of unorganized elastin was observed for BA and BAW grafts. On a similar note, collagen deposition followed a similar pattern as that of elastin with maximum collagen content present in BAW grafts, as revealed by Masson's trichrome (MT) staining of graft cross-section (**Figure 5.13A**).

ECM quantification data suggested an elevated presence of collagen and elastin in two months BAW explants compared to other experimental groups. The amount of collagen was comparable for the native jugular vein, BA, and BAW ($p=0.057$ for both); however, BM explants showed significantly lower collagen content than the jugular vein ($p=0.013$). No significant difference was observed among silk explants ($p>0.05$) (**Figure 5.13C**). Elastin quantification showed significantly lower levels in two months silk explants than native jugular vein (approximately 20%, 24%, and 36% for BM, BA, and BAW explants) ($p<0.01$). The elastin content for BAW explants was higher than BA ($p<0.05$), and BM ($p<0.01$) explants (**Figure 5.13D**). We also looked into any calcification in the silk graft by staining the explant sections with

alizarin red dye. The results revealed that the silk grafts and the native rabbit jugular vein were devoid of any calcium content (**Figure 5.14**).

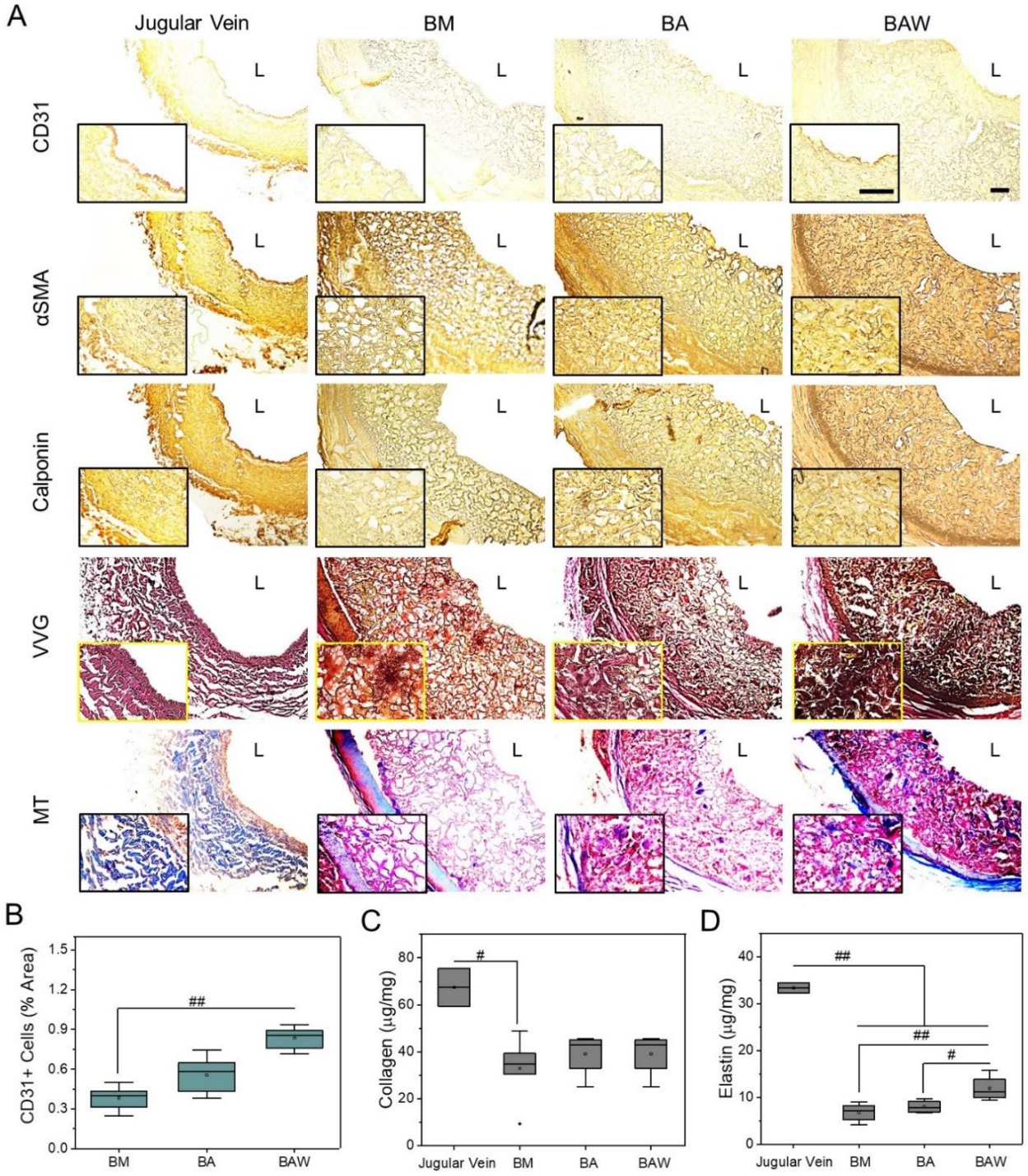

Figure 5.13. *Analysis of silk TEVG remodeling after two months implantation in rabbit jugular vein as interposition graft. (A) Representative immunostained histological images of native rabbit jugular vein and silk TEVG explants showing the presence of vascular cells (CD31: endothelial cell marker, calponin, and αSMA: smooth muscle cells marker at early and mid-differentiation*

phase respectively) in the remodeled grafts. Representative histological images of silk TEVG explants and rabbit jugular vein showing extracellular matrix deposition (Verhoeff Van Gieson (VVG) for Elastin: blue-black to black color and Masson's Trichrome (MT) for Collagen: blue color). Inset images are showing the magnified zone of interest for each specific stain. Lumen is marked as 'L'. Scale bar: 100 µm. (B) Graph representing quantification of percentage area covered by CD31+ cells (representing endothelial cells) in histological cross-sections of silk TEVG explants (n=6 images per experimental group). Quantification of (C) collagen, (D) elastin, in remodeled silk grafts compared with the native jugular vein (n=3). (#p<0.05, ##p<0.01)

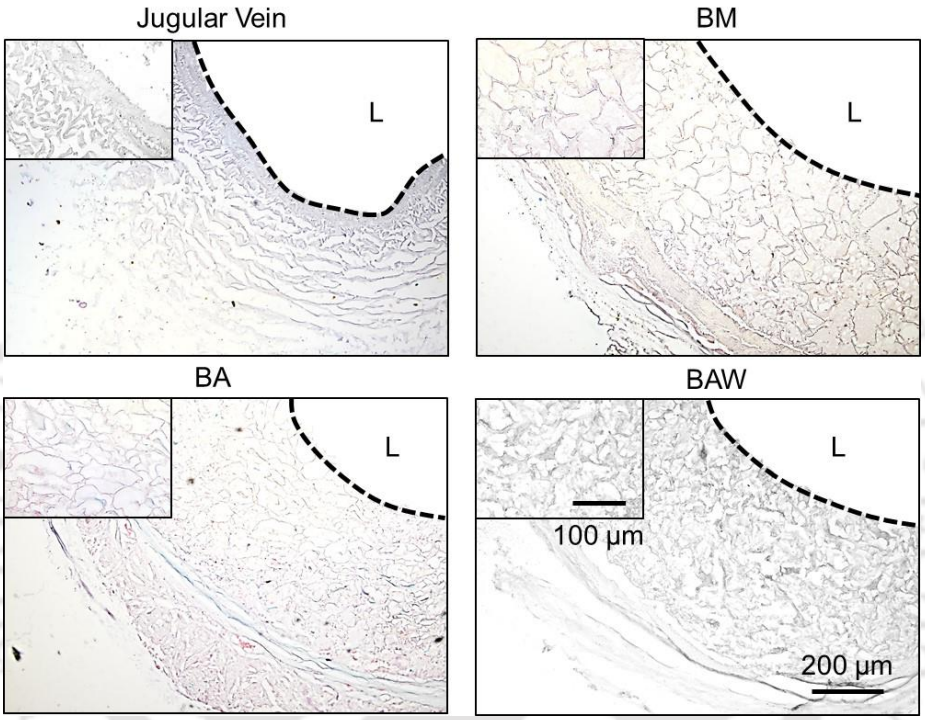

Figure 5.14. *Alizarin Red staining of silk TEVGs explanted after 2 months to characterize the presence of any traces of calcium deposition. 'L' represents scaffold lumen.*

For mechanistic analysis of graft remodeling post-implantation, histological sections were immunostained to mark the presence of tissue-resident macrophages as well as their phenotypes as a result of the inflammatory response (**Figure 5.15A**). Quantification of % area revealed a high population of $CD68^+$ cells in BAW (11.68 ± 1.58%) than BM and BA grafts (5.54 ± 0.74% and 7.36 ± 0.71%, respectively) ($p<0.05$), signifying increment of approximate two-fold than BM and 1.6 fold than BA grafts (**Figure 5.15B**). A similar trend was observed for M2 anti-inflammatory macrophage marker CD163, for which % area coverage was 5.95 ± 0.51 for BAW vs. 2.68 ± 0.4 and 4.38 ± 0.59 for BM ($p<0.01$) and BA grafts ($p<0.05$) respectively (**Figure 5.15C**). On the contrary, BA (5.76 ± 0.83%) and BAW grafts (6.34 ± 1.09%) showed a comparable population of

$CCR7^+$ cells (M1 pro-inflammatory marker) ($p>0.05$), which were significantly higher than BM grafts (3.42 ± 0.38%) ($p<0.05$) (**Figure 5.15D**). To assess the anti-inflammatory immunomodulatory behavior of dWJ functionalized silk grafts, the ratio of $CD163^+/CCR7^+$ was calculated. A significantly higher ratio for BAW grafts (0.96 ± 0.18) attested to the presence of comparatively higher M2 macrophages density, possibly improving pro-remodeling effects in BAW graft than other silk graft variants (**Figure 5.15E**).

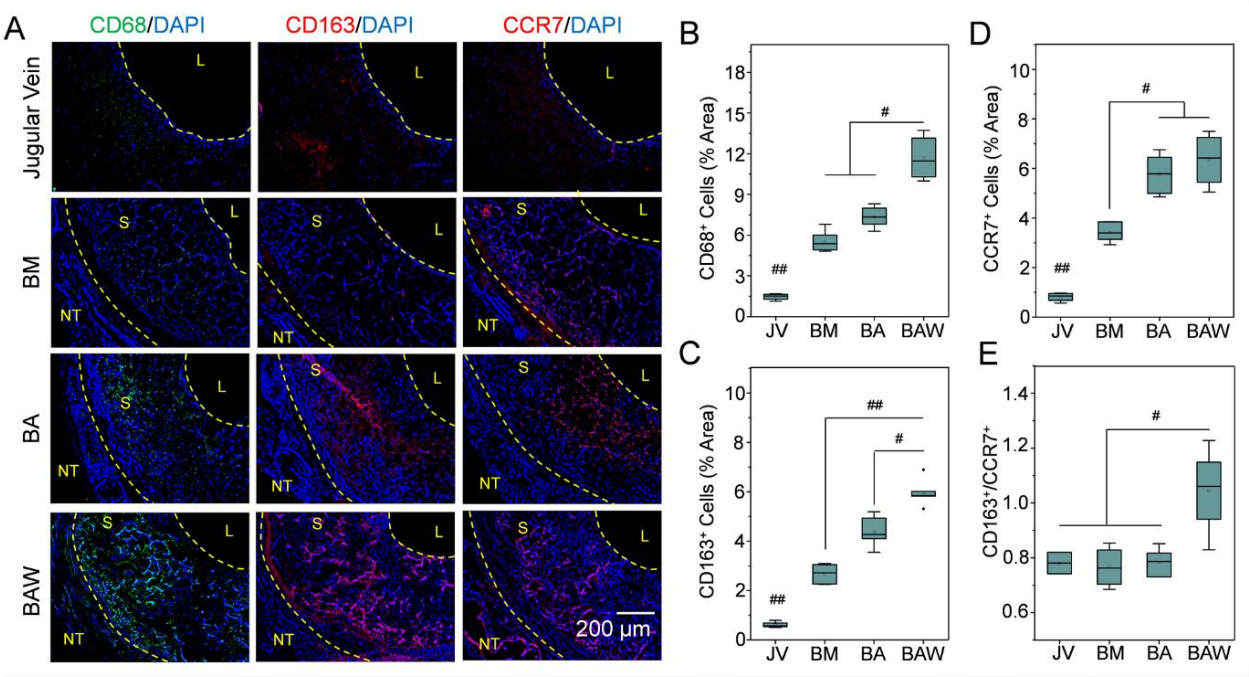

Figure 5.15. *Macrophages and their phenotype in silk TEVG explants. (A) Immunofluorescent histological images of vascular silk explants showing the presence of $CD68^+$ (pan macrophage marker), $CD163^+$ (anti-inflammatory marker) and $CCR7^+$(pro-inflammatory marker) cells. Lumen is marked as 'L'. Quantification of percent area of (B) CD68, (C) CD163 and (D) CCR7 markers obtained by processing the immunofluorescent images (n=6) using ImageJ. (F) Graph representing M2/M1 marker positive cells. (#p<0.05, ##p<0.01)*

5.3.8 Biomechanical characterization of TEVG explants

Uniaxial circumferential tensile testing data were obtained using tissue explant rings, as shown in **Figure 5.16A.** Stress-strain curves of BM and BA samples revealed a more linear pattern, which is representative of materials. On the other hand, BAW explants showed an exponential response (a J-shaped curve), a characteristic feature of soft biological tissues (**Figure 5.16B-D**). In the low stretch region, no significant modulus difference was recorded among silk TEVG explants; however, BAW explants revealed maximum high modulus (0.68 ± 0.38 MPa), significantly higher

than BM (0.18 ± 0.02 MPa, p=0.07) and BA (0.22 ± 0.07 MPa, p=0.09) counterparts (**Figure 5.16E-F**). Further exploration of stress values at failure point revealed a similar pattern, wherein BAW samples showed maximum stress (0.81 ± 0.23 MPa), significantly higher than BM (0.23 ± 0.03 MPa) and BA (0.36 ± 0.07 MPa) explants (p<0.01) (**Figure 5.16G**). The corresponding strain was comparable for all samples (p>0.05) (**Figure 5.16H**). Circumferential biomechanical properties of BAW silk explants were comparable to either native human saphenous vein (hSV) or porcine internal mammary artery (pIMA) (**Table 5.2**).

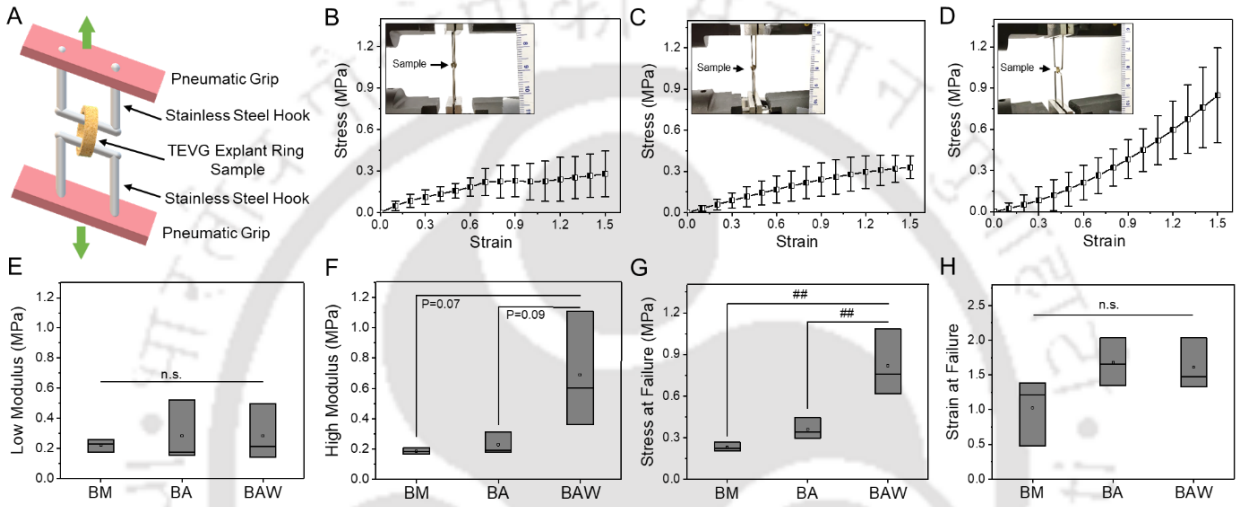

Figure 5.16. *Biomechanical assessment of silk TEVG explants. (A) Schematic representation of uniaxial circumferential tensile testing set-up. The tissue rings were mounted in stainless steel hooks through the lumen. Hooks were pulled apart at 2 mm/min crosshead speed until sample failure. Average representative stress-strain curves for (B) BM, (C) BA, and (D) BAW TEVG explants. Graphs are representing modulus in (E) low stretch (low modulus) and (F) high stretch (high modulus) regions. (G) maximum stress and (H) corresponding strain at failure points. (##p<0.01, n.s.=not significant)*

Table 5.2. *Biomechanical circumferential tensile properties of silk explants compared with previously reported hSV and pIMA.*

	BM	**BA**	**BAW**	**hSV [337]**	**pIMA [337]**
Stress at failure (MPa)	0.23 ± 0.03	0.36 ± 0.07	0.81 ± 0.23	3.7 ± 2.0	10.4 ± 7.1
Strain at failure	1.02 ± 0.48	1.67 ± 0.34	1.61 ± 0.37	1.7 ± 0.7	1.5 ± 0.2
Modulus (MPa)	Low: 0.22 ± 0.04 High: 0.18 ± 0.02	Low: 0.28 ± 0.20 High: 0.22 ± 0.07	Low: 0.28 ± 0.18 High: 0.68 ± 0.38	2.5 ± 1.0	0.4 ± 0.2

5.4 Discussion

Research impetus in the field of vascular tissue engineering is lately witnessing a lateral shift towards cell-free grafts. The goal is to reduce the clinical testing time and make the grafts readily available for patients in need. Cell-free polymeric grafts can be manufactured in large quantities with high fidelity circumventing the limitations of auto/allografts; however, their blood compatibility and remodeling ability remain questionable. In chapter 4, the remodeling ability of stromal vascular fraction (SVF) seeded bi-layered silk scaffolds was shown. Albeit, it is believed that acellular grafts would have better chances to enter into the clinic. With the latest advancements, studies have revealed that cell-seeding, be it either vascular cells or various MSCs, is not as vital for graft viability (in terms of patency, endothelialization, and remodeling). Acellular grafts functionalized with different bioactive molecules have shown comparable *in vivo* performance [5, 352]. There is now enough scientific evidence that MSC seeded grafts remodel via paracrine fashion. Among numerous soluble factors, MCP-1 has been identified to be playing a significant role in graft remodeling [44]. Other strategies towards successful grafting involve approaches for faster endothelialization to prevent acute thrombosis. The current rationally important requisite is to biologically functionalize the acellular polymeric grafts, which can prevent acute thrombosis, induce endothelialization, and help in constructive graft remodeling. The goal of the present study was to identify a novel cell-free solution for tissue-engineered polymeric vascular grafts aiming to expedite their clinical translation. Herein, as a potential alternative for cell seeding, we propose the functionalization of cell-free silk TEVGs with decellularized human Wharton's jelly (dWJ) matrix. The dWJ matrix obtained by a facile modified approach, is hypothesized to prevent the loss of bioactivity of in-house extracellular components due to the following reasons: 1) tissue is processed at 4°C, and 2) it avoids the use of detergents and enzymes. Considering the superior performance of BA grafts showed in our prior work (Chapter 4), herein we functionalized them with dWJ matrix (referred as BAW). The dWJ functionalization was aimed to support endothelialization and allow constructive remodeling after implantation, considering the intrinsic presence of angiogenic and immunomodulatory factors. We surmised that our dWJ functionalized TEVGs possess the benefit of WJMSCs' bioactivity. In addition, BM silk TEVGs were investigated as a silk control group in accordance with our previous study (Chapter 4).

Recruitment of host cells in the acellular polymer graft post-implantation is the starting point for their remodeling. The implanted TEVG is populated by host cells by either one of the following processes: trans-anastomotic, fall-out, and transmural migration [5]. Instantly after TEVG implantation, the scaffold wall is infused with blood, facilitating the infiltration of vascular progenitor cells and circulating monocytes via the fall-out process. These cells are envisioned to populate the graft in an acute response, in addition to the host inflammatory immune response. The sparse availability of circulatory vascular progenitor cells strengthens the idea that a vast majority of early phase infiltrated cells comprise circulatory monocytes. In addition, as a part of the host immune response, tissue-resident monocytes infiltrate the wound site and differentiate into macrophages. The recruited macrophages initially exhibit a pro-inflammatory (M1) phenotype known to stimulate angiogenesis, followed by a transition into a diverse anti-inflammatory (M2) population consisting of various subtypes participating in tissue remodeling [395]. Macrophage plasticity is effectively involved in TEVG remodeling, which is regulated by specific cytokines and other factors. Cytokine profiling of dWJ matrix revealed the following immunomodulatory factors: IL-8, IL-6, IL-10, IL-4, TNF-α, and GMCSF. Previous reports suggest that IFN-γ and TNF-α stimulate the M1 phenotype of macrophages. In addition, various subtypes of M2 phenotypes are stimulated by selective cytokines [396]. For instance, IL-4, IL-10, and IL-6 are reported to induce M2 phenotype (pro healing and pro remodeling) [396]. M2 phenotype also promotes the secretion of matrix metalloproteinases (MMPs), leading to tissue remodeling. Other cytokines like IL-8 are associated with neutrophil recruitment, the first inflammatory cell to reach the injury site. Prior studies suggest that M2 macrophages induce tissue remodeling by manipulating fibrosis and ECM deposition [396]. Notably, we observed significantly high recruitment of macrophage population in a 5-day subcutaneous explant of the BAW scaffold, possibly either due to the upregulation of MCP1 gene in the resident macrophages or intrinsic presence of MCP1 protein in dWJ matrix [388]. However, a detailed proteomic analysis is needed to ascertain the presence of MCP1 protein in dWJ matrix.

Considering the plasticity of macrophage phenotypes and the presence of immunomodulatory factors in dWJ matrix, we further delved into determining the fate of recruited macrophages. Short-term *in vitro* dWJ exposure to human macrophages (THP-1) downregulated M1-associated genes (TNF-α, CCR7, and IL-6) but did not affect the IL-10 expression. However, immunofluorescence images indicated CD163 expressing cells (representing M2 macrophages),

suggesting a possible switch towards the M2 phenotype. Further long-term *in vivo* rabbit subcutaneous implantation study validated the former observation, and a significantly higher $CD163^+$ cells was traced in BAW explants. Although, CCR7 expression was evident in all experimental groups. Interestingly, quantification analysis revealed the upregulation of M2 markers (IL-10 and TGF-β) in BAW scaffolds over time, whereas M1 markers (IL-1β, IL-6, and TNF-α) showed an ambiguous response. Overall, this data represents that dWJ functionalization of silk TEVGs should favor M2 anti-inflammatory macrophage phenotype and promote graft remodeling, which was corroborated by a significantly higher M2/M1 ratio for BAW TEVG explants, validating the role of dWJ functionalization in expediting the tissue remodeling.

Another indispensable pre-requisite for functional remodeling of the implanted TEVG is the formation of neo-tissue comprising of vascular cells (endothelial cells, smooth muscle cells, and fibroblasts). Vascular cells from the adjacent native tissue are believed to populate the implanted TEVG via transanastomotic and transmural migration. Herein, we observed that dWJ matrix treatment accelerated the *in vitro* migration rate of endothelial and fibroblast cells, which spurs the notion that bio-composite silk vascular grafts may demonstrate faster remodeling. Silk TEVG 2 month explants from rabbit jugular vein substantiated our *in vitro* findings as represented by higher cell infiltration in BAW explants than control groups (BM and BA). The role of the RGD cell-binding motif in AA silk should also be acknowledged [378]. TEVGs modified with RGD tripeptide showed 3-times higher endothelial coverage in rabbit carotid artery post four weeks. These grafts also recruited significantly more SMCs and showed superior patency compared to control unmodified ones [155]. Higher expression of integrin molecules in dWJ matrix treated group might be co-related with improved cell migration [381]. In addition, we speculate that the presence of bioactive growth factors in dWJ matrix, including VEGF, FGF might be responsible for such effects [380, 381]. Although, the presence of these peptide growth factors in dWJ matrix needs to be investigated to validate the former outcome.

The initial success of cell-free graft relies on faster endothelialization and decorating the graft with NO-producing molecules [58, 367, 371]. Rapid cellular migration in the presence of dWJ matrix *in vitro* is a positive attribute towards graft remodeling, ensuring the functionality of endothelial cells is also a crucial aspect for long-term graft success. *In vitro* data suggested that dWJ matrix treatment does not significantly alter the proliferation of ECs. However, interestingly, a drastic improvement in ECs' functionality in terms of NO production and expression of

functional markers (CD31, eNOS, and VE-Cadherin) substantiates the usefulness of dWJ matrix. Our observation is in co-relation with a prior study reporting the presence of an array of angiogenic factors in WJMSCs secretome (e.g., VEGF, WNT5A, AKT1, CD248, SPON2 etc.), which we assume to be present in the dWJ matrix [387]. Notably, the upregulation of endothelial functional genes, faster cell migration and increased NO production in the dWJ treatment group validate that our modified decellularization protocol preserves the bioactivity of dWJ matrix. In view of prior reports and our current investigation, it can be established that dWJ matrix is a reservoir of various angiogenic and immunomodulatory factors, which is an encouraging sign towards its application for cell-free vascular grafts.

Another aspect of TEVG remodeling is the degradation rate of implanted material. As of now, there is no general agreement about how fast the material should ideally degrade. Both slow and fast degrading materials have shown the TEVG remodeling and formed mature neo-vessels in animal models [352, 365]. The takeaway point is that the implanted graft should provide enough mechanical stability to allow the formation of neo-vessel without failing. *In vitro* degradation profile of silk scaffolds in the presence of protease enzyme revealed a faster degradation rate of BAW scaffolds than other controls. Such behavior could result from the availability of a higher number of enzyme cutting sites in BAW scaffolds due to intervening dWJ matrix in silk. Notably, none of our implanted silk TEVGs failed due to fast degradation and rupture. Qualitative assessment of the histological cross-sections of explanted TEVGs showed the presence of lesser scaffold struts and dense native tissue comparatively. Therefore, it can be argued that a relatively faster degradation rate of BAW TEVGs concurrently allowed faster neo-tissue formation and remodeling. The former observation is also supported by consistent endothelium and a dense medial layer found in BAW explants. It shows that dWJ functionalized TEVGs could recruit host vascular cells and maintain the vascular tone by providing a functional endothelium layer at the blood-graft interface. In addition, elevated levels of cellular infiltration, be it macrophages or vascular cells, resulted in the production of a higher amount of ECM proteins (collagen and elastin) in dWJ functionalized grafts, which could be correlated with BAW graft mechanical stability in rabbit jugular vein despite a considerably faster degradation rate. Histological images revealed organized collagen deposition on the outside of all silk TEVGs, which might indicate foreign body response leading to fibrous capsule formation [182]. Previous studies suggest that cell infiltration and neo-tissue formation starts in the lumen and ablumen sides of the implanted TEVGs, which

traverses through the scaffold walls eventually over time [397]. Dense unorganized collagen deposition observed in the scaffold wall (BAW) suggests the superior chances of these grafts to follow the constructive remodeling pathway, pending future long-term investigation. On the other hand, the exponential increment of the stress-strain curve of BAW explants is also suggestive of constructive graft remodeling. Comparing biomechanical properties of explanted silk TEVGs with previously reported values for native blood vessels (hSV and pIMA)[337] revealed a comparable strain failure but lower stress failure. In addition, while BM and BA explants showed lower modulus (both low and high), the linear modulus of BAW explants was comparable to pIMA. The biomechanical properties of TEVG rely on neo-tissue formation [5]. We envisage that a long-term *in vivo* implantation (~6 months) of silk TEVGs would facilitate superior mechanical properties.

This study establishes the role of a novel dWJ functionalized silk TEVG towards improved remodeling in a pre-clinical animal model. One of the challenges is to ascertain if the embedded bioactive components of the dWJ matrix vary between donors, which would crucially determine the clinical translation of this technology. Some of the future prospects of the present work might include a detailed proteomic analysis of dWJ matrix to identify the presence of additional cytokines and growth factors participating in the graft remodeling process to understand the underlying mechanism. The rationale behind the adverse effect of higher dWJ concentration (>1mg/mL) on vascular cells may be investigated. Future studies should explore alternate methods (temperature-induced water vapor annealing [143], protein self-assembly [398]) of β-sheet transformation in silk scaffolds avoiding the use of organic solvents. Adoption of these all-aqueous approaches is envisaged to preserve the bioactivity of intrinsic dWJ factors with better efficacy. In this study, a small *in vivo* sample size (n=3 each group) was investigated for a shorter time (2 months). A long-term *in vivo* analysis of silk TEVGs with a higher sample size would be required for precluding the possibility of intimal hyperplasia, tracking the graft degradation and complete neo-vessel formation over time. A few recent studies showed evidence that outcomes of implanted TEVGs differ based on their implantation site [399], which would be another interesting aspect to investigate.

5.5 Significant findings

1. This chapter describes the developement of a novel cell-free TEVG comprising of silk and dWJ matrix.
2. The Wharton's jelly matrix was decellularized, adopting a modified method to preserve intrinsic bioactive moieties.
3. In addition to angiogenic factors, dWJ is also a reservoir of immunomodulatory cytokines (IL-6, IL-8, IL-4, IL-10, and TNF-α).
4. *In vitro* exposure of dWJ matrix led to the upregulation of endothelial cell functional genes and promoted NO production, which helps in maintaining vascular tone. dWJ treatment also assisted in the faster migration of vascular cells.
5. Downregulation of M1-associated markers and upregulation of M2-associated markers validated the immunomodulatory aspect of dWJ matrix towards the pro-remodeling state, which further assisted in the constructive remodeling of vascular grafts in rabbit jugular vein.
6. The dWJ functionalized TEVGs exhibit 100% patency after two months, show no sign of calcification, and recruit more host cells (both inflammatory and vascular). BAW grafts also showed consistent endothelium and a dense medial layer comprising smooth muscle cells.
7. Moreover, elevated levels of collagen and elastin indicate constructive graft remodeling.
8. Biomechanical properties of explanted TEVGs were comparable with native human vessels.
9. These findings suggest that our composite TEVGs undergo superior remodeling and integrate with the native vessel by modulating the host immune response.
10. Further build-up on this proof of concept study may provide a readily available and clinically viable tissue-engineered vascular graft.

CHAPTER 6

Acellular silk lyogel conduits impregnated with bioactive polymeric microparticles as potential substitutes for vascular tissue engineering applications

This chapter demonstrates the fabrication of a cell-free tissue-engineered vascular graft (TEVG) capable of delivering any requisite biological payload to induce remodeling. The acellular nature of this technology potentially reduces risk, increases reproducibility, and results in a more cost-effective graft when compared to cell-based options. These grafts are aimed to endow ready availability, minimize regulatory hurdles and improve off-the-shelf clinical feasibility.

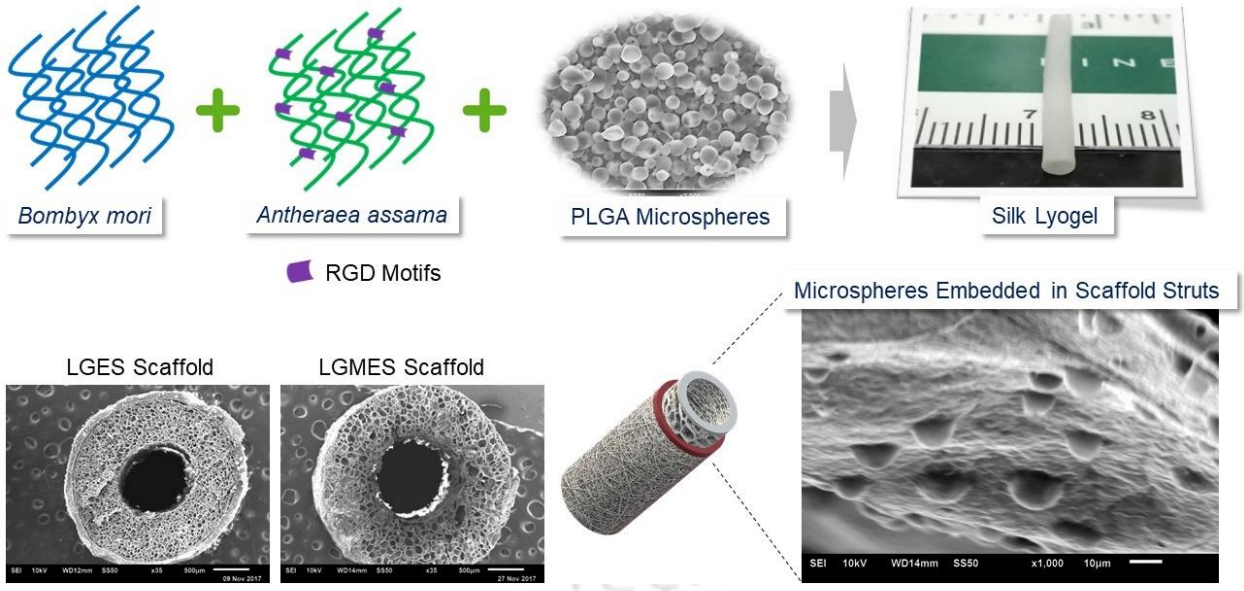

Publication:

*Katherine L Lorentz[#], **Prerak Gupta**[#], Mostafa S Shehabeldin, Eoghan M Cunnane, Aneesh K Ramaswamy, Kostas Verdelis, Morgan V Fedorchak, Steven R Little, Justin S Weinbaum, Charles S Sfeir, Biman B Mandal, David A Vorp. CCL2 Microparticles Promote Acute Patency in Silk-Based Vascular Grafts. (# Co-First Authors) (Revision submitted to '**Acta Biomaterialia**')*

ABSTRACT

This study outlines the development of a silk-based tissue-engineered vascular graft (TEVG) for use in arterial bypass or replacement surgery. It is believed that cell-free polymeric grafts have a better chance of clinical translation than their cell-seeded counterparts; however, their limited bioactivity challenges the overall idea. In this work, we propose a novel customized bi-layered lyogel silk scaffold that is combined with polymeric microparticles (MPs) capable of delivering a myriad of bioactive cargos/drug molecules to improve graft performance. The porosity of MP-loaded scaffolds was comparable to control scaffolds (53 ± 30 μm), sufficient to allow cell infiltration. Biodegradation analysis revealed a similar pattern for both scaffold types (LG and LGMP), wherein ~80% mass loss was recorded after 1 month in the presence of protease enzyme. MPs were stably integrated with scaffold wall struts, and insignificant dislodging was observed under physiological pulsatile flow. Fluorescent microscopic images showed FITC dye-loaded MPs in the scaffold cross-sections substantiating their loading efficacy. Moreover, MPs loaded scaffolds (LGMP) supported the growth of stromal vascular fraction (SVF) cells over 15 days without any detrimental impact. Lyogel scaffolds developed herein could potentially deliver any bioactive cargo molecule enabling a cell-free grafting strategy. This technology's acellular nature potentially reduces risk, increases reproducibility, and results in a more cost-effective graft compared to cell-based options.

6.1 Introduction

The success of a TEVG depends on the selection of a suitable scaffold and its bioactivity [400, 401]. Silk is a natural protein biomaterial, which has remarkable properties from a regenerative medicine perspective. The non-toxic nature of its degradation byproducts makes it a promising scaffolding material for vascular tissue engineering applications [140]. Much of our previous work has been on developing a TEVG using patient-derived stem or progenitor cells rapidly seeded into biodegradable tubular scaffolds. *In vivo* studies with cellularized TEVGs have demonstrated increased graft patency and more constructive remodeling over acellular scaffolds. It is hypothesized that the seeded cells play initial anti-thrombogenic and signaling roles, thereby preventing acute thrombosis and attracting host cells into the scaffold to remodel and repopulate the graft as the initially seeded cells evacuate [345, 402, 403]. While the cellular component provides positive effects for TEVG acceptance and remodeling, it is also a limiting factor in clinical translation due to exposure of the cells to animal-sourced cell culture materials, batch to batch variation, and high monetary costs to produce cell-based TEVGs.

A potential means of addressing these challenges is through the development of a cell-free TEVG that mimics the acute secretory effect of the seeded cells via the controlled delivery of selected factors. In our previous study (described in Chapter 5), we hypothesized that bioactive factors secreted by Wharton's Jelly stem cells were preserved in the extracellular matrix. Silk TEVGs functionalized with dWJ matrix showed superior patency and remodeling. Mechanistic investigation further revealed the presence of immunomodulatory cytokines in the dWJ matrix, which crucially regulated the overall tissue remodeling and neo-tissue formation. Although the study provides a cell-free bioactive vascular scaffold, identification of specific factors rendering the regenerative effects is of prodigious importance aiming clinical translation. While the litany of secreted factors and cell-to-cell signaling provided by seeded cells cannot be exactly mimicked, identification and utilization of selected key factors may be sufficient. For example, Hibino, *et al.*, has shown that seeded cells promote macrophage recruitment into the implanted graft, contributing to the remodeling process [404]. A need, therefore, exists for a vascular scaffold system capable of delivering a customizable payload following implantation.

This study developed a silk-based vascular scaffold with integral cell-mimicking microparticles capable of releasing bioactive cargo via burst release. While incorporating the microparticles, we leveraged our previously established silk-based, cross-linker free gelation

technique, wherein combining silk fibroin isolated from different silk varieties (referred to as lyogel mixture) forms a stable hydrogel [233, 332, 405]. Mixing polymeric microparticles carrying a bioactive payload with the lyogel mixture in the pre-gelation state allows for entrapment of the microparticles in the vascular scaffolds capable of delivering bioactive cargo facilitating constructive graft remodeling.

6.2 Materials and methods

6.2.1 PLGA microparticle fabrication

PLGA microparticles were fabricated using a water-oil-water double emulsion procedure as previously described [406]. Briefly, 28 μg of FITC and 15 mM NaCl in 200 μL of 1% w/v bovine serum albumin solution formed the aqueous solution. PLGA (Sigma-Aldrich, USA) was dissolved in 4 mL of dichloromethane to develop the oil solution. High-intensity pulses of sonication were used to form small PLGA droplets in a larger aqueous phase. This solution was stirred for several hours resulting in hardened MPs [406].

6.2.2 Fabrication of bi-layered silk lyogel scaffolds

The aqueous silk fibroin (SF) solutions were obtained from cocoons of *Bombyx mori* (BM) silk and glands of matured fifth instar larvae of *Antheraea assama* (AA) silk following previously published protocols [233, 332]. In brief, small pieces of BM silk cocoons were degummed and dissolved in 9.3M LiBr followed by dialysis against distilled water for 48h with a frequent water change. The SF extracted from AA silk glands was dissolved in 1% (w/v) sodium dodecyl sulfate (SDS) and dialyzed at 4°C against milli-Q water for 4h. A 12 kDa MWCO dialysis membrane was used for both SF proteins, and protein concentration was calculated following the conventional gravimetric method.

The bi-layered silk tissue-engineered vascular grafts (TEVG) were fabricated using a custom-designed 3D printed mold per our previous study (described in Chapter 4). For fabricating the inner porous layer, we took advantage of silk hydrogel formation as a result of mixing BM and AA silk at physiological temperature (37°C) [233, 332, 405]. A 1:1 (v/v) ratio of BM (6%, w/v) and AA (2%, w/v) was mixed to obtain a homogenous solution. The SF mixture was poured in the mold using a syringe and incubated at 37°C for 15 min to allow the hydrogel formation. The central stainless steel rod and mold cap were removed, leaving behind a void lumen. It was further frozen

at -20°C for overnight and lyophilized for 24h. The porous tubular silk scaffold, referred as lyogel hereafter, was pushed out from the mold and treated with 80% ethanol for 15 min. The outer electrospun layer was coated, as reported in Chapter 4. The electrospinning solution consisted of a mixture of 10% (w/v) polycaprolactone (Sigma-Aldrich, USA) and 10% (w/v) BM silk in 1,1,1,3,3,3-Hexafluoro-2-propanol (HFIP, Sigma-Aldrich, USA) at 1:1 ratio. The electrospinning parameters were as follows: tip-collector distance = 10 cm, flow rate = 100 µL/min, translational speed = 50 mm/sec, rotational speed = 200 rpm and temperature ~25°C. For preparing PLGA microparticle loaded silk lyogel scaffolds, 3 mg of microparticles were homogeneously blended with 1 mL of BM/AA silk mixture before injecting the solution into mold and hydrogel formation. The precaution was taken to avoid any bubble formation during the injection. Similar remaining steps were followed to obtain bi-layered silk TEVG. Hereafter silk lyogel scaffolds are designated as: (1) LG core- Inner porous layer (+), outer electrospun layer (-), PLGA microparticles (-); (2) LG- Inner porous layer (+), outer electrospun layer (+), PLGA microparticles (-); (3) LGMP core- Inner porous layer (+), outer electrospun layer (-), PLGA microparticles (+); (4) LGMP- Inner porous layer (+), outer electrospun layer (+), PLGA microparticles (+).

6.2.3 Scanning electron microscopy and micro-CT analysis

The cross-sections of bi-layered silk lyogel TEVG were assessed for their surface morphology and porosity. Dehydrated scaffold sections were gold coated using Sputter Coater (108 auto, Cressington Scientific Instruments, Cranberry Township, PA). The resulting samples were imaged using a scanning electron microscope (SEM, JEOL JSM-6510LV/LGS). The acquired images were processed using NIH ImageJ software to manually calculate the lumen diameter, outer diameter, and thickness of inner and outer scaffold layers. For each quantification, n=3 individual scaffolds were processed with at least n=15 measurements per sample. The scaffold porosity, pore size, and strut thickness of inner scaffold layers were further quantified by subjecting them to a Scanco microCT 50 (Scanco Medical, Bassersdorf, Switzerland) scanner following similar methodology described in Chapter 4.

6.2.4 Mechanical characterization

6.2.4.1 Uniaxial tensile test

The silk lyogel TEVGs were analyzed for their uniaxial and dynamic mechanical properties as described in Chapter 4. A 3 cm long tubular scaffolds were fabricated, and mechanical testing was performed with phosphate-buffered saline (PBS) soaked hydrated scaffolds. Uniaxial tensile properties were measured both in longitudinal (long) and circumferential (circ) directions (n=6 each). Scaffold minor dimensions i.e., wall thickness, inner and outer diameter, were calculated by processing the SEM images using NIH ImageJ software. Silk lyogel TEVGs were cut open through their lumen longitudinally, and both ends were fixed in between the pneumatic clamps of the universal testing machine (UTM, Instron, model 5543A). The load-displacement curves for longitudinal tensile testing were obtained at a crosshead speed of 2 mm/min until sample failure. For circumferential tensile properties, 2 mm scaffold rings were fitted along the lumen in a stainless steel hook attached to pneumatic grips. Load-displacement curves were obtained at the crosshead speed of 1 mm/min until failure. Stress-strain curves for both longitudinal and circumferential tensile testing were obtained to calculate the scaffold modulus in low and high-stress regions. Maximum stress at the failure point and the corresponding strain is also reported.

6.2.4.2 Suture retention strength

The suture retention strength of silk lyogel TEVG (n=6) was calculated following American national standard institute-association for the advancement of medical instruments (ANSI/AAMI) VP20 standards. A single loop of 7-0 polypropylene suture was created at a distance of 2mm from one end of the scaffold while the other end was secured in the pneumatic grip of UTM. The two ends were pulled apart at the crosshead speed of 2 mm/min and the maximum load at the failure point is reported as suture retention strength. The resultant value obtained by dividing the suture retention force at failure by scaffold wall thickness is reported as suture retention tension.

6.2.4.3 Dynamic compliance

The dynamic mechanical properties of silk lyogel TEVGs (LG and LGMP) were assessed at the physiological pressure conditions (120/80 mmHg) using our custom-made perfusion system. The scaffolds (n=6) were mounted in the testing chamber, and the pulsatile flow loop was initiated, maintaining physiological conditions using DI water at 37°C. The outer scaffold diameter and

intraluminal pressure were recorded until 7h. Dynamic compliance and β-stiffness were calculated per previous report [337].

6.2.4.4 Burst strength

The burst strength of lyogel silk TEVGs (n=6) was calculated manually by mounting the scaffold in a testing chamber and creating a closed loop. One end was connected to a digital manometer (Weiss), and the other was connected to a syringe pump. Saline was injected into the loop at a rate of 100 mL/min, and the maximum pressure before scaffold failure is reported as scaffold burst strength.

6.2.5 *In vitro* enzymatic degradation

The stability of silk lyogel TEVGs was investigated in the presence of a proteolytic enzyme (protease XIV, Sigma-Aldrich, USA) following the previously described protocol in Chapter 4. Briefly, the dry weight of LG and LGMP scaffolds (n=6) was recorded, followed by incubation in enzymatic solution (2 U/mL protease in PBS) at 37°C. The enzyme solution was replenished every 3 days to ensure adequate enzymatic activity throughout the experimental period. In a parallel control setup, both of the scaffold variants were incubated in PBS without protease enzyme. At predefined time points, the dry weight of the scaffolds was recorded and scaffold degradation is reported as the percentage of mass loss over time. We also subjected the scaffolds to SEM analysis at different time points for a closer observation of the degradation patterns.

6.2.6 Scaffold pulsatile perfusion and analysis of microparticle retention

Fluorescein isothiocyanate (FITC) loaded PLGA microparticles were used during LGMP silk lyogel scaffold fabrication to visualize the microparticles post perfusion. The LGMP scaffolds (n=4) were mounted in the testing chamber of our perfusion setup and subjected to physiological intraluminal pulsatile pressure (80/120 mmHg) for 1h using DI water at 37°C. Post perfusion, 10 μm scaffold sections were obtained using cryomicrotome, and fluorescent microscopic images were captured by Nikon 90i fully automated upright microscope. At least four different sections along the length of the scaffold were imaged for an individual scaffold. Scaffolds without perfusion were considered as control. Microparticle retention post perfusion was quantified by image processing using particle count plugin of Fiji-ImageJ (National Institute of Health, USA) software

implementing thresholding limit per microparticle size. We also validated the microparticle retention by imaging the scaffold lumen and wall using SEM.

6.2.7 Biocompatibility of silk lyogel TEVGs

The biocompatibility of bare and PLGA microparticle loaded silk lyogel scaffolds was assessed with stromal vascular fraction (SVF) cells obtained from human adipose tissue following previously published protocol [338]. Silk lyogel (LG core and LGMP core) circular discs (thickness 2 mm, diameter 8 mm, n=4) were seeded with 10^5 cells and cell viability was quantified by measuring the cell metabolic activity using AlamarBlue assay (Thermo Fisher Scientific, USA) at predefined time points following manufacturer instructions. The results were plotted as normalized values compared to day 1. In addition, cell attachment on to silk lyogel discs was validated by staining the cell nucleus with DAPI (Sigma-Aldrich, USA) followed by fluorescent microscopic imaging using Nikon 90i fully automated upright microscope.

6.2.8 Statistical analysis

Significant difference among different experimental groups was analyzed using one-way analysis of variance (ANOVA) following post hoc Tukey's test. The experimental values are represented as mean ± standard deviation (SD) for at least n=3 unless otherwise noted. p-value less than 0.05 is considered as significantly different.

6.3 Results

6.3.1 Morphological analysis of silk lyogel TEVGs

The bi-layered tubular silk lyogel TEVGs were obtained with high efficacy and reproducibility. The overall macroscopic inspection suggested a smoother TEVG surface without any sign of layer delamination for both LG and LGMP scaffolds (**Figure 6.1A**), which is in agreement with SEM micrographs. The cross-section analysis of scaffolds was suggestive of two distinct layers representing the inner porous lyophilized layer supported by an outer fibrous electrospun layer (**Figure 6.1B**). No significant difference was observed in the major scaffold dimensions among LG and LGMP types. The diameter of the PLGA microparticles was 10 ± 2 μm. The total wall thickness of bi-layered scaffolds was 580 ± 118 μm (490 ± 120 μm thick inner porous layer and

128 ± 18 µm thick outer electrospun layer). The inner and outer diameter of scaffolds were 1040 ± 82 µm and 2194 ± 230 µm, respectively.

The higher magnification images of LGMP showed uniform entrapment of PLGA microparticles in scaffold struts. The adequate pore-interconnectivity was also observed for both silk scaffold variants. The pore size distribution and overall scaffold porosity were quantified using micro-CT analysis by analyzing 3D scaffold images (**Figure 6.1C**). The micro-CT data obtained was in agreement with SEM images suggesting bi-layered scaffold morphology without any delamination between layers. A heterogeneous pore size distribution was observed for the inner layer of scaffolds (53 ± 30 µm and 43 ± 24 µm for LG and LGMP, respectively). LGMP scaffolds pore size spectra showed a broader peak, whereas a comparatively narrow peak was obtained for LG scaffolds. Overall porosity of inner layers of LG and LGMP scaffolds was 91.63 ± 1.56 % and 87.83 ± 2.12 %, respectively. Strut thickness for both scaffold types was in the range of 5 ± 2 µm **(Figure 6.1D-E)**.

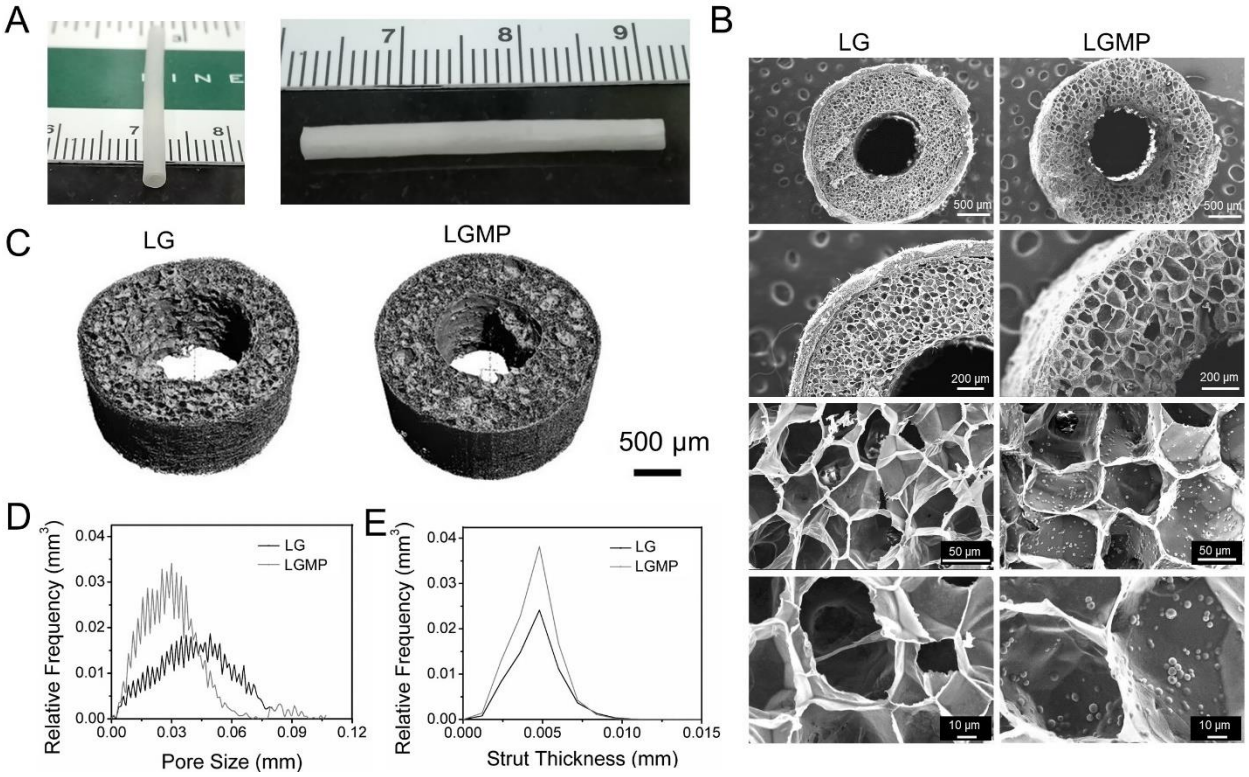

Figure 6.1. *Morphological analysis of silk lyogel scaffolds. (A) Gross appearance of silk lyogel scaffolds. (B) SEM analysis of silk scaffolds representing porosity and pore interconnectivity. (C) Micro-CT acquired 3D images of scaffolds. Quantification analysis of (D) pore size and (E) strut thickness of LG and LGMP scaffolds.*

6.3.2 Mechanical properties

Lyogel silk scaffolds were mechanically tested in longitudinal (long) and circumferential (circ) directions. In general, the long stress-strain curves showed a higher slope than the circ ones (**Figure 6.2A-D**). For all scaffolds, the modulus in the low-stress region (low modulus) was significantly higher than the high-stress region (high modulus) ($p<0.05$). As reflected by the stress-strain curves, a higher modulus value was obtained in longitudinal direction than the circumferential modulus. No significant difference was observed in the mechanical properties of lyogel silk scaffolds after incorporation of PLGA microparticles (LG core vs. LGMP core and LG vs. LGMP, $p>0.05$). The low modulus values were significantly high for long vs. circ direction (3.65 ± 0.54 MPa vs. 0.07 ± 0.01 MPa for LG, 1.35 ± 0.16 MPa vs. 0.47 ± 0.09 MPa for LG core, 1.96 ± 0.4 MPa vs. 0.12 ± 0.06 MPa for LGMP, and 1.03 ± 0.34 MPa vs. 0.16 ± 0.07 MPa for LGMP core) respectively ($p<0.01$). Moreover, the coating of the inner lyogel layer with the outer electrospun layer improved the low modulus in the long direction ($p<0.01$) (**Figure 6.2E**). A similar trend was observed for high modulus of lyogel scaffolds with an electrospun layer for long vs. circ (0.37 ± 0.02 MPa vs. 0.24 ± 0.05 MPa for LG and 0.37 ± 0.02 MPa vs. 0.2 ± 0.06 MPa for LGMP) respectively ($p<0.01$). On the contrary, no significant difference was observed between long vs. circ values for LG core ($p=0.96$) and LGMP core ($p=0.12$) scaffolds. The effect of the electrospun layer was also characterized by an increment in high modulus in the long direction ($p<0.01$) (**Figure 6.2F**). Stress values at failure did not show any significant difference between long and circ directions ($p>0.01$), but a higher strain was recorded in circ direction for all scaffold types ($p<0.05$) (**Figure 6.2G-H**).

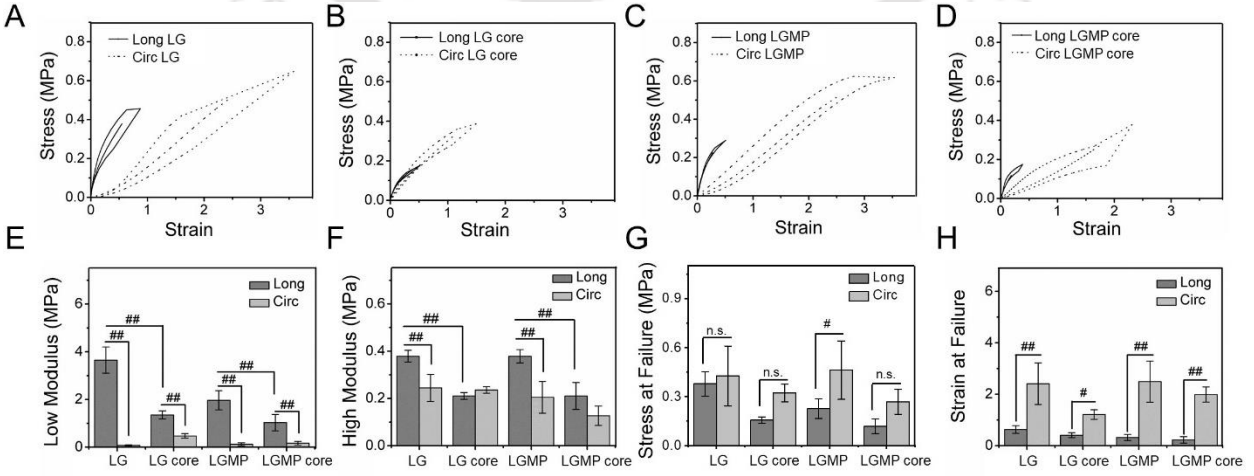

Figure 6.2. *Uniaxial tensile test of silk lyogel TEVGs. Representative average stress-strain curves of (A) LG, (B) LG core, (C) LGMP, and (D) LGMP core silk scaffolds in longitudinal (long) and*

circumferential (circ) directions. Graphs are representing scaffold modulus in (E) low-stress region (low modulus) and (F) high-stress region (high modulus). Graphs representing (G) stress and (H) strain at the scaffold failure points. (#p<0.05, ##p<0.01, n.s.=not significant)

A comparative analysis of bi-layered silk lyogel scaffolds suggested no significant difference in suture retention force between LG (0.26 ± 0.04 N) and LGMP (0.25 ± 0.10 N) scaffolds (p=0.80) (**Figure 6.3A**). Suture retention tension (458.49 ± 78.91 N/m for LG vs. 438.26 ± 175.78 N/m for LGMP) also showed a similar trend (p=0.80) (**Figure 6.3B**). A comparison of dynamic mechanical properties of scaffolds at 1h (initial) and 7h (final) suggested no significant difference between LG and LGMP scaffolds at different time points. Under physiological pulsatile pressure, β-stiffness (200.97 ± 12.69 vs. 180.05 ± 10.04 at initial and 292.77 ± 70.19 vs. 280.65 ± 109.52 at the final time point for LG vs. LGMP respectively) and dynamic compliance (1.07 ± 0.15×10^{-4} $mmHg^{-1}$ vs. 1.62 ± 0.69×10^{-4} $mmHg^{-1}$ at initial and 0.8 ± 0.27×10^{-4} $mmHg^{-1}$ vs. 0.99 ± 0.3×10^{-4} $mmHg^{-1}$ at the final time point for LG vs. LGMP respectively) did not vary over time (p>0.05) (**Figure 6.3C-D**). In addition, the scaffold diameter remained stable over time as characterized by creep analysis (**Figure 6.3E**). The burst strength of the silk scaffolds ranged 948.10 ± 58.29 mmHg for LG and 1029 ± 107.65 mmHg for LGMP scaffolds with no significant difference between groups (p=0.22) (**Figure 6.3F**).

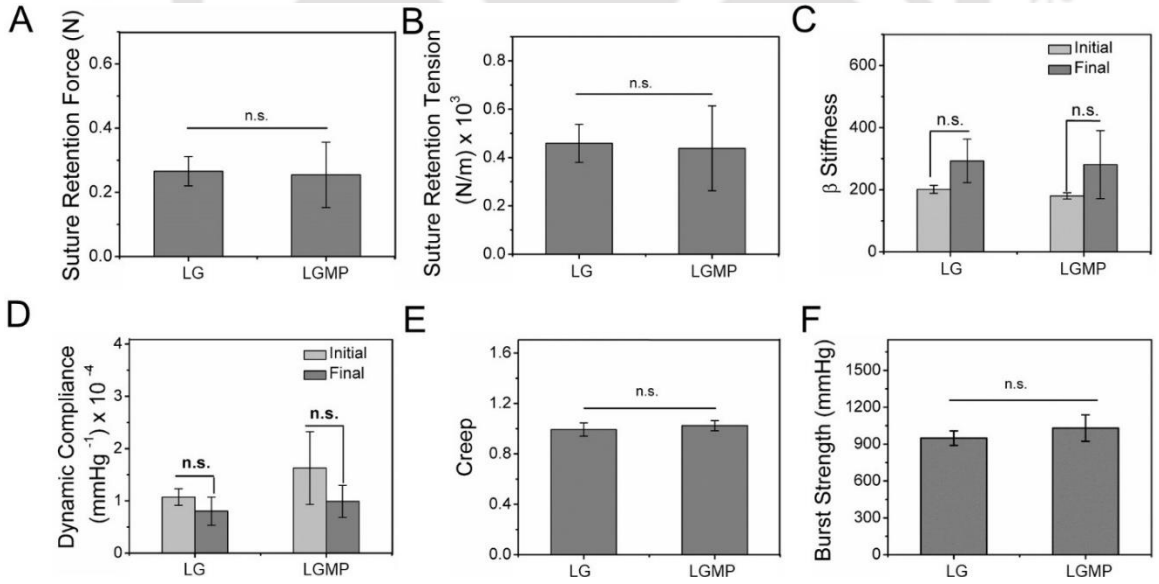

Figure 6.3. *Mechanical properties of silk lyogel TEVGs. Comparison of approximate (A) suture retention force, (B) suture retention tension, (C) β-stiffness, (D) dynamic compliance, (E) creep and (L) burst strength of bi-layered (LG vs. LGMP) lyogel silk scaffolds. (n.s.=not significant)*

6.3.3 Biodegradation of lyogel silk scaffolds

The qualitative and quantitative degradation of silk scaffolds was analyzed in the presence of protease XIV enzyme. No structural difference was observed for both scaffold variants kept in PBS (without enzyme) over time. However, we observed structural deformation of the inner porous layer for the scaffolds kept in protease enzyme (LG/PRT and LGMP/PRT). High resolution scanning electron micrographs suggested degradation of scaffold struts (**Figure 6.4A**). Owing to structural deformation and mechanical delamination of the outer electrospun layer, we could not capture SEM images of scaffold cross-sections after 15 days. The degradation of silk scaffolds was further quantified by recording the mass loss over time. No significant difference was observed after 4 days between any scaffold group ($p>0.05$). Both silk scaffolds showed minimal degradation in PBS, having 76.25 ± 10.5 and 65.89 ± 8.65 percent remaining mass for LG and LGMP, respectively. On the contrary, scaffolds kept in protease solution degraded at a faster rate with only 27.08 ± 5.83 (LG) and 15.4 ± 2.51 (LGMP) percent remaining mass after 30 days, significantly less than PBS merged scaffolds ($p<0.01$) (**Figure 6.4B**).

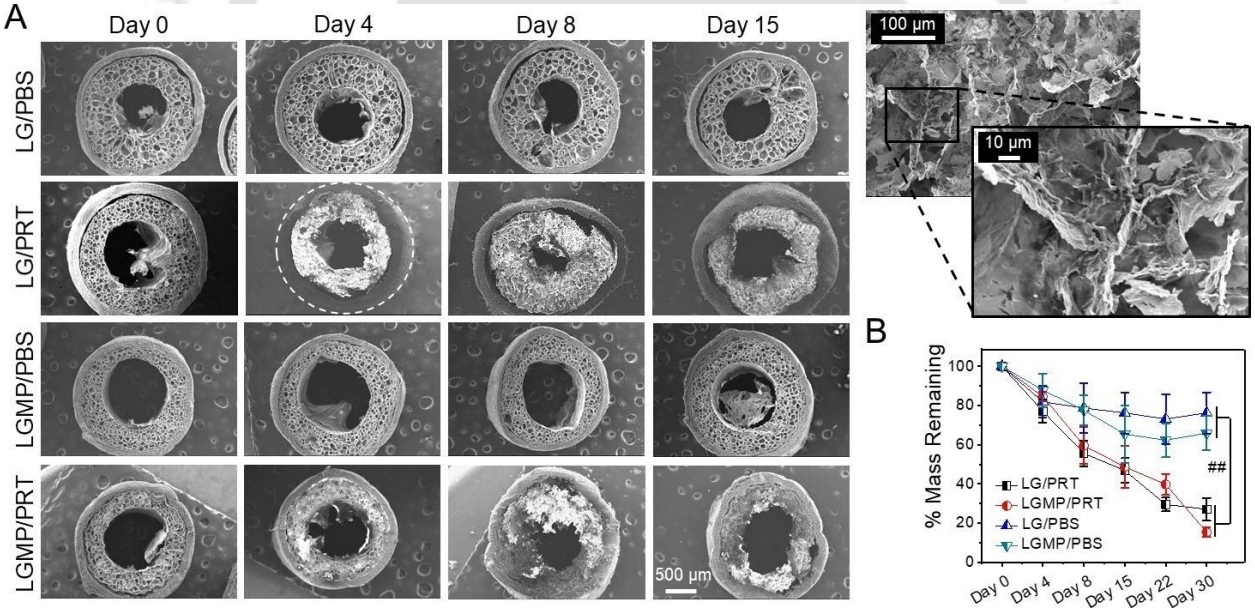

Figure 6.4. *Degradation of silk lyogel scaffolds. (A) Representative scanning electron micrographic images showing the cross-section of silk lyogel scaffolds in the presence of protease XIV enzyme over 15 days. High-resolution images on the right show the degradation pattern of scaffold struts after 15 days of protease treatment. (B) Quantitative analysis of scaffold degradation over time in the presence of protease enzyme. Control group (samples kept in PBS without enzyme: LG/PBS and LGMP/PBS). Experimental group (samples kept in protease enzyme: LG/PRT and LGMP/PRT). (##p<0.01)*

6.3.4 Microparticle retention after perfusion

Silk lyogel scaffolds were mounted in the testing chamber (**Figure 6.5A**) and perfused with physiologically relevant pulsatile pressure for 1h (**Figure 6.5B**) to analyze the microparticle retention over time. Fluorescent microscopic images of scaffold cross-sections validated the presence of microparticles post perfusion. The bright green particles entrapped in the scaffold struts represent the FITC tagged microparticles in the fluorescent images (**Figure 6.5C**). The scanning electron micrographs of scaffold cross-sections corroborated the fluorescent microscopic data and suggested the presence of intact microparticles embedded in the scaffold struts in both control and perfusion groups (**Figure 6.5D**). High magnification SEM micrographs showed the presence of microparticles along the lumen of the lyogel scaffolds (LGMES) (**Figure 6.5E**). The fluorescent microscopic images were further processed to quantify the microparticles present in scaffolds before and after perfusion (n=6). The data suggested an insignificant difference between control and perfusion groups ($p>0.05$), confirming that scaffold perfusion does not wash off the microparticles embedded in lyogel silk scaffolds (**Figure 6.5F**).

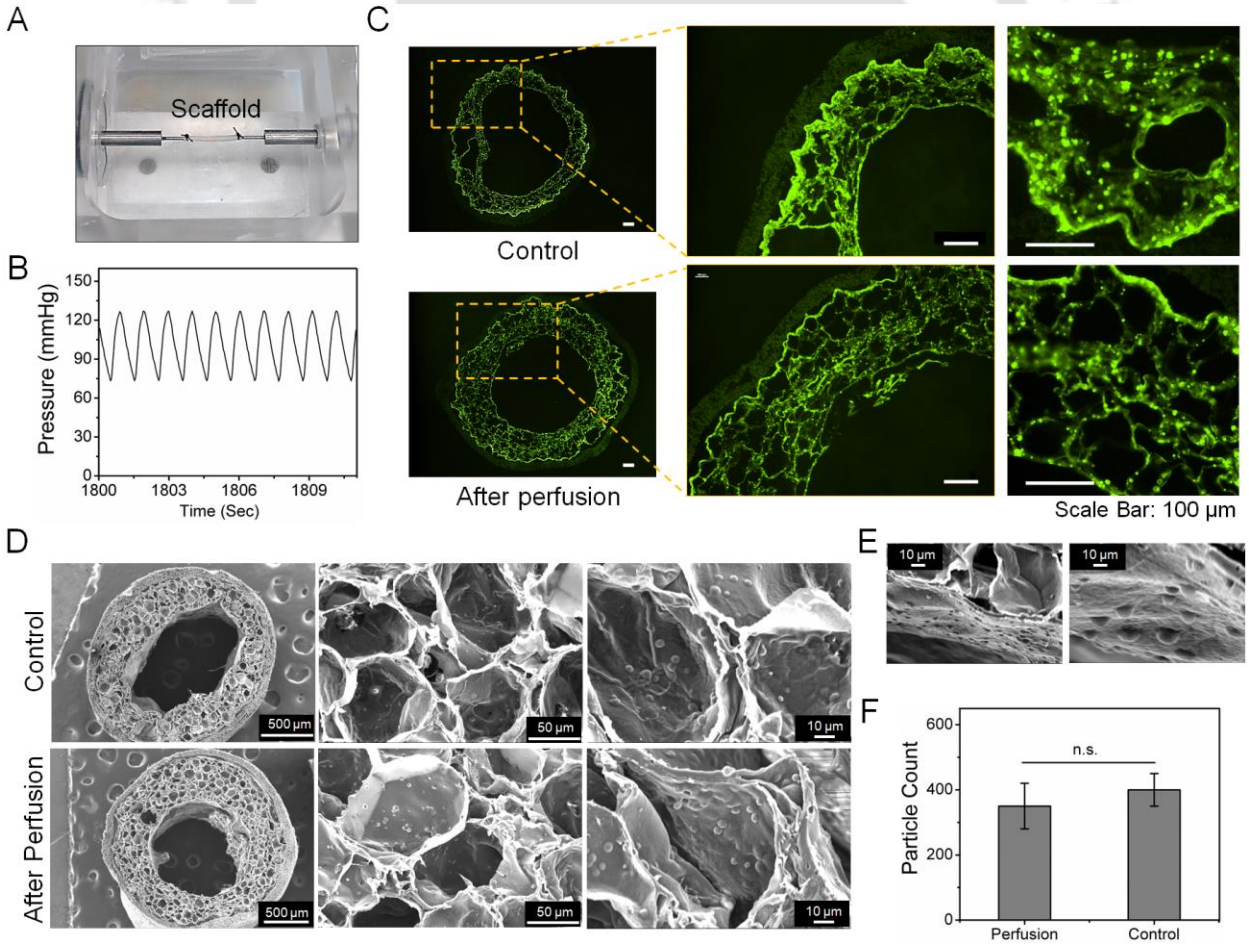

Figure 6.5. *Microparticle retention in silk lyogel scaffolds after physiologically relevant pulsatile perfusion. (A) Representative image showing silk scaffold mounted on a testing chamber of pulsatile flow setup. (B) The representative curve is showing the intraluminal pulsatile pressure over time. (C) Fluorescent microscopic images are showing microparticle retention after 1h of pulsatile perfusion. Microparticles were tagged with FITC fluorescent dye (green color particles are visible in the high-resolution images on the right). Scaffolds without perfusion represent the control group. Scanning electron microscopic images showing microparticle retention after 1h perfusion in (D) cross-section and (E) lumen of scaffolds. (F) Graph showing the quantitative analysis of microparticle retention obtained by processing the fluorescent microscopic images. (n.s.=not significant)*

6.3.5 Biocompatibility assessment of silk lyogel scaffolds

The ability of LG core and LGMP core (with blank microparticles) scaffolds to support SVF cell growth, proliferation was assessed by AlamarBlue assay, and results are reported as normalized values as compared to day 1. The cells were seeded on lyogel discs of 6 x 2 mm (**Figure 6.6A**). As shown in **Figure 6.6B**, both scaffolds supported SVF proliferation throughout the experimental time, and no significant difference was recorded between the two experimental groups ($p>0.01$). Cells started proliferation after seeding on silk scaffolds from day one onwards. A significant increment was observed at each successive time point with approximately a 1.4-fold increase in cell population on day 15 ($p<0.01$). DAPI stained images of SVF cells cultured on silk lyogel discs are shown in **Figure 6.6C**.

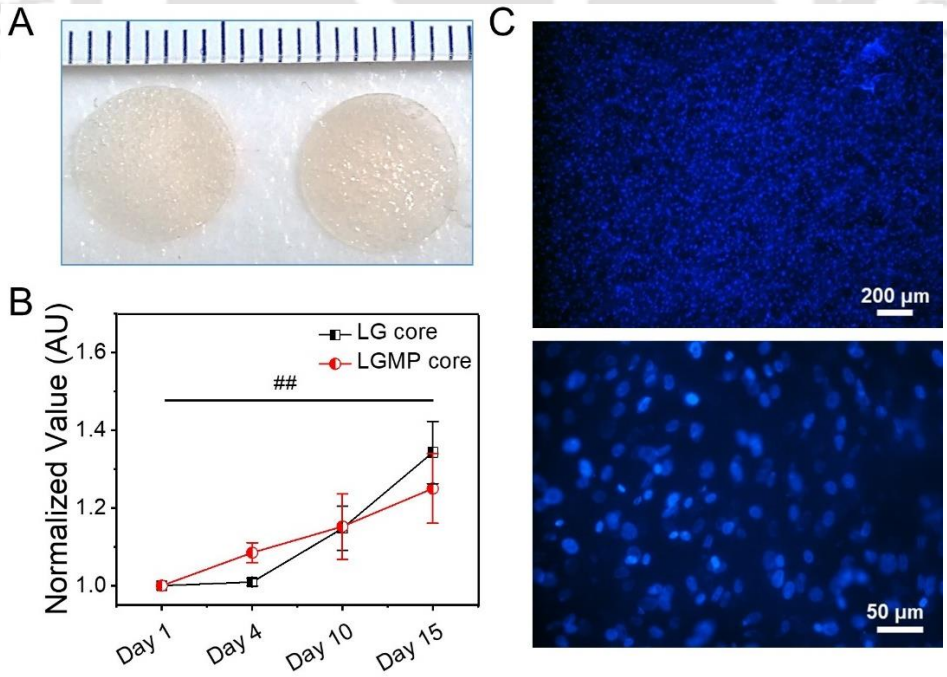

Figure 6.6. *Biocompatibility of silk lyogel scaffolds. (A) Representative image showing lyogel silk scaffold discs used for biocompatibility analysis. (B) Quantification of SVF cell proliferation over*

time cultured on silk lyogel discs using AlamarBlue assay. The values are normalized with day 1 data. (C) DAPI stained (blue color nucleus) fluorescent microscopic images showing adhesion of SVF cells onto lyogel silk scaffolds. (##p<0.01)

6.4 Discussion

Readily available, bioactive, cell-free grafts have remarkable potential for clinical translation. Much of prior literature has shown encouraging effects of MSCs seeding on TEVGs' *in vivo* performance [44, 342, 407]; however, they are reported to act in a paracrine fashion and leave the implanted graft after a particular time [44]. Considering the aforementioned fact, researchers are now investing their efforts in identifying the stem cell-secreted factors that prevent acute thrombosis and assist in overall graft remodeling. CCL2/MCP1 is one of the identified factors that is now believed to involve the former process and enact by recruiting macrophages onto the remodeling site. Such information can be capitalized to fabricate cell-free grafts having similar bioactivity as cell-seeding.

In this study, we successfully developed a novel, silk-based, bi-layered vascular scaffold that is intrinsically capable of delivering bioactive cargo via loaded MPs. The scaffold is designed to match the dimensions of *in vivo* model of a rat aorta [408], along with having appropriate mechanical properties (**Table 6.1**) and pore characteristics that encourage cellular infiltration of host cells *in vivo* [409-411]. Graft success crucially depends on a delicate balance between degradation of scaffold biomaterial and rate of neo-tissue formation. *In vitro* degradation analysis of silk lyogel scaffolds revealed that MP incorporation does not significantly alter the TEVG degradation rate compared to control scaffolds (LG). Moreover, qualitative analysis of scaffolds degradation pattern revealed local degradation of struts without compromising the overall mechanical stability. These outcomes suggest the suitability of lyogel scaffolds for *in vivo* implantation and are envisaged to allow neo-tissue formation.

The dynamic microenvironment of blood vessels resulting from pulsatile blood flow through the lumen renders diverse mechanical forces onto scaffold walls, including radial tension and shear stress [412]. In order to ensure the stable integration of MPs in the lyogel scaffolds, they were further characterized using a custom-designed pulsatile flow set up under the influence of physiologically relevant pressure and flow. Qualitative and quantitative analysis suggested MPs' stability in the scaffold walls, substantiated by no significant dislodging. FITC loaded MPs were shown to be embedded in the scaffolds, corroborating their cargo loading efficiency. The lyogel

scaffolds were compatible with SVF cells and supported their growth *in vitro* without any detrimental impact. This observation suggests the suitability of MP loaded lyogel TEVG system for the growth and maturation of host cells post-implantation.

This study demonstrates the fabrication of a cell-free tissue-engineered vascular graft capable of delivering any requisite biological payload to induce remodeling. With the advent of technological advancements, it is imperative to identify a set of MSC secreted factors facilitating the favorable outcomes in terms of neo-tissue formation. This technology's acellular nature potentially reduces risk, increases reproducibility, and results in a cost-effective graft compared to cell-based options. These grafts are aimed to endow ready availability, minimize regulatory hurdles and improve off-the-shelf clinical feasibility.

Table 6.1. *Mechanical properties of silk scaffolds compared with hSV and pIMA.*

	LG Scaffold	**LGMP Scaffold**	**hSV [337]**	**pIMA [337]**
Circumferential stress at failure (MPa)	0.42 ± 0.18	0.4 ± 0.17	3.7 ± 2.0	10.4 ± 7.1
Circumferential strain at failure	2.41 ± 0.81	2.49 ± 0.80	1.7 ± 0.7	1.5 ± 0.2
Circumferential Modulus (MPa)	Low: 0.07 ± 0.01 High: 0.24 ± 0.05	Low: 0.12 ± 0.06 High: 0.20 ± 0.06	2.5 ± 1.0	0.4 ± 0.2
β Stiffness	Initial: 200.97 ± 12.69 Final: 292.77 ± 70.19	Initial: 180.05 ± 10.04 Final: 280.65 ± 109.52	40 ± 10	15 ± 10
Dynamic compliance $(mmHg^{-1})*10^{-4}$	Initial: 1.07 ± 0.15 Final: 0.80 ± 0.27	Initial: 1.62 ± 0.69 Final: 0.99 ± 0.30	3.4 ± 2.0	11.2 ± 6.0
Suture retention tension $(N/m)*10^{3}$	0.45 ± 0.07	0.43 ± 0.17	6.0 ± 2.2	4.0 ± 2.0
Suture retention force (N)	0.26 ± 0.04	0.25 ± 0.10	2.5 ± 0.8	1.0 ± 0.8
Burst pressure (mmHg)	948.10 ± 58.29	1029 ± 107.65	1000.0 ± 400	2300 ± 100

6.5 Significant findings

1. The microparticle-loaded silk lyogel TEVG system developed herein provides a clinically relevant means of delivering required bioactive cargos to emulate the effect of cell seeding.
2. Adequate scaffold porosity of lyogel silk scaffolds was observed, which is envisaged to encourage host cell infiltration post-implantation.
3. Mechanical properties (static and dynamic) of developed silk scaffolds were comparable to the native human blood vessel.
4. Stable integration of PLGA microparticles in the struts of lyogel silk scaffolds was validated by exposing them to the physiologically relevant pulsatile flow.
5. The developed lyogel TEVG scaffolds were biodegradable, and the loading of microparticles did not affect the degradation rate.
6. Scaffold discs simulating the inner layer of bi-layered lyogel scaffold supported the growth and proliferation of SVF cells.
7. Microparticles were successfully loaded with a fluorescent dye (FITC), substantiating their loading efficiency.

Note: The lyogel scaffolds described in this chapter were further investigated for their *in vivo* performance in collaboration with Prof. David A. Vorp, University of Pittsburgh, PA, USA, which is not a part of this thesis work, hence not presented. Microparticles were loaded with CCL2/MCP1, which significantly improved the acute patency (100%) of grafts implanted in the abdominal rat aorta. *In vivo* results partially validate the hypothesis of creating readily available cell-free TEVGs loaded with cell-mimicking microparticles.

SUMMARY AND FUTURE PERSPECTIVES

SUMMARY AND FUTURE PERSPECTIVES

Blood vessel-related diseases remain a pressing human health concern. Currently available clinical options rely on the availability of a healthy autologous vessel to replace the diseased counterpart. Such treatment modalities are prevalently limited due to donor site morbidity and shortage of healthy vessels. This thesis aims to orchestrate alternate engineered solutions that can effectively replace the diseased portion of blood vessels to restore the adequate blood supply to the target organ. The overall concept of tissue-engineered vascular grafts (TEVGs) essentially involves the following steps: 1) graft fabrication, 2) implantation, 3) remodelling (infiltration of host cells and balanced degradation of graft biomaterial), 4) neo-tissue formation, 5) complete removal of biomaterial recapitulating a native-like remodelled tissue with growth potential. Herein, we have progressively hypothesized and validated multiple approaches to designing small-diameter TEVGs using various silk biomaterials. The implication of non-mulberry silk for vascular regeneration is one of the novel highlights of this work.

We first identified crucial parameters required to improve the clinical feasibility of TEVGs as follows: 1) bioactivity/biocompatibility, 2) anti-thrombogenicity, 3) biodegradability, 4) mechanical properties, 5) immune compatibility, 6) affordability, 7) minimizing fabrication time and 8) minimizing regulatory hurdles. A comprehensive analysis of cell-biomaterial interaction revealed the biocompatibility of silk with vascular cells. The non-mulberry silk variety (*Antheraea assama*) showed superior outcomes in terms of cell proliferation, migration, mechanics and biodegradation. Micropatterned engineered surfaces could recapitulate the native-like cellular alignment, which was further capitalized to fabricate multi-layered cellular conduits comprised of autologous vascular cells (described in Chapter 3). While this approach provides a patient-specific solution, a higher fabrication time (over a month) is a potential setback towards clinical translation. A novel bi-layered scaffold is further designed consisting of an inner porous lyophilized layer coated with an outer electrospun nanofibrous layer (described in Chapter 4). Human SVF cells (seeded in the inner layer) assisted in graft remodelling by preventing the blood clotting and recruitment of host cells via paracrine signalling after implantation in rat aorta via end-to-end anastomosis. SVF seeding of vascular scaffolds brought down the fabrication time from months to a couple of days.

Clinical feasibility of the silk-based TEVGs was further improved by developing acellular/cell-free approaches aiming to confer ready availability (described in Chapter 5&6), while contemporaneously minimizing the regulatory hurdles. We hypothesized the preservation of Wharton's jelly MSCs secreted factors in the surrounding matrix. Capitalizing on this concept, dWJ functionalized grafts were developed containing a plethora of MSC secreted bioactive factors, including immunomodulatory cytokines. The functional assessment revealed faster *in situ* remodelling and neo-tissue formation after implantation in rabbit jugular vein. The mechanistic analysis reflected the immunomodulation-assisted remodelling. This approach provides a ready available bioactive TEVG. While dWJ functionalization enables superior remodelling, it is believed that apparently, the whole MSCs secretome is not crucial; a fraction of bioactive factors may provide comparable remodelling outcomes. In addition, the ambiguous presence of yet unknown factors in dWJ matrix is envisaged to be a roadblock towards clinical 'off the shelf' translation. Hence, in the follow-up endeavour, we designed a TEVG system capable of delivering a specific bioactive cargo (CCL2) by incorporating cell-mimicking PLGA microparticles in the bi-layered scaffolds. Overall, the work presented in this thesis disclosed a new bi-layered design of vascular scaffold, minimized the TEVG fabrication time by ensuring their ready availability and conferred superior chances of regulatory clearances.

Future perspectives of this thesis work are enumerated in the following sections:

1) Identification of specific MSCs secreted bioactive factors, which are essentially involved in the *in situ* graft remodelling while conferring adequate bioactivity.
2) Recruitment of host cells in the implanted scaffold may follow either of the following three mechanisms: transanastomotic ingrowth, transmural capillary formation, and fall out process. The remodelling process would crucially depend on graft length. Herein, nearly 1cm long TEVGs were investigated in small animal models (rats/rabbits). Analysis of overall remodelling of longer grafts in larger animal models (sheep/porcine) would further ascertain their pre-clinical efficacy.
3) Aged people are prone to cardiovascular diseases. The effect of patient age on graft remodelling and neo-tissue formation would provide clinically relevant data based on target patient demographics.

4) Implementation of induced pluripotent stem cells (iPSCs) may provide an option for patient-specific precision medicine.
5) Fabrication immune-informed TEVGs may improve their performance by targeting key players of the immune system involved in the remodelling process.
6) Emerging technologies can now develop advanced computational models, predicting graft remodelling and neo-tissue formation more accurately. Implementation of these models would assist in identifying the ideal parameters (rate of degradation, pore size, porosity, graft mechanics, surface topography, rate of ECM formation, etc.) to predict the required outcomes.
7) Further validation through various phases of human clinical trials could enable technology transfer.

BIBLIOGRAPHY

[1] C.D. Mathers, D. Loncar, Projections of global mortality and burden of disease from 2002 to 2030, PLoS medicine 3(11) (2006) e442.
[2] W.H. Organization, The global burden of disease: 2004 update. Geneva: World Health Organization; 2008, 2010.
[3] L.E. Niklason, J.H. Lawson, Bioengineered human blood vessels, Science 370(6513) (2020).
[4] F.J. Veith, C.M. Moss, S. Sprayregen, C. Montefusco, Preoperative saphenous venography in arterial reconstructive surgery of the lower extremity, Surgery 85(3) (1979) 253-256.
[5] C.E. Stowell, Y. Wang, Quickening: Translational design of resorbable synthetic vascular grafts, Biomaterials 173 (2018) 71-86.
[6] P. Zilla, M. Deutsch, D. Bezuidenhout, N.H. Davies, T. Pennel, Progressive Reinvention or Destination Lost? Half a Century of Cardiovascular Tissue Engineering, Frontiers in Cardiovascular Medicine 7 (2020).
[7] D. Wang, Y.-Y. Xu, l. wang, X. Wang, c. ren, b. zhang, Q. Li, J. Thomson, L.-S. Turng, Expanded Polytetrafluoroethylene Blood Vessel Grafts with Embedded Reactive Oxygen Species (ROS) Responsive Antithrombogenic Drug for Elimination of Thrombosis, ACS Applied Materials & Interfaces (2020).
[8] S. Fleischer, D.N. Tavakol, G. Vunjak-Novakovic, From Arteries to Capillaries: Approaches to Engineering Human Vasculature, Advanced Functional Materials (2020) 1910811.
[9] C.B. Weinberg, E. Bell, A blood vessel model constructed from collagen and cultured vascular cells, Science 231(4736) (1986) 397-400.
[10] F.G. Omenetto, D.L. Kaplan, New opportunities for an ancient material, Science 329(5991) (2010) 528-531.
[11] G.H. Altman, F. Diaz, C. Jakuba, T. Calabro, R.L. Horan, J. Chen, H. Lu, J. Richmond, D.L. Kaplan, Silk-based biomaterials, Biomaterials 24(3) (2003) 401-416.
[12] D. Chouhan, B.B. Mandal, Silk biomaterials in wound healing and skin regeneration therapeutics: From bench to bedside, Acta biomaterialia 103 (2020) 24-51.
[13] G. Janani, M. Kumar, D. Chouhan, J.C. Moses, A. Gangrade, S. Bhattacharjee, B.B. Mandal, Insight into silk-based biomaterials: From physicochemical attributes to recent biomedical applications, ACS Applied Bio Materials 2(12) (2019) 5460-5491.
[14] D.N. Rockwood, R.C. Preda, T. Yücel, X. Wang, M.L. Lovett, D.L. Kaplan, Materials fabrication from Bombyx mori silk fibroin, Nature protocols 6(10) (2011) 1612.
[15] T. Asakura, T. Tanaka, R. Tanaka, Advanced silk fibroin biomaterials and application to small-diameter silk vascular grafts, ACS Biomaterials Science & Engineering 5(11) (2019) 5561-5577.
[16] S. Pradhan, O.A. Banda, C.J. Farino, J.L. Sperduto, K.A. Keller, R. Taitano, J.H. Slater, Biofabrication strategies and engineered in vitro systems for vascular mechanobiology, Advanced healthcare materials 9(8) (2020) 1901255.
[17] P. Libby, P.M. Ridker, A. Maseri, Inflammation and atherosclerosis, Circulation 105(9) (2002) 1135-1143.

[18] G.K. Hansson, A. Hermansson, The immune system in atherosclerosis, Nature immunology 12(3) (2011) 204-212.
[19] R. Goetz, Internal mammary-coronary artery anastomosis-a nonsuture method employing tantalum rings, J Thorac Cardiovasc Surg 41 (1961) 378-386.
[20] L. Melly, G. Torregrossa, T. Lee, J.-L. Jansens, J.D. Puskas, Fifty years of coronary artery bypass grafting, Journal of thoracic disease 10(3) (2018) 1960.
[21] S. Verma, P.E. Szmitko, R.D. Weisel, D. Bonneau, D. Latter, L. Errett, Y. LeClerc, S.E. Fremes, Should radial arteries be used routinely for coronary artery bypass grafting?, Circulation 110(5) (2004) e40-e46.
[22] A. Chaikhouni, F.A. Crawford, P.J. Kochel, L.S. Olanoff, P.V. Halushka, Human internal mammary artery produces more prostacyclin than saphenous vein, The Journal of thoracic and cardiovascular surgery 92(1) (1986) 88-91.
[23] O. Ohta, A. Kusaba, Development of vasa vasorum in the arterially implanted autovein bypass graft and its anastomosis in the dog, International angiology: a journal of the International Union of Angiology 16(3) (1997) 197-203.
[24] F. Otsuka, K. Yahagi, K. Sakakura, R. Virmani, Why is the mammary artery so special and what protects it from atherosclerosis?, Annals of cardiothoracic surgery 2(4) (2013) 519.
[25] M.R. Kapadia, D.A. Popowich, M.R. Kibbe, Modified prosthetic vascular conduits, Circulation 117(14) (2008) 1873-1882.
[26] C.H. Sparks, Development of a successful silicone rubber arterial graft, The Annals of thoracic surgery 2(4) (1966) 585-593.
[27] R.W. Hallin, W.R. Sweetman, The Sparks' mandril graft: A seven year follow-up of mandril grafts placed by Charles H. Sparks and his associates, The American Journal of Surgery 132(2) (1976) 221-223.
[28] M. Deutsch, J. Meinhart, P. Zilla, N. Howanietz, M. Gorlitzer, A. Froeschl, A. Stuempflen, D. Bezuidenhout, M. Grabenwoeger, Long-term experience in autologous in vitro endothelialization of infrainguinal ePTFE grafts, Journal of vascular surgery 49(2) (2009) 352-362.
[29] N. L'heureux, S. Paquet, R. Labbé, L. Germain, F.A. Auger, A completely biological tissue-engineered human blood vessel, The FASEB Journal 12(1) (1998) 47-56.
[30] N. L'Heureux, T.N. McAllister, L.M. de la Fuente, Tissue-engineered blood vessel for adult arterial revascularization, New England Journal of Medicine 357(14) (2007) 1451-1453.
[31] T.N. McAllister, M. Maruszewski, S.A. Garrido, W. Wystrychowski, N. Dusserre, A. Marini, K. Zagalski, A. Fiorillo, H. Avila, X. Manglano, Effectiveness of haemodialysis access with an autologous tissue-engineered vascular graft: a multicentre cohort study, The Lancet 373(9673) (2009) 1440-1446.
[32] W. Wystrychowski, L. Cierpka, K. Zagalski, S. Garrido, N. Dusserre, S. Radochonski, T.N. McAllister, N. L'Heureux, Case study: first implantation of a frozen, devitalized tissue-engineered vascular graft for urgent hemodialysis access, The journal of vascular access 12(1) (2011) 67-70.

[33] L. Niklason, J. Gao, W. Abbott, K. Hirschi, S. Houser, R. Marini, R. Langer, Functional arteries grown in vitro, Science 284(5413) (1999) 489-493.
[34] S.L. Dahl, J. Koh, V. Prabhakar, L.E. Niklason, Decellularized native and engineered arterial scaffolds for transplantation, Cell transplantation 12(6) (2003) 659-666.
[35] J.H. Lawson, M.H. Glickman, M. Ilzecki, T. Jakimowicz, A. Jaroszynski, E.K. Peden, A.J. Pilgrim, H.L. Prichard, M. Guziewicz, S. Przywara, Bioengineered human acellular vessels for dialysis access in patients with end-stage renal disease: two phase 2 single-arm trials, The Lancet 387(10032) (2016) 2026-2034.
[36] T. Shin'oka, Y. Imai, Y. Ikada, Transplantation of a tissue-engineered pulmonary artery, New England Journal of Medicine 344(7) (2001) 532-533.
[37] N. Hibino, E. McGillicuddy, G. Matsumura, Y. Ichihara, Y. Naito, C. Breuer, T. Shinoka, Late-term results of tissue-engineered vascular grafts in humans, The Journal of thoracic and cardiovascular surgery 139(2) (2010) 431-436. e2.
[38] J.D. Drews, H. Miyachi, T. Shinoka, Tissue-engineered vascular grafts for congenital cardiac disease: Clinical experience and current status, Trends in cardiovascular medicine 27(8) (2017) 521-531.
[39] T. Shin'oka, G. Matsumura, N. Hibino, Y. Naito, M. Watanabe, T. Konuma, T. Sakamoto, M. Nagatsu, H. Kurosawa, Midterm clinical result of tissue-engineered vascular autografts seeded with autologous bone marrow cells, The Journal of thoracic and cardiovascular surgery 129(6) (2005) 1330-1338.
[40] J.D. Drews, V.K. Pepper, C.A. Best, J.M. Szafron, J.P. Cheatham, A.R. Yates, K.N. Hor, J.C. Zbinden, Y.-C. Chang, G.J. Mirhaidari, Spontaneous reversal of stenosis in tissue-engineered vascular grafts, Science Translational Medicine 12(537) (2020).
[41] I. Arhuidese, T. Reifsnyder, T. Islam, O. Karim, B. Nejim, T. Obeid, U. Qazi, M. Malas, Bovine carotid artery biologic graft outperforms expanded polytetrafluoroethylene for hemodialysis access, Journal of Vascular Surgery 65(3) (2017) 775-782.
[42] P.T. Kennealey, N. Elias, M. Hertl, D.S. Ko, R.F. Saidi, J.F. Markmann, E.E. Smoot, D.A. Schoenfeld, T. Kawai, A prospective, randomized comparison of bovine carotid artery and expanded polytetrafluoroethylene for permanent hemodialysis vascular access, Journal of vascular surgery 53(6) (2011) 1640-1648.
[43] J. Merola, D.D. Jane-Wit, J.S. Pober, Recent advances in allograft vasculopathy, Current opinion in organ transplantation 22(1) (2017) 1.
[44] J.D. Roh, R. Sawh-Martinez, M.P. Brennan, S.M. Jay, L. Devine, D.A. Rao, T. Yi, T.L. Mirensky, A. Nalbandian, B. Udelsman, Tissue-engineered vascular grafts transform into mature blood vessels via an inflammation-mediated process of vascular remodeling, Proceedings of the National Academy of Sciences 107(10) (2010) 4669-4674.
[45] N. Hibino, D. Mejias, N. Pietris, E. Dean, T. Yi, C. Best, T. Shinoka, C. Breuer, The innate immune system contributes to tissue-engineered vascular graft performance, The FASEB Journal 29(6) (2015) 2431-2438.

[46] Z. Julier, A.J. Park, P.S. Briquez, M.M. Martino, Promoting tissue regeneration by modulating the immune system, Acta biomaterialia 53 (2017) 13-28.
[47] A. Sandoo, J.J.V. van Zanten, G.S. Metsios, D. Carroll, G.D. Kitas, The endothelium and its role in regulating vascular tone, The open cardiovascular medicine journal 4 (2010) 302.
[48] D. Radke, W. Jia, D. Sharma, K. Fena, G. Wang, J. Goldman, F. Zhao, Tissue engineering at the blood-contacting surface: A review of challenges and strategies in vascular graft development, Advanced healthcare materials 7(15) (2018) 1701461.
[49] A.P. McGuigan, M.V. Sefton, The influence of biomaterials on endothelial cell thrombogenicity, Biomaterials 28(16) (2007) 2547-2571.
[50] S. Aslani, M. Kabiri, S. HosseinZadeh, H. Hanaee-Ahvaz, E.S. Taherzadeh, M. Soleimani, The applications of heparin in vascular tissue engineering, Microvascular Research (2020) 104027.
[51] M. Badv, F. Bayat, J.I. Weitz, T.F. Didar, Single and multi-functional coating strategies for enhancing the biocompatibility and tissue integration of blood-contacting medical implants, Biomaterials (2020) 120291.
[52] J. Zhao, Y. Feng, Surface Engineering of Cardiovascular Devices for Improved Hemocompatibility and Rapid Endothelialization, Advanced Healthcare Materials 9(18) (2020) 2000920.
[53] P. Li, Y. Wang, X. Jin, J. Dou, X. Han, X. Wan, J. Yuan, J. Shen, Fabrication of PCL/keratin composite scaffolds for vascular tissue engineering with catalytic generation of nitric oxide potential, Journal of Materials Chemistry B 8(28) (2020) 6092-6099.
[54] P. Li, Y. Wang, X. Jin, J. Dou, X. Han, X. Wan, J. Yuan, J. Shen, Catalytic Generation of Nitric Oxide from Poly (ε-caprolactone)/Phosphobetainized Keratin Mats for a Vascular Tissue Engineering Scaffold, Langmuir 36(16) (2020) 4396-4404.
[55] Z. Wang, Y. Lu, K. Qin, Y. Wu, Y. Tian, J. Wang, J. Zhang, J. Hou, Y. Cui, K. Wang, Enzyme-functionalized vascular grafts catalyze in-situ release of nitric oxide from exogenous NO prodrug, Journal of Controlled Release 210 (2015) 179-188.
[56] N. Tran, A. Le, M. Ho, N. Dang, H.H. Thi Thanh, L. Truong, D.P. Huynh, N.T. Hiep, Polyurethane/polycaprolactone membrane grafted with conjugated linoleic acid for artificial vascular graft application, Science and technology of advanced materials 21(1) (2020) 56-66.
[57] R. Devine, M.J. Goudie, P. Singha, C. Schmiedt, M. Douglass, E.J. Brisbois, H. Handa, Mimicking the Endothelium: Dual Action Heparinized Nitric Oxide Releasing Surface, ACS Applied Materials & Interfaces 12(18) (2020) 20158-20171.
[58] S. Dimitrievska, J. Wang, T. Lin, A. Weyers, H. Bai, L. Qin, G. Li, C. Cai, A. Kypson, N. Kristofik, Glycocalyx-Like Hydrogel Coatings for Small Diameter Vascular Grafts, Advanced Functional Materials (2020) 1908963.
[59] P.F. Sánchez, E.M. Brey, J.C. Briceño, Endothelialization mechanisms in vascular grafts, Journal of tissue engineering and regenerative medicine 12(11) (2018) 2164-2178.
[60] J. Cordelle, S. Mantero, Insight on the endothelialization of small silk-based tissue-engineered vascular grafts, The International Journal of Artificial Organs (2020) 0391398820906547.

[61] M. Lemson, J. Tordoir, M. Daemen, P. Kitslaar, Intimal hyperplasia in vascular grafts, European Journal of Vascular and Endovascular Surgery 19(4) (2000) 336-350.
[62] P. Zilla, D. Bezuidenhout, P. Human, Prosthetic vascular grafts: wrong models, wrong questions and no healing, Biomaterials 28(34) (2007) 5009-5027.
[63] M. Hong-De Wu, Q. Shi, A.R. Wechezak, A.W. Clowes, I.L. Gordon, L.R. Sauvage, Definitive proof of endothelialization of a Dacron arterial prosthesis in a human being, Journal of vascular surgery 21(5) (1995) 862-867.
[64] Z. Zhang, Z. Wang, S. Liu, M. Kodama, Pore size, tissue ingrowth, and endothelialization of small-diameter microporous polyurethane vascular prostheses, Biomaterials 25(1) (2004) 177-187.
[65] Y. Jeong, Y. Yao, E.K. Yim, Current understanding of intimal hyperplasia and effect of compliance in synthetic small diameter vascular grafts, Biomaterials Science 8(16) (2020) 4383-4395.
[66] J.J. Castellot, M.L. Addonizio, R. Rosenberg, M.J. Karnovsky, Cultured endothelial cells produce heparinlike inhibitor of smooth muscle cell growth, The Journal of cell biology 90(2) (1981) 372-379.
[67] G. Li, S.-J. Chen, S. Oparil, Y.-F. Chen, J.A. Thompson, Direct in vivo evidence demonstrating neointimal migration of adventitial fibroblasts after balloon injury of rat carotid arteries, Circulation 101(12) (2000) 1362-1365.
[68] A. Post, P. Diaz-Rodriguez, B. Balouch, S. Paulsen, S. Wu, J. Miller, M. Hahn, E. Cosgriff-Hernandez, Elucidating the role of graft compliance mismatch on intimal hyperplasia using an ex vivo organ culture model, Acta biomaterialia 89 (2019) 84-94.
[69] I. Baek, C.Z. Bai, J. Hwang, J. Park, J.-S. Park, D.J. Kim, Suppression of neointimal hyperplasia by sirolimus-eluting expanded polytetrafluoroethylene (ePTFE) haemodialysis grafts in comparison with paclitaxel-coated grafts, Nephrology Dialysis Transplantation 27(5) (2012) 1997-2004.
[70] Y. Yang, D. Lei, H. Zou, S. Huang, Q. Yang, S. Li, F.-L. Qing, X. Ye, Z. You, Q. Zhao, Hybrid electrospun rapamycin-loaded small-diameter decellularized vascular grafts effectively inhibit intimal hyperplasia, Acta biomaterialia 97 (2019) 321-332.
[71] S. Tara, H. Kurobe, J. de Dios Ruiz Rosado, C.A. Best, T. Shoji, N. Mahler, T. Yi, Y.-U. Lee, T. Sugiura, N. Hibino, Cilostazol, not aspirin, prevents stenosis of bioresorbable vascular grafts in a venous model, Arteriosclerosis, thrombosis, and vascular biology 35(9) (2015) 2003-2010.
[72] F. Innocente, D. Mandracchia, E. Pektok, B. Nottelet, J.-C. Tille, S. de Valence, G. Faggian, A. Mazzucco, A. Kalangos, R. Gurny, Paclitaxel-eluting biodegradable synthetic vascular prostheses: a step towards reduction of neointima formation?, Circulation 120(11_suppl_1) (2009) S37-S45.
[73] H. Miyachi, S. Tara, S. Otsuru, T. Yi, Y.-U. Lee, J.D. Drews, H. Nakayama, S. Miyamoto, T. Sugiura, T. Shoji, Imatinib attenuates neotissue formation during vascular remodeling in an arterial bioresorbable vascular graft, JVS: Vascular Science (2020).

[74] N. Ding, C. Dou, Y. Wang, F. Liu, G. Guan, D. Huo, Y. Li, J. Yang, K. Wei, M. Yang, Antishear Stress Bionic Carbon Nanotube Mesh Coating with Intracellular Controlled Drug Delivery Constructing Small-Diameter Tissue–Engineered Vascular Grafts, Advanced Healthcare Materials 7(11) (2018) 1800026.
[75] C. Terraza, C. Suazo, G. Zavala, M. Ocaña, C.A. Wilkens, M. Khoury, J.P. Acevedo, T.L. Akentjew, J.J. Blaker, L.M. Valenzuela, Rapid fabrication of reinforced and cell-laden vascular grafts structurally inspired by human coronary arteries, Nature Communications 10(1) (2019).
[76] D.-H. Kim, P.P. Provenzano, C.L. Smith, A. Levchenko, Matrix nanotopography as a regulator of cell function, Journal of Cell Biology 197(3) (2012) 351-360.
[77] K.H. Nakayama, V.N. Surya, M. Gole, T.W. Walker, W. Yang, E.S. Lai, M.A. Ostrowski, G.G. Fuller, A.R. Dunn, N.F. Huang, Nanoscale patterning of extracellular matrix alters endothelial function under shear stress, Nano letters 16(1) (2016) 410-419.
[78] M. Avci-Adali, G. Ziemer, H.P. Wendel, Induction of EPC homing on biofunctionalized vascular grafts for rapid in vivo self-endothelialization—a review of current strategies, Biotechnology Advances 28(1) (2010) 119-129.
[79] Y. Cao, Y.F. Poon, J. Feng, S. Rayatpisheh, V. Chan, M.B. Chan-Park, Regulating orientation and phenotype of primary vascular smooth muscle cells by biodegradable films patterned with arrays of microchannels and discontinuous microwalls, Biomaterials 31(24) (2010) 6228-6238.
[80] Y. Wang, H. Shi, J. Qiao, Y. Tian, M. Wu, W. Zhang, Y. Lin, Z. Niu, Y. Huang, Electrospun tubular scaffold with circumferentially aligned nanofibers for regulating smooth muscle cell growth, ACS applied materials & interfaces 6(4) (2014) 2958-2962.
[81] Q. Xing, Z. Qian, M. Tahtinen, A.H. Yap, K. Yates, F. Zhao, Aligned nanofibrous cell-derived extracellular matrix for anisotropic vascular graft construction, Advanced healthcare materials 6(10) (2017) 1601333.
[82] Z. Wang, C. Liu, D. Zhu, X. Gu, Y. Xu, Q. Qin, N. Dong, S. Zhang, J. Wang, Untangling the co-effects of oriented nanotopography and sustained anticoagulation in a biomimetic intima on neovessel remodeling, Biomaterials 231 (2020) 119654.
[83] L. Pocivavsek, S.-H. Ye, J. Pugar, E. Tzeng, E. Cerda, S. Velankar, W.R. Wagner, Active wrinkles to drive self-cleaning: A strategy for anti-thrombotic surfaces for vascular grafts, Biomaterials 192 (2019) 226-234.
[84] N.N. Nath, L. Pocivavsek, J.A. Pugar, Y. Gao, K. Salem, N. Pitre, R. McEnaney, S. Velankar, E. Tzeng, Dynamic Luminal Topography: A Potential Strategy to Prevent Vascular Graft Thrombosis, Frontiers in Bioengineering and Biotechnology 8 (2020) 1044.
[85] J. Oswald, S. Boxberger, B. Jørgensen, S. Feldmann, G. Ehninger, M. Bornhäuser, C. Werner, Mesenchymal stem cells can be differentiated into endothelial cells in vitro, Stem cells 22(3) (2004) 377-384.
[86] G. Matsumura, S. Miyagawa-Tomita, T. Shin'oka, Y. Ikada, H. Kurosawa, First evidence that bone marrow cells contribute to the construction of tissue-engineered vascular autografts in vivo, Circulation 108(14) (2003) 1729-1734.

[87] N. Hibino, T. Shin'oka, G. Matsumura, Y. Ikada, H. Kurosawa, The tissue-engineered vascular graft using bone marrow without culture, The Journal of Thoracic and Cardiovascular Surgery 129(5) (2005) 1064-1070.
[88] J.T. Krawiec, D.A. Vorp, Adult stem cell-based tissue engineered blood vessels: a review, Biomaterials 33(12) (2012) 3388-3400.
[89] D. Hielscher, C. Kaebisch, B.J.V. Braun, K. Gray, E. Tobiasch, Stem cell sources and graft material for vascular tissue engineering, Stem Cell Reviews and Reports 14(5) (2018) 642-667.
[90] R.D. Kirkton, M. Santiago-Maysonet, J.H. Lawson, W.E. Tente, S.L. Dahl, L.E. Niklason, H.L. Prichard, Bioengineered human acellular vessels recellularize and evolve into living blood vessels after human implantation, Science translational medicine 11(485) (2019).
[91] L.P. Neff, B.W. Tillman, S.K. Yazdani, M.A. Machingal, J.J. Yoo, S. Soker, B.W. Bernish, R.L. Geary, G.J. Christ, Vascular smooth muscle enhances functionality of tissue-engineered blood vessels in vivo, Journal of vascular surgery 53(2) (2011) 426-434.
[92] Z.H. Syedain, M.L. Graham, T.B. Dunn, T. O'Brien, S.L. Johnson, R.J. Schumacher, R.T. Tranquillo, A completely biological "off-the-shelf" arteriovenous graft that recellularizes in baboons, Science translational medicine 9(414) (2017).
[93] L. Magnan, G. Labrunie, M. Fénelon, N. Dusserre, M.-P. Foulc, M. Lafourcade, I. Svahn, E. Gontier, T.N. McAllister, N. L'Heureux, Human textiles: A cell-synthesized yarn as a truly "bio" material for tissue engineering applications, Acta Biomaterialia 105 (2020) 111-120.
[94] W. He, A. Nieponice, L. Soletti, Y. Hong, B. Gharaibeh, M. Crisan, A. Usas, B. Peault, J. Huard, W.R. Wagner, Pericyte-based human tissue engineered vascular grafts, Biomaterials 31(32) (2010) 8235-8244.
[95] T. Colunga, S. Dalton, Building blood vessels with vascular progenitor cells, Trends in molecular medicine 24(7) (2018) 630-641.
[96] P. Campagnolo, A.J. Gormley, L.W. Chow, A.G. Guex, P.A. Parmar, J.L. Puetzer, J.A. Steele, A. Breant, P. Madeddu, M.M. Stevens, Pericyte seeded dual peptide scaffold with improved endothelialization for vascular graft tissue engineering, Advanced healthcare materials 5(23) (2016) 3046-3055.
[97] A.J. Melchiorri, L.G. Bracaglia, L.K. Kimerer, N. Hibino, J.P. Fisher, In vitro endothelialization of biodegradable vascular grafts via endothelial progenitor cell seeding and maturation in a tubular perfusion system bioreactor, Tissue Engineering Part C: Methods 22(7) (2016) 663-670.
[98] E.M. Cunnane, J.S. Weinbaum, F.J. O'Brien, D.A. Vorp, Future perspectives on the role of stem cells and extracellular vesicles in vascular tissue regeneration, Frontiers in Cardiovascular Medicine 5 (2018) 86.
[99] J. Luo, L. Qin, L. Zhao, L. Gui, M.W. Ellis, Y. Huang, M.H. Kural, J.A. Clark, S. Ono, J. Wang, Tissue-Engineered Vascular Grafts with Advanced Mechanical Strength from Human iPSCs, Cell Stem Cell 26(2) (2020) 251-261. e8.

[100] M. Generali, E.A. Casanova, D. Kehl, D. Wanner, S.P. Hoerstrup, P. Cinelli, B. Weber, Autologous endothelialized small-caliber vascular grafts engineered from blood-derived induced pluripotent stem cells, Acta Biomaterialia 97 (2019) 333-343.
[101] Z. Li, X. Li, T. Xu, L. Zhang, Acellular small-diameter tissue-engineered vascular grafts, Applied Sciences 9(14) (2019) 2864.
[102] C.E. Stowell, X. Li, M.H. Matsunaga, C.B. Cockreham, K.M. Kelly, J. Cheetham, E. Tzeng, Y. Wang, Resorbable vascular grafts show rapid cellularization and degradation in the ovine carotid, Journal of Tissue Engineering and Regenerative Medicine 14(11) (2020) 1673-1684.
[103] T. Fukunishi, C.S. Ong, C. Lui, I. Pitaktong, C. Smoot, J. Harris, P. Gabriele, L. Vricella, L. Santhanam, S. Lu, Formation of Neoarteries with Optimal Remodeling Using Rapidly Degrading Textile Vascular Grafts, Tissue Engineering Part A 25(7-8) (2019) 632-641.
[104] C.K. Hashi, Y. Zhu, G.-Y. Yang, W.L. Young, B.S. Hsiao, K. Wang, B. Chu, S. Li, Antithrombogenic property of bone marrow mesenchymal stem cells in nanofibrous vascular grafts, Proceedings of the National Academy of Sciences 104(29) (2007) 11915-11920.
[105] C.-H. Lin, K. Hsia, H. Ma, H. Lee, J.-H. Lu, In vivo performance of decellularized vascular grafts: a review article, International journal of molecular sciences 19(7) (2018) 2101.
[106] N. Hibino, P. McConnell, T. Shinoka, M. Malik, M. Galantowicz, Preliminary experience in the use of an extracellular matrix (CorMatrix) as a tube graft: word of caution, Seminars in thoracic and cardiovascular surgery, Elsevier, 2015, pp. 288-295.
[107] L.E. Niklason, W. Abbott, J. Gao, B. Klagges, K.K. Hirschi, K. Ulubayram, N. Conroy, R. Jones, A. Vasanawala, S. Sanzgiri, Morphologic and mechanical characteristics of engineered bovine arteries, Journal of vascular surgery 33(3) (2001) 628-638.
[108] R.D. Kirkton, M. Santiago-Maysonet, J.H. Lawson, W.E. Tente, S.L. Dahl, L.E. Niklason, H.L. Prichard, Bioengineered human acellular vessels recellularize and evolve into living blood vessels after human implantation, Science translational medicine 11(485) (2019) eaau6934.
[109] P. Gutowski, S.M. Gage, M. Guziewicz, M. Ilzecki, A. Kazimierczak, R. Kirkton, L.E. Niklason, A. Pilgrim, H.L. Prichard, S. Przywara, Arterial reconstruction with human bioengineered acellular blood vessels in patients with peripheral arterial disease, Journal of Vascular Surgery (2020).
[110] J.J. Morrison, J. McMahon, J.J. DuBose, T.M. Scalea, J.H. Lawson, T.E. Rasmussen, Clinical implementation of the Humacyte human acellular vessel: Implications for military and civilian trauma care, Journal of Trauma and Acute Care Surgery 87(1S) (2019) S44-S47.
[111] N. L'Heureux, N. Dusserre, G. Konig, B. Victor, P. Keire, T.N. Wight, N.A. Chronos, A.E. Kyles, C.R. Gregory, G. Hoyt, Human tissue-engineered blood vessels for adult arterial revascularization, Nature medicine 12(3) (2006) 361-365.
[112] W. Wystrychowski, T.N. McAllister, K. Zagalski, N. Dusserre, L. Cierpka, N. L'Heureux, First human use of an allogeneic tissue-engineered vascular graft for hemodialysis access, Journal of vascular surgery 60(5) (2014) 1353-1357.

[113] Z. Syedain, J. Reimer, M. Lahti, J. Berry, S. Johnson, R. Bianco, R.T. Tranquillo, Tissue engineering of acellular vascular grafts capable of somatic growth in young lambs, Nature communications 7(1) (2016) 1-10.
[114] C. Vepari, D.L. Kaplan, Silk as a biomaterial, Progress in polymer science 32(8-9) (2007) 991-1007.
[115] R. Konwarh, B.K. Bhunia, B.B. Mandal, Opportunities and challenges in exploring Indian nonmulberry silk for biomedical applications, Proceedings of the Indian National Science Academy 83(1) (2017).
[116] A. Bandyopadhyay, S.K. Chowdhury, S. Dey, J.C. Moses, B.B. Mandal, Silk: a promising biomaterial opening new vistas towards affordable healthcare solutions, Journal of the Indian Institute of Science (2019) 1-43.
[117] S. Kundu, B. Kundu, S. Talukdar, S. Bano, S. Nayak, J. Kundu, B.B. Mandal, N. Bhardwaj, M. Botlagunta, B.C. Dash, Nonmulberry silk biopolymers, Biopolymers 97(6) (2012) 455-467.
[118] B.B. Mandal, S. Kundu, A novel method for dissolution and stabilization of non-mulberry silk gland protein fibroin using anionic surfactant sodium dodecyl sulfate, Biotechnology and bioengineering 99(6) (2008) 1482-1489.
[119] H.-J. Jin, D.L. Kaplan, Mechanism of silk processing in insects and spiders, Nature 424(6952) (2003) 1057-1061.
[120] Y. Qi, H. Wang, K. Wei, Y. Yang, R.-Y. Zheng, I.S. Kim, K.-Q. Zhang, A review of structure construction of silk fibroin biomaterials from single structures to multi-level structures, International journal of molecular sciences 18(3) (2017) 237.
[121] S.K. Chae, E. Kang, A. Khademhosseini, S.H. Lee, Micro/Nanometer-Scale Fiber with Highly Ordered Structures by Mimicking the Spinning Process of Silkworm, Advanced materials 25(22) (2013) 3071-3078.
[122] S. Inoue, K. Tanaka, H. Tanaka, K. Ohtomo, T. Kanda, M. Imamura, G.X. Quan, K. Kojima, T. Yamashita, T. Nakajima, Assembly of the silk fibroin elementary unit in endoplasmic reticulum and a role of L-chain for protection of α1, 2-mannose residues in N-linked oligosaccharide chains of fibrohexamerin/P25, European journal of biochemistry 271(2) (2004) 356-366.
[123] K. Yukuhiro, H. Sezutsu, N. Yonemura, Evolutionary divergence of lepidopteran and trichopteran fibroins, Biotechnology of silk, Springer2014, pp. 25-47.
[124] C.Z. Zhou, F. Confalonieri, M. Jacquet, R. Perasso, Z.G. Li, J. Janin, Silk fibroin: structural implications of a remarkable amino acid sequence, Proteins: Structure, Function, and Bioinformatics 44(2) (2001) 119-122.
[125] C. Holland, K. Numata, J. Rnjak-Kovacina, F.P. Seib, The biomedical use of silk: past, present, future, Advanced healthcare materials 8(1) (2019) 1800465.
[126] A. Gupta, K. Mita, K.P. Arunkumar, J. Nagaraju, Molecular architecture of silk fibroin of Indian golden silkmoth, Antheraea assama, Scientific reports 5 (2015) 12706.
[127] H. Sezutsu, K. Yukuhiro, Dynamic rearrangement within the Antheraea pernyi silk fibroin gene is associated with four types of repetitive units, Journal of Molecular Evolution 51(4) (2000) 329-338.

[128] A. Datta, A.K. Ghosh, S.C. Kundu, Differential expression of the fibroin gene in developmental stages of silkworm, Antheraea mylitta (Saturniidae), Comparative Biochemistry and Physiology Part B: Biochemistry and Molecular Biology 129(1) (2001) 197-204.
[129] H. SEZUTSU, K. UCHINO, I. KOBAYASHI, T. TAMURA, K. YUKUHIRO, Extensive sequence rearrangements and length polymorphism in fibroin genes in the wild silkmoth, Antheraea yamamai (Lepidoptera, Saturniidae), International journal of wild silkmoth & silk 15 (2010) 35-50.
[130] H. Sezutsu, K. Yukuhiro, The complete nucleotide sequence of the Eri-silkworm (Samia cynthia ricini) fibroin gene, Journal of Insect Biotechnology and Sericology 83(3) (2014) 3_059-3_070.
[131] J. Fu, M. Wang, I. De Vlaminck, Y. Wang, Thick PCL Fibers Improving Host Remodeling of PGS-PCL Composite Grafts Implanted in Rat Common Carotid Arteries, Small (2020) 2004133.
[132] J.C. Zbinden, K.M. Blum, A.G. Berman, A.B. Ramachandra, J.M. Szafron, K.E. Kerr, J.L. Anderson, G.S. Sangha, C.C. Earl, N.R. Nigh, Effects of Braiding Parameters on Tissue Engineered Vascular Graft Development, Advanced Healthcare Materials (2020) 2001093.
[133] R. Khosravi, A.B. Ramachandra, J.M. Szafron, D.E. Schiavazzi, C.K. Breuer, J.D. Humphrey, A computational bio-chemo-mechanical model of in vivo tissue-engineered vascular graft development, Integrative Biology 12(3) (2020) 47-63.
[134] J.M. Szafron, A.B. Ramachandra, C.K. Breuer, A.L. Marsden, J.D. Humphrey, Optimization of tissue-engineered vascular graft design using computational modeling, Tissue Engineering Part C: Methods 25(10) (2019) 561-570.
[135] Y. Matsuzaki, R. Iwaki, J.W. Reinhardt, Y.-C. Chang, S. Miyamoto, J. Kelly, J. Zbinden, K. Blum, G. Mirhaidari, A. Ulziibayar, The effect of pore diameter on neo-tissue formation in electrospun biodegradable tissue-engineered arterial grafts in a large animal model, Acta Biomaterialia 115 (2020) 176-184.
[136] E. Saino, M.L. Focarete, C. Gualandi, E. Emanuele, A.I. Cornaglia, M. Imbriani, L. Visai, Effect of electrospun fiber diameter and alignment on macrophage activation and secretion of proinflammatory cytokines and chemokines, Biomacromolecules 12(5) (2011) 1900-1911.
[137] A.D. Malay, R. Sato, K. Yazawa, H. Watanabe, N. Ifuku, H. Masunaga, T. Hikima, J. Guan, B.B. Mandal, S. Damrongsakkul, Relationships between physical properties and sequence in silkworm silks, Scientific reports 6 (2016) 27573.
[138] Z. Peng, X. Yang, C. Liu, Z. Dong, F. Wang, X. Wang, W. Hu, X. Zhang, P. Zhao, Q. Xia, Structural and mechanical properties of silk from different instars of Bombyx mori, Biomacromolecules 20(3) (2019) 1203-1216.
[139] G. Fang, S. Sapru, S. Behera, J. Yao, Z. Shao, S.C. Kundu, X. Chen, Exploration of the tight structural–mechanical relationship in mulberry and non-mulberry silkworm silks, Journal of Materials Chemistry B 4(24) (2016) 4337-4347.

[140] K. Tanaka, D. Fukuda, Y. Higashikuni, Y. Hirata, I. Komuro, T. Saotome, Y. Yamashita, T. Asakura, M. Sata, Biodegradable Extremely-Small-Diameter Vascular Graft Made of Silk Fibroin can be Implanted in Mice, Journal of Atherosclerosis and Thrombosis (2020) 52720.
[141] T. Tanaka, R. Tanaka, Y. Ogawa, Y. Takagi, T. Asakura, Development of Small-diameter Polyester Vascular Grafts Coated with Silk Fibroin Sponge, Organogenesis 16(1) (2020) 1-13.
[142] D. Chouhan, B. Chakraborty, S.K. Nandi, B.B. Mandal, Role of non-mulberry silk fibroin in deposition and regulation of extracellular matrix towards accelerated wound healing, Acta Biomaterialia 48 (2017) 157-174.
[143] X. Hu, K. Shmelev, L. Sun, E.-S. Gil, S.-H. Park, P. Cebe, D.L. Kaplan, Regulation of Silk Material Structure by Temperature-Controlled Water Vapor Annealing, Biomacromolecules 12(5) (2011) 1686-1696.
[144] K. Yazawa, K. Ishida, H. Masunaga, T. Hikima, K. Numata, Influence of Water Content on the β-Sheet Formation, Thermal Stability, Water Removal, and Mechanical Properties of Silk Materials, Biomacromolecules 17(3) (2016) 1057-1066.
[145] S. Kaewpirom, S. Boonsang, Influence of alcohol treatments on properties of silk-fibroin-based films for highly optically transparent coating applications, RSC Advances 10(27) (2020) 15913-15923.
[146] Y. Cao, B. Wang, Biodegradation of silk biomaterials, International journal of molecular sciences 10(4) (2009) 1514-1524.
[147] D. Umuhoza, F. Yang, D. Long, Z. Hao, J. Dai, A. Zhao, Strategies for Tuning the Biodegradation of Silk Fibroin-Based Materials for Tissue Engineering Applications, ACS Biomaterials Science & Engineering 6(3) (2020) 1290-1310.
[148] G. Guan, L. Wang, M. Li, L. Bai, In vivo biodegradation of porous silk fibroin films implanted beneath the skin and muscle of the rat, Bio-medical materials and engineering 24(1) (2014) 789-797.
[149] Z. Sheikh, P.J. Brooks, O. Barzilay, N. Fine, M. Glogauer, Macrophages, foreign body giant cells and their response to implantable biomaterials, Materials 8(9) (2015) 5671-5701.
[150] D.P. Vasconcelos, A.P. Águas, M.A. Barbosa, P. Pelegrín, J.N. Barbosa, The inflammasome in host response to biomaterials: bridging inflammation and tissue regeneration, Acta biomaterialia 83 (2019) 1-12.
[151] J. Brown, C.-L. Lu, J. Coburn, D.L. Kaplan, Impact of silk biomaterial structure on proteolysis, Acta biomaterialia 11 (2015) 212-221.
[152] G. Huang, D. Yang, C. Sun, J. Huang, K. Chen, C. Zhang, H. Chen, Q. Yao, A quicker degradation rate is yielded by a novel kind of transgenic silk fibroin consisting of shortened silk fibroin heavy chains fused with matrix metalloproteinase cleavage sites, Journal of Materials Science: Materials in Medicine 25(8) (2014) 1833-1842.
[153] X. Zhang, C.B. Baughman, D.L. Kaplan, In vitro evaluation of electrospun silk fibroin scaffolds for vascular cell growth, Biomaterials 29(14) (2008) 2217-2227.
[154] A. Alessandrino, A. Chiarini, M. Biagiotti, I. Dal Prà, G.A. Bassani, V. Vincoli, P. Settembrini, P. Pierimarchi, G. Freddi, U. Armato, Three-layered silk fibroin tubular scaffold for

the repair and regeneration of small caliber blood vessels: from design to in vivo pilot tests, Frontiers in bioengineering and biotechnology 7 (2019) 356.
[155] W. Zheng, Z. Wang, L. Song, Q. Zhao, J. Zhang, D. Li, S. Wang, J. Han, X.-L. Zheng, Z. Yang, Endothelialization and patency of RGD-functionalized vascular grafts in a rabbit carotid artery model, Biomaterials 33(10) (2012) 2880-2891.
[156] Q. Lu, S. Zhang, K. Hu, Q. Feng, C. Cao, F. Cui, Cytocompatibility and blood compatibility of multifunctional fibroin/collagen/heparin scaffolds, Biomaterials 28(14) (2007) 2306-2313.
[157] Y. Tamada, Sulfation of silk fibroin by chlorosulfonic acid and the anticoagulant activity, Biomaterials 25(3) (2004) 377-383.
[158] M. Lovett, G. Eng, J. Kluge, C. Cannizzaro, G. Vunjak-Novakovic, D.L. Kaplan, Tubular silk scaffolds for small diameter vascular grafts, Organogenesis 6(4) (2010) 217-224.
[159] A. Motta, C. Migliaresi, A.W. Lloyd, S.P. Denyer, M. Santin, Serum protein absorption on silk fibroin fibers and films: Surface opsonization and binding strength, Journal of bioactive and compatible polymers 17(1) (2002) 23-35.
[160] A. Motta, D. Maniglio, C. Migliaresi, H.-J. Kim, X. Wan, X. Hu, D.L. Kaplan, Silk fibroin processing and thrombogenic responses, Journal of Biomaterials Science, Polymer Edition 20(13) (2009) 1875-1897.
[161] M.F. Elahi, G. Guan, L. Wang, Hemocompatibility of surface modified silk fibroin materials: a review, Rev Adv Mater Sci 38(2) (2014) 148-59.
[162] B. Kundu, C.J. Schlimp, S. Nürnberger, H. Redl, S. Kundu, Thromboelastometric and platelet responses to silk biomaterials, Scientific reports 4(1) (2014) 1-9.
[163] X. Ji, M. Hou, Novel agents for anti-platelet therapy, Journal of hematology & oncology 4(1) (2011) 1-7.
[164] S. Wang, Y. Zhang, H. Wang, Z. Dong, Preparation, characterization and biocompatibility of electrospinning heparin-modified silk fibroin nanofibers, International journal of biological macromolecules 48(2) (2011) 345-353.
[165] F.P. Seib, M. Herklotz, K.A. Burke, M.F. Maitz, C. Werner, D.L. Kaplan, Multifunctional silk–heparin biomaterials for vascular tissue engineering applications, Biomaterials 35(1) (2014) 83-91.
[166] M. Zhu, K. Wang, J. Mei, C. Li, J. Zhang, W. Zheng, D. An, N. Xiao, Q. Zhao, D. Kong, Fabrication of highly interconnected porous silk fibroin scaffolds for potential use as vascular grafts, Acta biomaterialia 10(5) (2014).
[167] C. Saitow, D.L. Kaplan, J.J. Castellot Jr, Heparin stimulates elastogenesis: application to silk-based vascular grafts, Matrix Biology 30(5-6) (2011) 346-355.
[168] X. Ma, C. Cao, H. Zhu, The biocompatibility of silk fibroin films containing sulfonated silk fibroin, Journal of Biomedical Materials Research Part B: Applied Biomaterials: An Official Journal of The Society for Biomaterials, The Japanese Society for Biomaterials, and The Australian Society for Biomaterials and the Korean Society for Biomaterials 78(1) (2006) 89-96.

[169] K. Lau, A. Waterhouse, B. Akhavan, L. Gao, H.N. Kim, F. Tang, J.M. Whitelock, M.M. Bilek, M.S. Lord, J. Rnjak-Kovacina, Biomimetic silk biomaterials: Perlecan-functionalized silk fibroin for use in blood-contacting devices, Acta Biomaterialia (2021).
[170] J.M. Anderson, A. Rodriguez, D.T. Chang, Foreign body reaction to biomaterials, Seminars in immunology, Elsevier, 2008, pp. 86-100.
[171] P. Aramwit, S. Kanokpanont, W. De-Eknamkul, T. Srichana, Monitoring of inflammatory mediators induced by silk sericin, Journal of bioscience and bioengineering 107(5) (2009) 556-561.
[172] M. Dewair, X. Baur, K. Ziegler, Use of immunoblot technique for detection of human IgE and IgG antibodies to individual silk proteins, Journal of allergy and clinical immunology 76(4) (1985) 537-542.
[173] S. Kurosaki, H. Otsuka, M. Kunitomo, M. Koyama, R. Pawankar, K. Matumoto, Fibroin allergy IgE mediated hypersensitivity to silk suture materials, Journal of Nippon Medical School 66(1) (1999) 41-44.
[174] M. Bhattacharjee, E. Schultz-Thater, E. Trella, S. Miot, S. Das, M. Loparic, A.R. Ray, I. Martin, G.C. Spagnoli, S. Ghosh, The role of 3D structure and protein conformation on the innate and adaptive immune responses to silk-based biomaterials, Biomaterials 34(33) (2013) 8161-8171.
[175] B. Panilaitis, G.H. Altman, J. Chen, H.-J. Jin, V. Karageorgiou, D.L. Kaplan, Macrophage responses to silk, Biomaterials 24(18) (2003) 3079-3085.
[176] L. Meinel, S. Hofmann, V. Karageorgiou, C. Kirker-Head, J. McCool, G. Gronowicz, L. Zichner, R. Langer, G. Vunjak-Novakovic, D.L. Kaplan, The inflammatory responses to silk films in vitro and in vivo, Biomaterials 26(2) (2005) 147-155.
[177] J. Rnjak-Kovacina, L.S. Wray, J.M. Golinski, D.L. Kaplan, Arrayed hollow channels in silk-based scaffolds provide functional outcomes for engineering critically sized tissue constructs, Advanced functional materials 24(15) (2014) 2188-2196.
[178] B.B. Mandal, A. Grinberg, E.S. Gil, B. Panilaitis, D.L. Kaplan, High-strength silk protein scaffolds for bone repair, Proc Natl Acad Sci U S A 109(20) (2012) 7699-7704.
[179] C.E. Witherel, K. Sao, B.K. Brisson, B. Han, S.W. Volk, R.J. Petrie, L. Han, K.L. Spiller, Regulation of extracellular matrix assembly and structure by hybrid M1/M2 macrophages, Biomaterials (2021) 120667.
[180] C.E. Witherel, D. Abebayehu, T.H. Barker, K.L. Spiller, Macrophage and Fibroblast Interactions in Biomaterial-Mediated Fibrosis, Advanced Healthcare Materials 8(4) (2019) 1801451.
[181] K.L. Spiller, R.R. Anfang, K.J. Spiller, J. Ng, K.R. Nakazawa, J.W. Daulton, G. Vunjak-Novakovic, The role of macrophage phenotype in vascularization of tissue engineering scaffolds, Biomaterials 35(15) (2014) 4477-4488.
[182] A.E. Thurber, F.G. Omenetto, D.L. Kaplan, In vivo bioresponses to silk proteins, Biomaterials 71 (2015) 145-157.

[183] S. Ghanaati, R.E. Unger, M.J. Webber, M. Barbeck, C. Orth, J.A. Kirkpatrick, P. Booms, A. Motta, C. Migliaresi, R.A. Sader, Scaffold vascularization in vivo driven by primary human osteoblasts in concert with host inflammatory cells, Biomaterials 32(32) (2011) 8150-8160.
[184] N. Kuboyama, H. Kiba, K. Arai, R. Uchida, Y. Tanimoto, U.K. Bhawal, Y. Abiko, S. Miyamoto, D. Knight, T. Asakura, Silk fibroin-based scaffolds for bone regeneration, Journal of Biomedical Materials Research Part B: Applied Biomaterials 101(2) (2013) 295-302.
[185] M. Jewell, W. Daunch, B. Bengtson, E. Mortarino, The development of SERI® Surgical Scaffold, an engineered biological scaffold, Annals of the New York Academy of Sciences 1358(1) (2015) 44-55.
[186] D. Almesberger, N. Zingaretti, C. Di Loreto, S. Massarut, A. Pasqualucci, P.C. Parodi, Seri™: A surgical scaffold for breast reconstruction or for bacterial growth?, Journal of Plastic, Reconstructive & Aesthetic Surgery 68(6) (2015) 870-871.
[187] A.A. van Turnhout, C.J. Franke, E.J. Vriens-Nieuwenhuis, W.B. van der Sluis, The use of SERI™ Surgical Scaffolds in direct-to-implant reconstruction after skin-sparing mastectomy: A retrospective study on surgical outcomes and a systematic review of current literature, Journal of Plastic, Reconstructive & Aesthetic Surgery 71(5) (2018) 644-650.
[188] M. Rodriguez, J.A. Kluge, D. Smoot, M.A. Kluge, D.F. Schmidt, C.R. Paetsch, P.S. Kim, D.L. Kaplan, Fabricating mechanically improved silk-based vascular grafts by solution control of the gel-spinning process, Biomaterials 230 (2020) 119567.
[189] S. Enomoto, M. Sumi, K. Kajimoto, Y. Nakazawa, R. Takahashi, C. Takabayashi, T. Asakura, M. Sata, Long-term patency of small-diameter vascular graft made from fibroin, a silk-based biodegradable material, Journal of vascular surgery 51(1) (2010) 155-164.
[190] Y. Nakazawa, M. Sato, R. Takahashi, D. Aytemiz, C. Takabayashi, T. Tamura, S. Enomoto, M. Sata, T. Asakura, Development of small-diameter vascular grafts based on silk fibroin fibers from Bombyx mori for vascular regeneration, Journal of Biomaterials Science, Polymer Edition 22(1-3) (2011) 195-206.
[191] T. Fukayama, Y. Ozai, H. Shimokawatoko, Y. Kimura, D. Aytemiz, R. Tanaka, N. Machida, T. Asakura, Evaluation of endothelialization in the center part of graft using 3 cm vascular grafts implanted in the abdominal aortae of the rat, Journal of Artificial Organs 20(3) (2017) 221-229.
[192] T. Yagi, M. Sato, Y. Nakazawa, K. Tanaka, M. Sata, K. Itoh, Y. Takagi, T. Asakura, Preparation of double-raschel knitted silk vascular grafts and evaluation of short-term function in a rat abdominal aorta, Journal of Artificial Organs 14(2) (2011) 89-99.
[193] D. Aytemiz, W. Sakiyama, Y. Suzuki, N. Nakaizumi, R. Tanaka, Y. Ogawa, Y. Takagi, Y. Nakazawa, T. Asakura, Small-Diameter Silk Vascular Grafts (3 mm Diameter) with a Double-Raschel Knitted Silk Tube Coated with Silk Fibroin Sponge, Advanced healthcare materials 2(2) (2013) 361-368.
[194] T. Fukayama, Y. Ozai, H. Shimokawadoko, D. Aytemiz, R. Tanaka, N. Machida, T. Asakura, Effect of fibroin sponge coating on in vivo performance of knitted silk small diameter vascular grafts, Organogenesis 11(3) (2015) 137-151.

[195] S. Yamamoto, H. Okamoto, M. Haga, K. Shigematsu, T. Miyata, T. Watanabe, Y. Ogawa, Y. Takagi, T. Asakura, Rapid endothelialization and thin luminal layers in vascular grafts using silk fibroin, Journal of Materials Chemistry B 4(5) (2016) 938-946.
[196] T. Tanaka, Y. Abe, C.-J. Cheng, R. Tanaka, A. Naito, T. Asakura, Development of Small-Diameter Elastin-Silk Fibroin Vascular Grafts, Frontiers in Bioengineering and Biotechnology 8 (2021) 1531.
[197] M. Haga, S. Yamamoto, H. Okamoto, K. Hoshina, T. Asakura, T. Watanabe, Histological reactions and the in vivo patency rates of small silk vascular grafts in a canine model, Annals of vascular diseases 10(2) (2017) 132-138.
[198] H. Li, Y. Wang, X. Sun, W. Tian, J. Xu, J. Wang, Steady-state behavior and endothelialization of a silk-based small-caliber scaffold in vivo transplantation, Polymers 11(8) (2019) 1303.
[199] H. Li, G. Song, W. Tian, M. Ding, X. Sun, J. Xu, F. Dong, A. Wang, P. Ning, Y. Yin, Motility and function of smooth muscle cells in a silk small-caliber tubular scaffold after replacement of rabbit common carotid artery, Materials Science and Engineering: C 114 (2020) 110977.
[200] S. Kiritani, J. Kaneko, D. Ito, M. Morito, T. Ishizawa, N. Akamatsu, M. Tanaka, T. Iida, T. Tanaka, R. Tanaka, Silk fibroin vascular graft: A promising tissue-engineered scaffold material for abdominal venous system replacement, Scientific Reports 10(1) (2020) 1-9.
[201] I. Cattaneo, M. Figliuzzi, N. Azzollini, V. Catto, S. Farè, M.C. Tanzi, A. Alessandrino, G. Freddi, A. Remuzzi, In vivo regeneration of elastic lamina on fibroin biodegradable vascular scaffold, The International journal of artificial organs 36(3) (2013) 166-174.
[202] E.C. Filipe, M. Santos, J. Hung, B.S. Lee, N. Yang, A.H. Chan, M.K. Ng, J. Rnjak-Kovacina, S.G. Wise, Rapid Endothelialization of Off-the-Shelf Small Diameter Silk Vascular Grafts, JACC: Basic to Translational Science 3(1) (2018) 38-53.
[203] A.R. Park, Y.-H. Park, H.J. Kim, M.-K. Kim, S.-G. Kim, H. Kweon, S.C. Kundu, Tri-layered silk fibroin and poly-ε-caprolactone small diameter vascular grafts tested in vitro and in vivo, Macromolecular Research 23(10) (2015) 924-936.
[204] D. Jin, J. Hu, D. Xia, A.l. Liu, H. Kuang, J. Du, X. Mo, M. Yin, Evaluation of a simple off-the-shelf bi-layered vascular scaffold based on poly (L-lactide-co-ε-caprolactone)/silk fibroin in vitro and in vivo, International journal of nanomedicine 14 (2019) 4261.
[205] A.H. Chan, E.C. Filipe, R.P. Tan, M. Santos, N. Yang, J. Hung, J. Feng, S. Nazir, A.J. Benn, M.K. Ng, Altered processing enhances the efficacy of small-diameter silk fibroin vascular grafts, Scientific reports 9(1) (2019) 1-14.
[206] H. Kuang, Y. Wang, Y. Shi, W. Yao, X. He, X. Liu, X. Mo, S. Lu, P. Zhang, Construction and performance evaluation of Hep/silk-PLCL composite nanofiber small-caliber artificial blood vessel graft, Biomaterials 259 (2020) 120288.
[207] S.A. Riboldi, M. Tozzi, M. Bagardi, G. Ravasio, G. Cigalino, L. Crippa, S. Piccolo, A. Nahal, M. Spandri, V. Catto, A Novel Hybrid Silk Fibroin/Polyurethane Arteriovenous Graft for

Hemodialysis: Proof-of-Concept Animal Study in an Ovine Model, Advanced Healthcare Materials 9(20) (2020) 2000794.
[208] J. Barthes, H. Özçelik, M. Hindié, A. Ndreu-Halili, A. Hasan, N.E. Vrana, Cell Microenvironment Engineering and Monitoring for Tissue Engineering and Regenerative Medicine: The Recent Advances, BioMed Research International 2014 (2014) 921905.
[209] D.-H. Kim, P.P. Provenzano, C.L. Smith, A. Levchenko, Matrix nanotopography as a regulator of cell function, J Cell Biol 197(3) (2012) 351-360.
[210] K. Bhadriraju, C.S. Chen, Engineering cellular microenvironments to improve cell-based drug testing, Drug discovery today 7(11) (2002) 612-620.
[211] K.M. Warren, M.M. Islam, P.R. LeDuc, R. Steward Jr, 2D and 3D mechanobiology in human and nonhuman systems, ACS applied materials & interfaces 8(34) (2016) 21869-21882.
[212] C.J. Bettinger, R. Langer, J.T. Borenstein, Engineering substrate topography at the micro- and nanoscale to control cell function, Angewandte Chemie International Edition 48(30) (2009) 5406-5415.
[213] P.W. Alford, A.P. Nesmith, J.N. Seywerd, A. Grosberg, K.K. Parker, Vascular smooth muscle contractility depends on cell shape, Integrative Biology 3(11) (2011) 1063-1070.
[214] R. Sinha, S. Le Gac, N. Verdonschot, A. Van Den Berg, B. Koopman, J. Rouwkema, Endothelial cell alignment as a result of anisotropic strain and flow induced shear stress combinations, Scientific reports 6 (2016) 29510.
[215] J.S. Choi, Y. Piao, T.S. Seo, Circumferential alignment of vascular smooth muscle cells in a circular microfluidic channel, Biomaterials 35(1) (2014) 63-70.
[216] R.G. Thakar, F. Ho, N.F. Huang, D. Liepmann, S. Li, Regulation of vascular smooth muscle cells by micropatterning, Biochemical and biophysical research communications 307(4) (2003) 883-890.
[217] W. Li, J. Chen, P. Xu, M. Zhu, Y. Wu, Z. Wang, T. Zhao, Q. Cheng, K. Wang, G. Fan, Long-term evaluation of vascular grafts with circumferentially aligned microfibers in a rat abdominal aorta replacement model, Journal of Biomedical Materials Research Part B: Applied Biomaterials (2018).
[218] M. Zhu, Z. Wang, J. Zhang, L. Wang, X. Yang, J. Chen, G. Fan, S. Ji, C. Xing, K. Wang, Circumferentially aligned fibers guided functional neoartery regeneration in vivo, Biomaterials 61 (2015) 85-94.
[219] P. Rajendran, T. Rengarajan, J. Thangavel, Y. Nishigaki, D. Sakthisekaran, G. Sethi, I. Nishigaki, The vascular endothelium and human diseases, International journal of biological sciences 9(10) (2013) 1057.
[220] Z. Wang, S.H. Teoh, M. Hong, F. Luo, E.Y. Teo, J.K.Y. Chan, E.S. Thian, Dual-microstructured porous, anisotropic film for biomimicking of endothelial basement membrane, ACS applied materials & interfaces 7(24) (2015) 13445-13456.
[221] M.-C. Tsai, L. Chen, J. Zhou, Z. Tang, T.-F. Hsu, Y. Wang, Y.-T. Shih, H.-H. Peng, N. Wang, Y. Guan, Shear stress induces synthetic-to-contractile phenotypic modulation in smooth

muscle cells via peroxisome proliferator-activated receptor α/δ activations by prostacyclin released by sheared endothelial cells, Circulation research 105(5) (2009) 471-480.
[222] K. Webb, V. Hlady, P.A. Tresco, Relationships among cell attachment, spreading, cytoskeletal organization, and migration rate for anchorage-dependent cells on model surfaces, Journal of biomedical materials research 49(3) (2000) 362.
[223] F. Kessler, D. Steffens, G.A. Lando, P. Pranke, D.E. Weibel, Wettability and cell spreading enhancement in poly (sulfone) and polyurethane surfaces by UV-assisted treatment for tissue engineering purposes, Tissue Engineering and Regenerative Medicine 11(1) (2014) 23-31.
[224] L. Bacakova, E. Filova, M. Parizek, T. Ruml, V. Svorcik, Modulation of cell adhesion, proliferation and differentiation on materials designed for body implants, Biotechnology advances 29(6) (2011) 739-767.
[225] Y. Shen, M. Gao, Y. Ma, H. Yu, F.-z. Cui, H. Gregersen, Q. Yu, G. Wang, X. Liu, Effect of surface chemistry on the integrin induced pathway in regulating vascular endothelial cells migration, Colloids and Surfaces B: Biointerfaces 126 (2015) 188-197.
[226] X.Q. Brown, K. Ookawa, J.Y. Wong, Evaluation of polydimethylsiloxane scaffolds with physiologically-relevant elastic moduli: interplay of substrate mechanics and surface chemistry effects on vascular smooth muscle cell response, Biomaterials 26(16) (2005) 3123-3129.
[227] X. Ren, Y. Feng, J. Guo, H. Wang, Q. Li, J. Yang, X. Hao, J. Lv, N. Ma, W. Li, Surface modification and endothelialization of biomaterials as potential scaffolds for vascular tissue engineering applications, Chemical Society Reviews 44(15) (2015) 5680-5742.
[228] T.-W. Chung, D.-Z. Liu, S.-Y. Wang, S.-S. Wang, Enhancement of the growth of human endothelial cells by surface roughness at nanometer scale, Biomaterials 24(25) (2003) 4655-4661.
[229] C. Xu, F. Yang, S. Wang, S. Ramakrishna, In vitro study of human vascular endothelial cell function on materials with various surface roughness, Journal of Biomedical Materials Research Part A: An Official Journal of The Society for Biomaterials, The Japanese Society for Biomaterials, and The Australian Society for Biomaterials and the Korean Society for Biomaterials 71(1) (2004) 154-161.
[230] S. Choudhary, M. Berhe, K.M. Haberstroh, T.J. Webster, Increased endothelial and vascular smooth muscle cell adhesion on nanostructured titanium and CoCrMo, International journal of nanomedicine 1(1) (2006) 41.
[231] B. Trappmann, J.E. Gautrot, J.T. Connelly, D.G. Strange, Y. Li, M.L. Oyen, M.A.C. Stuart, H. Boehm, B. Li, V. Vogel, Extracellular-matrix tethering regulates stem-cell fate, Nature materials 11(7) (2012) 642.
[232] P. Gupta, G.H.N. SN, U. Kasiviswanathan, T. Agarwal, K. Senthilguru, D. Mukhopadhyay, K. Pal, S. Giri, T.K. Maiti, I. Banerjee, Substrate stiffness does affect the fate of human keratinocytes, RSC Advances 6(5) (2016) 3539-3551.
[233] D. Chouhan, T.u. Lohe, P.K. Samudrala, B.B. Mandal, In situ forming injectable silk fibroin hydrogel promotes skin regeneration in full thickness burn wounds, Advanced healthcare materials 7(24) (2018) 1801092.

[234] P. Gupta, M. Adhikary, M. Kumar, N. Bhardwaj, B.B. Mandal, Biomimetic, osteoconductive non-mulberry silk fiber reinforced tricomposite scaffolds for bone tissue engineering, ACS applied materials & interfaces 8(45) (2016) 30797-30810.
[235] R. Konwarh, B.K. Bhunia, B.B. Mandal, Opportunities and Challenges in Exploring Indian Non-mulberry Silk for Biomedical Applications, Proc Indian Natn Sci Acad, 2017, pp. 85-101.
[236] T. Asakura, J. Yao, T. Yamane, K. Umemura, A.S. Ulrich, Heterogeneous structure of silk fibers from Bombyx M Ori Resolved by 13C Solid-State NMR spectroscopy, Journal of the American Chemical Society 124(30) (2002) 8794-8795.
[237] C.-Z. Zhou, F. Confalonieri, N. Medina, Y. Zivanovic, C. Esnault, T. Yang, M. Jacquet, J. Janin, M. Duguet, R. Perasso, Fine organization of Bombyx mori fibroin heavy chain gene, Nucleic acids research 28(12) (2000) 2413-2419.
[238] T. Lefèvre, M.-E. Rousseau, M. Pézolet, Protein secondary structure and orientation in silk as revealed by Raman spectromicroscopy, Biophysical journal 92(8) (2007) 2885-2895.
[239] G. Bratzel, M.J. Buehler, Sequence-structure correlations in silk: Poly-Ala repeat of N. clavipes MaSp1 is naturally optimized at a critical length scale, Journal of the mechanical behavior of biomedical materials 7 (2012) 30-40.
[240] E.S. Gil, B.B. Mandal, S.-H. Park, J.K. Marchant, F.G. Omenetto, D.L. Kaplan, Helicoidal multi-lamellar features of RGD-functionalized silk biomaterials for corneal tissue engineering, Biomaterials 31(34) (2010) 8953-8963.
[241] A.S. Lammel, X. Hu, S.-H. Park, D.L. Kaplan, T.R. Scheibel, Controlling silk fibroin particle features for drug delivery, Biomaterials 31(16) (2010) 4583-4591.
[242] P. Garidel, H. Schott, Fourier-transform midinfrared spectroscopy for analysis and screening of liquid protein formulations, Bioprocess international 4(6) (2006) 48-55.
[243] H. Hao, P. Ropraz, V. Verin, E. Camenzind, A. Geinoz, M.S. Pepper, G. Gabbiani, M.-L. Bochaton-Piallat, Heterogeneity of smooth muscle cell populations cultured from pig coronary artery, Arteriosclerosis, thrombosis, and vascular biology 22(7) (2002) 1093-1099.
[244] Z. Yang, Q. Tu, M.F. Maitz, S. Zhou, J. Wang, N. Huang, Direct thrombin inhibitor-bivalirudin functionalized plasma polymerized allylamine coating for improved biocompatibility of vascular devices, Biomaterials 33(32) (2012) 7959-7971.
[245] J.C. Moses, S.K. Nandi, B.B. Mandal, Multifunctional Cell Instructive Silk-Bioactive Glass Composite Reinforced Scaffolds Toward Osteoinductive, Proangiogenic, and Resorbable Bone Grafts, Advanced healthcare materials (2018) 1701418.
[246] J.G. Xu, S.Y. Zhu, B.C. Heng, W.L. Dissanayaka, C.F. Zhang, TGF-β1-induced differentiation of SHED into functional smooth muscle cells, Stem cell research & therapy 8(1) (2017) 10.
[247] Q. Lu, X. Hu, X. Wang, J.A. Kluge, S. Lu, P. Cebe, D.L. Kaplan, Water-insoluble silk films with silk I structure, Acta biomaterialia 6(4) (2010) 1380-1387.
[248] R.C. Braun-Dullaeus, M.J. Mann, D.G. Sedding, S.W. Sherwood, E. Heiko, V.J. Dzau, Cell Cycle–Dependent Regulation of Smooth Muscle Cell Activation, Arteriosclerosis, thrombosis, and vascular biology 24(5) (2004) 845-850.

[249] T. Dimitris, K. Anna-Maria, P. Costas Tentolouris Nikolaos, S. Christodoulos, The Role of Nitric Oxide on Endothelial Function, Current Vascular Pharmacology 10(1) (2012) 4-18.
[250] J. Xu, G.-P. Shi, Vascular wall extracellular matrix proteins and vascular diseases, Biochimica et Biophysica Acta (BBA)-Molecular Basis of Disease 1842(11) (2014) 2106-2119.
[251] S. Chang, S. Song, J. Lee, J. Yoon, J. Park, S. Choi, J.-K. Park, K. Choi, C. Choi, Phenotypic modulation of primary vascular smooth muscle cells by short-term culture on micropatterned substrate, PLoS One 9(2) (2014) e88089.
[252] E. Vatankhah, M.P. Prabhakaran, D. Semnani, S. Razavi, M. Zamani, S. Ramakrishna, Phenotypic modulation of smooth muscle cells by chemical and mechanical cues of electrospun tecophilic/gelatin nanofibers, ACS applied materials & interfaces 6(6) (2014) 4089-4101.
[253] J. Feng, M.B. Chan-Park, J. Shen, V. Chan, Quick layer-by-layer assembly of aligned multilayers of vascular smooth muscle cells in deep microchannels, Tissue engineering 13(5) (2007) 1003-1012.
[254] H. Jeon, J.H. Tsui, S.I. Jang, J.H. Lee, S. Park, K. Mun, Y.C. Boo, D.-H. Kim, Combined effects of substrate topography and stiffness on endothelial cytokine and chemokine secretion, ACS applied materials & interfaces 7(8) (2015) 4525-4532.
[255] Y. Ding, Z. Yang, C.W. Bi, M. Yang, S.L. Xu, X. Lu, N. Huang, P. Huang, Y. Leng, Directing vascular cell selectivity and hemocompatibility on patterned platforms featuring variable topographic geometry and size, ACS applied materials & interfaces 6(15) (2014) 12062-12070.
[256] P. Zorlutuna, Z. Rong, P. Vadgama, V. Hasirci, Influence of nanopatterns on endothelial cell adhesion: Enhanced cell retention under shear stress, Acta Biomaterialia 5(7) (2009) 2451-2459.
[257] J.Z. Gasiorowski, S.J. Liliensiek, P. Russell, D.A. Stephan, P.F. Nealey, C.J. Murphy, Alterations in gene expression of human vascular endothelial cells associated with nanotopographic cues, Biomaterials 31(34) (2010) 8882-8888.
[258] J.A. Beamish, P. He, K. Kottke-Marchant, R.E. Marchant, Molecular regulation of contractile smooth muscle cell phenotype: implications for vascular tissue engineering, Tissue Engineering Part B: Reviews 16(5) (2010) 467-491.
[259] P. Van Wachem, A. Hogt, T. Beugeling, J. Feijen, A. Bantjes, J. Detmers, W. Van Aken, Adhesion of cultured human endothelial cells onto methacrylate polymers with varying surface wettability and charge, Biomaterials 8(5) (1987) 323-328.
[260] P. Van Wachem, T. Beugeling, J. Feijen, A. Bantjes, J. Detmers, W. Van Aken, Interaction of cultured human endothelial cells with polymeric surfaces of different wettabilities, Biomaterials 6(6) (1985) 403-408.
[261] J. Lu, M.P. Rao, N.C. MacDonald, D. Khang, T.J. Webster, Improved endothelial cell adhesion and proliferation on patterned titanium surfaces with rationally designed, micrometer to nanometer features, Acta biomaterialia 4(1) (2008) 192-201.
[262] M. Moffa, A.G. Sciancalepore, L.G. Passione, D. Pisignano, Combined Nano-and Micro-Scale Topographic Cues for Engineered Vascular Constructs by Electrospinning and Imprinted Micro-Patterns, Small 10(12) (2014) 2439-2450.

[263] P. Kämmerer, M. Heller, J. Brieger, M. Klein, B. Al-Nawas, M. Gabriel, Immobilisation of linear and cyclic RGD-peptides on titanium surfaces and their impact on endothelial cell adhesion and proliferation, Eur Cell Mater 21 (2011) 364-372.
[264] Y.-T. Yeh, S.S. Hur, J. Chang, K.-C. Wang, J.-J. Chiu, Y.-S. Li, S. Chien, Matrix stiffness regulates endothelial cell proliferation through septin 9, PloS one 7(10) (2012) e46889.
[265] C. Golias, A. Charalabopoulos, K. Charalabopoulos, Cell proliferation and cell cycle control: a mini review, International journal of clinical practice 58(12) (2004) 1134-1141.
[266] S.O. Marx, H. Totary-Jain, A.R. Marks, Vascular smooth muscle cell proliferation in restenosis, Circulation: Cardiovascular Interventions 4(1) (2011) 104-111.
[267] X. Gong, J. Yao, H. He, X. Zhao, X. Liu, F. Zhao, Y. Sun, Y. Fan, Combination of flow and micropattern alignment affecting flow-resistant endothelial cell adhesion, Journal of the mechanical behavior of biomedical materials 74 (2017) 11-20.
[268] K.H. Nakayama, V.N. Surya, M. Gole, T.W. Walker, W. Yang, E.S. Lai, M.A. Ostrowski, G.G. Fuller, A.R. Dunn, N.F. Huang, Nanoscale patterning of extracellular matrix alters endothelial function under shear stress, Nano letters 16(1) (2015) 410-419.
[269] J.M. Sneddon, J.R. Vane, Endothelium-derived relaxing factor reduces platelet adhesion to bovine endothelial cells, Proceedings of the National Academy of Sciences 85(8) (1988) 2800-2804.
[270] J.C. Kohn, D.W. Zhou, F. Bordeleau, A.L. Zhou, B.N. Mason, M.J. Mitchell, M.R. King, C.A. Reinhart-King, Cooperative effects of matrix stiffness and fluid shear stress on endothelial cell behavior, Biophysical journal 108(3) (2015) 471-478.
[271] J.-y. Chen, M. Hu, H. Zhang, B.-c. Li, H. Chang, K.-f. Ren, Y.-b. Wang, J. Ji, Improved Antithrombotic Function of Oriented Endothelial Cell Monolayer on Microgrooves, ACS Biomaterials Science & Engineering 4(6) (2017) 1976-1985.
[272] Y.M. Shin, H.J. Shin, Y. Heo, I. Jun, Y.-W. Chung, K. Kim, Y.M. Lim, H. Jeon, H. Shin, Engineering an aligned endothelial monolayer on a topologically modified nanofibrous platform with a micropatterned structure produced by femtosecond laser ablation, Journal of Materials Chemistry B 5(2) (2017) 318-328.
[273] L. Hakanpaa, T. Sipila, V.-M. Leppanen, P. Gautam, H. Nurmi, G. Jacquemet, L. Eklund, J. Ivaska, K. Alitalo, P. Saharinen, Endothelial destabilization by angiopoietin-2 via integrin β1 activation, Nature communications 6 (2015) 5962.
[274] H.A. Strobel, A.D. Dikina, K. Levi, L.D. Solorio, E. Alsberg, M.W. Rolle, Cellular self-assembly with microsphere incorporation for growth factor delivery within engineered vascular tissue rings, Tissue Engineering Part A 23(3-4) (2017) 143-155.
[275] A. Bhattacharyya, S. Lin, M. Sandig, K. Mequanint, Regulation of vascular smooth muscle cell phenotype in three-dimensional coculture system by Jagged1-selective Notch3 signaling, Tissue Engineering Part A 20(7-8) (2014) 1175-1187.
[276] J. Yipeng, X. Yongde, W. Yuanyi, S. Jilei, G. Jiaxiang, G. Jiangping, Y. Yong, Microtissues Enhance Smooth Muscle Differentiation and Cell Viability of hADSCs for Three Dimensional Bioprinting, Frontiers in physiology 8 (2017) 534.

[277] J.M. Carthy, Z. Luo, B.M. McManus, WNT3A induces a contractile and secretory phenotype in cultured vascular smooth muscle cells that is associated with increased gap junction communication, Laboratory Investigation 92(2) (2012) 246.
[278] N. Zempo, R.D. Kenagy, Y.T. Au, M. Bendeck, M.M. Clowes, M.A. Reidy, A.W. Clowes, Matrix metalloproteinases of vascular wall cells are increased in balloon-injured rat carotid artery, Journal of vascular surgery 20(2) (1994) 209-217.
[279] W.S. Edwards, W. Holdefer, M. Mohtashemi, The importance of proper caliber of lumen in femoral-popliteal artery reconstruction, Surgery, gynecology & obstetrics 122(1) (1966) 37.
[280] R.Y. Kannan, H.J. Salacinski, P.E. Butler, G. Hamilton, A.M. Seifalian, Current status of prosthetic bypass grafts: a review, Journal of Biomedical Materials Research Part B: Applied Biomaterials 74(1) (2005) 570-581.
[281] M. Lovett, C. Cannizzaro, L. Daheron, B. Messmer, G. Vunjak-Novakovic, D.L. Kaplan, Silk fibroin microtubes for blood vessel engineering, Biomaterials 28(35) (2007) 5271-5279.
[282] M.L. Lovett, C.M. Cannizzaro, G. Vunjak-Novakovic, D.L. Kaplan, Gel spinning of silk tubes for tissue engineering, Biomaterials 29(35) (2008) 4650-4657.
[283] A. Hasan, A. Memic, N. Annabi, M. Hossain, A. Paul, M.R. Dokmeci, F. Dehghani, A. Khademhosseini, Electrospun scaffolds for tissue engineering of vascular grafts, Acta biomaterialia 10(1) (2014) 11-25.
[284] M.J. McClure, D.G. Simpson, G.L. Bowlin, Tri-layered vascular grafts composed of polycaprolactone, elastin, collagen, and silk: Optimization of graft properties, Journal of the mechanical behavior of biomedical materials 10 (2012) 48-61.
[285] S. Liu, C. Dong, G. Lu, Q. Lu, Z. Li, D.L. Kaplan, H. Zhu, Bilayered vascular grafts based on silk proteins, Acta biomaterialia 9(11) (2013) 8991-9003.
[286] H. Liu, S.G. Wise, J. Rnjak-Kovacina, D.L. Kaplan, M.M. Bilek, A.S. Weiss, J. Fei, S. Bao, Biocompatibility of silk-tropoelastin protein polymers, Biomaterials 35(19) (2014) 5138-5147.
[287] N. L'heureux, S. Pâquet, R. Labbé, L. Germain, F.A. Auger, A completely biological tissue-engineered human blood vessel, The FASEB Journal 12(1) (1998) 47-56.
[288] S. Rayatpisheh, D.E. Heath, A. Shakouri, P.-O. Rujitanaroj, S.Y. Chew, M.B. Chan-Park, Combining cell sheet technology and electrospun scaffolding for engineered tubular, aligned, and contractile blood vessels, Biomaterials 35(9) (2014) 2713-2719.
[289] H. Ahn, Y.M. Ju, H. Takahashi, D.F. Williams, J.J. Yoo, S.J. Lee, T. Okano, A. Atala, Engineered small diameter vascular grafts by combining cell sheet engineering and electrospinning technology, Acta biomaterialia 16 (2015) 14-22.
[290] J.J. Stankus, J. Guan, K. Fujimoto, W.R. Wagner, Microintegrating smooth muscle cells into a biodegradable, elastomeric fiber matrix, Biomaterials 27(5) (2006) 735-744.
[291] B.B. Mandal, S. Das, K. Choudhury, S.C. Kundu, Implication of silk film RGD availability and surface roughness on cytoskeletal organization and proliferation of primary rat bone marrow cells, Tissue Engineering Part A 16(7) (2010) 2391-2403.
[292] A. Gupta, K. Mita, K.P. Arunkumar, J. Nagaraju, Molecular architecture of silk fibroin of Indian golden silkmoth, Antheraea assama, Sci. Rep. 5 (2015) 12706.

[293] C.Y. Hayashi, N.H. Shipley, R.V. Lewis, Hypotheses that correlate the sequence, structure, and mechanical properties of spider silk proteins, International journal of biological macromolecules 24(2-3) (1999) 271-275.
[294] B.B. Mandal, S.-H. Park, E.S. Gil, D.L. Kaplan, Multilayered silk scaffolds for meniscus tissue engineering, Biomaterials 32(2) (2011) 639-651.
[295] L.W. Tien, E.S. Gil, S.H. Park, B.B. Mandal, D.L. Kaplan, Patterned silk film scaffolds for aligned lamellar bone tissue engineering, Macromolecular bioscience 12(12) (2012) 1671-1679.
[296] B.B. Mandal, S. Kapoor, S.C. Kundu, Silk fibroin/polyacrylamide semi-interpenetrating network hydrogels for controlled drug release, Biomaterials 30(14) (2009) 2826-2836.
[297] J.T. Butcher, R.M. Nerem, Porcine aortic valve interstitial cells in three-dimensional culture: comparison of phenotype with aortic smooth muscle cells, Journal of Heart Valve Disease 13(3) (2004) 478-486.
[298] M.F. Cutiongco, D.E. Anderson, M.T. Hinds, E.K. Yim, In vitro and ex vivo hemocompatibility of off-the-shelf modified poly (vinyl alcohol) vascular grafts, Acta biomaterialia 25 (2015) 97-108.
[299] B.B. Mandal, S.C. Kundu, Osteogenic and adipogenic differentiation of rat bone marrow cells on non-mulberry and mulberry silk gland fibroin 3D scaffolds, Biomaterials 30(28) (2009) 5019-5030.
[300] B.B. Mandal, S.-H. Park, E.S. Gil, D.L. Kaplan, Stem cell-based meniscus tissue engineering, Tissue Engineering Part A 17(21-22) (2011) 2749-2761.
[301] J. Kong, S. Yu, Fourier transform infrared spectroscopic analysis of protein secondary structures, Acta biochimica et biophysica Sinica 39(8) (2007) 549-559.
[302] I.C. Um, H. Kweon, Y.H. Park, S. Hudson, Structural characteristics and properties of the regenerated silk fibroin prepared from formic acid, International journal of biological macromolecules 29(2) (2001) 91-97.
[303] B.B. Mandal, S.C. Kundu, Non-bioengineered silk gland fibroin protein: Characterization and evaluation of matrices for potential tissue engineering applications, Biotechnology and bioengineering 100(6) (2008) 1237-1250.
[304] W. Tao, M. Li, C. Zhao, Structure and properties of regenerated Antheraea pernyi silk fibroin in aqueous solution, International journal of biological macromolecules 40(5) (2007) 472-478.
[305] L.W. Dunne, T. Iyyanki, J. Hubenak, A.B. Mathur, Characterization of dielectrophoresis-aligned nanofibrous silk fibroin–chitosan scaffold and its interactions with endothelial cells for tissue engineering applications, Acta biomaterialia 10(8) (2014) 3630-3640.
[306] B.D. Lawrence, J.K. Marchant, M.A. Pindrus, F.G. Omenetto, D.L. Kaplan, Silk film biomaterials for cornea tissue engineering, Biomaterials 30(7) (2009) 1299-1308.
[307] E.S. Gil, S.H. Park, J. Marchant, F. Omenetto, D.L. Kaplan, Response of human corneal fibroblasts on silk film surface patterns, Macromolecular bioscience 10(6) (2010) 664-673.
[308] T. Asakura, H. Yoshimizu, F. Yoshizawa, NMR of silk fibroin. 9. Sequence and conformation analyses of the silk fibroins from Bombyx mori and Philosamia cynthia ricini by 15N NMR spectroscopy, Macromolecules 21(7) (1988) 2038-2041.

[309] R.L. Horan, K. Antle, A.L. Collette, Y. Wang, J. Huang, J.E. Moreau, V. Volloch, D.L. Kaplan, G.H. Altman, In vitro degradation of silk fibroin, Biomaterials 26(17) (2005) 3385-3393.
[310] M. Li, M. Ogiso, N. Minoura, Enzymatic degradation behavior of porous silk fibroin sheets, Biomaterials 24(2) (2003) 357-365.
[311] N. Bhardwaj, W.T. Sow, D. Devi, K.W. Ng, B.B. Mandal, N.-J. Cho, Silk fibroin–keratin based 3D scaffolds as a dermal substitute for skin tissue engineering, Integrative Biology 7(1) (2015) 53-63.
[312] U.-J. Kim, J. Park, H.J. Kim, M. Wada, D.L. Kaplan, Three-dimensional aqueous-derived biomaterial scaffolds from silk fibroin, Biomaterials 26(15) (2005) 2775-2785.
[313] C.S. Chen, M. Mrksich, S. Huang, G.M. Whitesides, D.E. Ingber, Geometric control of cell life and death, Science 276(5317) (1997) 1425-1428.
[314] C. Michiels, Endothelial cell functions, Journal of cellular physiology 196(3) (2003) 430-443.
[315] T. Fukayama, K. Takagi, R. Tanaka, Y. Hatakeyama, D. Aytemiz, Y. Suzuki, T. Asakura, Biological reaction to small-diameter vascular grafts made of silk fibroin implanted in the abdominal aortae of rats, Annals of vascular surgery 29(2) (2015) 341-352.
[316] F.P. Seib, M.F. Maitz, X. Hu, C. Werner, D.L. Kaplan, Impact of processing parameters on the haemocompatibility of Bombyx mori silk films, Biomaterials 33(4) (2012) 1017-1023.
[317] J. Rosenman, R.F. Kempczinski, W. Pearce, E.B. Silberstein, Kinetics of endothelial cell seeding, Journal of vascular surgery 2(6) (1985) 778-784.
[318] P.A. Schneider, S.R. Hanson, T.M. Price, L.A. Harker, Durability of confluent endothelial cell monolayers on small-caliber vascular prostheses in vitro, Surgery 103(4) (1988) 456-462.
[319] D. Seliktar, R.A. Black, R.P. Vito, R.M. Nerem, Dynamic mechanical conditioning of collagen-gel blood vessel constructs induces remodeling in vitro, Annals of biomedical engineering 28(4) (2000) 351-362.
[320] S.I. Jeong, J.H. Kwon, J.I. Lim, S.-W. Cho, Y. Jung, W.J. Sung, S.H. Kim, Y.H. Kim, Y.M. Lee, B.-S. Kim, Mechano-active tissue engineering of vascular smooth muscle using pulsatile perfusion bioreactors and elastic PLCL scaffolds, Biomaterials 26(12) (2005) 1405-1411.
[321] T. Minamino, H. Miyauchi, T. Yoshida, K. Tateno, T. Kunieda, I. Komuro, Vascular cell senescence and vascular aging, Journal of molecular and cellular cardiology 36(2) (2004) 175-183.
[322] L.D. Black, P.G. Allen, S.M. Morris, P.J. Stone, B. Suki, Mechanical and failure properties of extracellular matrix sheets as a function of structural protein composition, Biophysical journal 94(5) (2008) 1916-1929.
[323] B. Marelli, A. Alessandrino, S. Farè, G. Freddi, D. Mantovani, M.C. Tanzi, Compliant electrospun silk fibroin tubes for small vessel bypass grafting, Acta Biomaterialia 6(10) (2010) 4019-4026.
[324] A. Patel, B. Fine, M. Sandig, K. Mequanint, Elastin biosynthesis: the missing link in tissue-engineered blood vessels, Cardiovascular research 71(1) (2006) 40-49.

[325] T. Gillman, Reduplication, remodeling, regeneration, repair, and degeneration of arterial elastic membranes; some implications for the pathogenesis of arterial diseases, AMA archives of pathology 67(6) (1959) 624-642.
[326] C.E. Stowell, Y. Wang, Quickening: Translational design of resorbable synthetic vascular grafts, Biomaterials (2018).
[327] S. Ling, Z. Qin, C. Li, W. Huang, D.L. Kaplan, M.J. Buehler, Polymorphic regenerated silk fibers assembled through bioinspired spinning, Nature communications 8(1) (2017) 1387.
[328] G. Janani, M. Kumar, D. Chouhan, J.C. Moses, A. Gangrade, S. Bhattacharjee, B.B. Mandal, Insight into Silk-Based Biomaterials: From Physicochemical Attributes to Recent Biomedical Applications, ACS Applied Bio Materials (2019).
[329] J.M. Szafron, A. B. Ramachandra, C.K. Breuer, A.L. Marsden, J.D. Humphrey, Optimization of Tissue Engineered Vascular Graft Design Using Computational Modeling, Tissue Engineering (ja) (2019).
[330] T. Tanaka, A. Uemura, R. Tanaka, Y. Tasei, T. Asakura, Comparison of the knitted silk vascular grafts coated with fibroin sponges prepared using glycerin, poly (ethylene glycol diglycidyl ether) and poly (ethylene glycol) as porogens, Journal of biomaterials applications 32(9) (2018) 1239-1252.
[331] A. Gupta, K. Mita, K.P. Arunkumar, J. Nagaraju, Molecular architecture of silk fibroin of Indian golden silkmoth, Antheraea assama, Scientific reports 5(1) (2015) 1-17.
[332] M. Kumar, P. Gupta, S. Bhattacharjee, S.K. Nandi, B.B. Mandal, Immunomodulatory injectable silk hydrogels maintaining functional islets and promoting anti-inflammatory M2 macrophage polarization, Biomaterials 187 (2018) 1-17.
[333] G. Janani, S.K. Nandi, B.B. Mandal, Functional hepatocyte clusters on bioactive blend silk matrices towards generating bioartificial liver constructs, Acta biomaterialia 67 (2018) 167-182.
[334] E. Tamimi, D. Ardila, D. Haskett, T. Doetschman, M. Slepian, R. Kellar, J.V. Geest, Biomechanical comparison of glutaraldehyde-crosslinked gelatin fibrinogen electrospun scaffolds to porcine coronary arteries, Journal of biomechanical engineering 138(1) (2016) 011001.
[335] J.J. Stankus, L. Soletti, K. Fujimoto, Y. Hong, D.A. Vorp, W.R. Wagner, Fabrication of cell microintegrated blood vessel constructs through electrohydrodynamic atomization, Biomaterials 28(17) (2007) 2738-2746.
[336] G.A. Holzapfel, Determination of material models for arterial walls from uniaxial extension tests and histological structure, Journal of theoretical biology 238(2) (2006) 290-302.
[337] L. Soletti, Y. Hong, J. Guan, J.J. Stankus, M.S. El-Kurdi, W.R. Wagner, D.A. Vorp, A bilayered elastomeric scaffold for tissue engineering of small diameter vascular grafts, Acta biomaterialia 6(1) (2010) 110-122.
[338] D.G. Haskett, K.S. Saleh, K.L. Lorentz, A.D. Josowitz, S.K. Luketich, J.S. Weinbaum, L.E. Kokai, A. D'Amore, K.G. Marra, J.P. Rubin, An exploratory study on the preparation and evaluation of a “same-day” adipose stem cell–based tissue-engineered vascular graft, The Journal of thoracic and cardiovascular surgery 156(5) (2018) 1814-1822. e3.

[339] J.T. Krawiec, H.-T. Liao, L.L. Kwan, A. D'Amore, J.S. Weinbaum, J.P. Rubin, W.R. Wagner, D.A. Vorp, Evaluation of the stromal vascular fraction of adipose tissue as the basis for a stem cell-based tissue-engineered vascular graft, Journal of vascular surgery 66(3) (2017) 883-890. e1.
[340] L. Soletti, A. Nieponice, J. Guan, J.J. Stankus, W.R. Wagner, D.A. Vorp, A seeding device for tissue engineered tubular structures, Biomaterials 27(28) (2006) 4863-4870.
[341] J. Horakova, P. Mikes, A. Saman, V. Jencova, A. Klapstova, T. Svarcova, M. Ackermann, V. Novotny, T. Suchy, D. Lukas, The effect of ethylene oxide sterilization on electrospun vascular grafts made from biodegradable polyesters, Materials Science and Engineering: C 92 (2018) 132-142.
[342] A. Nieponice, L. Soletti, J. Guan, Y. Hong, B. Gharaibeh, T.M. Maul, J. Huard, W.R. Wagner, D.A. Vorp, In vivo assessment of a tissue-engineered vascular graft combining a biodegradable elastomeric scaffold and muscle-derived stem cells in a rat model, Tissue Engineering Part A 16(4) (2010) 1215-1223.
[343] H. Stegemann, K. Stalder, Determination of hydroxyproline, Clinica chimica acta 18(2) (1967) 267-273.
[344] B. Starcher, A ninhydrin-based assay to quantitate the total protein content of tissue samples, Analytical biochemistry 292(1) (2001) 125-129.
[345] J.T. Krawiec, J.S. Weinbaum, H.-T. Liao, A.K. Ramaswamy, D.J. Pezzone, A.D. Josowitz, A. D'Amore, J.P. Rubin, W.R. Wagner, D.A. Vorp, In vivo functional evaluation of tissue-engineered vascular grafts fabricated using human adipose-derived stem cells from high cardiovascular risk populations, Tissue Engineering Part A 22(9-10) (2016) 765-775.
[346] L. Zhang, X. Liu, G. Li, P. Wang, Y. Yang, Tailoring degradation rates of silk fibroin scaffolds for tissue engineering, Journal of Biomedical Materials Research Part A 107(1) (2019) 104-113.
[347] C.A. Best, J.M. Szafron, K.A. Rocco, J. Zbinden, E.W. Dean, M.W. Maxfield, H. Kurobe, S. Tara, P.S. Bagi, B.V. Udelsman, Differential outcomes of venous and arterial tissue engineered vascular grafts highlight the importance of coupling long-term implantation studies with computational modeling, Acta biomaterialia (2019).
[348] B.B. Mandal, S.C. Kundu, Cell proliferation and migration in silk fibroin 3D scaffolds, Biomaterials 30(15) (2009) 2956-2965.
[349] K.S. Miller, R. Khosravi, C.K. Breuer, J.D. Humphrey, A hypothesis-driven parametric study of effects of polymeric scaffold properties on tissue engineered neovessel formation, Acta biomaterialia 11 (2015) 283-294.
[350] Z. Wang, Y. Cui, J. Wang, X. Yang, Y. Wu, K. Wang, X. Gao, D. Li, Y. Li, X.-L. Zheng, The effect of thick fibers and large pores of electrospun poly (ε-caprolactone) vascular grafts on macrophage polarization and arterial regeneration, Biomaterials 35(22) (2014) 5700-5710.
[351] L.R. Madden, D.J. Mortisen, E.M. Sussman, S.K. Dupras, J.A. Fugate, J.L. Cuy, K.D. Hauch, M.A. Laflamme, C.E. Murry, B.D. Ratner, Proangiogenic scaffolds as functional templates

for cardiac tissue engineering, Proceedings of the National Academy of Sciences 107(34) (2010) 15211-15216.
[352] W. Wu, R.A. Allen, Y. Wang, Fast-degrading elastomer enables rapid remodeling of a cell-free synthetic graft into a neoartery, Nature medicine 18(7) (2012) 1148.
[353] S. Sengupta, S.-H. Park, G.E. Seok, A. Patel, K. Numata, C.-L. Lu, D.L. Kaplan, Quantifying osteogenic cell degradation of silk biomaterials, Biomacromolecules 11(12) (2010) 3592-3599.
[354] M. Zamani, M. Khafaji, M. Naji, M. Vossoughi, I. Alemzadeh, N. Haghighipour, A biomimetic heparinized composite silk-based vascular scaffold with sustained antithrombogenicity, Scientific reports 7(1) (2017) 4455.
[355] W.J. Geelhoed, L. Moroni, J.I. Rotmans, Utilizing the foreign body response to grow tissue engineered blood vessels in vivo, Journal of cardiovascular translational research 10(2) (2017) 167-179.
[356] X. Dong, X. Yuan, L. Wang, J. Liu, A.C. Midgley, Z. Wang, K. Wang, J. Liu, M. Zhu, D. Kong, Construction of a bilayered vascular graft with smooth internal surface for improved hemocompatibility and endothelial cell monolayer formation, Biomaterials 181 (2018) 1-14.
[357] J.A. Beamish, A.Y. Fu, A.-j. Choi, N.A. Haq, K. Kottke-Marchant, R.E. Marchant, The influence of RGD-bearing hydrogels on the re-expression of contractile vascular smooth muscle cell phenotype, Biomaterials 30(25) (2009) 4127-4135.
[358] Y. Yang, D. Le, H. Zou, S. Huang, Q. Yang, S. Li, F.-L. Qing, X. Ye, Z. You, Q. Zhao, Hybrid Electrospun Rapamycin-Loaded Small-Diameter Decellurized Vascular Grafts Effectively Inhibit Intimal Hyperplasia, Available at SSRN 3368397 (2019).
[359] P. Gupta, B.B. Mandal, Tissue-Engineered Vascular Grafts: Emerging Trends and Technologies, Advanced Functional Materials (2021) 2100027.
[360] A.-M. Kajbafzadeh, R. Khorramirouz, S.M. Kameli, K. Fendereski, S.S. Daryabari, S.M. Tavangar, B.A. Garajegayeh, Three-year efficacy and patency follow-up of decellularized human internal mammary artery as a novel vascular graft in animal models, The Journal of thoracic and cardiovascular surgery 157(4) (2019) 1494-1502.
[361] P. Mallis, E. Michalopoulos, A. Dinou, M.S. Vlachou, E. Panagouli, A. Papapanagiotou, E. Kassi, C.S. Giokas, Development of HLA-matched vascular grafts utilizing decellularized human umbilical artery, Human immunology 79(12) (2018) 855-860.
[362] L. Dall'Olmo, I. Zanusso, R. Di Liddo, T. Chioato, T. Bertalot, E. Guidi, M.T. Conconi, Blood vessel-derived acellular matrix for vascular graft application, BioMed research international 2014 (2014).
[363] M. Zhu, Y. Wu, W. Li, X. Dong, H. Chang, K. Wang, P. Wu, J. Zhang, G. Fan, L. Wang, Biodegradable and elastomeric vascular grafts enable vascular remodeling, Biomaterials 183 (2018) 306-318.
[364] M. Eilenberg, M. Enayati, D. Ehebruster, C. Grasl, I. Walter, B. Messner, S. Baudis, P. Potzmann, C. Kaun, B.K. Podesser, Long Term Evaluation of Nanofibrous, Bioabsorbable Polycarbonate Urethane Grafts for Small Diameter Vessel Replacement in Rodents, European Journal of Vascular and Endovascular Surgery (2019).

[365] J. Fu, X. Ding, C.E. Stowell, Y.-L. Wu, Y. Wang, Slow degrading poly (glycerol sebacate) derivatives improve vascular graft remodeling in a rat carotid artery interposition model, Biomaterials 257 (2020) 120251.
[366] M. Rafique, T. Wei, Q. Sun, A.C. Midgley, Z. Huang, T. Wang, M. Shafiq, D. Zhi, J. Si, H. Yan, The effect of hypoxia-mimicking responses on improving the regeneration of artificial vascular grafts, Biomaterials 271 (2021) 120746.
[367] R.J. Smith, B. Nasiri, J. Kann, D. Yergeau, J.E. Bard, D.D. Swartz, S.T. Andreadis, Endothelialization of arterial vascular grafts by circulating monocytes, Nature communications 11(1) (2020) 1-16.
[368] B. Nasiri, S. Row, R.J. Smith Jr, D.D. Swartz, S.T. Andreadis, Cell-Free Vascular Grafts That Grow with the Host, Advanced Functional Materials n/a(n/a) (2020) 2005769.
[369] D. Hao, Y. Fan, W. Xiao, R. Liu, C. Pivetti, T. Walimbe, F. Guo, X. Zhang, D.L. Farmer, F. Wang, Rapid endothelialization of small diameter vascular grafts by a bioactive integrin-binding ligand specifically targeting endothelial progenitor cells and endothelial cells, Acta Biomaterialia (2020).
[370] M. Wen, D. Zhi, L. Wang, C. Cui, Z. Huang, Y. Zhao, K. Wang, D. Kong, X. Yuan, Local Delivery of Dual MicroRNAs in Trilayered Electrospun Grafts for Vascular Regeneration, ACS Applied Materials & Interfaces 12(6) (2020) 6863-6875.
[371] H. Qiu, P. Qi, J. Liu, Y. Yang, X. Tan, Y. Xiao, M.F. Maitz, N. Huang, Z. Yang, Biomimetic engineering endothelium-like coating on cardiovascular stent through heparin and nitric oxide-generating compound synergistic modification strategy, Biomaterials 207 (2019) 10-22.
[372] R. Daum, D. Visser, C. Wild, L. Kutuzova, M. Schneider, G. Lorenz, M. Weiss, S. Hinderer, U.A. Stock, M. Seifert, Fibronectin Adsorption on Electrospun Synthetic Vascular Grafts Attracts Endothelial Progenitor Cells and Promotes Endothelialization in Dynamic In Vitro Culture, Cells 9(3) (2020) 778.
[373] Y. Duan, S. Yu, P. Xu, X. Wang, X. Feng, Z. Mao, C. Gao, Co-immobilization of CD133 antibodies, vascular endothelial growth factors, and REDV peptide promotes capture, proliferation, and differentiation of endothelial progenitor cells, Acta biomaterialia 96 (2019) 137-148.
[374] X. Liang, Y. Ding, Y. Zhang, H.-F. Tse, Q. Lian, Paracrine mechanisms of mesenchymal stem cell-based therapy: current status and perspectives, Cell transplantation 23(9) (2014) 1045-1059.
[375] Y. Wei, Y. Wu, R. Zhao, K. Zhang, A.C. Midgley, D. Kong, Z. Li, Q. Zhao, MSC-derived sEVs enhance patency and inhibit calcification of synthetic vascular grafts by immunomodulation in a rat model of hyperlipidemia, Biomaterials 204 (2019) 13-24.
[376] W. Chen, M. Yang, J. Bai, X. Li, X. Kong, Y. Gao, L. Bi, L. Xiao, B. Shi, Exosome-Modified Tissue Engineered Blood Vessel for Endothelial Progenitor Cell Capture and Targeted siRNA Delivery, Macromolecular bioscience 18(2) (2018) 1700242.

[377] E.M. Cunnane, K.L. Lorentz, A.K. Ramaswamy, P. Gupta, B.B. Mandal, F.J. O'Brien, J.S. Weinbaum, D.A. Vorp, Extracellular Vesicles Enhance the Remodeling of Cell-Free Silk Vascular Scaffolds in Rat Aortae, ACS Applied Materials & Interfaces 12(24) (2020) 26955-26965.
[378] P. Gupta, K.L. Lorentz, D.G. Haskett, E.M. Cunnane, A.K. Ramaswamy, J.S. Weinbaum, D.A. Vorp, B.B. Mandal, Bioresorbable silk grafts for small diameter vascular tissue engineering applications: In vitro and in vivo functional analysis, Acta Biomaterialia 105 (2020) 146-158.
[379] S. Jadalannagari, G. Converse, C. McFall, E. Buse, M. Filla, M.T. Villar, A. Artigues, A.J. Mellot, J. Wang, M.S. Detamore, Decellularized Wharton's Jelly from human umbilical cord as a novel 3D scaffolding material for tissue engineering applications, PLoS One 12(2) (2017).
[380] K. Sobolewski, A. Małkowski, E. Bańkowski, S. Jaworski, Wharton's jelly as a reservoir of peptide growth factors, Placenta 26(10) (2005) 747-752.
[381] P. Dan, É. Velot, G. Francius, P. Menu, V. Decot, Human-derived extracellular matrix from Wharton's jelly: an untapped substrate to build up a standardized and homogeneous coating for vascular engineering, Acta biomaterialia 48 (2017) 227-237.
[382] N. Bakhtyar, M.G. Jeschke, E. Herer, M. Sheikholeslam, S. Amini-Nik, Exosomes from acellular Wharton's jelly of the human umbilical cord promotes skin wound healing, Stem cell research & therapy 9(1) (2018) 193.
[383] B. Beiki, B. Zeynali, E. Seyedjafari, Fabrication of a three dimensional spongy scaffold using human Wharton's jelly derived extra cellular matrix for wound healing, Materials Science and Engineering: C 78 (2017) 627-638.
[384] R.W. Chan, M.L. Rodriguez, P.S. McFetridge, The human umbilical vein with Wharton's jelly as an allogeneic, acellular construct for vocal fold restoration, Tissue engineering Part A 15(11) (2009) 3537-3546.
[385] M. Kehtari, B. Beiki, B. Zeynali, F.S. Hosseini, F. Soleimanifar, M. Kaabi, M. Soleimani, S.E. Enderami, M. Kabiri, H. Mahboudi, Decellularized Wharton's jelly extracellular matrix as a promising scaffold for promoting hepatic differentiation of human induced pluripotent stem cells, Journal of cellular biochemistry 120(4) (2019) 6683-6697.
[386] D. Li, G. Chiu, B. Lipe, R.A. Hopkins, J. Lillis, J.M. Ashton, S. Paul, O.S. Aljitawi, Decellularized Wharton jelly matrix: a biomimetic scaffold for ex vivo hematopoietic stem cell culture, Blood advances 3(7) (2019) 1011-1026.
[387] D. Kehl, M. Generali, A. Mallone, M. Heller, A.-C. Uldry, P. Cheng, B. Gantenbein, S.P. Hoerstrup, B. Weber, Proteomic analysis of human mesenchymal stromal cell secretomes: a systematic comparison of the angiogenic potential, NPJ Regenerative medicine 4(1) (2019) 1-13.
[388] P.R. Amable, M.V.T. Teixeira, R.B.V. Carias, J.M. Granjeiro, R. Borojevic, Protein synthesis and secretion in human mesenchymal cells derived from bone marrow, adipose tissue and Wharton's jelly, Stem cell research & therapy 5(2) (2014) 53.
[389] M.M. De Santis, H.N. Alsafadi, S. Tas, D.A. Bölükbas, S. Prithiviraj, I.A. Da Silva, M. Mittendorfer, C. Ota, J. Stegmayr, F. Daoud, Extracellular-Matrix-Reinforced Bioinks for 3D Bioprinting Human Tissue, Advanced Materials 33(3) (2021) 2005476.

[390] P. Gupta, M. Kumar, N. Bhardwaj, J.P. Kumar, C. Krishnamurthy, S.K. Nandi, B.B. Mandal, Mimicking form and function of native small diameter vascular conduits using mulberry and non-mulberry patterned silk films, ACS applied materials & interfaces 8(25) (2016) 15874-15888.
[391] N. Saha, R. Shah, P. Gupta, B.B. Mandal, R. Alexandrova, M.D. Sikiric, P. Sáha, PVP-CMC hydrogel: An excellent bioinspired and biocompatible scaffold for osseointegration, Materials Science and Engineering: C 95 (2019) 440-449.
[392] P. Gupta, J.C. Moses, B.B. Mandal, Surface Patterning and Innate Physicochemical Attributes of Silk Films Concomitantly Govern Vascular Cell Dynamics, ACS Biomaterials Science & Engineering 5(2) (2019) 933-949.
[393] S. Bhowmick, A. Jana, K. Singh, P. Gupta, A. Gangrade, B.B. Mandal, N. Das, Coordination-driven self-assembly of ionic irregular hexagonal metallamacrocycles via an organometallic clip and their cytotoxicity potency, Inorganic chemistry 57(7) (2017) 3615-3625.
[394] P.M. Crapo, T.W. Gilbert, S.F. Badylak, An overview of tissue and whole organ decellularization processes, Biomaterials 32(12) (2011) 3233-3243.
[395] P. Graney, S. Ben-Shaul, S. Landau, A. Bajpai, B. Singh, J. Eager, A. Cohen, S. Levenberg, K. Spiller, Macrophages of diverse phenotypes drive vascularization of engineered tissues, Science Advances 6(18) (2020) eaay6391.
[396] C.E. Witherel, D. Abebayehu, T.H. Barker, K.L. Spiller, Macrophage and Fibroblast Interactions in Biomaterial-Mediated Fibrosis, Advanced healthcare materials 8(4) (2019) 1801451.
[397] S. Row, H. Peng, E.M. Schlaich, C. Koenigsknecht, S.T. Andreadis, D.D. Swartz, Arterial grafts exhibiting unprecedented cellular infiltration and remodeling in vivo: The role of cells in the vascular wall, Biomaterials 50 (2015) 115-126.
[398] D. Yao, H. Liu, Y. Fan, Fabrication of water-stable silk fibroin scaffolds through self-assembly of proteins, RSC advances 6(66) (2016) 61402-61409.
[399] T. Sologashvili, S.A. Saat, J.-C. Tille, S. De Valence, D. Mugnai, J.P. Giliberto, J. Dillon, A. Yakub, Z. Dimon, R. Gurny, Effect of implantation site on outcome of tissue-engineered vascular grafts, European Journal of Pharmaceutics and Biopharmaceutics 139 (2019) 272-278.
[400] T. Sugiura, S. Tara, H. Nakayama, H. Kurobe, T. Yi, Y.-U. Lee, A.Y. Lee, C.K. Breuer, T. Shinoka, Novel bioresorbable vascular graft with sponge-type scaffold as a small-diameter arterial graft, The Annals of thoracic surgery 102(3) (2016) 720-727.
[401] Y. Hong, S.-H. Ye, A. Nieponice, L. Soletti, D.A. Vorp, W.R. Wagner, A small diameter, fibrous vascular conduit generated from a poly (ester urethane) urea and phospholipid polymer blend, Biomaterials 30(13) (2009) 2457-2467.
[402] J.T. Patterson, T. Gilliland, M.W. Maxfield, S. Church, Y. Naito, T. Shinoka, C.K. Breuer, Tissue-engineered vascular grafts for use in the treatment of congenital heart disease: from the bench to the clinic and back again, Regenerative medicine 7(3) (2012) 409-419.
[403] Y.-U. Lee, N. Mahler, C.A. Best, S. Tara, T. Sugiura, A.Y. Lee, T. Yi, N. Hibino, T. Shinoka, C. Breuer, Rational design of an improved tissue-engineered vascular graft: determining the optimal cell dose and incubation time, Regenerative medicine 11(2) (2016) 159-167.

[404] N. Hibino, T. Yi, D.R. Duncan, A. Rathore, E. Dean, Y. Naito, A. Dardik, T. Kyriakides, J. Madri, J.S. Pober, A critical role for macrophages in neovessel formation and the development of stenosis in tissue-engineered vascular grafts, The FASEB Journal 25(12) (2011) 4253-4263.
[405] B.K. Bhunia, B.B. Mandal, Exploring gelation and physicochemical behavior of in situ bioresponsive silk hydrogels for disc degeneration therapy, ACS Biomaterials Science & Engineering 5(2) (2018) 870-886.
[406] Z. Zhuang, S. Yoshizawa-Smith, A. Glowacki, K. Maltos, C. Pacheco, M. Shehabeldin, M. Mulkeen, N. Myers, R. Chong, K. Verdelis, Induction of M2 macrophages prevents bone loss in murine periodontitis models, Journal of dental research 98(2) (2019) 200-208.
[407] J.T. Krawiec, J.S. Weinbaum, C.M. St. Croix, J.A. Phillippi, S.C. Watkins, J.P. Rubin, D.A. Vorp, A cautionary tale for autologous vascular tissue engineering: impact of human demographics on the ability of adipose-derived mesenchymal stem cells to recruit and differentiate into smooth muscle cells, Tissue Engineering Part A 21(3-4) (2015) 426-437.
[408] E.H. Phillips, A.A. Yrineo, H.D. Schroeder, K.E. Wilson, J.-X. Cheng, C.J. Goergen, Morphological and biomechanical differences in the elastase and AngII apoE−/− rodent models of abdominal aortic aneurysms, BioMed research international 2015 (2015).
[409] T. Afewerki, S. Ahmed, D. Warren, Emerging regulators of vascular smooth muscle cell migration, Journal of Muscle Research and Cell Motility 40(2) (2019) 185-196.
[410] I. Bružauskaitė, D. Bironaitė, E. Bagdonas, E. Bernotienė, Scaffolds and cells for tissue regeneration: different scaffold pore sizes—different cell effects, Cytotechnology 68(3) (2016) 355-369.
[411] Q.L. Loh, C. Choong, Three-dimensional scaffolds for tissue engineering applications: role of porosity and pore size, Tissue Engineering Part B: Reviews 19(6) (2013) 485-502.
[412] C.A. Best, J.M. Szafron, K.A. Rocco, J. Zbinden, E.W. Dean, M.W. Maxfield, H. Kurobe, S. Tara, P.S. Bagi, B.V. Udelsman, R. Khosravi, T. Yi, T. Shinoka, J.D. Humphrey, C.K. Breuer, Differential outcomes of venous and arterial tissue engineered vascular grafts highlight the importance of coupling long-term implantation studies with computational modeling, Acta Biomaterialia 94 (2019) 183-194.

LIST OF PUBLICATIONS

LIST OF PUBLICATIONS

Publications from Ph.D. Thesis:

(A) Journal Publications:

1. **Prerak Gupta** and Biman B. Mandal. Tissue-engineered vascular grafts: Emerging trends and technologies. ***Advanced Functional Materials***. 2021; 2100027. (DOI: 10.1002/adfm.202100027)
2. **Prerak Gupta** and Biman B. Mandal. Implications of silk biomaterials for vascular tissue engineering applications. (Revision submitted to *'**Acta Biomaterialia**'*)
3. **Prerak Gupta**, Joseph Christakiran Moses and Biman B. Mandal. Surface patterning and innate physicochemical attributes of silk films concomitantly govern vascular cell dynamics. ***ACS Biomaterials Science & Engineering***. 2019; 5:933-49.
4. **Prerak Gupta**, Manishekhar Kumar, Nandana Bhardwaj, Jadi Praveen Kumar, CS Krishnamurthy and Biman B. Mandal. Mimicking form and function of native small diameter vascular conduits using mulberry and non-mulberry patterned silk films. ***ACS Applied Materials & Interfaces***. 2016; 8:15874-88.
5. **Prerak Gupta**, Katherine L. Lorentz, Darren G. Haskett, Eoghan M. Cunnane, Aneesh Ramaswamy, Justin S. Weinbaum, David A. Vorp and Biman B. Mandal. Bioresorbable silk grafts for small diameter vascular tissue engineering applications: *In vitro* and *in vivo* functional analysis. ***Acta Biomaterialia***. 2020; 105: 146-158.
6. **Prerak Gupta**[#], Gaurab Ranjan Chaudhuri[#], G. Janani, Manoj Agarwala, Debaki Ghosh, Samit K. Nandi, Biman B. Mandal. functionalized silk vascular grafts with decellularized human Wharton's jelly improves remodeling via immunomodulation in rabbit jugular vein. (#Co-First Authors) (Revision submitted to '***Advanced Healthcare Materials***')
7. Katherine L Lorentz[#], **Prerak Gupta**[#], Mostafa S Shehabeldin, Eoghan M Cunnane, Aneesh K Ramaswamy, Kostas Verdelis, Morgan V Fedorchak, Steven R Little, Justin S Weinbaum, Charles S Sfeir, Biman B Mandal, David A Vorp. CCL2 microparticles promote acute patency in silk-based vascular grafts. (#Co-First Authors) (Revision submitted to '***Acta Biomaterialia***')

(B) Patents:

1. **Prerak Gupta** & Biman B. Mandal- Patterned silk film based vascular graft construct and its use thereof. (Indian patent application number 1246/KOL/2015, Dated 04/12/2015).
2. **Prerak Gupta** & Biman B. Mandal - Bi-layered porous silk vascular grafts and their uses thereof. (Indian patent application number 201931024432, Dated 16/06/2021).

(C) Book Chapters:

1. **Prerak Gupta** and Biman B. Mandal. Chapter 11: Fabrication of small diameter vascular conduits using mulberry and non-mulberry silk biomaterial. Editors: Feng Zhao and Kam W. Leong. ***Vascular Tissue Engineering: Methods and Protocols, Methods in Molecular Biology***, *vol. 2375,* Springer Nature; 2020. (Accepted) (DOI:10.1007/978-1-0716-1708-3_11,

(D) Conference Publications:

1. **Prerak Gupta**, Katherine L. Lorentz, Darren G. Haskett, Eoghan M. Cunnane, Aneesh K. Ramaswamy, Justin S. Weinbaum, David A. Vorp, Biman B. Mandal. Functional analysis of tubular bi-layered silk scaffolds in a rat aortic model for vascular tissue engineering applications. ***The International Journal of Artificial Organs***, 2019; 42 (1): 1–26.
2. **Prerak Gupta,** Biman B. Mandal. Surface Topography of silk films influences the functional behaviour of vascular cells. ***Tissue Engineering Part A***, 2017; S57-S.
3. **Prerak Gupta**, Manishekhar Kumar, Nandana Bhardwaj, Jadi Praveen Kumar, C. S. Krishnamurthy, Samit K. Nandi and Biman B. Mandal. Bioengineered silk vascular grafts for coronary artery bypass surgery. ***European Cells & Materials***, 2016; 31:231.

(E) Conference, Seminar, Workshop Participation/Presentations:

1. **Prerak Gupta**, Gaurab Ranjan Chaudhuri, G. Janani, Manoj Agarwala, Debaki Ghosh, Samit K. Nandi, Biman B. Mandal. Decellularized human Wharton's jelly facilitates remodeling of cell-free silk vascular grafts in rabbit jugular vein via immunomodulation. Cardiovascular Metabolic Week (CVMW2020). Organized by The International Society for Applied Cardiovascular Biology in Tokyo, Japan; March 12-13, 2021. (Virtual Oral Presentation)
2. **Prerak Gupta**, Gaurab Ranjan Chaudhuri, G. Janani, Manoj Agarwala, Debaki Ghosh, Samit K. Nandi, Biman B. Mandal. Human Wharton's Jelly-Silk Composite Grafts for Small-Diameter Vascular Tissue Engineering Applications. International Conference on Biomedical Materials Innovation-2020 (ICBMI-2020), virtual conference organized by Bharathiar University, India; Dec 6-9, 2020. (Oral Presentation)
3. **Prerak Gupta**, Katherine L. Lorentz, Darren G. Haskett, Eoghan M. Cunnane, Aneesh Ramaswamy, Justin S. Weinbaum, David A. Vorp, Biman B. Mandal. Functional analysis of tubular bi-layered silk scaffolds in rat aortic model for vascular tissue engineering applications. Combined symposium of The International Society for Applied Cardiovascular Biology and International Society of Vascular Tissue Engineering (ISACB + ISVTE 2019), University of Zurich, Zurich, Switzerland; June 19-21, 2019. (3-minute lightening talk and Poster presentation)

4. **Prerak Gupta**, Katherine L. Lorentz, Darren G. Haskett, Eoghan M. Cunnane, Aneesh Ramaswamy, Justin S. Weinbaum, David A. Vorp, Biman B. Mandal. Functional in vivo performance of adipose stem cells seeded small diameter silk vascular grafts. Research Conclave 2019, IIT Guwahati, India; March 14-17, 2019. (**1st prize in poster presentation**)
5. **Prerak Gupta**, Katherine L. Lorentz, Darren G. Haskett, Eoghan M. Cunnane, Aneesh Ramaswamy, Justin S. Weinbaum, David A. Vorp, Biman B. Mandal. In vitro and in vivo evaluation of bi-layered tubular silk scaffolds for vascular tissue engineering applications. ICFNM-2019, IIT BHU, Varanasi, India; February 22-25, 2019. **(1st prize in oral presentation)**
6. **Prerak Gupta**, Katherine L. Lorentz, Darren G. Haskett, Eoghan M. Cunnane, Justin S. Weinbaum, David A. Vorp and Biman B. Mandal. Bi-layered tubular silk scaffolds for vascular tissue engineering applications. Sixteenth annual Richard L. Simmon lecture in surgical science and department, University of Pittsburgh, PA, USA; May 2, 2018. (Poster Presentation)
7. **Prerak Gupta** and Biman B. Mandal. Surface topography of silk films influence the functional behavior of vascular cells. TERMIS–Americas, Charlotte, NC, USA; December 3-6, 2017. (Poster Presentation)
8. **Prerak Gupta**, Manishekhar Kumar, Nandana Bhardwaj, Jadi Praveen Kumar, C. S. Krishnamurthy, Samit Kumar Nandi and Biman B. Mandal, Mimicking form and function of native small diameter vascular conduits using mulberry and non-mulberry patterned silk films. Research Conclave 2017, IIT Guwahati, India (Poster presentation, **Best Poster Award both at Department and Institute level)**
9. **Prerak Gupta**, Biman B. Mandal. Bioengineered silk grafts for small diameter blood vessel replacement. BiTERM 2016, IIT Delhi, India. (Poster presentation)

Publications from Other Collaborative Research Projects:

(A) Journal Publications:

1. **Prerak Gupta**, Mimi Adhikary, Joseph Christakiran Moses, Manishekhar Kumar, Nandana Bhardwaj and Biman B. Mandal. Biomimetic, osteoconductive non-mulberry silk fiber reinforced tricomposite scaffolds for bone tissue engineering. ***ACS Applied Materials & Interfaces***. 2016; 8:30797-810.
2. Manishekhar Kumar, **Prerak Gupta**, Sohenii Bhattacharjee, Samit K. Nandi and Biman B. Mandal. Immunomodulatory injectable silk hydrogels maintaining functional islets and promoting anti-inflammatory M2 macrophage polarization. ***Biomaterials***. 2018; 187:1-17.
3. Rocktotpal Konwarh, **Prerak Gupta** and Biman B. Mandal. Silk-microfluidics for advanced biotechnological applications: A progressive review. ***Biotechnology Advances***. 2016; 34:845-58.

4. Charanya Ramachandran, **Prerak Gupta**, Swatilekha Hazra and Biman B. Mandal. *In vitro* culture of human corneal endothelium on silk fibroin films for tissue regeneration. ***Translational Vision Science & Technology***. 2020; 9(4): 12-12.
5. Nabanita Saha, Rushita Shah, **Prerak Gupta**, Biman B. Mandal, Radostina Alexandrova, Maja Dutour Sikiric and Petr Saha. PVP-CMC hydrogel: An excellent bioinspired and biocompatible scaffold for osseointegration. ***Materials Science and Engineering: C***. 2019; 95: 440-9.
6. Rituparna Duarah, Yogendra Pratap Singh, **Prerak Gupta**, Biman B. Mandal and Niranjan Karak. Smart self-tightening surgical suture from a tough bio-based hyperbranched polyurethane/reduced carbon dot nanocomposite. ***Biomedical Materials***. 2018;13:045004.
7. Rituparna Duarah, Yogendra Pratap Singh, **Prerak Gupta**, Biman B. Mandal and Niranjan Karak. High performance bio-based hyperbranched polyurethane/carbon dot-silver nanocomposite: a rapid self-expandable stent. ***Biofabrication***. 2016;8:045013.
8. Eoghan M. Cunnane, Katherine L. Lorentz, Aneesh K. Ramaswamy, **Prerak Gupta**, Biman B. Mandal, Fergal J. O'Brien, Justin S. Weinbaum, and David A. Vorp. Extracellular vesicles enhance the remodeling of cell-free silk vascular scaffolds in rat aortae. ***ACS Applied Materials & Interfaces***. 2020; 12(24): 26955-26965.
9. Sourav Bhowmick, Achintya Jana, Subba R. Marri, **Prerak Gupta**, J.N. Behera, Biman B. Mandal and Neeladri Das. Pyrazine based Pt (II) bis-alkynyl organometallic complexes: Synthesis, characterization, and cytotoxic effect on A549 human lung carcinoma cells. ***Applied Organometallic Chemistry***. 2017; 31:e3824.
10. Sourav Bhowmick, Achintya Jana, Khushwant Singh, **Prerak Gupta**, Ankit Gangrade, Biman B. Mandal and Neeladri Das. Coordination-driven self-assembly of ionic irregular hexagonal metallamacrocycles via an organometallic clip and their cytotoxicity potency. ***Inorganic Chemistry***. 2017; 57:3615-25.
11. Manishekhar Kumar, Deepak Jain, Nandana Bhardwaj, **Prerak Gupta**, Samit K. Nandi, Biman B. Mandal. Native honeybee silk membrane: a potential matrix for tissue engineering and regenerative medicine. ***RSC Advances***. 2016;6:54394-403.

(B) <u>Book Chapters:</u>

1. Promita Bhattacharjee, **Prerak Gupta**, Joseph Christakiran Moses, Samit K. Nandi and Biman B. Mandal. Chapter 12: Silk-based matrices for bone tissue engineering applications. Editor: Alexandru Mihai Grumezescu. ***Nanostructures for the Engineering of Cells, Tissues and Organs***: Elsevier; 2018: 439-72.

(C) <u>Conference Publications</u>

1. Joseph Christakiran Moses, **Prerak Gupta**, Biman B. Mandal. Osteoinductive and proangiogenic bioactive glass silk composite scaffolds towards resorbable and

vascularized bone grafts. ***Tissue Engineering Part A***: Mary Ann Liebert, INC 140 Huguenot street, 3rd fl, New Rochelle, NY 10801 USA; 2017. p. S89-S.

2. Mimi Adhikary, **Prerak Gupta**, Manishekhar Kumar, Salma Jasmine, Nandana Bhardwaj, Dimple Chouhan and Biman B. Mandal. Hydroxyapatite-silk fiber-silk fibroin tri-composite scaffolds for bone tissue engineering. ***European Cells & Materials***, 2016; 31:18.

Awards & Achievements:

1. **DST Travel Grant Award 2019 (SERB)** to attend ISACB + ISVTE 2019, Zurich, Switzerland (June 19-21, 2019).
2. **Fulbright Nehru Doctoral Research Fellowship (Aug 2017-May 2018),** visited University of Pittsburgh for 9 months, award financed by United States India Education Foundation (USIEF) and Institute of International Education (IIE) New York.
3. **Student Scientist Award** at TERMIS–Americas 2017, Charlotte, NC, USA. (**Cash award 400 USD**)